Thermo-Microstructural-Mechanical Modeling for Laser Wire Deposition of Titanium Alloys

Qi Zhang

Department of Mining and Materials Engineering

McGill University, Montreal, Quebec, Canada

December 2024
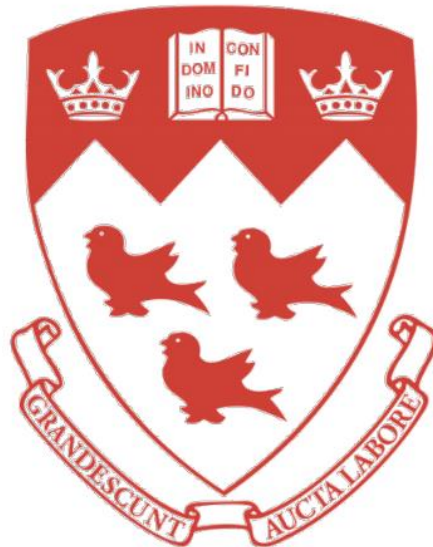
A thesis submitted to McGill University in partial fulfillment of the requirements of the degree of Doctor of Philosophy

Abstract

Additive manufacturing (AM) is attracting significant attention for its ability to fabricate near-net-shape components in a layer-by-layer fashion and to reduce the buy-to-fly (BTF) ratio compared to traditional manufacturing methods. Titanium alloys have been of great interest to the aerospace industry due to their high specific strength and excellent corrosion resistance. However, the fabrication of qualified AM titanium alloy components still requires exploration over a large amount of processing parameters, and it remains challenging to understand the process-structure-property relationship for AM Ti-6Al-4V. This research introduced a new manufacturing methodology based on reverse engineering methods to propose a recipe of processing parameters based on the service property requirements for AM Ti-6Al-4V components. This methodology, comprised of three mechanistic models to predict and control the key variables in the AM process: thermal history, microstructure, and mechanical properties. In addition, this research aims to fill the knowledge gap by investigating the effect of travel speed, wire diameter, and oxygen content on cooling rates, microstructure, and mechanical properties of single bead width parts made from laser wire deposition (LWD) of Ti-6Al-4V.

First, a 10-layer 3D transient heat transfer finite element analysis (FEA) model with the same size specification as the deposits was developed to simulate the LWD process. The predicted cooling rates were compared with the calculated cooling rates measured using a thermal camera, and the deviation was found below 10%, which confirmed the accuracy of the FEA model. The study of the correlation between the evolution of the cooling rates and layers demonstrated that the cooling rate reached a plateau after the deposition of about 6 layers indicating, that the 10-layer model can be used to infer the cooling rates for the deposits with hundreds of layers. This research then builds on a microstructure model based on the internal state variable approach from the literature, which predicted α/β phase fractions and α lath width from the input thermal history. The comparison between the predicted microstructure and the experimentally quantified microstructure confirmed the reliability of the microstructure model. In this research, the constitutive equations developed based on an artificial neural network (ANN) and genetic algorithm (GA) from the literature were used to predict the yield strength of Ti-6Al-4V based on the microstructural quantified features including phase fractions, grain size, element concentration, and dislocation density. The predicted yield strength was compared with the tensile yield strength, and the model showed high accuracy

with a deviation of less than 10%. The yield strength model incorporated the main strengthening mechanisms such as intrinsic strength, solid solution strengthening (SSS), Hall-Petch strength, and Taylor hardening. The SSS strengthening mechanism was found to be the most sensitive in affecting the total absolute yield strength over the controlled range of corresponding microstructural features.

Next, to validate the aforementioned models, a series of LWD Ti-6Al-4V coupons were fabricated in two geometries with different travel speeds, wire diameters and oxygen content to extract tensile coupons along the build direction (Z) and travel direction (X). Anisotropic tensile strength was found for all deposits between Z and X directions, which can be explained by three mechanisms: the difference in texture, the columnar β grain morphology, and the presence of grain boundary α from different tensile directions.

First, for the set of coupons with varied travel speeds, it was found that cooling rates increased with the increase of the travel speed, resulting in finer grains and higher tensile strength. In addition to the major columnar prior β grains, the macrostructure showed some equiaxed grains at the edge and certain areas of the deposits due to columnar to equiaxed transition (CET). Comparison between the calculated thermal gradient G, growth rate R and the solidification map confirmed the morphology of the solidification structure. The CET was discussed to be induced by the altered solidification conditions during deposition. For example, the heat accumulation at the edge lowered G and promoted the development of equiaxed grains.

Second, for the set of coupons with varied wire diameters, it was found that increasing wire diameter resulted in non-uniform melt pool width and inconsistent wall profiles due to unstable thermal conditions during deposition. Increased heat input and decreased cooling rates were found with increased wire diameter. As a result, coarser grains and lower tensile strength were reported with increased wire diameter. In addition, the colony α structure was observed near the prior β grain boundaries for deposits with increased wire diameter which could facilitate crack propagation and reduce elongation. Moreover, fractography indicated pre-existing defects such as pores induced by lack of fusion for deposits fabricated with increased wire diameter which could lead to premature failure and reduced elongation.

Finally, for the set of coupons fabricated at various oxygen levels, it was found that the deposit fabricated with increased oxygen content exhibited dramatically higher strength and hardness due to

lattice parameter expansion by interstitial oxygen. A combination of columnar and equiaxed morphology was found and confirmed by the comparison between solidification conditions (*G* and *R*) and the solidification map. The deposits with increased oxygen content were able to maintain both excellent tensile strength and elongation. The yield strength model confirmed that the great enhancement came from the contribution of the solid solution strengthening mechanism.

All mechanistic models were validated by experimental results with high accuracy. This proves that the methodology can be further applied to the fabrication of qualified LWD Ti-6Al-4V components.

Résumé

La fabrication additive (AM) suscite une attention particulière en raison de sa capacité à fabriquer des composants de forme quasi nette couche par couche et à réduire le rapport achat-vol (BTF) par rapport aux méthodes de fabrication traditionnelles. Les alliages de titane suscitent un grand intérêt dans l'industrie aérospatiale en raison de leur résistance spécifique élevée et de leur excellente résistance à la corrosion. Cependant, la fabrication de composants en alliage de titane AM qualifiés nécessite encore l'exploration d'un grand nombre de paramètres de traitement, et il reste difficile de comprendre la relation processus-structure-propriété pour l'AM Ti-6Al-4V. Cette recherche a introduit une nouvelle méthodologie de fabrication basée sur des méthodes d'ingénierie inverse pour proposer une recette de paramètres de traitement basée sur les exigences de propriétés de service pour les composants AM Ti-6Al-4V. Cette méthodologie, composée de trois modèles mécanistes pour prédire et contrôler les variables clés du processus AM : l'historique thermique, la microstructure et les propriétés mécaniques. De plus, cette recherche vise à combler le manque de connaissances en étudiant l'effet de la vitesse de déplacement, du diamètre du fil et de la teneur en oxygène sur les taux de refroidissement, la microstructure et les propriétés mécaniques des pièces à largeur de cordon unique fabriquées à partir du dépôt de fil laser (LWD) de Ti-6Al-4V.

Tout d'abord, un modèle d'analyse par éléments finis (FEA) de transfert de chaleur transitoire 3D à 10 couches avec la même spécification de taille que les dépôts a été développé pour simuler le processus LWD. Les taux de refroidissement prévus ont été comparés aux taux de refroidissement calculés mesurés à l'aide d'une caméra thermique, et l'écart a été trouvé inférieur à 10 %, ce qui a confirmé la précision du modèle FEA. L'étude de la corrélation entre l'évolution des taux de refroidissement et des couches a démontré que le taux de refroidissement a atteint un plateau après le dépôt d'environ 6 couches indiquant que le modèle à 10 couches peut être utilisé pour déduire les taux de refroidissement des dépôts avec des centaines de couches. Cette recherche s'appuie ensuite sur un modèle de microstructure basé sur l'approche des variables d'état internes de la littérature, qui prédit les fractions de phase α/β et la largeur de la latte α à partir de l'historique thermique d'entrée. La comparaison entre la microstructure prédite et la microstructure quantifiée expérimentalement a confirmé la fiabilité du modèle de microstructure. Dans cette recherche, les équations constitutives développées sur la base d'un réseau neuronal artificiel (RNA) et d'un algorithme génétique (GA) de la littérature ont été utilisées pour prédire la limite d'élasticité du Ti-6Al-4V en fonction des caractéristiques microstructurelles quantifiées, notamment les fractions de phase, la taille des grains,

la concentration en éléments et la densité de dislocations. La limite d'élasticité prédite a été comparée à la limite d'élasticité en traction, et le modèle a montré une grande précision avec un écart inférieur à 10 %. Le modèle de limite d'élasticité intègre les principaux mécanismes de renforcement tels que la résistance intrinsèque, le renforcement en solution solide (SSS), la résistance Hall-Petch et le durcissement de Taylor. Le mécanisme de renforcement SSS s'est avéré le plus sensible pour affecter la limite d'élasticité absolue totale sur la plage contrôlée des caractéristiques microstructurelles correspondantes.

Ensuite, pour valider les modèles susmentionnés, une série de coupons Ti-6Al-4V LWD ont été fabriqués dans deux géométries avec des vitesses de déplacement, des diamètres de fil et une teneur en oxygène différents pour extraire les coupons de traction le long de la direction de construction (Z) et de la direction de déplacement (X). Une résistance à la traction anisotrope a été trouvée pour tous les dépôts entre les directions Z et X, ce qui peut s'expliquer par trois mécanismes : la différence de texture, la morphologie des grains β colonnaires et la présence de joints de grains α provenant de différentes directions de traction.

Tout d'abord, pour l'ensemble des coupons avec des vitesses de déplacement variées, il a été constaté que les taux de refroidissement augmentaient avec l'augmentation de la vitesse de déplacement, ce qui se traduisait par des grains plus fins et une résistance à la traction plus élevée. En plus des principaux grains β colonnaires a priori, la macrostructure présentait des grains équiaxes sur le bord et certaines zones des dépôts en raison de la transition colonnaire à équiaxe (CET). La comparaison entre le gradient thermique calculé G, le taux de croissance R et la carte de solidification a confirmé la morphologie de la structure de solidification. Il a été discuté que le CET était induit par les conditions de solidification modifiées pendant le dépôt. Par exemple, l'accumulation de chaleur au bord a abaissé G et favorisé le développement de grains équiaxes.

Deuxièmement, pour l'ensemble des coupons avec des diamètres de fil variés, il a été constaté que l'augmentation du diamètre du fil entraînait une largeur de bain de fusion non uniforme et des profils de paroi incohérents en raison de conditions thermiques instables pendant le dépôt. Un apport de chaleur accru et des taux de refroidissement réduits ont été constatés avec un diamètre de fil accru. En conséquence, des grains plus grossiers et une résistance à la traction plus faible ont été signalés avec un diamètre de fil accru. De plus, la structure de la colonie α a été observée près des limites de grains β antérieures pour les dépôts avec un diamètre de fil accru, ce qui pourrait faciliter

la propagation des fissures et réduire l'allongement. De plus, la fractographie a indiqué des défauts préexistants tels que des pores induits par le manque de fusion pour les dépôts fabriqués avec un diamètre de fil accru, ce qui pourrait entraîner une défaillance prématurée et une réduction de l'allongement.

Enfin, pour l'ensemble des coupons fabriqués à différents niveaux d'oxygène, il a été constaté que le dépôt fabriqué avec une teneur en oxygène accrue présentait une résistance et une dureté considérablement plus élevées en raison de l'expansion des paramètres de réseau par l'oxygène interstitiel. Une combinaison de morphologie colonnaire et équiaxe a été trouvée et confirmée par la comparaison entre les conditions de solidification (G et R) et la carte de solidification. Les dépôts à teneur en oxygène accrue ont pu maintenir à la fois une excellente résistance à la traction et un excellent allongement. Le modèle de limite d'élasticité a confirmé que la grande amélioration provenait de la contribution du mécanisme de renforcement de la solution solide.

Tous les modèles mécanistes ont été validés par des résultats expérimentaux avec une grande précision. Cela prouve que la méthodologie peut être appliquée à la fabrication de composants LWD Ti-6Al-4V qualifiés.

Table of Contents

List of Figures

XII

XIII

XV

List of Tables

List of Abbreviations

AM – Additive Manufacturing

AMS – Aerospace Material Specifications

ANN – Artificial Neural Network

ASTM – American Society for Testing and Materials

BOR – Burgers Orientation Relationship

BTF – Buy to Fly

CA – Cellular Automata

CCT – Continuous Cooling Transformation

CET – Columnar to Equiaxed Transition

CRSS – Critical Resolved Shear Stress

CU – Constitutional Undercooling

DED – Directed Energy Deposition

EBAM – Electron Beam Additive Manufacturing

FEA – Finite Element Analysis

G – Thermal Gradient

GA – Genetic Algorithms

LPD – Laser Powder Deposition

LWD – Laser Wire Deposition

MC – Monte Carlo

PBF – Powder Bed Fusion

PF – Phase Field

R – Solidification Rate

SEM – Scanning Electron Microscope

SMD – Shaped Metal Deposition

TEM – Transmission Electron Microscope

TTT – Time Temperature Transformation

UTS – Ultimate Tensile Strength

YS – Yield Strength

Acknowledgments

Above all, I would like to thank my family for their unconditional love and support throughout my PhD study. Thank you, Mom, for your financial support and always believing in me especially when I needed it the most. I am so lucky to have you as my role model who taught me to be brave, caring, and strong. I could not have started and completed my PhD study alone in a foreign country without your constant support especially during pandemic time. Thank you, Qidong, my life partner, for providing such generous emotional support and enduring all my negativity during the long-distance relationship. You will always be the "co-author" of my life.

Contributions of Authors

This thesis contains three manuscripts, which have been submitted in peer reviewed journals. Each of three manuscripts is listed in Chapter 5, 6, and 7, respectively. The contributions of the authors of each manuscript are summarized below.

1. Zhang, Q., Sikan, F., Chekir, N., & Brochu, M. (2024). Thermo-Microstructural-Mechanical Modeling on Effect of Travel Speeds on Thin Ti-6Al-4V Deposits Developed by Laser Wire Deposition. Journal of Materials Research and Technology. https://doi.org/10.1016/j.jmrt.2024.11.120

2. Zhang, Q., Chekir, N., & Brochu, M. (2024). Thermo-microstructural-mechanical modeling of the effect of wire diameters on single-bead Ti-6Al-4V wall deposits by laser wire deposition. Journal of Alloys and Metallurgical Systems. https://doi.org/10.1016/j.jalmes.2024.100134

3. Zhang, Q., Chekir, N., & Brochu, M. (Submitted). Effect of Oxygen Content on Thin Ti-6Al-4V Deposits Developed by Laser Wire Deposition. Journal of Alloys and Compounds. (JALCOM-D-24-14183)

Ms. Qi Zhang, as the first author, developed the main idea of the study, conducted all the experiments, analyzed all the results, and wrote all the manuscripts.

Dr. Fatih Sikan offered technical expertise on finite element modeling and participated in the discussion of the results for Chapter 5.

Dr. Nejib Chekir provided support for the sample fabrication and offered technical and scientific advice for each manuscript.

Prof. Mathieu Brochu supervised the entire project and supplied technical and scientific advice for each manuscript.

Chapter 1: Introduction

1.1 Background

Additive Manufacturing (AM), a layer-by-layer manufacturing process, has gained great interest for producing near-net-shape components with complicated geometry. It is defined by the ASTM F42 Technical Committee as "a process of joining materials to make objects from three-dimensional (3D) model data, usually layer upon layer, as opposed to subtractive manufacturing methodologies" [1]. Over the past few decades, AM has revolutionized the manufacturing industry by providing cost savings over traditional subtractive manufacturing techniques that produce large amounts of waste [2]. AM is considered to be a tool-free, cost-efficient and digital approach to manufacturing that offers key benefits such as providing superior characteristics to those of cast and forged parts, being able to produce complex 3D geometries that are not possible with other traditional processes, such as recesses for configurational cooling channels, and eliminating production and assembly steps, thus reducing material waste and environmental impact [3]. Such advantages could change the industrial paradigms such as aerospace, automotive, biomedical and consumer goods.

There are two major categories of metallic AM fusion-based processes. The two families are powder bed fusion (PBF) and directed energy deposition (DED). In PBF, a heat source, either a laser or an electron beam, melts metal powder in a powder bed layer which consolidates them together [4]. DED is characterized by the simultaneous feeding of powder or a wire into a melt pool with a focused energy source such as an electron beam, laser beam, or plasma arc. It is defined by the ASTM F2792 Standard Terminology for AM Technologies specification as "additive manufacturing processes in which focused thermal energy is used to fuse materials by melting as they are being deposited" [5]. The two AM processes could provide different capabilities in terms of production efficiency, maximum component size, surface finish, and final part resolution [6]. Although PBF generally exhibits better spatial resolution and surface quality of fabricated parts, [4] DED could present unique advantages for its potential to fabricate functionally graded and pure metal components as well as its potential to repair and clad valuable parts that cannot be effectively repaired by other traditional methods [7]. Besides, DED typically uses much higher laser power (up to a few kW) and larger spot sizes (up to 10 mm) than PBF, resulting in much higher deposition rates, which are essential for manufacturing large aerospace components. Over the last decades, most research efforts have been devoted to PBF or powder-based DED processes, but wire exhibits

a higher purity of starting material than powder and reduced contamination due to the reduced surface area, which could be critical for aerospace components that require high material quality and repeatability [8-9]. This thesis focuses on a Laser wire-based DED process called laser wire deposition (LWD).

Although AM of metallic parts has attracted considerable interest compared to conventional subtractive methods, it still faces considerable scientific, technological, and commercial challenges. These challenges include the difficulty of controlling microstructure, properties, and defects (voids, lack of fusion, and cracks due to thermal and residual stresses), as well as the lack of standards, a slow rate of printing, scarcity of feedstock materials for many commercial alloys, and cost-competitiveness [10]. AM processes are characterized by a large number of parameters, including travel speed, laser power, and material feed rate, etc. Parameter selection is critical as it affects the resulting thermal cycle and solidification conditions, which in turn affects the evolution of the microstructure and determines the final properties. Currently, parts are qualified by trial-and-error building and testing of parts. Numerous studies [11-19] have been conducted to investigate the effects of processing parameters on DED parts. However, improving part quality through trial and error is not optimal for AM because of the high number of experiments required to explore a wide range of process parameters, which results in higher costs. For instance, data show that variations in travel speed and power could lead to extreme 10000-fold differences in cooling rates, as well as vast differences in solidification conditions [20]. It is well known that cooling rates and heat input during AM determine the evolution of the microstructure which in turn affects the final properties and defects. Predicting the thermal profile, microstructure, and mechanical properties before printing will be useful for parameter selection and greatly reduce the time and effort required for qualification. Mechanistic models and machine learning provide the connection between process variables, part geometry, composition, microstructure and mechanical properties for a given alloy. However, due to the complexity of the AM process, these models have to make assumptions by ignoring the less important processes and compromise the fidelity to the extent confirmed by comparing model predictions with experimental results [20-21]. Nevertheless, machine learning along with mechanistic models could address the difficulties in controlling attributes of printed parts with the selection of process parameters and assist on improving part quality, lowering costs, and reducing the number of trial-and-error experiments.

1.2 References

[1] DebRoy, T., Wei, H. L., Zuback, J. S., Mukherjee, T., Elmer, J. W., Milewski, J. O., Beese, A. M., Wilson-Heid, A., De, A., & Zhang, W. (2018). Additive manufacturing of metallic components – Process, structure and properties. Progress in Materials Science, 92, 112–224.

[2] Brandl, E., Schoberth, A., & Leyens, C. (2012). Morphology, microstructure, and hardness of titanium (Ti-6Al-4V) blocks deposited by wire-feed additive layer manufacturing (ALM). Materials Science and Engineering: A, 532, 295–307.

[3] Gorsse, S., Hutchinson, C., Gouné, M., & Banerjee, R. (2017). Additive manufacturing of metals: a brief review of the characteristic microstructures and properties of steels, Ti-6Al-4V and high-entropy alloys. Science and Technology of advanced MaTerialS, 18(1), 584-610.

[4] Liu, Z., He, B., Lyu, T., & Zou, Y. (2021). A review on additive manufacturing of titanium alloys for aerospace applications: directed energy deposition and beyond Ti-6Al-4V. Jom, 73, 1804-1818.

[5] Chekir, N. (2019). Laser wire deposition additive manufacturing of Ti-6Al-4V for the aerospace industry. McGill University (Canada).

[6] Sikan, F. (2022). Electron Beam Wire-fed Deposition of Titanium Alloys for Repair Applications. McGill University (Canada).

[7] Saboori, A., Gallo, D., Biamino, S., Fino, P., & Lombardi, M. (2017). An overview of additive manufacturing of titanium components by directed energy deposition: microstructure and mechanical properties. Applied Sciences, 7(9), 883.

[8] Brandl, E., Palm, F., Michailov, V., Viehweger, B., & Leyens, C. (2011). Mechanical properties of additive manufactured titanium (Ti–6Al–4V) blocks deposited by a solid-state laser and wire. Materials & Design, 32(10), 4665-4675.

[9] Brandl, E., Baufeld, B., Leyens, C., & Gault, R. (2010). Additive manufactured Ti-6Al-4V using welding wire: comparison of laser and arc beam deposition and evaluation with respect to aerospace material specifications. Phys. Procedia, 5(Pt 2), 595-606.

[10] Tofail, S. A., Koumoulos, E. P., Bandyopadhyay, A., Bose, S., O'Donoghue, L., & Charitidis, C. (2018). Additive manufacturing: scientific and technological challenges, market uptake and opportunities. Materials today, 21(1), 22-37.

[11] Chekir, N., Tian, Y., Gauvin, R., Brodusch, N., Sixsmith, J. J., & Brochu, M. (2018). Effect of travel speed and stress relief on thin Ti-6Al-4V laser wire deposits. Materials Science and Engineering: A, 724, 335-347.

[12] Baufeld, B., Brandl, E., & Van der Biest, O. (2011). Wire based additive layer manufacturing: Comparison of microstructure and mechanical properties of Ti–6Al–4V components fabricated by laser-beam deposition and shaped metal deposition. Journal of Materials Processing Technology, 211(6), 1146-1158.

[13] Narayana, P. L., Kim, J. H., Lee, J., Choi, S.-W., Lee, S., Park, C. H., Yeom, J.-T., Reddy, N. G. S., & Hong, J.-K. (2021). Optimization of process parameters for direct energy deposited Ti-6Al-4V alloy using neural networks. The International Journal of Advanced Manufacturing Technology, 114(11–12), 3269–3283.

[14] Kistler, N. A., Corbin, D. J., Nassar, A. R., Reutzel, E. W., & Beese, A. M. (2019). Effect of processing conditions on the microstructure, porosity, and mechanical properties of Ti-6Al-4V repair fabricated by directed energy deposition. Journal of Materials Processing Technology, 264, 172–181.

[15] Brandl, E., Michailov, V., Viehweger, B., & Leyens, C. (2011). Deposition of Ti–6Al–4V using laser and wire, part I: Microstructural properties of single beads. Surface and Coatings Technology, 206(6), 1120-1129.

[16] Shamsaei, N., Yadollahi, A., Bian, L., & Thompson, S. M. (2015). An overview of Direct Laser Deposition for additive manufacturing; Part II: Mechanical behavior, process parameter optimization and control. Additive manufacturing, 8, 12-35.

[17] Baufeld, B. (2012). Effect of deposition parameters on mechanical properties of shaped metal deposition parts. Proceedings of the Institution of Mechanical Engineers, Part B: Journal of Engineering Manufacture, 226(1), 126-136.

[18] Brandl, E., Michailov, V., Viehweger, B., & Leyens, C. (2011). Deposition of Ti–6Al–4V using laser and wire, part II: Hardness and dimensions of single beads. Surface and Coatings Technology, 206(6), 1130-1141.

[19] Thompson, S. M., Bian, L., Shamsaei, N., & Yadollahi, A. (2015). An overview of Direct Laser Deposition for additive manufacturing; Part I: Transport phenomena, modeling and diagnostics. Additive Manufacturing, 8, 36-62.

[20] DebRoy, T., Mukherjee, T., Wei, H. L., Elmer, J. W., & Milewski, J. O. (2021). Metallurgy, mechanistic models and machine learning in metal printing. Nature Reviews Materials, 6(1), 48-68.

[21] Baykasoglu, C., Akyildiz, O., Candemir, D., Yang, Q., & To, A. C. (2018). Predicting microstructure evolution during directed energy deposition additive manufacturing of Ti-6Al-4V. Journal of Manufacturing Science and Engineering, 140(5), 051003.

Chapter 2: Research Objectives

The objective of this research is to propose a new platform with reverse engineering methodology to help control the thermal profile, microstructure, and mechanical properties of titanium alloys by LWD. This includes the use of computational modeling to predict the thermal profile, microstructure and mechanical properties of printed parts followed by validation with experimental results from fabricated LWD Ti-6Al-4V deposits. Besides, this research aims to expand the existing knowledge on LWD Ti-6Al-4V by providing a better understanding of how various key process parameters can affect the microstructural development of the printed component and eventually the subsequent material properties. Specifically, the study focuses on the following aspects.

➢ Investigate the effect of travel speed on cooling rates, microstructure and mechanical properties of single bead wall Ti-6Al-4V deposits.

➢ Investigate the effect of wire diameter on dimensional accuracy, microstructure and mechanical properties of single bead wall Ti-6Al-4V deposits.

➢ Investigate the effect of oxygen content on the microstructure, mechanical properties, and strengthening mechanisms of single bead wall Ti-6Al-4V deposits.

Chapter 3: Literature Review

3.1 Directed Energy Deposition

This section focuses on the general principles of DED, the advantages and disadvantages of various types of heat sources and feedstock material, and the major processing parameters as well as their effects.

DED can be adapted for the deposition of various materials such as titanium alloys, stainless steels, tool steels, nickel-based superalloys, aluminum alloys, ceramics, composites and functionally graded materials, etc [1]. In this process, a melt pool is formed on the substrate or last deposited layer by using a relatively high energy density heat source (laser, electron beam, or plasma/electric arc). Simultaneously, the feedstock material, either powder or wire, is delivered into the melt pool. As the heat source moves forward, the molten material solidifies and forms a deposition track. The tracks overlap according to the predefined hatch spacing. After one layer is completed, the heat source and feedstock delivery system move up by a predefined small distance to deposit the subsequent layer. Deposition of all layers follows a sliced 3D computer-aided drawing (CAD) file to achieve the desired geometry [2]. The CAD model is created prior to deposition and specifies the slice thickness, hatch spacing, and deposition path for each layer [1]. Depending on the different energy source and type of feedstock, different technologies are commonly referred to as DED processes, such as Laser Wire Deposition (LWD), Laser Powder Deposition (LPD), Shaped Metal Deposition (SMD), or Electron Beam Additive Manufacturing (EBAM). DED can achieve high deposition rates (0.5 kg/h to 10 kg/h) and huge working envelope (e.g., 6×1.4×1.4 m) [1].

Table 3.1 compares the DED process with different heat sources in terms of processing features and properties. The DED process can be quite different in terms of build volume, final part resolution, deposition rate, and contamination rate. For instance, electron beams and plasma/electric arcs could provide a higher deposition rate and enable faster production of large components for DED than laser due to the potential for higher power, but they lack dimensional accuracy and often result in higher surface roughness than laser. As a result, post-machining is necessary to achieve the acquired geometry.

[1]Table 3.1. Comparison of DED processes with various heat sources adapted from [1,3].

6

Heat source	Build volume	Resolution	Deposition rate	Contamination rate
Laser	Middle	Middle	Middle	Middle
Electron beam	High	Low	High	High
Plasma/electric arc	Middle	Low	High	Middle

The DED process can be quite different in terms of processing features and final part quality with various types of feedstock materials. Table 3.2 compares the DED process with powder feedstock and wire feedstock. The deposition rate for the powder-fed DED process is limited due to the limitations in powder spreading rates and small layer thickness, but it has the potential to fabricate more complex geometry with higher resolution and dimensional accuracy. On the other hand, wire enables a low contamination rate since it exhibits higher purity of starting feedstock due to reduced surface area. The wire-fed process could fabricate larger parts at lower cost due to the high deposition rate.

[2]Table 3.2. Comparison of DED processes with powder feedstock vs. wire feedstock [2].

Type of feedstock	Wire	Powder
Deposition rate	√	
Cost	√	
Power efficiency	√	
Large part scale	√	
Lower porosity	√	
Lower contamination rate	√	
Higher resolution		√
More complex geometry		√
Dimensional accuracy		√

Thesis focused on LWD processes. Figure 3.1(a) demonstrates the LWD system (Liburdi LAWS 1000 automated deposition system equipped with an IPG Yb:YAG fiber laser reaching up to 1 kW power) used to fabricate all samples in this research and Figure 3.1(b) illustrates the LWD process during deposition with key parameters denoted. A protective argon atmosphere is used during

deposition to prevent oxidation. The DED process is associated with numerous processing variables that control the thermal history and solidification, thus significantly affecting the microstructure and mechanical properties of the deposit. The complicated and repeated thermal cycles, the large number of processing parameters and their cross-linking interactions make it difficult to characterize and understand the effect of each parameter on the deposited material. For wire-fed DED processes, the processing parameters can be classified into three main categories: (1) system dependent, (2) wire dependent, (3) process parameter dependent. Figure 3.2 presents these main variables. The influence of the key parameters on the microstructure and behavior of the deposited material is reviewed subsequently.
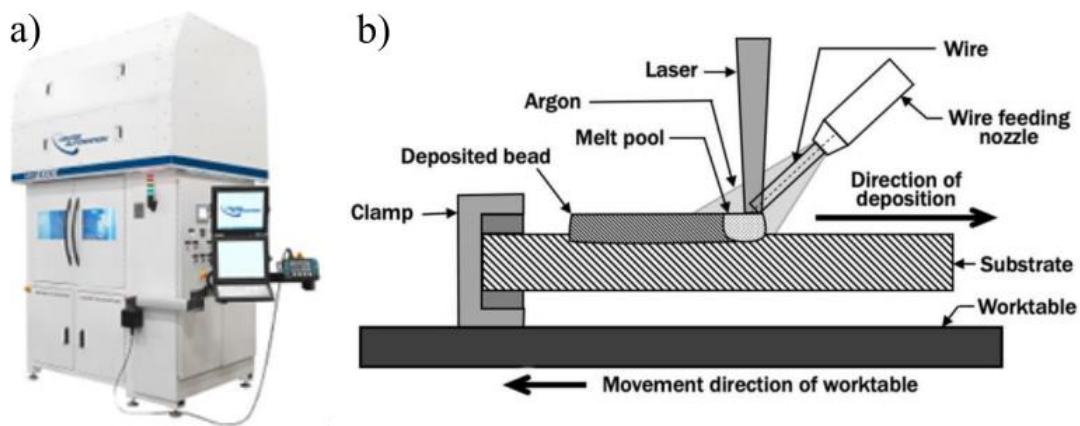
[1]Figure 3.1. a) Liburdi LAWS 1000 automated welding system b) schematic diagram of LWD system during deposition, adapted from [4].
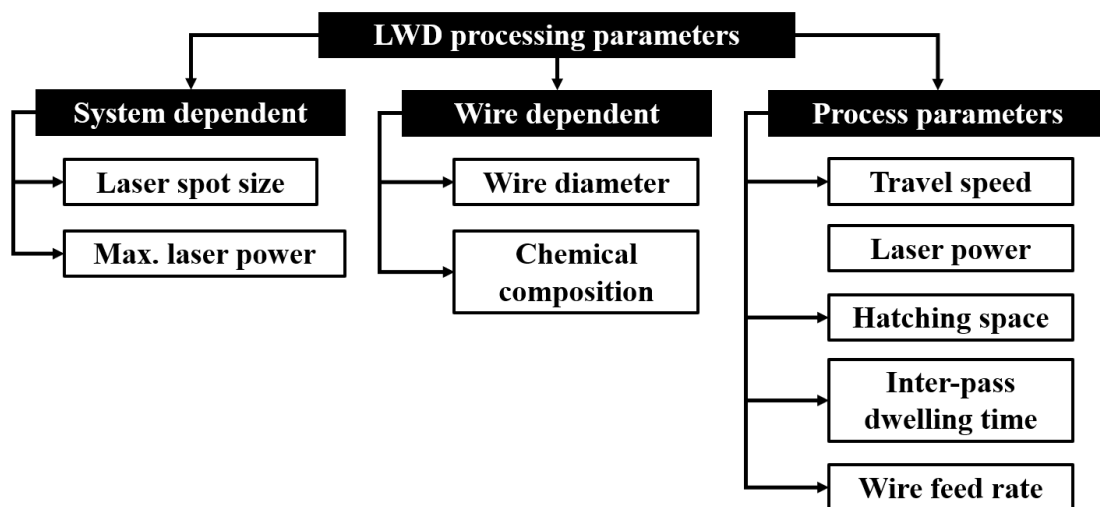
[2]Figure 3.2. Main variables of LWD system.

The laser beam configuration (system dependent), such as spot size, can affect most of the parameters in general. More specifically, the beam diameter and profile of the laser beam affect the minimum size of the feature and the formation of the molten pool. Effective energy density, E (J/mm2), is commonly used to express the combination of dominant processing parameters for correlation with continuous deposition and deposition aspect ratio:

$$E = \frac{P}{vd}$$
<div align="right">Equation 3.1</div>

where P is the laser power (J/s), v is the laser scan speed (mm/s), and d is the laser beam diameter (mm). Kladovasilakis et al. [5] illustrated the effect of laser beam configuration on the hatching distance (the distance between the centers of the laser beams in two consecutive laser paths) and the overlap percentage (the percentage of an area scanned by a consecutive laser path from a previous laser path) in the Laser Powder Bed Fusion (LPBF) process. Figure 3.3 graphically exhibits how the paths are scanned by the laser beam, as well as the formation of the hatching distance and the creation of overlapping regions between two consecutive passes of the laser beam. Additional factors, such as the configuration of the wire, need to be considered in wire-fed DED process. Fayazfar et al. [6] explained the overlap by the ratio of hatch distance to laser beam diameter and how it affects the relative density of the parts, and reported that a wide range of densities is achievable while the average hatch distance to laser beam diameter is mainly set from 0.6 to 1.5.
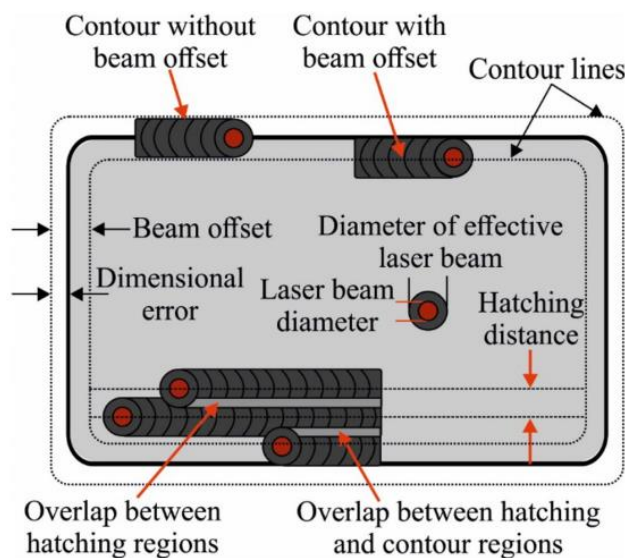
[3]Figure 3.3. Graphical illustration of laser beam diameters [5].

The feedstock material has a dominant effect on the quality of the final parts. Poor feedstock quality could lead to reduced mechanical properties and component failure. Key feedstock features for wire-fed DED processes are wire diameter and chemical composition. Kladovasilakis et al. [5] reported that a larger wire diameter could have a negative influence on surface roughness and dimensional accuracy. Besides, at constant travel speed and wire feed rate, higher wire diameter leads to increased material feed rate, which can result in undesired phenomena such as low deposition efficiency and lack of fusion porosity. On the contrast, a low feed rate could generate an excessive amount of energy-provoking defects due to the keyhole effect. Gibson et al. [7] used a large wire diameter of 1.6 mm and reported inconsistent wall geometry when there was no closed-loop control of melt pool size during the deposition process. Shaikh et al. [8] attempted to use micro fine wire (0.1 mm) to improve dimensional accuracy and geometry resolution. However, the deposition rate was substantially decreased, and the fine wire could increase surface roughness and create voids or defects when the subsequent layer is deposited. Salminen [9] compared the laser weld quality with different welding parameters. The wire diameters studied were 0.8 mm and 1 mm. This study reported that laser welding with filler wire can be used with the correct parameter combinations, where the wire diameter should be less than the air gap width, and there is an optimum welding speed and wire feed rate for different wire diameters to ensure complete fusion.

The dominant process parameters are travel speed, laser power, and wire feed rate. Numerous research has been conducted to investigate the effects [10-18]. The combination of higher travel speed and lower laser power results in lower incident energy at the top of the part, typically resulting in finer microstructures due to higher cooling rates. In contrast, lower cooling rates and coarser microstructures can be garnered by decreasing the travel speed and increasing laser power [15]. Besides, Gor et al. [19] reported that an optimal combination of travel speed, laser power and wire feed rate could produce an optimal range of energy density that would result in a denser part with improved strength. Increased hatching distance could lead to decreased energy density, which would yield a less dense part [5]. Brandl et al. [14] reported that increased wire feed rate would result in increased absorbed heat, which would lead to decreased cooling rate and the melt pool shape would be elongated rather than elliptical. Grain dimensions were increased with an increased wire feed rate. However, extreme values of laser power and/or travel speed could lead to defects

such as porosity and cracking [5]. Solidification conditions could be affected by other processing parameters such as inter-pass dwell time. For instance, increasing inter-pass dwell time could cool down the part and reduce the thermal gradient.

As wire-fed DED parts and their unique capabilities such as repair application, high deposition rate and large component size are increasingly in demand for high-impact industrial applications, efficient process optimization becomes a necessity.

3.2 Titanium Alloys

3.2.1 History and Industrial Applications

Titanium was first discovered in 1791 by William Gregor, a British reverend, mineralogist and chemist [20]. The Berlin chemist Martin Heinrich Klaproth first independently isolated titanium oxide from a Hungarian mineral, now known as "rutile", in 1794 [20-21]. It took more than 100 years for Matthew Albert Hunter from Rensselaer Polytechnic Institute in Troy, N.Y., to isolate the metal in 1910 by heating titanium tetrachloride ($TiCl_4$) with sodium in a steel bomb [20,22]. In 1932, Wilhelm Justin Kroll from Luxembourg produced significant quantities of titanium by combining $TiCl_4$ with calcium [20]. This extraction method was demonstrated in the U.S. during World War II and has since been widely used since then known as the "Kroll process" [20]. Titanium and titanium alloys were first commercially produced by the DuPont Company in 1948 [21]. They were considered key materials for aircraft engines. Until today, aerospace remains the primary consumer of titanium and its alloys [5]. Figure 3.4 presents the increased usage of titanium in aircraft in recent years.
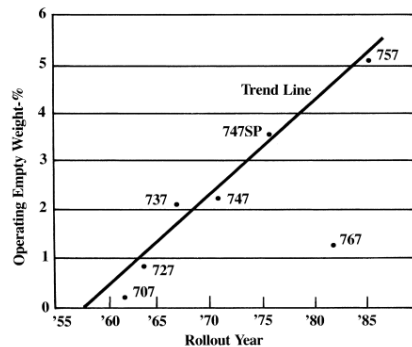
[4]Figure 3.4. Titanium usage in Boeing aircraft from the first commercial jet to the Boeing 757 [21].

11

Titanium ranks as the ninth most plentiful element and the fourth most abundant structural metal in the Earth's crust (about 0.6%) [23]. Titanium and its alloys stand out primarily due to some significant facts and/or important benefits:

1. High strength-to-weight ratio (specific strength) at relatively high temperatures. The density of titanium is only about 60% of that of steel or nickel-based superalloys. However, the tensile strength of titanium alloys can be comparable to that of lower-strength martensitic stainless steel and better than that of austenitic or ferritic stainless steel. Moreover, the ultimate strength of titanium alloys is comparable to iron-based superalloys and cobalt alloys such as A286 and L605 [21]. Figure 3.5 presents the specific strength versus working temperature of selected materials compared to titanium alloys [20]. Only at temperatures below 573 K, carbon fiber reinforced plastics (CFRP) have a higher specific strength than titanium alloys. Titanium alloys can provide attractive strength at higher temperatures. However, the maximum application temperature is limited by their oxidation behavior [20]. At high temperatures, the diffusion of oxygen becomes too fast, resulting in excessive growth of the oxide layer and embrittlement of the adjacent oxygen-rich layer of the titanium alloy [23]. This makes titanium alloys especially interesting for applications at temperatures just above 773 K [3].
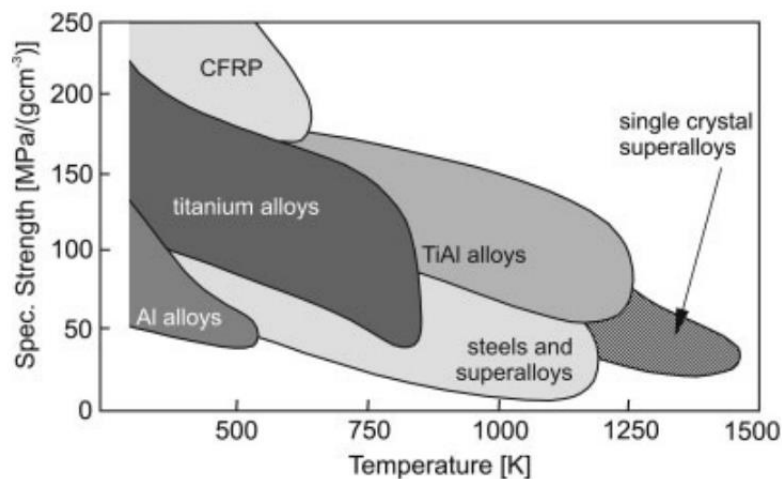
[5]Figure 3.5. Specific strength vs temperature of selected material compared with titanium alloys [20].

2. Titanium and its alloys have exceptional corrosion resistance. They exceed the resistance of stainless steel in most environments and have outstanding corrosion resistance in the human body [21]. The high reactivity with oxygen leads to the immediate formation of a stable and adherent oxide surface layer when exposed to air, resulting in the superior corrosion resistance of titanium, especially in aqueous acid environments [23].

3. The cost of titanium and its alloys is comparable to that of superalloys [23]. The price is related to the market need, especially the fluctuation of the aerospace market demand. Figure 3.6 demonstrates the price fluctuation of titanium during the years 1959-1998. The price increase in the period 1977-1981 is in response to the rapid increase in commercial aircraft orders, and the reduction in the period 1982-1984 is due to the subsequent collapse in aircraft sales [23].
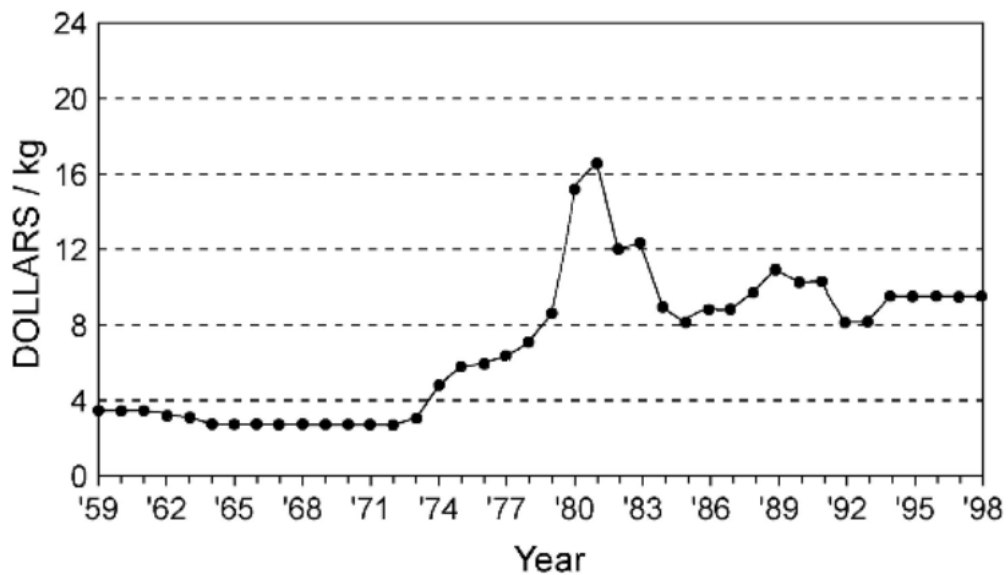
[6]Figure 3.6. Development of titanium price in US dollars/kg over the years 1959-1998 [23].

4. Titanium can be processed by various methods such as forging, wrought, casting, fusion welding, brazing, bonding, diffusion bonding, fasteners and P/M technology [21]. It is formable and easily machinable with reasonable care.

In addition to the aerospace industry, titanium and its alloys have more established applications in the biomedical field [23], automobiles [23], architecture [20], and transportation [20].

3.2.2 Crystal Structure

Titanium exhibits allotropic phase transformation from a body-centered cubic crystal structure (β phase) at higher temperatures to a hexagonal close-packed crystal structure (α phase) at lower temperatures. The complete transformation from one crystal structure to the other is called allotropic transformation [20]. The transformation temperature for pure titanium is about 882 °C [23]. For titanium alloys, it is affected by interstitial and substitutional elements. Figure 3.7 presents the crystal structure of α phase and β phase for pure titanium. The lattice parameters of the α phase are noted as a (0.295 nm) and c (0.468 nm), resulting in a c/a ratio of 1.587. The lattice parameter of pure β titanium at 900 °C is noted as 0.332 nm. The most densely packed lattice planes are the basal plane (0002), prismatic planes $\{10\bar{1}0\}$ and pyramidal planes $\{10\bar{1}1\}$ for α phase, and $\{110\}$ for β phase. The densely packed directions are $<11\bar{2}0>$ for α phase and $<111>$ for β phase. During the allotropic phase transformation, the most densely packed planes of the β phase transform to the basal plane of the α phase following Burgers Orientation Relationship (BOR) [23]:

$\{0001\}_\alpha // \{110\}_\beta$

$\langle 1120 \rangle_\alpha // \langle 111 \rangle_\beta$

The six slip planes and two slip directions of the β phase give a maximum of 12 variants of orientation of the α phase [23]. The BOR indicated that 12 possible α variants can nucleate at the boundary of β grains [3].
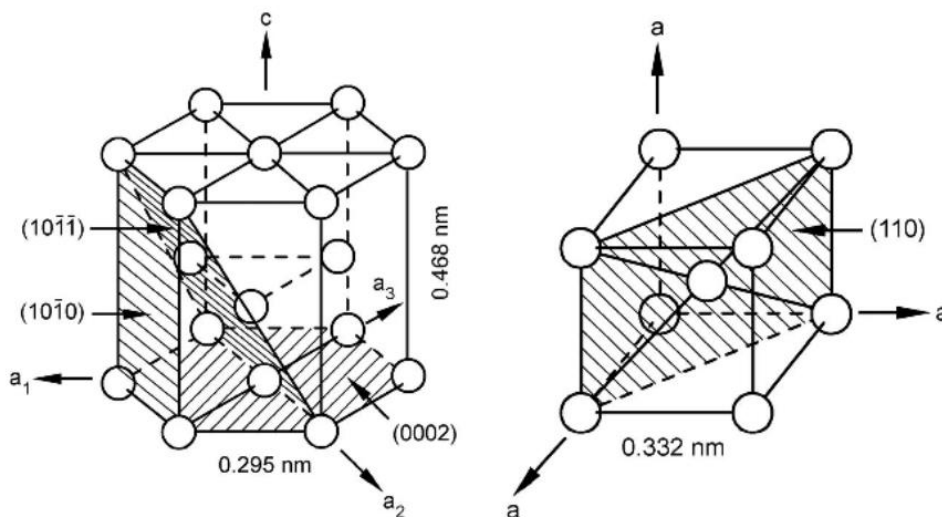
[7]Figure 3.7. Titanium crystal structure of α phase (left) and β phase (right) [23].

3.2.3 Classification of Titanium Alloys

Alloying elements can be classified as α-stabilizers or β-stabilizers depending on whether they increased or decreased the phase transformation temperature. There are a few elements with negligible effect on the phase transformation temperature that are classified as neutral, such as Zirconium (Zr) and Tin (Sn). However, these elements are usually considered as α-stabilizers due to the isomorphous property of Zr with titanium and Sn acting as α-stabilizers when Aluminum (Al) is present [22].

Figure 3.8 illustrates the effect of various alloying elements on the phase diagram of titanium alloys. Strong α-stabilizers include the substitutional element Al and the interstitial elements O, N and C. They all increase the phase transformation temperature with increasing solute content. Al has been widely used due to its high solubility in both α and β phases. Oxygen is a promising alloying element as it can be used to obtain the desired strength level. Other α-stabilizers include B, Ga, Ge and the rare earth elements, but their solid solubilities are much lower. The β stabilizers are divided into β isomorphous elements and β eutectoid forming elements depending on the resultant binary phase diagrams. For Ti-x alloys with various elements, the effective equivalencies of various alloying elements have been studied and it is expressed as equivalent Al content by establishing the following equation [23]:

$$[Al]_{eq.} = [Al] + 0.17[Zr] + 0.33[Sn] + 10[O] \hspace{2cm} \text{Equation 3.2}$$
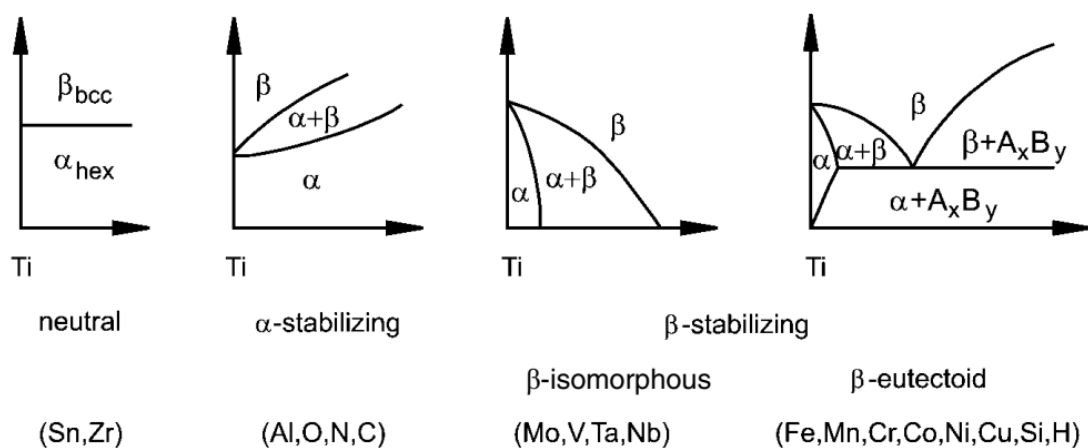
[8]Figure 3.8. Influence of alloying elements on phase diagram of titanium alloys [23].

Titanium alloys are usually classified as α, $\alpha + \beta$, and β alloys. Figure 3.9 illustrates the classification with a three-dimensional phase diagram with an α stabilizer and a β stabilizer. When only α-stabilizer is present, the alloys care comprised of pure titanium. After adding minor fractions of β-stabilizers, they are referred to as near-α alloys. The $\alpha + \beta$ alloys have a β phase volume fraction of about 5 – 40 % [20] and are the most widely used group of alloys. By further increasing the β-stabilizers, the class of metastable β-alloys is reached, where there is no martensite phase transformation upon fast quenching. It should be noted that these alloys are still in the two-phase field and can still reveal an equilibrium α volume fraction of more than 50%. Finally, the single phase β alloys mark the end of the alloying scale of conventional titanium alloys.
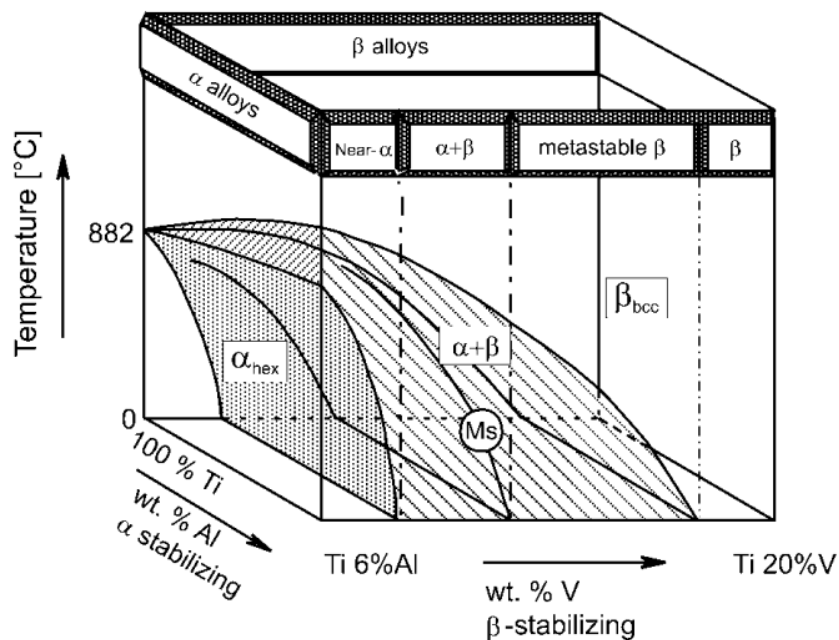
[9]Figure 3.9. Three-dimensional phase diagram to classify Ti alloys schematically [20].

3.3 DED Ti-6Al-4V

Ti-6Al-4V is an $\alpha + \beta$ alloy containing about 6 wt. % Al and 4 wt. % Vanadium (V). Table 3.3 presents the main characteristics provided by various titanium alloy groups. The properties of titanium alloys are primarily determined by the arrangement, volume fraction and individual properties of the two phases α and β. The density of α alloys is lower due to the lower specific weight of most α-stabilizing elements. The densely packed hexagonal crystal structure of the α phase is more densely packed and has an anisotropic property and low diffusion rate, leading to

higher resistance to plastic deformation, reduced ductility and increased creep resistance compared to the body centered cubic β phase. However, β-alloys can be hardened to high strength levels as compensation for the lower ductility. The high affinity of titanium for oxygen enables the formation of a dense oxide layer on the surface and explains the excellent corrosion behavior. The high reactivity with oxygen could cause embrittlement and require either a vacuum or inert gas atmosphere for welding. The α-Ti alloy exhibits higher weldability but relatively low formability since it requires higher stress to trigger the slip systems [24]. Ti-6Al-4V has been the most widely used titanium alloy considering the combination of strength, workability and formability [4]. The typical application is in the aerospace industry such as pressure vessels, aircraft gas turbine disks, and compressor blades [20].

[3]Table 3.3. Main characteristics of α, $\alpha + \beta$, and β alloys.

	α	$\alpha + \beta$	β
Density	+	+	−
Strength	−	+	+ +
Ductility	−/+	+	+/−
Creep strength	+	+/−	−
Corrosion behavior	+ +	+	+/−
Oxidation behavior	+ +	+/−	−
Weldability	+	+/−	−

The morphologies of $\alpha + \beta$ Ti-6Al-4V microstructure can be different depending on various thermomechanical treatments, including a complex sequence of solution heat treatment, deformation, crystallization, aging, and annealing for stress relief. All these treatments are developed around the β-transus temperature, T_β. There are two distinct morphologies for the α phase: equiaxed (globular) and lamellar.

Figure 3.10 presents a schematic of lamellar microstructure formation as a function of cooling rate. During solidification, prior β grains are formed first. Once the temperature is below T_β, the α phase starts to nucleate at the β grain boundary. This formation follows the BOR relationship as described in the previous sections. At a relatively low cooling rate, the α phase, which is incoherent with

respect to the β phase, first preferentially nucleates at the β grain boundaries, leading to a continuous α layer along the β grain boundaries, known as grain boundary α [23]. During continued cooling, the α plates nucleate either at the interface of the grain boundary α or at the β grain boundary and grow into the β grain as parallel plates of the same variant. They continue to grow into the β grain interior until they meet other α plates nucleated with other variants of the BOR relationship. This leads to a characteristic microstructure called a "basketweave" structure or Widmanstätten structure. The lamellar grain size depends on the cooling rate. During continued cooling, at low cooling rates such as furnace cooling, coarse lamellar α-grains are formed. However, at high cooling rates, such as water quenching, fine lamellar α grains are formed. Besides, α' martensite phase with a needle-like morphology can be formed when the material is cooled down at a high cooling rate from a temperature above the martensite start (MS) temperature (650 ℃). Figure 3.11 shows that fully martensitic microstructures can be obtained at cooling rates above 410 ℃/s when the material is cooled down from a temperature above the MS, which is about 575 ℃ [25-26]. The martensite phase transformation is nonequilibrium and diffusionless, and it involves the movement of atoms by a shear-type process, resulting in the transformation of the body-centered cubic into the hexagonal crystal lattice over a given volume [23]. Generally, the martensitic phase contains high dislocation density, stacking faults, and sometimes twins [26]. The martensitic phase is known to increase strength and hardness; however, the ductility of the alloy decreases dramatically [27-28].
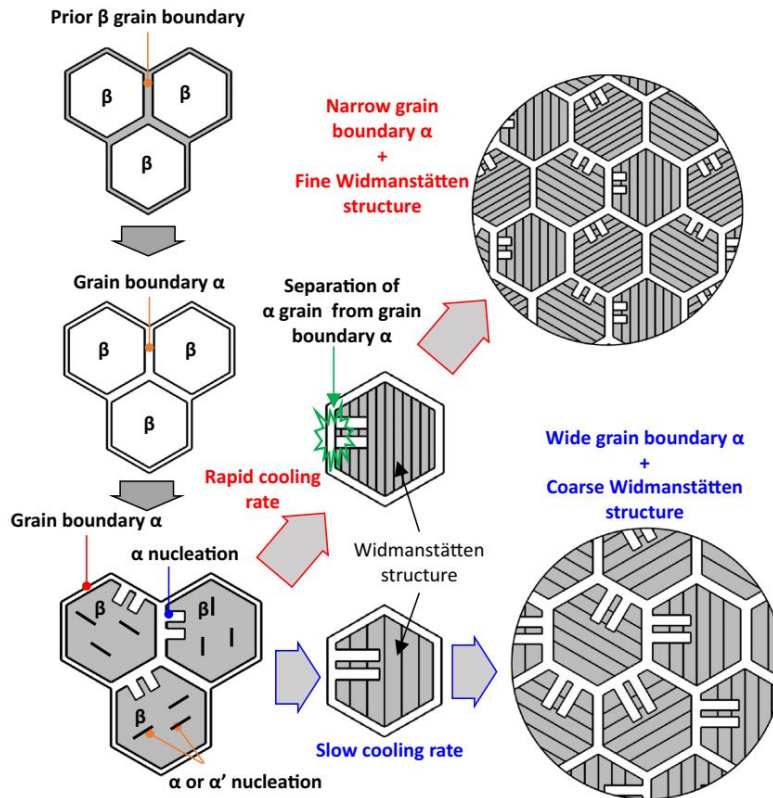
[10]Figure 3.10. Schematic of the lamellar microstructure formation for Ti-6Al-4V alloy, adapted from [25].
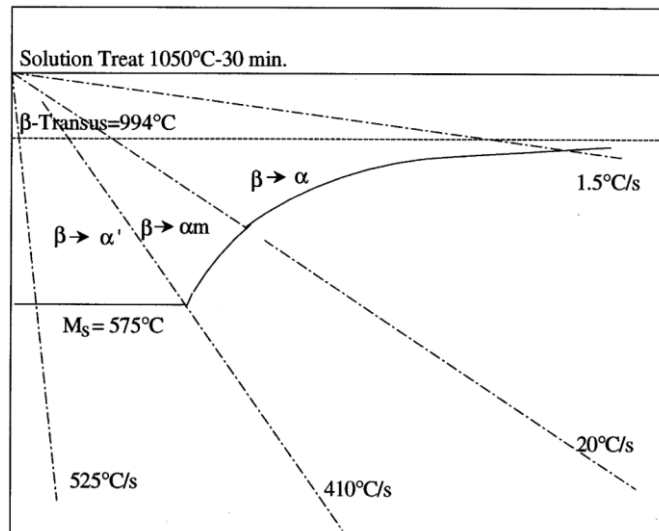
[11]Figure 3.11. Schematic continuous cooling diagram for Ti–6Al–4V β-solution treated at 1050°C for 30 min, adapted from [26].

The various microstructure can considerably affect the mechanical behaviour of Ti-6AL-4V. The fine-scale microstructure can increase the strength and hardness mainly due to the Hall-Petch strengthening mechanism [29-30]. Equiaxed microstructures could provide high ductility and fatigue strength, while lamellar structures have high fracture toughness and creep resistance [21]. Bimodal structures could exhibit a combined advantage of both morphologies.

This study focused primarily on DED Ti-6Al-4V. The solidification behavior, microstructure and mechanical properties of typical DED Ti-6Al-4V will be reviewed in the subsequent sections.

3.3.1 Solidification

Solidification is the transformation of a liquid phase into a solid phase. Understanding the mechanism of solidification is critical to explain the relationship between various processing parameters and the final macrostructure/microstructure, including grain size, grain morphology, defects, and the resultant mechanical properties of DED components. The solidification condition in DED is rather complex compared to traditional manufacturing methods such as casting, as the melt pool generated has a relatively small and non-linear free-form solidification interface. DED-fabricated components are characterized by unique microstructural characteristics (including nucleation, grain growth, and solid phase transformation) and different resultant mechanical properties compared to traditional manufacturing methods as a direct result of the unique melting and solidification conditions of DED. Solidification occurs through nucleation and grain growth. The following sections describe the underlying theories with DED Ti-6Al-4V.

The driving force for any phase transformation, including solidification, is the change in free energy:

$$\Delta G = G_L - G_S \qquad\qquad \text{Equation 3.3}$$

where G_L and G_S are the free energies of the liquid and solid phases (J), respectively, and ΔG is the change in free energy due to solidification (J).

Elementary thermodynamics demonstrates that solidification cannot happen unless there is some undercooling below the melting temperature [31]. Five types of solidification undercooling have been identified: kinetic undercooling, thermal undercooling, constitutional undercooling, curvature

undercooling, and pressure undercooling [31]. Nucleation is the first step in the solidification process. There are two typical nucleation theories: homogeneous nucleation and heterogeneous nucleation. The detailed introduction and thermodynamic derivation can be found in most solidification books [32-34]. Homogeneous nucleation results from the stabilization of a transient grouping of atoms so that a nucleus consisting of many atoms is formed at once [32]. It is quite difficult for homogeneous nucleation to happen as the relatively high activation barrier requires a rather high undercooling. (420 K for pure iron) [34]. In the DED process, since there is a pre-existing base metal grain, solidification can be intentionally induced. This nucleation, which occurs on solid substrates to the metal, is called heterogeneous nucleation. Figure 3.12 shows a schematic of a spherical cap of a crystal nucleated from a liquid on a planar substrate. The parameters γ_{LC}, γ_{LS}, and γ_{CS} are the surface energies of the liquid–crystal interface, the liquid–substrate interface, and the crystal–substrate interface, respectively. The heterogeneous nucleation barrier for the crystal to nucleate on the substrate is: [34]

$$\Delta G_H = \frac{4\pi\gamma_{LC}^3 T_m^2}{3(\Delta H_m \Delta T)^2}(2 - 3cos\theta + cos^3\theta) \qquad \text{Equation 3.4}$$

where T_m is the equilibrium melting temperature (K), ΔH_m is the latent heat of melting (J/kg), ΔT is the undercooling (K), and θ is the contact angle (°).
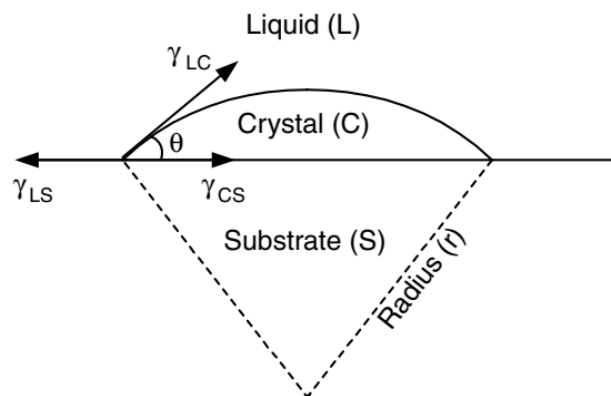
[12]Figure 3.12. A spherical cap of a crystal nucleated on a planar substrate from a liquid, adapted from [34].

In the DED process, the liquid metal of the melt pool is in intimate contact with these substrate grains and wets them completely ($\theta = 0$). The crystal can nucleate from the liquid metal by arranging atoms from the liquid metal on the substrate grains without altering their existing crystallographic orientations, which is known as epitaxial growth. Figure 3.13(a) presents the epitaxial growth of metal inheriting the crystallographic orientations. In terms of the nucleation behaviour of Ti-6Al-4V, epitaxial growth is quite common since it saves more energy if nucleation starts from partially melted grains in the previous grains in the previous layer rather than generating a new one, and sometimes a single crystal can run through multiple deposited layers [4]. Figure 3.13(b) shows the schematic of the epitaxial growth of the prior β grains for DED-fabricated TI-6Al-4V. During solidification, prior β grains grow preferentially along the <100> crystallographic direction and align with the thermal gradient direction where the driving force for solidification is maximum. The β grains with their favoured orientations aligned with the thermal gradient direction have the growth advantage and are able to outgrow the less favoured adjacent grains during the competitive grain growth process.
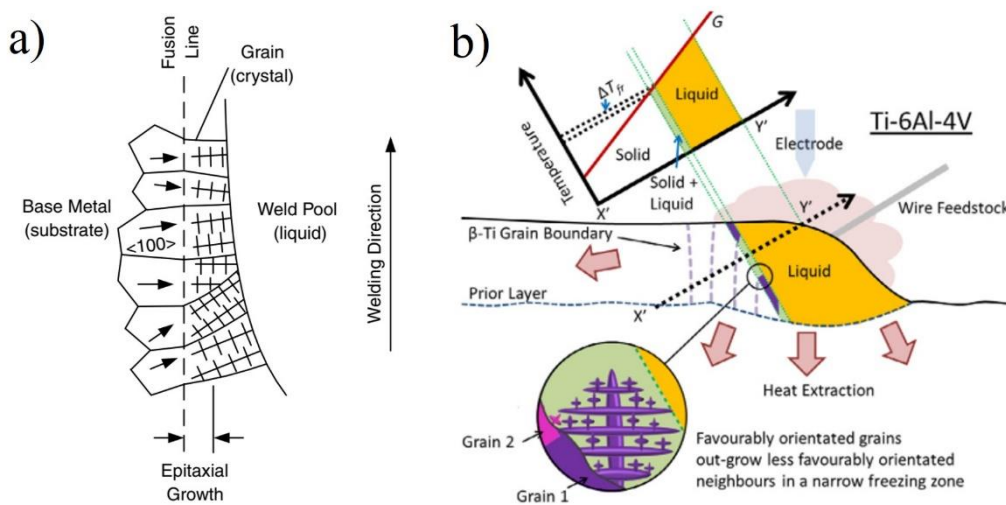
[13]Figure 3.13. a) Epitaxial growth of metal from the base metal, adapted from [33]. b) Schematic of deposition process for DED Ti-6Al-4V with epitaxial growth of prior β grains, adapted from [35].

This study will focus on constitutional undercooling as it is believed to be the main contribution to the solidification of an alloy system. A detailed explanation of other undercooling mechanisms can be found in most solidification books [31]. During solidification, solutes are rejected from the solid. Figure 3.14(a) presents the phase diagram that demonstrates this process. For a given temperature

T^*, the solid composition, C_S, is smaller than the liquid composition, C_L. The ratio $k = C_S/C_L$ is known as the partition coefficient. The case $k<1$ is used to demonstrate in the phase diagram. Due to solid rejection, a boundary layer richer in solute than the base solid is formed at the solid/liquid interface. Figure 3.14(b) demonstrates the formation of the boundary layer ahead of the solid/liquid interface. This leads to a lower liquidus temperature at the solid/liquid interface than away from it. The heat flow from the liquid to the solid creates a thermal gradient, G_T, indicating the local temperature. If G_T is lower than the liquidus gradient G_L, a constitutionally undercooled region is generated.
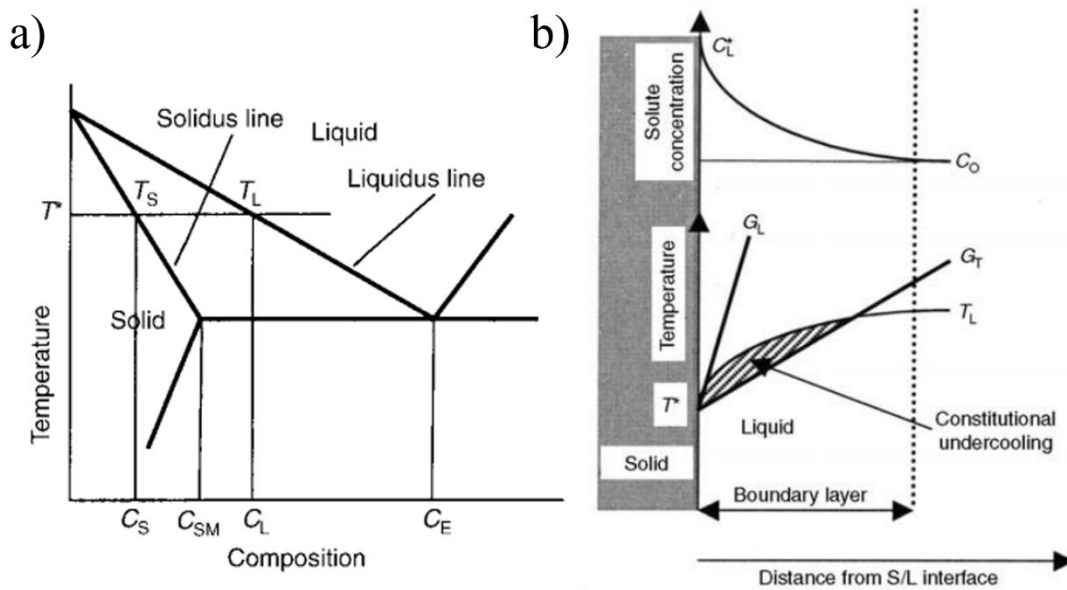
[14]Figure 3.14. a) Binary phase diagram demonstrating the solidification process. b) Formation of constitutionally undercooled region (dashed area) ahead of the solid-liquid interface [31].

The size of constitutional undercooling can greatly affect the solidification modes for grain growth. There are typically four solidification modes: planar, cellular, columnar dendritic, and equiaxed dendritic. Figure 3.15 demonstrates the effect of constitutional undercooling on various solidification modes and presents micrographs of various solid/liquid interfaces. A planar interface can be achieved when the thermal gradient in the liquid at the solid/liquid interface is larger than the liquidus temperature gradient. It is believed to occur only for pure metals and is difficult to achieve in real industrial practice [4]. For small constitutional undercooling, the instabilities will grow only in the solidification direction and a cellular interface will form. As the constitutional undercooling increases, the spacing between the cells increases, and constitutional undercooling can occur

perpendicular to the growth direction [31]. Instability will form at the cell sides, leading to dendrite formation. If the constitutional undercooling is even greater, equiaxed grains can nucleate in the liquid away from the solid/liquid interface.
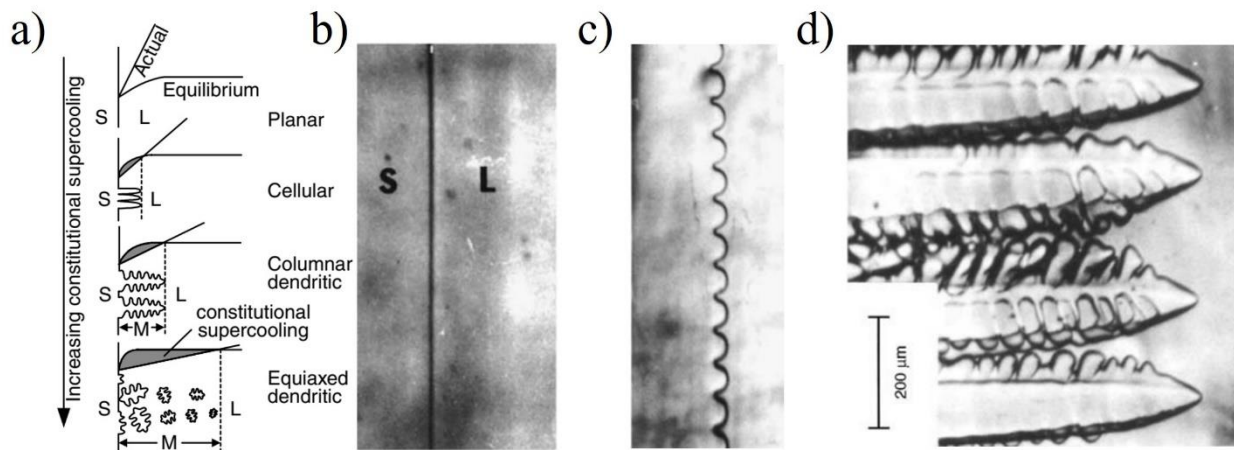
[15]Figure 3.15. a) Effect of constitutional undercooling on solidification mode, adapted from [33]. Different solid/liquid interface: b) planar, c) cellular, and d) columnar dendritic, adapted from [31].

The solidification modes are mainly affected by the thermal gradient (G) and the solidification rate (R). Figure 3.16(a) presents that the ratio G/R determines the morphology of the solidification microstructure, while the product $G*R$ determines the size of the solidification microstructure. Figure 3.16(b) demonstrates the resultant solidification structure of Ti-6Al-4V for typical solidification conditions of AM technologies. DED and PBF both locate at the fully columnar and mixed area due to the high G resulted from typical processing parameters. However, the solidification structure of PBF is finer since the PBF process tends to have a higher solidification rate than the DED process due to the higher travel speeds.
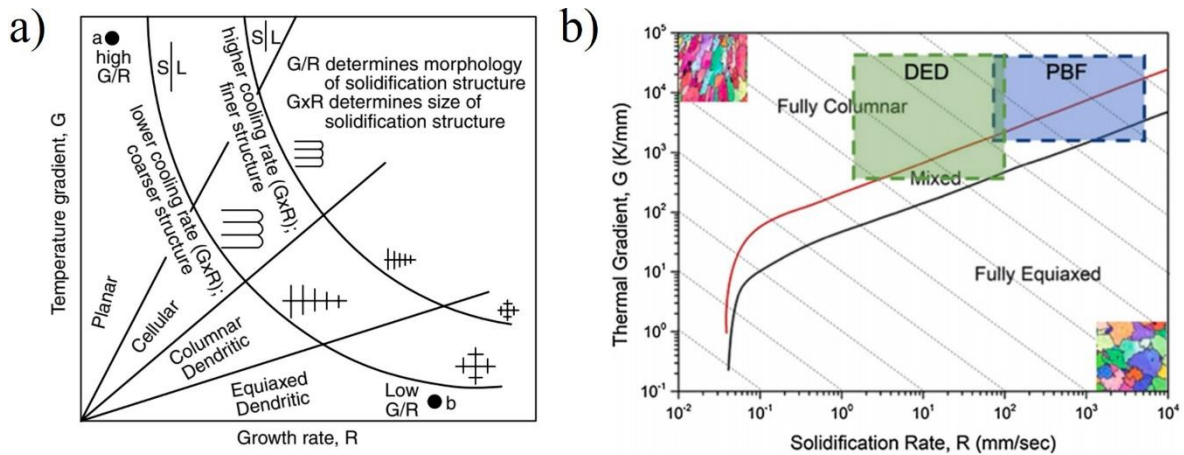
[16]Figure 3.16. a) Effect of G and R on the morphology and size of solidification microstructure, adapted from [33]. b) A solidification map for DED and PBF fabricated Ti-6Al-4V under varying ranges of G and R, adapted from [36].

3.3.2 Structure Development

Figure 3.17 shows the typical macrostructure for DED fabricated Ti-6Al-4V. The columnar prior β grains, which are parallel to the build direction and grow epitaxially through multiple layers, dominate the macrostructure. During the solidification process, prior β grains tend to grow perpendicular to the solid/liquid interface as the direction of the maximum thermal gradient associated with the maximum driving force for solidification. It should be noted that equiaxed structure is rarely produced for AM Ti-6Al-4V, although the composition of alloying elements is close to 10 wt. % and the solidification rates are quite high [39]. This is because the partition coefficients of Al and V are close to 1, indicating that the solidification range from liquidus to solidus temperature is narrow, resulting in limited constitutional undercooling [40-42]. Moreover, the steep G and lack of potent nucleating particles prevent further nucleation ahead of the solidification front [35]. Zhang et al. [43] reported the development of titanium-copper alloys which achieved high constitutional undercooling capacity due to partitioning of the alloying element during solidification. Currently, there is no commercial grain refiner for Ti-6Al-4V to achieve columnar to equiaxed transformation due to inadequate constitutional undercooling [4]. Another characteristic of the macrostructure is the repetitive banding structure. In AM, due to the moving heat source from the sequential deposition passes, each location experienced a cyclic thermal history with the peak temperature decreasing. Banding occurs due to the cyclic property and the

similar thermal history experienced by all layers. Kelly and Kamper [44] reported the banding phenomenon and identified two main regions associated with the complex thermal history experienced by the deposit: the steady-state region and the transient region. They are differentiated by the presence of banding structure. Figure 3.17(c) presents the steady-state region in the middle and the transient region at the top. The material in the steady state region experiences heating to a temperature below phase transformation temperature in addition to the β anneal and rapid cooling. On the contrary, all layers in the transient region are fully β-annealed and then rapidly cooled during the last layer deposition. Kelly and Kamper [44] reported the formation of a colony of α plates between the layer bands compared to the typical basketweave structure. Ho et al. [45] attributed the colony structure to heterogeneous nucleation of packets of individual α variants during cooling on the low density of α plates that survived reheating at temperatures just below the phase transformation temperature. Sikan et al. [46] investigated the mechanical properties of both regions using miniature tensile specimens and reported similar tensile properties and microhardness regardless of the distinct microstructural features.
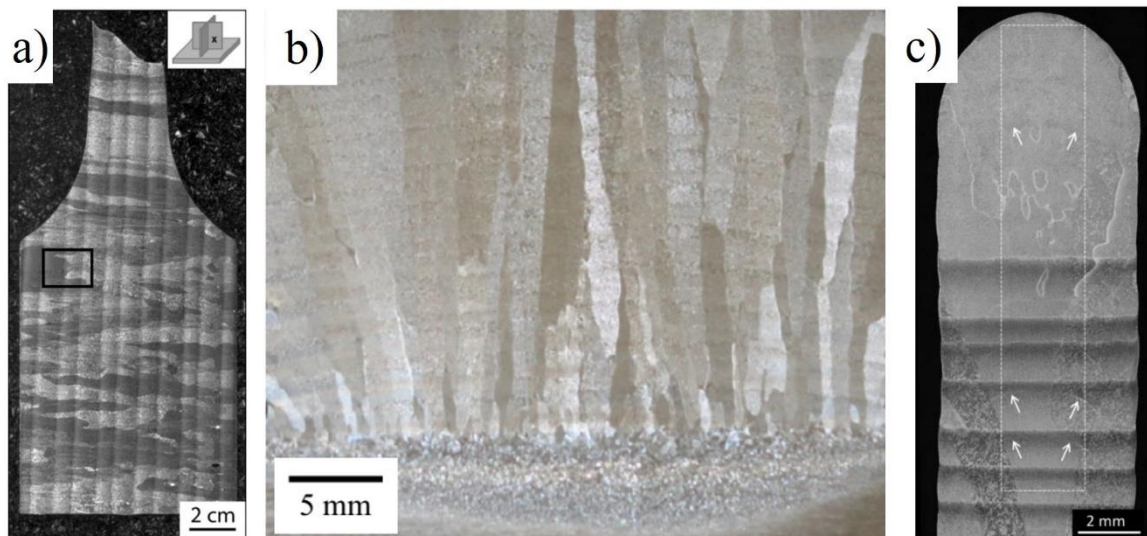
[17]Figure 3.17. a) Optical micrograph demonstrating long and horizontal prior β grains of Ti-6Al-4V fabricated by the DED process where build layers are vertical, adapted from [37]. b) Macrostructure of DED fabricated Ti-6Al-4V, adapted from [38]. c) Optical cross-section of DED fabricated Ti-6Al-4V, adapted from [45].

When further cooled down below the β-transus temperature, the α phase starts to nucleate and form. Figures 3.18(a and b) show the typical microstructure of Ti-6Al-4V fabricated by DED. The

basketweave structure is dominant for DED-fabricated Ti-6Al-4V The size of α plates depends greatly on the cooling rates. Carroll et al. [37] reported a finer microstructure at the bottom of the DED fabricated Ti-6Al-4V wall compared to that at the top, and this was due to the higher cooling rate experienced at the bottom since it was closer to the substrate, which acted as a heat sink and increased the cooling rate. However, depending on the processing parameters and part geometry, there may be other forms of microstructure. For instance, Figures 3.18(c and d) present α' martensite structure in PBF fabricated TI-6Al-4V due to the high cooling rate resulted from the small melt pool size and high travel speeds. It is difficult to predict the local microstructure for AM Ti-6Al-4V as the applied cooling rate can vary locally. The morphology and scale of the final microstructure are strongly dependent on the process parameters and the resultant thermal history [3]. For instance, it has been widely reported that α phase lamellar spacing varies significantly at various locations in a single layer [38,48].
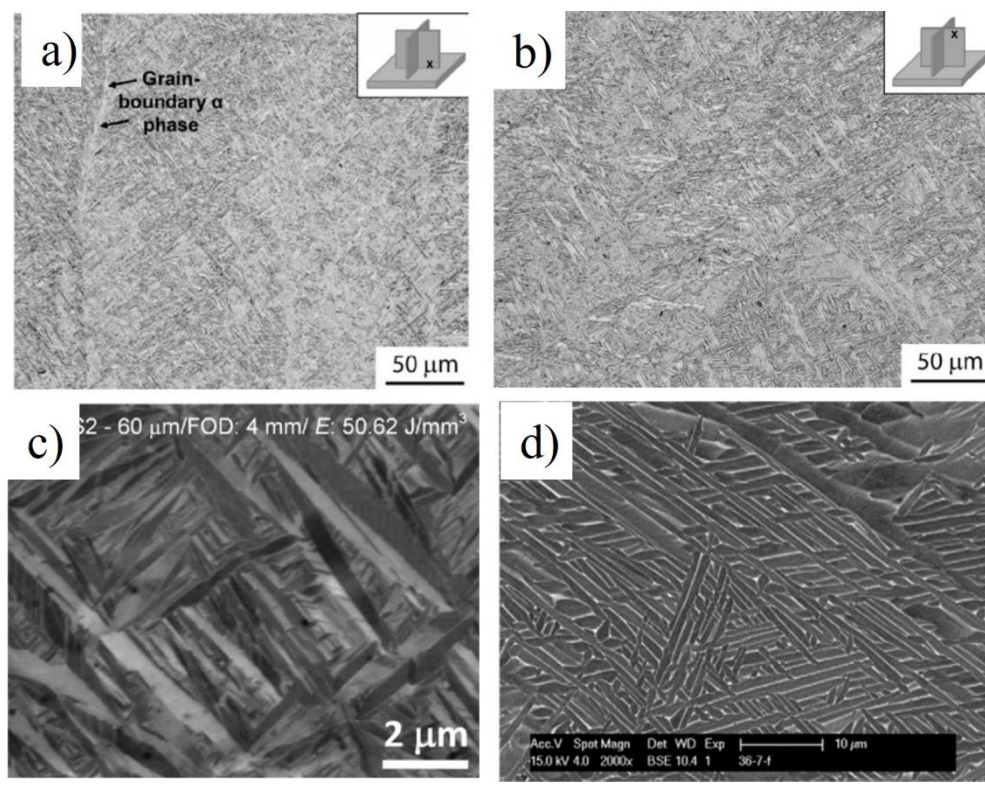
[18]Figure 3.18. The lamellar structure of DED fabricated Ti-6Al-4V walls at the bottom a) and the top b), adapted from [37]. c) Lamellar structure of PBF fabricated Ti-6Al-4V, adapted from [47]. d) Microstructure predominantly consisting of acicular α' martensite of PBF fabricated Ti-6Al-4V, adapted from [11].

3.3.3 Mechanical Properties

The hexagonal crystal structure of the α phase exhibits an anisotropic property which affects the elastic properties at various loading conditions. Figure 3.19(a) presents the effect of the declination angle γ on the elastic modulus of the α phase. Relative to the hexagonal axis in alpha, the strength (and modulus) is high in the parallel direction and low in the normal direction. It can be seen that the elastic modulus of α phase varies between 145 GPa (stress axis parallel to the c-axis) and 100 GPa (stress axis perpendicular to the c-axis) [23]. Since β phase is not stable for pure titanium at room temperature, the elastic modulus has been measured with binary titanium alloys containing sufficiently high concentrations of β stabilizing elements such as Ti-20V. It has been reported that the β phase generally has a lower modulus of elasticity than the α phase. Typical values are 70-90 GPa for the as-quenched condition and 100-105 GPa for the annealed condition of commercial β alloys [23]. The explanation for the lower value is mainly focused on the transformation to stress-induced martensite from the retained metastable β phase during loading and/or simply because the β-stabilizing elements severely disturb and reduce the bonding force of the lattice [23]. Figure 3.19(b) shows that the alloying elements and temperature can greatly affect the elastic modulus of the material. An increase in temperature results in a linear decrease in elastic modulus. Alloying elements such as α-stabilizing elements, Al, can strongly increase the elastic modulus due to the associated change in the crystal structure [21].
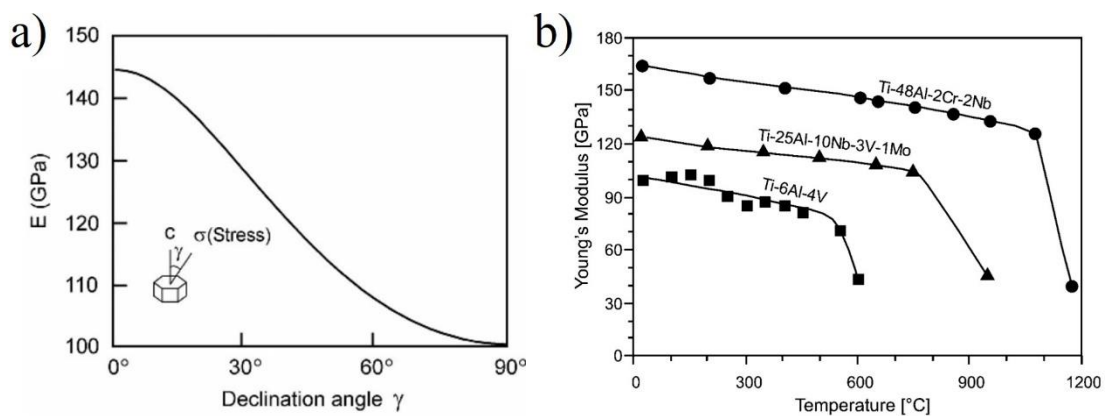
[19]Figure 3.19. a) Elastic modulus of α phase as a function of declination angle γ, adapted from [23]. b) Effect of temperature on the elastic modulus of various titanium alloys, adapted from [21].

The $\alpha+\beta$ alloy Ti-6Al-4V derives its strength from several sources. The major source is the substitutional and interstitial alloying elements in solid solution in α and β phases. Oxygen, nitrogen, hydrogen and carbon are the interstitial elements that generally increase strength and decrease ductility. It is well documented that the addition of oxygen could dramatically enhance the strength and hardness of titanium alloys via solid solution strengthening [49-55]. This is because the addition of oxygen solute could increase the lattice parameters (*c/a* ratio) and restrict the number of slip planes, thus enhancing the tensile strength of titanium alloys [52]. Aluminum, as the most important substitutional elements, can improve the mechanical properties by solid solution strengthening as well. The previous section discussed the linear effect of Al on the elastic modulus.

Besides, the processing parameters can greatly affect the mechanical properties of DED-fabricated Ti-6Al-4V since they directly affect the thermal history and cooling rates. For instance, higher cooling rates tend to result in a finer microstructure. Figure 3.20(a) presents the effect of grain size on the yield strength (YS) of lamellar Ti-6Al-4V. The increase in microstructure scale can lead to decreased YS, ultimate tensile strength and hardness mainly by the Hell-Patch strengthening relationship. Figure 3.20(b) presents the effect of linear heat input regarding various process parameters on the tensile strength of Ti-6Al-4V for various AM processes. Hrabe and Quinn [56] reported that increased energy input leads to larger melt pool size, which results in lower G and therefore increased grain size and decreased mechanical property.
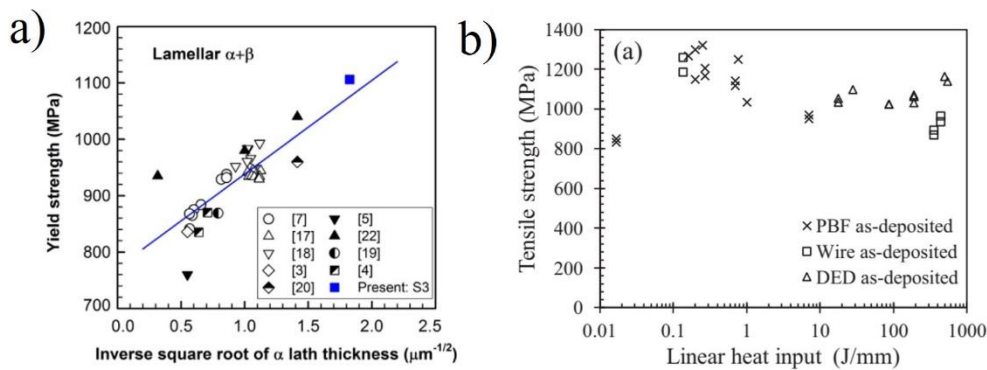
[20]Figure 3.20. a) The effect of α lath thickness on YS for lamellar Ti-6Al-4V, adapted from [47]. b) Tensile strength of Ti-6Al-4V as a function of liner heat input, adapted from [38].

Table 3.4 summarizes the tensile properties of as-built Ti-6Al-4V fabricated by various DED technologies from X (perpendicular to the build direction) and Z directions (parallel to the build direction). Anisotropic tensile properties have been widely reported for DED Ti-6Al-4V parts. It is generally reported that the tensile specimens extracted along the Z direction exhibit a higher strength and lower elongation. The anisotropy is attributed to the difference in texture, columnar β grain morphology, and the presence of grain boundary α from different tensile directions. Strong texture of β phase generates strong α texture obeying Burger's relationship, which will result in the difference of critical resolved shear stress (CRSS) along different loading directions [61]. The tensile strength of the specimens along the build direction was reduced according to the Hall-Petch relationship [62]. The prior β grain boundary is decorated with grain boundary α, which is well documented to tend to reduce elongation by furnishing a preferential path for damage accumulation along the prior β grain boundary [37,63]. However, it is not always the case that lower elongation is related to the X direction as it depends on the presence of the grain boundary α [60].

Table 3.4 also compares the tensile properties of DED fabricated Ti-6Al-4V with the minimum requirement tensile properties of cast and wrought Ti-6Al-4V according to ASTM F1108 and AMS 4911P respectively. Ti-6Al-4V samples fabricated by laser-DED exhibit excellent strength in both X and Z directions compared to that of cast and wrought Ti-6Al-4V samples due to the fine microstructure resulted from high cooling rates. However, the ductility is highly dependent on the orientation. Depending on the purpose of the components, orientation in the Z direction is preferred when the highest ductility is desired. On the other hand, with the assistance of post-heat treatment, it is very promising to achieve both excellent strength and comparable ductility in the cast and wrought products [10-11,64].

[4]Table 3.4. Tensile properties of as-built Ti-6Al-4V fabricated by various DED technologies. (X and Z denote perpendicular and parallel to the build direction, respectively)

Process	Orientation	YS (MPa)	UTS (MPa)	Elongation (%)	Ref.
L-W	Z	860 ± 10	935 ± 15	9.6 ± 1.2	[57]
	X	980 ± 70	1060 ± 70	4 ± 0.8	
L-W	Z	900 ± 53	883 ± 34	-	[10]
	X	875 ± 17	870 ± 23	-	

L-W	Z	1035 ± 44	1034 ± 5	-	
	X	1034 ± 17	1001 ± 6	-	
L-W	Z	860 ± 17	935 ± 20	11 ± 3.5	[11]
	X	890 ± 30	965 ± 15	4 ± 1	
TIG-W	Z	792 ± 15	870 ± 20	17 ± 3.5	[11]
	X	818 ± 30	895 ± 40	8 ± 2	
L-W	Z	1099	1186	8.5	[58]
	X	1162	1260	8.1	
L-P	Z	916 ± 34	1032 ± 31	19 ± 4	[59]
	X	961 ± 40	1072 ± 33	17 ± 4	
EB-W	Z	849 ± 13	915 ± 11	13 ± 1	[60]
	X	860 ± 14	934 ± 12	13 ± 1	
ASTM F1108	-	758	860	8	-
AMS 4911P	-	869	920	10	-

L-W: Laser-Wire, TIG-W: Tungsten Inert Gas-Wire, L-P: Laser-Powder, EB-W: Electron Beam-Wire, YS: Yield Strength, UTS: Ultimate Tensile Strength.

3.4 Mechanistic Models for AM Ti-6Al-4V

In previous sections, the challenge of reducing the number of trial-and-error experiments and the goal of using mechanistic models to help predict and control the performance of DED fabricated Ti-6Al-4V were introduced. In this section, three major features are selected: thermal history, microstructure, and mechanical properties. The recent progress and development of mechanistic models targeting these features in the literature are described.

3.4.1 Thermal Model

AM includes heating, melting, solidification, and solid phase transformations, as well as the evolution of fusion zone geometry, microstructure, grain structure, defects, mechanical properties, residual stresses, and distortion [38]. A comprehensive understanding of the above processes begins with the simulation of the transient temperature field. The complex thermal features of the AM process are mainly attributed to two reasons: the complex interacting physical phenomena and the

multi-scale characteristics, as these different phenomena occur at different length scales [65]. Generally, the scale can be classified into micro, meso, and macro (part scale). It is important to specify the length scale of the model before setting up the model, and it depends on the research focus. For example, if grain growth and phase formation are to be investigated, then the model should be set up as a micro-scale. If keyhole porosity formation is the predicted output, then a mesoscale model is the solution. And macro (part scale) would be the setup if macroscopic deformation is the objective. Figure 3.21 shows some of the most common modeling techniques at both the meso and macro scales. It demonstrates that heat transfer is the core of any simulation model, from which all physical phenomena such as fluid flow and stress formation can be derived. Heat transfer can be coupled with other models as needed. For example, by coupling fluid dynamics, the detailed thermo-fluid behavior within the melt pool can be studied. Likewise, by coupling heat transfer to a mechanical solver, the thermo-mechanical behavior during the process can be simulated.

Finite Element Analysis (FEA) is widely employed to model the cyclic heat transfer in the AM process. In the case of thermal analysis for AM, there are mainly three aspects to be considered: 1) the heat input from the energy source, 2) the heat losses to the build environment, and 3) the selection and accuracy of the material properties [72]. Figure 3.22 presents the dominant heat transfer modes in the DED process. Heat losses occur through a combination of conduction, convection, and radiation. The governing 3D energy balance equation of heat transfer can be expressed as Equation 3.5:

$$\frac{\partial}{\partial x}\left(k\frac{\partial T}{\partial x}\right) + \frac{\partial}{\partial y}\left(k\frac{\partial T}{\partial y}\right) + \frac{\partial}{\partial z}\left(k\frac{\partial T}{\partial z}\right) + Q = \frac{\partial(\rho C_p T)}{\partial t} \qquad \text{Equation 3.5}$$

where T is the temperature (K), k is the temperature-dependent thermal conductivity (W/(m*k)), C_p is the temperature-dependent specific heat (J/(kg*K)), ρ is the density (kg/m^3) and assumed to be independent of temperature, t is the time (s), Q is the power (W) generated per unit volume, and x, y, and z are the local coordinates of a point on the part geometry.
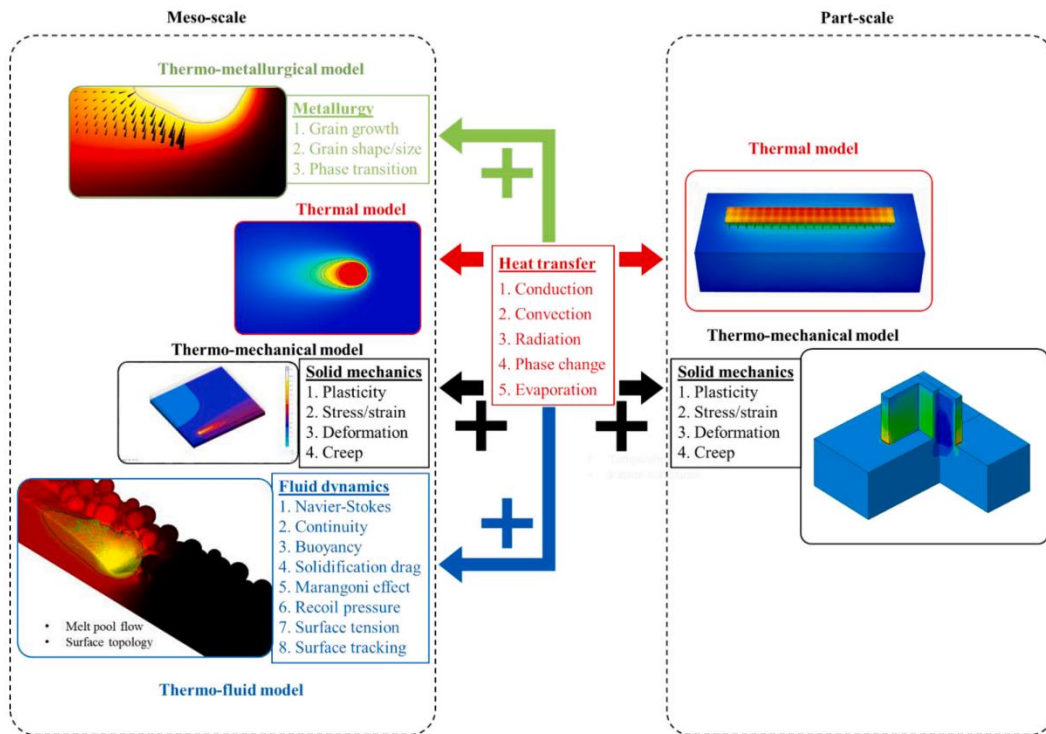
[21]Figure 3.21. An overview of current modeling techniques for AM at both meso- and macro-scale, adapted from [65].
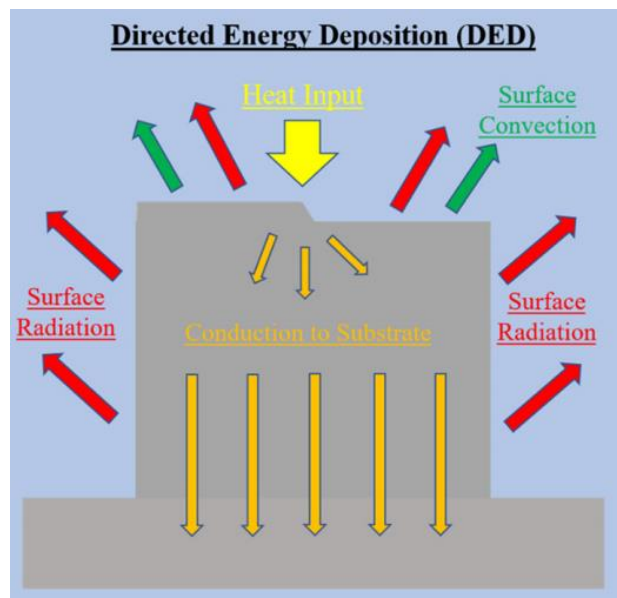
[22]Figure 3.22. Dominant heat transfer modes in DED process, adapted from [66].

Heat sources are generally modeled in the form of a Gaussian distribution where the energy input is highest at the center and decreases to zero toward the outer diameter of the spot. The heat source models generally follow the equation dependent on the distance from the center of the beam x:

$$Q = \frac{f\eta P}{\pi r^2} e^{\left(-\frac{f x^2}{r^2}\right)} \hspace{4cm} \text{Equation 3.6}$$

where P is the total power flux (W), f is the distribution factor of the heat source, η is the heat source efficiency, and r is the radius of the heat source (m).

Table 3.5 lists the typical heat source models used for AM thermal modeling. Most AM processes use either a laser or electron beam as the heat source. The surface-gaussian model is one of the first attempts at a distributed heat source. It has been used as the foundation for the development of other models. Goldak et al. [74] developed a double ellipsoid model considering the heat source to have a Gaussian distribution with a non-axisymmetric ellipsoid shape. This model ensures that the heat flux differentiates between locations close to the substrate, which receive higher heat inputs, and locations away from the substrate, which receive lower heat inputs. The parameters of the ellipsoid are adapted from the dimensions of the melt pool and the data can be extracted from the experimental results. The double ellipsoid model has been widely used to simulate laser heat sources [79]. However, compared to the laser source, the electron beam has a high heat source efficiency, so the electron beam penetrates deeper into the material. Due to this penetration capability of the electron beam, it is generally modeled as a conical heat source following a Gaussian distribution with a graded intensity change through the depth. Other reported heat source models include cylindrical and decay function which has a Gaussian planar profile and exponential decaying function distributions in the vertical direction [77-78].

[5]Table 3.5. Typical heat source equations used for AM thermal modeling.

Name	Expression	Reference
Surface-Gaussian	$\dfrac{2\eta P}{\pi r} e^{\left(-\frac{2x^2}{r^2}\right)}$	[73]
Ellipsoidal	$\dfrac{6\sqrt{3}\eta P}{abc\pi\sqrt{\pi}} e^{\left(-3\frac{x^2}{a^2}-3\frac{y^2}{b^2}-3\frac{z^2}{c^2}\right)}$	[74]

Conical	$$\frac{2\eta P}{h\pi r^2} e^{-\frac{2(x^2+y^2)}{r^2}}\left(1-\frac{z}{h}\right)$$	[75-76]
Cylindrical	$$\frac{2\eta P}{h\pi r^2} e^{-\frac{2(x^2+y^2)}{r^2}}$$	[75,77]
Decay-function	$$\frac{2\eta P}{h\pi r^2} e^{-\frac{2(x^2+y^2)}{r^2}}\left(e^{-\left(\frac{z}{a}\right)}\right)$$	[78]

The thermal heat losses on the part were simulated by thermal boundary conditions. The surface heat losses due to convection and radiation are given by Equation 3.7 and Equation 3.8, respectively:

$$q_{conv} = h(T_{srf} - T_\infty) \qquad\qquad \text{Equation 3.7}$$

$$q_{rad} = \varepsilon\sigma(T_{srf}^4 - T_\infty^4) \qquad\qquad \text{Equation 3.8}$$

where h is the convection coefficient (W/m^2), T_{srf} is the surface temperature of the part (K), T_∞ is the ambient temperature (298 K), ε is the emissivity, and σ is the Stefan–Boltzmann constant (W/(m^{-3}K^{-4})). In laser DED processes, convection plays a significant role in accurately modeling heat loss to the environment, as the forced flow of inert gas across the surface of the deposited material significantly increases convective heat transfer and reduces overall surface temperatures [66]. Radiative losses are due to blackbody radiation from any material, which can become significant at the high temperatures used in AM processes [72].

Figure 3.23(a) shows the typical approach to simulating the deposition process called the "element birth" technique. Initially, all elements are set to inactive, and as the deposition starts, a certain number of elements are activated at the liquidus temperature during each step. The number of newly activated elements over a time interval is a function of the travel speed. Figure 3.23(b) presents the temperature-time history for the first 3 layers of a laser-DED process for 316 stainless steels. It could be seen that the peak temperature and minimum temperature increase with the deposition of subsequent layers due to heat accumulation in the part. Besides, due to the cyclic heating and cooling, the material could experience multiple phase transformations throughout the deposition process, which could lead to repetitive microstructural features.
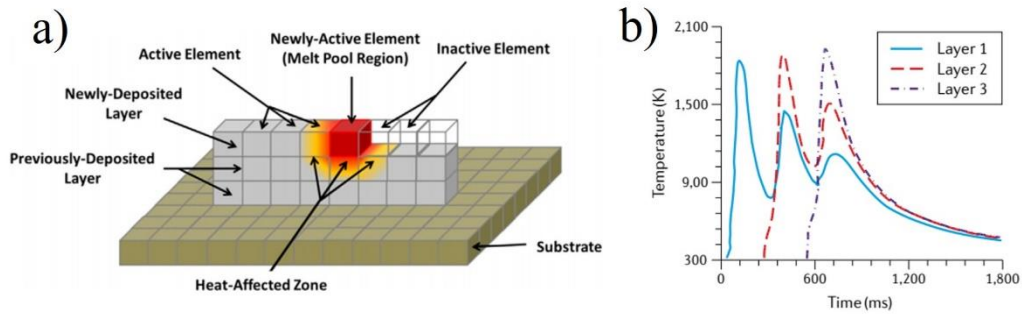
[23]Figure 3.23. a) Schematic of element birth technique implemented for AM process, adapted from [18]. b) Temperature history with respect to time at a monitoring location in different layers during laser-DED of SS 316 steel, adapted from [80].

Computational time is another concern for modeling in AM. Various strategies have been reported to reduce the computational time, focusing on narrowing both the scope and size of the model. Vasinonta. et al. [67] employed one technique by replacing the 3D part with a 2D model and focusing only on heat transfer phenomena. This strategy significantly reduced the computational domain and corresponding computational time. However, it cannot provide insight for building large components and complex geometries because the out-of-plane heat transfer and distortion were negligible. For 3D simulations, it is common for researchers to save computational time by reducing the computational domain to half of the actual build size, taking advantage of the fact that the heat source is symmetric along the build direction [68]. Figure 3.24 presents typical ways adapted by researchers to save computational time in FEA models. Finer mesh could provide more accurate results of FEA models but dramatically increase the computational time. Hence, a graded mesh is adapted by most researchers, whereas coarser mesh is designed for parts not of interest and to save computational time [69]. Besides, it has been reported by several researchers to simplify the process by lumping of layers strategy [70-71]. This method replaced the method of activating elements one by one by activating a certain number of layers at once and significantly reduced the computational time.
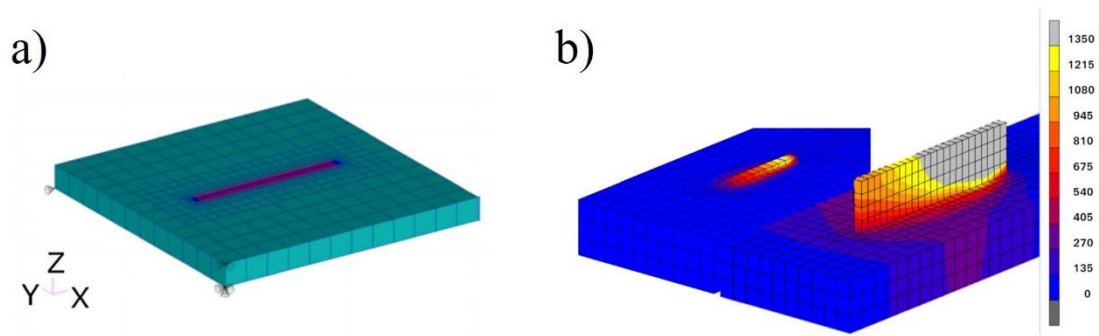
[24]Figure 3.24. a) A general mesh around the build substrate and the area with finer mesh where the heat source will be applied, adapted from [69]. b) History reduction by lumping of welds. On the left is the case without lumping, and the case on the right shows where 14 layers of welds are added simultaneously, represented by four layers of elements, adapted from [71].

3.4.2 Microstructure Model

Literature has reported the direct impact of processing history on the resulting microstructure, which determines the mechanical behavior of AM parts. Therefore, microstructure prediction models for AM deposits are generally based on the thermal history developed from various processing parameters. Thermal models could provide information such as cooling and solidification rates, which could be used as input to predict the microstructure of AM deposits. Currently, there are four conventional microstructure prediction models for AM deposits: Monte Carlo (MC), Cellular Automata (CA), Phase Field (PF) model, and internal state variable approach. Table 6 presents the features of all four models as well as the comparison among them. All models face the trade-off between computational efficiency and accuracy.

MC modeling is a completely probabilistic simulation of the grain structure and provides the shape and size of the grains. It is based on atomistic simulation and minimization of total system energy [81]. The model represents the microstructure using a set of lattice sites. Each site is given a certain orientation, which is compared to the neighbor site. If there is a difference, a new random orientation for the site will be generated and will be accepted if it is smaller than the predefined threshold probability. This algorithm runs iteratively for each time step and for each site. The MC method is simple and effective for simulating grain growth behavior and recrystallization [82-84]. However, it does not allow direct coupling of thermal models and does not consider growth kinetics.

Rodgers et al. [85] modified the MC model by predefining the parameters of the Heat Affected Zone (HAZ) in the AM process and simulated the microstructure evolution for metal AM.

CA is similar to MC in that it is also a probabilistic model. Both do not calculate dendritic structures but simulate grain structures on a larger scale. CA represents the microstructure as a grid of discrete cells with corresponding variables. It is typically coupled to a temperature-time field and the state of each cell is reassigned accordingly at each time step to simulate microstructure evolution. The two main steps in CA are heterogeneous nucleation and grain growth [72]. Nucleation is determined through a probabilistic approach depending on the undercooling of the cells, and grain growth is predicted based on the dendrite tip growth kinetics theory. The nucleation rate and dendrite direction are probabilistic, while the preferred crystallographic direction is taken from theory. Zinovieva et al. [86] modeled the 3D grain structure evolution in a multilayer Ti-6Al-4V component produced by PBF using the coupled CA and FEA methods. The model was able to reproduce experimentally observed columnar grain coarsening and texture formation.

The PF methods simulate the microstructure with all variables continuous across the interface, which means that the interface can be a fraction of both solid and liquid. Mathematically, the description of the interface is represented by an order parameter. The variation of the order parameter represents various phases and interfaces. The evolution of the microstructure with time leads to the variation of the free energy of the system, which is governed by the evolution of the order parameter. PF can capture subgrain features such as dendrites. However, the limitation of the size of the interface in PF makes it difficult to simulate large domains as computational resources are a limiting factor.

Figure 3.25 demonstrates the typical simulation results of MC, CA and PF for AM metal. It could be seen that MC and CA could provide information such as grain shape and size for a large domain, while PF could simulate finer features such as dendrites. However, PF is limited to a small domain and is computationally costly.
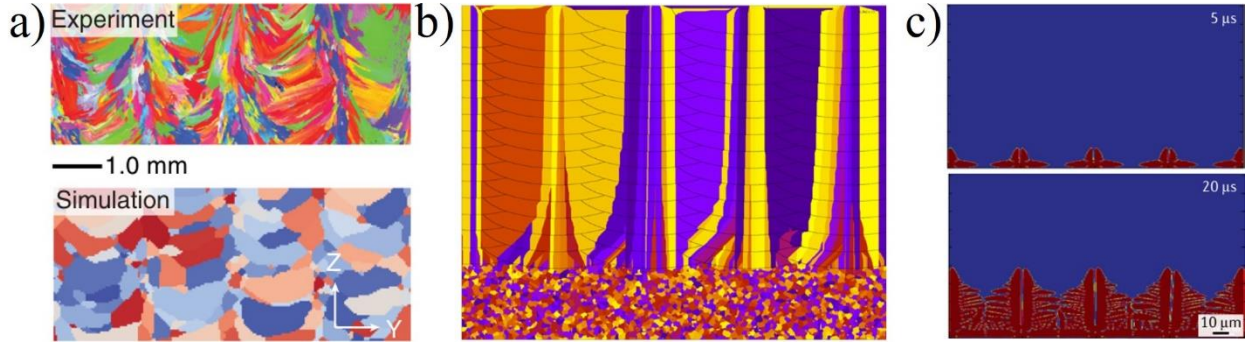
[25]Figure 3.25. a) Comparison between experimental and modified MC simulation of grain growth for AM metal, adapted from [85]. b) CA simulation of grain structure generated in SLM process, adapted from [87]. c) PF simulations of microstructure evolution for EB-AM of Ti–6Al–4V, adapted from [88].

The internal state variable approach is based on the phase transformation kinetics during cooling can predict the phase transformation and scale of microstructural features. This approach is widely applied for common alloy systems with clear physical implications and application backgrounds, such as Ti-6Al-4V. The computational cost is much lower compared to the aforementioned microstructure modeling methods. For the microstructure modeling of AM Ti-6Al-4V, this approach is most commonly applied in combination with the lath width model developed by Charles and J€arvstra˚t [90]. This approach is used to calculate the resulting α and β phases and the corresponding α lath width. The phase fraction of the resulting α and β phases (f_i) is calculated by the following equation:

$$f_{i,\alpha} = f_{eq,\alpha}\zeta_\alpha, \text{ and } f_{i,\alpha} + f_{i,\beta} = 1 \qquad\qquad \text{Equation 3.9}$$

where $f_{eq,\alpha}$ is the equilibrium fraction of α that can be modeled as the function of temperature, ζ_α is the extent of the reaction in the range of 0-1 and can be modeled using the JMAK equation with a time-temperature-transformation (TTT) diagram:

$$\zeta_\alpha = 1 - exp(-kt^n) \qquad\qquad \text{Equation 3.10}$$

where k and n are material parameters extracted from TTT diagram, and t is the time counted from the start to the end of the transformation (s).

The α lath width can be modeled with the approach proposed by Charles and J€arvstra˚t [90]:

$$w_i = \left(w_{i-1}f_{i-1,\alpha} + w_{eq}(f_{i,\alpha} - f_{i-1,\alpha})\right)/f_{i,\alpha} \qquad \text{Equation 3.11}$$

where w_{i-1} and $f_{i-1,\alpha}$ is the α lath width (μm) and α phase fraction from the previous time-step, and w_{eq} is the equilibrium value of α lath width (μm) which can be calculated using an Arrhenius equation:

$$w_{eq} = k_w exp\left(-\frac{T_{act}}{T_i}\right) \qquad \text{Equation 3.12}$$

where the prefactor k_w and activation temperature T_{act} (K) are material constants that can be optimized based on the thermal history [91].

Sufficient simulation and experimental work have been conducted to validate the microstructure model for AM Ti-6Al-4V [79,90-95]. Most of the microstructure models consider only the colony and basketweave α phase fractions during the diffusion controlled phase transformation. The martensite transformations are not included mainly for two reasons: 1) For general processing windows of DED processes, the cooling rate is not more than 410 ℃/s, indicating no martensite transformation. 2) There is a wide discrepancy in the data defining the martensite starting temperature, as well as a lack of standard test method to distinguish and quantify the amount of martensite phase fraction [79]. Besides, the martensite phase bears the same HCP crystal structure and comparable lattice constants, so no distinctions were made by some researchers [95]. The simulation of the basketweave and colony α phase fractions depends on the intragranular nucleation temperature (T_{IG} =827 ℃) [92]. If the current temperature is greater than T_{IG}, the transformed α becomes part of the colony, otherwise, it becomes a basketweave morphology. On the other hand, during heating, whether the dissolved α is taken from the colony or basketweave morphology depends on T_{IG}. If the current temperature is less than T_{IG}, only the basketweave morphology

dissolves; otherwise, both basketweave and colony dissolve proportionally [79]. Figure 3.26 presents the results of the microstructure model for DED Ti-6Al-4V, demonstrating the change in α phase fraction and colony α phase fraction with temperature. The microstructure models have been validated by DED produced Ti-6Al-4V with various processing parameters and revealed good agreement. However, the amounts of colony and basketweave α morphologies show lower agreement with the experimental results. Nevertheless, the model could be used to determine the dominant morphology.
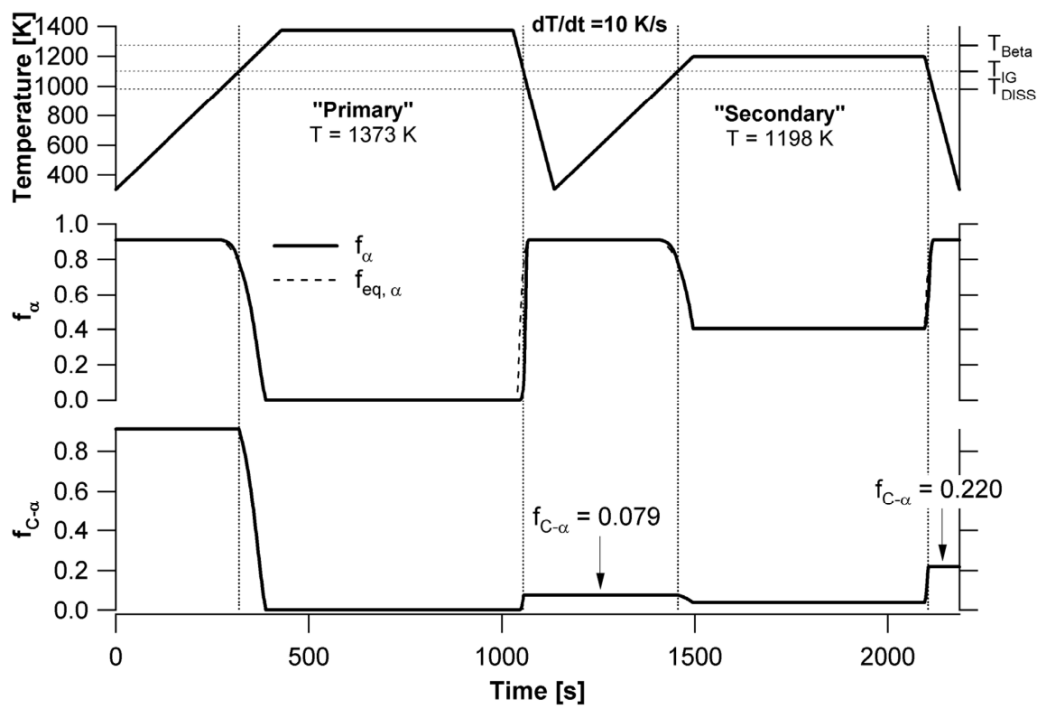
[26]Figure 3.26. The results of microstructure modeling for DED Ti-6Al-4V indicating the change of α phase fraction and colony α phase fraction with temperature, adapted from [92].

Table 3.6. Comparison of microstructure prediction models in AM.

Method	Computational cost	Features	Applications	Benefits	Challenges
Monte Carlo method (MC)	Intermediate	Based on probabilistic approaches.	Grain growth, solidification structure, texture	Enable simulating large domains	Can not simulate phase transformation and crystallographic texture formation
Cellular Automata (CA)	High/intermediate (depending on the spatial scale considered)[72]	Represent microstructure by a grid of discrete cells which change based on temperature field with each time step.	Grain growth, solidification structure, texture	Can simulate crystallographic texture formation	Accuracy depends on the cell size
Phase Field (PF) model	Very high	Based on calculating an order parameter from free energy representing the state of the microstructure.	Nucleation, grain growth, phase evolution, precipitate formation, phase transformation.	Can simulate both solidification and phase transformation, High accuracy and resolution	High computational cost, Not suitable for large domain

Internal state variable approach (TTT-based, CCT-based, and JMA-based models)	Low	Based on phase transformation kinetics during cooling	Quantitative phase fraction prediction	High computational efficiency, Widely explored by common alloy system (Ti-6Al-4V)	Can not predict crystallographic texture formation

3.4.3 Mechanical Property Model

It is well known that the mechanical properties and application of alloys depend essentially on the characteristics of the microstructures. A qualitative understanding of the relationship between microstructures and mechanical properties can provide guidance to improve properties with a controlled variable. For example, researchers have reported that finer grain size would yield higher strength according to the Hall-Petch relationship. However, it is important to establish a quantitative prediction model for the properties to understand the expected statistical performance of the material. This is particularly important in AM as it provides a means of quantifying the confidence of the predicted property to minimize the unknown risk of material or component failure in service [96]. However, quantitative prediction of the mechanical properties from microstructures is challenging due to the complex interrelationships among composition, microstructure and properties. Ti-6Al-4V produced by DED generally exhibits complex $\alpha + \beta$ phases, which are rich in various microstructure features interconnected across length scales. Literature has reported an integrated approach to determining a constitutive equation from a database. Figure 3.27 describes this approach, which combines artificial neural networks (ANN), genetic algorithms (GA), and Monte Carlo (MC) simulation. ANN is used to capture the hidden inter-relationship between composition, microstructure, and subsequently predicted properties. Research efforts have demonstrated that ANN can be trained on a high-fidelity database to capture the inter-relationships through a summation of weighted and biased hyperbolic tangent functions [97]. A typical advantage of ANN is the ability to investigate the influence of separate compositional or microstructural variables on the given output material property by conducting virtual experiments [98]. To accomplish this, a database containing a certain amount of experimental data, such as microstructural features and output properties, should first be built. For example, Hayes et al. [99] prepared about 500 specimens to extract compositional, microstructural, and YS data for the experimental database. Typically, the database was separated into two parts, one for training and one for testing the accuracy of the model [96]. However, the outcomes of ANN are quite complex with unclear indications of the inter-relationship. Therefore, after determining the dependence of given inputs, the inter-relationship was described in well-established forms of equations for strengthening mechanisms. An example of a rather general equation that can be presumed for the YS of Ti-6Al-4V incorporating potential strengthening mechanisms is shown in Equation 3.13:

$$\sigma_{ys} = \sigma_0 + \sigma_{ss} + \sigma_{grainsize} + \sigma_{bw} + \cdots \qquad \text{Equation 3.13}$$

where σ_0 is the intrinsic flow strength of the material (MPa), σ_{ss} is the contribution from solid solution strengthening (MPa), $\sigma_{grainsize}$ is the contribution from Hall-Petch strengthening (MPa), and σ_{bw} is the contribution from basketweave morphology (MPa). Based on the outcomes of the ANN, the following equation can be populated: [99]

$$\sigma_{ys} = F_V^\alpha \sigma_0^\alpha + F_V^\beta \sigma_0^\beta + \qquad\qquad \text{Intrinsic strengthening}$$
$$F_V^\alpha \left(A_{Al} x_{Al}^{n_{Al}} + A_O x_O^{n_O} \right) + \qquad\qquad \text{Solid solution strengthening for } \alpha$$
$$F_V^\beta \left(\left(A_V x_V^{n_V} \right)^{n_1} + \left(A_{Fe} x_{Fe}^{n_{Fe}} \right)^{n_2} \right)^{n_3} + \qquad\qquad \text{Solid solution strengthening for } \beta$$
$$F_V^{Col} A_{\alpha-lath} (t_{\alpha-lath})^{n_4} (t_{\beta-rib})^{n_5} + \qquad\qquad \text{Hall-Petch strengthening (} \alpha \text{ lath)}$$
$$F_V^{Col} A_{Col} (t_{Col})^{n_6} + \qquad\qquad \text{Hall-Petch strengthening for (} \alpha \text{ colonies)}$$
$$F_V^{BW} \alpha MGb\sqrt{\rho} \qquad\qquad \text{Basketweave strengthening}$$

where F_V represents the volume fraction of certain phases, σ_0 is the intrinsic flow stress of certain phases (MPa), x_B represents the concentration of element B (wt. %), t_i represents the thickness of the given feature (m), A_i and n_i are unknown parameters, $\alpha, M, G, and\ b$ are the material constants that could be obtained from the literature, and ρ is the dislocation density (m^{-2}). GA is then used to determine the values of the unknown parameters. The strategy of GA is analogous to natural selection, and it can seek the global extrema of a problem by running successive generations toward an optimal solution [98]. MC simulation is an approach that incorporates random events to calculate a probabilistic solution to a problem [97]. It could be used to determine whether the results of GA and ANN are statistically equivalent. In other words, MC could confirm that, given the individual statistical uncertainties of the microstructural measurements for each data point in the database, the optimized phenomenological equation inspired by GA and the complex sum of the hyperbolic tangent function from ANN are statistically equivalent. The agreement of both results validates the premise of this hybrid ANN + GA approach. Literature has reported great progress in establishing the constitutive equations for the YS of Ti-6Al-4V [96-101]. The most recent model for DED Ti-6Al-4V was developed by Hayes et al. [99]. This constitutive equation was found to be accurate in predicting the YS of DED Ti-6Al-4V under three different post-deposition heat treatments with a deviation of less than 5 %. The optimization made by this model is to incorporate the strengthening effect of the basketweave morphology with the Talyor hardening strengthening component. Figure

3.28(a) shows the comparison between predicted and experimental YS, and they are all within the range of 5%.
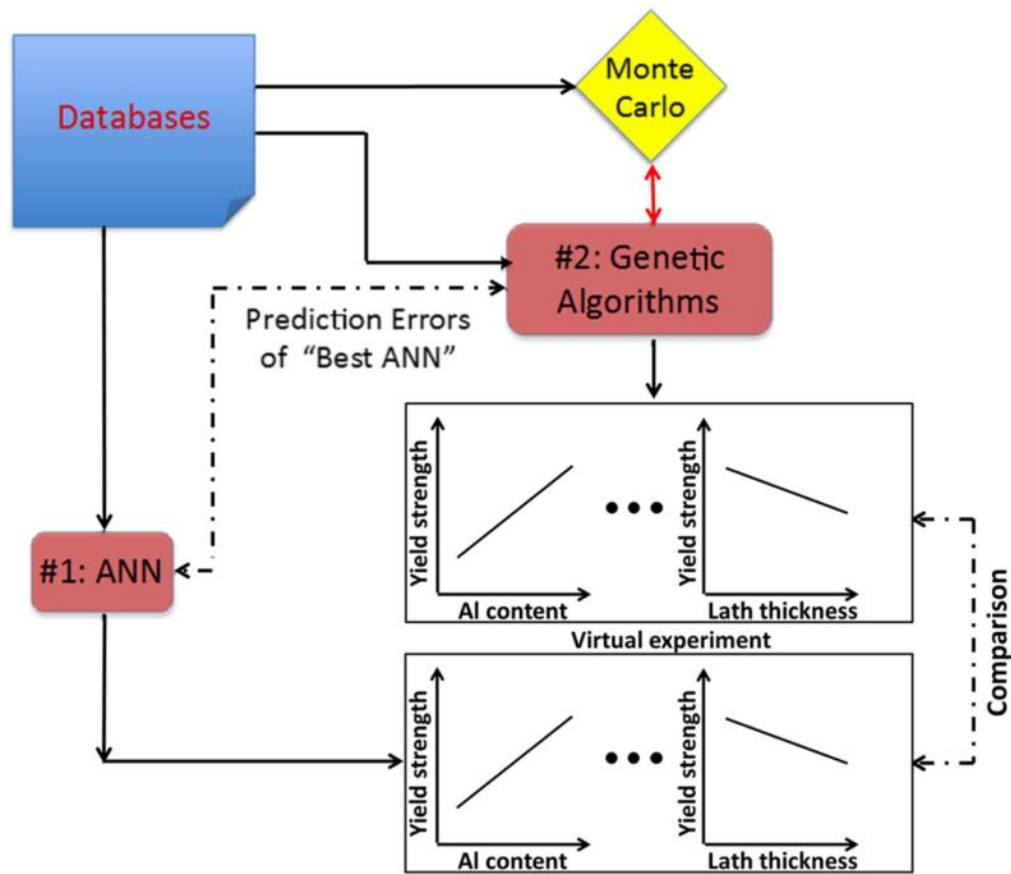
[27]Figure 3.27. The integrated approach combining artificial neural networks, genetic algorithms, and Monte Carlo simulation to determine a constitutive equation from a database, adapted from [96].

More recently, progress has been made to predict other mechanical properties. Quintana et al. [101] extended the constitutive equation for YS by leveraging the Kocks–Mecking–Estrin (KME) model to predict the true stress, true strain behavior of AM Ti-6Al-4V. The author identified the major difficulty in predicting the UTS as the dislocation evolution beyond the yield points, which relies on dynamic variables such as the evolution of dislocation density with changing strain as opposed to the static variables for the YS prediction equation. The KME model proposed by Yasnikov et al. [102] is the solution as it describes how the dislocation density changes with the change in strain. Figure 3.28 b) presents the results for comparing the predicted and experimental UTS and they are in good agreement within 5%.
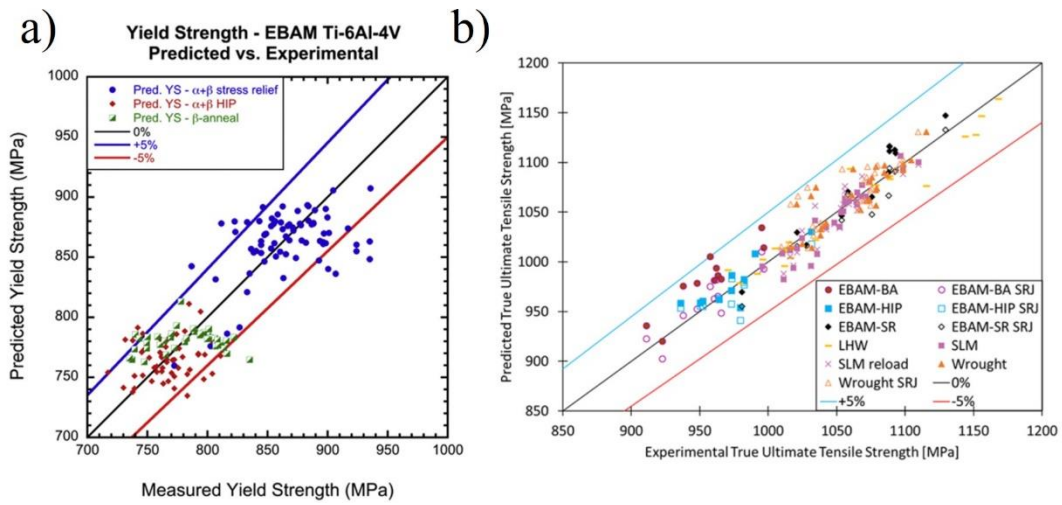
[28]Figure 3.28. a) The comparison between predicted and experimental YS of DED Ti-6Al-4V with different post-deposition heat treatments, adapted from [99]. b) Predicted vs experimental UTS for various material conditions, adapted from [101].

3.5 References

[1] Svetlizky, D., Das, M., Zheng, B., Vyatskikh, A. L., Bose, S., Bandyopadhyay, A., Schoenung, J. M., Lavernia, E. J., & Eliaz, N. (2021). Directed energy deposition (DED) additive manufacturing: Physical characteristics, defects, challenges and applications. Materials Today, 49, 271–295.

[2] Saboori, A., Gallo, D., Biamino, S., Fino, P., & Lombardi, M. (2017). An overview of additive manufacturing of titanium components by directed energy deposition: microstructure and mechanical properties. Applied Sciences, 7(9), 883.

[3] Sikan, F. (2022). Electron Beam Wire-fed Deposition of Titanium Alloys for Repair Applications. McGill University (Canada).

[4] Li, J. (2021). Solidification Microstructure Simulation of Ti6Al4V in Laser Wire Deposition Additive Manufacturing. McGill University (Canada).

[5] Kladovasilakis, N., Charalampous, P., Kostavelis, I., Tzetzis, D., & Tzovaras, D. (2021). Impact of metal additive manufacturing parameters on the powder bed fusion and direct energy deposition processes: A comprehensive review. Progress in Additive Manufacturing, 6, 349-365.

[6] Fayazfar, H., Salarian, M., Rogalsky, A., Sarker, D., Russo, P., Paserin, V., & Toyserkani, E. (2018). A critical review of powder-based additive manufacturing of ferrous alloys: Process parameters, microstructure and mechanical properties. Materials & Design, 144, 98-128.

[7] Gibson, B. T., Bandari, Y. K., Richardson, B. S., Henry, W. C., Vetland, E. J., Sundermann, T. W., & Love, L. J. (2020). Melt pool size control through multiple closed-loop modalities in laser-wire directed energy deposition of Ti-6Al-4V. Additive Manufacturing, 32, 100993.

[8] Shaikh, M. O., Chen, C.-C., Chiang, H.-C., Chen, J.-R., Chou, Y.-C., Kuo, T.-Y., Ameyama, K., & Chuang, C.-H. (2019). Additive manufacturing using fine wire-based laser metal deposition. Rapid Prototyping Journal, 26(3), 473–483.

[9] Salminen, A. (2010). The filler wire-laser beam interaction during laser welding with low alloyed steel filler wire. Mechanics, 84(4), 67-74.

[10] Chekir, N., Tian, Y., Gauvin, R., Brodusch, N., Sixsmith, J. J., & Brochu, M. (2018). Effect of travel speed and stress relief on thin Ti-6Al-4V laser wire deposits. Materials Science and Engineering: A, 724, 335-347.

[11] Baufeld, B., Brandl, E., & Van der Biest, O. (2011). Wire based additive layer manufacturing: Comparison of microstructure and mechanical properties of Ti–6Al–4V components fabricated by laser-beam deposition and shaped metal deposition. Journal of Materials Processing

Technology, 211(6), 1146-1158.

[12] Narayana, P. L., Kim, J. H., Lee, J., Choi, S.-W., Lee, S., Park, C. H., Yeom, J.-T., Reddy, N. G. S., & Hong, J.-K. (2021). Optimization of process parameters for direct energy deposited Ti-6Al-4V alloy using neural networks. The International Journal of Advanced Manufacturing Technology, 114(11–12), 3269–3283.

[13] Kistler, N. A., Corbin, D. J., Nassar, A. R., Reutzel, E. W., & Beese, A. M. (2019). Effect of processing conditions on the microstructure, porosity, and mechanical properties of Ti-6Al-4V repair fabricated by directed energy deposition. Journal of Materials Processing Technology, 264, 172-181.

[14] Brandl, E., Michailov, V., Viehweger, B., & Leyens, C. (2011). Deposition of Ti–6Al–4V using laser and wire, part I: Microstructural properties of single beads. Surface and Coatings Technology, 206(6), 1120-1129.

[15] Shamsaei, N., Yadollahi, A., Bian, L., & Thompson, S. M. (2015). An overview of Direct Laser Deposition for additive manufacturing; Part II: Mechanical behavior, process parameter optimization and control. Additive manufacturing, 8, 12-35.

[16] Baufeld, B. (2012). Effect of deposition parameters on mechanical properties of shaped metal deposition parts. Proceedings of the Institution of Mechanical Engineers, Part B: Journal of Engineering Manufacture, 226(1), 126-136.

[17] Brandl, E., Michailov, V., Viehweger, B., & Leyens, C. (2011). Deposition of Ti–6Al–4V using laser and wire, part II: Hardness and dimensions of single beads. Surface and Coatings Technology, 206(6), 1130-1141.

[18] Thompson, S. M., Bian, L., Shamsaei, N., & Yadollahi, A. (2015). An overview of Direct Laser Deposition for additive manufacturing; Part I: Transport phenomena, modeling and diagnostics. Additive Manufacturing, 8, 36-62.

[19] Gor, M., Soni, H., Wankhede, V., Sahlot, P., Grzelak, K., Szachgluchowicz, I., & Kluczyński, J. (2021). A critical review on effect of process parameters on mechanical and microstructural properties of powder-bed fusion additive manufacturing of ss316l. Materials, 14(21), 6527.

[20] Leyens, C., & Peters, M. (Eds.). (2006). Titanium and titanium alloys: fundamentals and applications. Wiley-vch.

[21] Donachie, M. J. (2000). Titanium: a technical guide. ASM international.

[22] Chekir, N. (2019). Laser wire deposition additive manufacturing of Ti-6Al-4V for the aerospace industry. McGill University (Canada).

[23] Lütjering, G., Williams, J. C., Lütjering, G., & Williams, J. C. (2003). Titanium matrix

composites (pp. 313-328). Springer Berlin Heidelberg.

[24] JI, X. (2018). Mechanical Properties and Deformation Mechanisms in β-type Ti-Mo Alloys.

[25] Yi, H. J., Kim, J. W., Kim, Y. L., & Shin, S. (2020). Effects of cooling rate on the microstructure and tensile properties of wire-arc additive manufactured Ti–6Al–4V alloy. Metals and Materials International, 26, 1235-1246.

[26] Ahmed, T., & Rack, H. J. (1998). Phase transformations during cooling in α+ β titanium alloys. Materials Science and Engineering: A, 243(1-2), 206-211.

[27] Galarraga, H., Warren, R. J., Lados, D. A., Dehoff, R. R., Kirka, M. M., & Nandwana, P. (2017). Effects of heat treatments on microstructure and properties of Ti-6Al-4V ELI alloy fabricated by electron beam melting (EBM). Materials Science and Engineering: A, 685, 417-428.

[28] Muhammad, M., Pegues, J. W., Shamsaei, N., & Haghshenas, M. (2019). Effect of heat treatments on microstructure/small-scale properties of additive manufactured Ti-6Al-4V. The International Journal of Advanced Manufacturing Technology, 103, 4161-4172.

[29] Vrancken, B., Thijs, L., Kruth, J. P., & Van Humbeeck, J. (2012). Heat treatment of Ti6Al4V produced by Selective Laser Melting: Microstructure and mechanical properties. Journal of Alloys and Compounds, 541, 177-185.

[30] Fan, W., Peng, Y., Wang, Y., Qi, Y., Feng, Z., Tan, H., Zhang, F., & Lin, X. (2024). Effect of grain boundary Widmanstätten α colony on the anisotropic tensile properties of directed energy deposited Ti-6Al-4V alloy. Journal of Materials Science & Technology, 184, 145–156.

[31] Stefanescu, D. M., & Ruxanda, R. (2004). Fundamentals of Solidification. Metallography and Microstructures, 71–92.

[32] Kurz, W., Fisher, D. J., & Rappaz, M. (2023). Fundamentals of Solidification 5th edition - Solutions Manual. Scientific Books Collection.

[33] Kou, S. (2003). Welding metallurgy. New Jersey, USA, 431(446), 223-225.

[34] Stefanescu, D. M. (2015). Science and engineering of casting solidification. Springer.

[35] Bermingham, M. J., Kent, D., Zhan, H., StJohn, D. H., & Dargusch, M. S. (2015). Controlling the microstructure and properties of wire arc additive manufactured Ti–6Al–4V with trace boron additions. Acta Materialia, 91, 289-303.

[36] Clare, A. T., Mishra, R. S., Merklein, M., Tan, H., Todd, I., Chechik, L., Li, J., & Bambach, M. (2022). Alloy design and adaptation for additive manufacture. Journal of Materials Processing Technology, 299, 117358.

[37] Carroll, B. E., Palmer, T. A., & Beese, A. M. (2015). Anisotropic tensile behavior of Ti–6Al–4V components fabricated with directed energy deposition additive manufacturing. Acta

Materialia, 87, 309-320.

[38] DebRoy, T., Wei, H. L., Zuback, J. S., Mukherjee, T., Elmer, J. W., Milewski, J. O., Beese, A. M., Wilson-Heid, A., De, A., & Zhang, W. (2018). Additive manufacturing of metallic components – Process, structure and properties. Progress in Materials Science, 92, 112–224.

[39] Vrancken, B., Thijs, L., Kruth, J. P., & Van Humbeeck, J. (2014). Microstructure and mechanical properties of a novel β titanium metallic composite by selective laser melting. Acta Materialia, 68, 150-158.

[40] Kawakami, A. (2002). Study on segregation behavior of alloying elements in titanium alloys during solidification (Doctoral dissertation, University of British Columbia).

[41] Doridot, E., Hans, S., Jardy, A., & Bellot, J. P. (2020). Industrial applications of modelling tools to simulate the PAMCHR casting and VAR process for Ti64. In MATEC Web of Conferences (Vol. 321, p. 10011). EDP Sciences.

[42] Bermingham, M. J., McDonald, S. D., Dargusch, M. S., & StJohn, D. H. (2008). Grain-refinement mechanisms in titanium alloys. Journal of Materials Research, 23(1), 97-104.

[43] Zhang, D., Qiu, D., Gibson, M. A., Zheng, Y., Fraser, H. L., StJohn, D. H., & Easton, M. A. (2019). Additive manufacturing of ultrafine-grained high-strength titanium alloys. Nature, 576(7785), 91-95.

[44] Kelly, S. M., & Kampe, S. L. (2004). Microstructural evolution in laser-deposited multilayer Ti-6Al-4V builds: Part I. Microstructural characterization. Metallurgical and Materials Transactions A, 35, 1861-1867.

[45] Ho, A., Zhao, H., Fellowes, J. W., Martina, F., Davis, A. E., & Prangnell, P. B. (2019). On the origin of microstructural banding in Ti-6Al4V wire-arc based high deposition rate additive manufacturing. Acta Materialia, 166, 306-323.

[46] Sikan, F., Wanjara, P., Gholipour, J., & Brochu, M. (2023). Use of miniature tensile specimens for measuring mechanical properties in the steady-state and transient zones of Ti–6Al–4V wire-fed electron beam deposits. Materials Science and Engineering: A, 862, 144487.

[47] Xu, W., Brandt, M., Sun, S., Elambasseril, J., Liu, Q., Latham, K., Xia, K., & Qian, M. (2015). Additive manufacturing of strong and ductile Ti–6Al–4V by selective laser melting via in situ martensite decomposition. Acta Materialia, 85, 74–84.

[48] Martina, F., Mehnen, J., Williams, S. W., Colegrove, P., & Wang, F. (2012). Investigation of the benefits of plasma deposition for the additive layer manufacture of Ti–6Al–4V. Journal of Materials Processing Technology, 212(6), 1377-1386.

[49] Sun, B., Li, S., Imai, H., Mimoto, T., Umeda, J., & Kondoh, K. (2013). Fabrication of high-

strength Ti materials by in-process solid solution strengthening of oxygen via P/M methods. Materials Science and Engineering: A, 563, 95-100.

[50] Wei, Q., Wang, L., Fu, Y., Qin, J., Lu, W., & Zhang, D. (2011). Influence of oxygen content on microstructure and mechanical properties of Ti–Nb–Ta–Zr alloy. Materials & Design, 32(5), 2934-2939.

[51] Carrozza, A., Aversa, A., Mazzucato, F., Lombardi, M., Biamino, S., Valente, A., & Fino, P. (2020). An innovative approach on directed energy deposition optimization: A study of the process environment's influence on the quality of Ti-6Al-4V samples. Applied Sciences, 10(12), 4212.

[52] Oh, J. M., Lee, B. G., Cho, S. W., Lee, S. W., Choi, G. S., & Lim, J. W. (2011). Oxygen effects on the mechanical properties and lattice strain of Ti and Ti-6Al-4V. Metals and Materials International, 17, 733-736.

[53] Cai, Z., Xiang, T., Bao, W., Chen, J., Gao, T., & Xie, G. (2022). Enhancing strength and ductility of pure titanium by interstitial oxygen atoms. Materials Science and Engineering: A, 854, 143806.

[54] Kwasniak, P., Garbacz, H., & Kurzydlowski, K. J. (2016). Solid solution strengthening of hexagonal titanium alloys: Restoring forces and stacking faults calculated from first principles. Acta Materialia, 102, 304-314.

[55] Yu, Q., Qi, L., Tsuru, T., Traylor, R., Rugg, D., Morris, J. W., Asta, M., Chrzan, D. C., & Minor, A. M. (2015). Origin of dramatic oxygen solute strengthening effect in titanium. Science, 347(6222), 635–639.

[56] Hrabe, N., & Quinn, T. (2013). Effects of processing on microstructure and mechanical properties of a titanium alloy (Ti–6Al–4V) fabricated using electron beam melting (EBM), part 1: Distance from build plate and part size. Materials Science and Engineering: A, 573, 264-270.

[57] Brandl, E., Palm, F., Michailov, V., Viehweger, B., & Leyens, C. (2011). Mechanical properties of additive manufactured titanium (Ti–6Al–4V) blocks deposited by a solid-state laser and wire. Materials & Design, 32(10), 4665-4675.

[58] Palanivel, S., Dutt, A. K., Faierson, E. J., & Mishra, R. S. (2016). Spatially dependent properties in a laser additive manufactured Ti–6Al–4V component. Materials Science and Engineering: A, 654, 39-52.

[59] Keist, J. S., & Palmer, T. A. (2016). Role of geometry on properties of additively manufactured Ti-6Al-4V structures fabricated using laser based directed energy deposition. Materials & Design, 106, 482-494.

[60] Wanjara, P., Watanabe, K., de Formanoir, C., Yang, Q., Bescond, C., Godet, S., Brochu, M., Nezaki, K., Gholipour, J., & Patnaik, P. (2019). Titanium Alloy Repair with Wire-Feed Electron Beam Additive Manufacturing Technology. Advances in Materials Science and Engineering, 2019, 1–23.

[61] Dharmendra, C., Hadadzadeh, A., Amirkhiz, B. S., Lloyd, A., & Mohammadi, M. (2020). Deformation mechanisms and fracture of electron beam melted Ti–6Al–4V. Materials Science and Engineering: A, 771, 138652.

[62] Shrestha, S., Panakarajupally, R. P., Kannan, M., Morscher, G., Gyekenyesi, A. L., & Scott-Emuakpor, O. E. (2021). Analysis of microstructure and mechanical properties of additive repaired Ti–6Al–4V by Direct Energy Deposition. Materials Science and Engineering: A, 806, 140604.

[63] Tian, X., Zhu, Y., Lim, C. V. S., Williams, J., Boyer, R., Wu, X., Zhang, K., & Huang, A. (2021). Isotropic and improved tensile properties of Ti-6Al-4V achieved by in-situ rolling in direct energy deposition. Additive Manufacturing, 46, 102151.

[64] Chekir, N., Tian, Y., Sixsmith, J. J., & Brochu, M. (2018). Effect of travel speed and sub-β transus post deposition heat treatments on thin Ti-6Al-4V laser wire deposits. Materials Science and Engineering: A, 724, 376-384.

[65] Bayat, M., Dong, W., Thorborg, J., To, A. C., & Hattel, J. H. (2021). A review of multi-scale and multi-physics simulations of metal additive manufacturing processes with focus on modeling strategies. Additive Manufacturing, 47, 102278.

[66] Bandyopadhyay, A., & Traxel, K. D. (2018). Invited review article: Metal-additive manufacturing—Modeling strategies for application-optimized designs. Additive manufacturing, 22, 758-774.

[67] Vasinonta, A., Beuth, J. L., & Griffith, M. (2006). Process Maps for Predicting Residual Stress and Melt Pool Size in the Laser-Based Fabrication of Thin-Walled Structures. Journal of Manufacturing Science and Engineering, 129(1), 101–109.

[68] Mukherjee, T., Zhang, W., & DebRoy, T. (2017). An improved prediction of residual stresses and distortion in additive manufacturing. Computational Materials Science, 126, 360-372.

[69] Irwin, J., & Michaleris, P. (2016). A line heat input model for additive manufacturing. Journal of Manufacturing Science and Engineering, 138(11), 111004.

[70] Kiran, A., Li, Y., Hodek, J., Brázda, M., Urbánek, M., & Džugan, J. (2022). Heat source modeling and residual stress analysis for metal directed energy deposition additive manufacturing. Materials, 15(7), 2545.

[71] Malmelöv, A. (2016). Modeling of additive manufacturing with reduced computational effort. Master's thesis. Luleå University of Technology, Luleå, Sweden.

[72] Gatsos, T., Elsayed, K. A., Zhai, Y., & Lados, D. A. (2020). Review on computational modeling of process–microstructure–property relationships in metal additive manufacturing. Jom, 72, 403-419.

[73] Chekir, N., Tian, Y., Gauvin, R., Brodusch, N., Sixsmith, J. J., & Brochu, M. (2018). Laser wire deposition of thick Ti-6Al-4V buildups: Heat transfer model, microstructure, and mechanical properties evaluations. Metallurgical and Materials Transactions A, 49, 6490-6508.

[74] Goldak, J., Chakravarti, A., & Bibby, M. (1984). A new finite element model for welding heat sources. Metallurgical transactions B, 15, 299-305.

[75] Bayat, M., Mohanty, S., & Hattel, J. H. (2019). A systematic investigation of the effects of process parameters on heat and fluid flow and metallurgical conditions during laser-based powder bed fusion of Ti6Al4V alloy. International Journal of Heat and Mass Transfer, 139, 213-230.

[76] Sikan, F., Wanjara, P., Gholipour, J., Kumar, A., & Brochu, M. (2021). Thermo-mechanical modeling of wire-fed electron beam additive manufacturing. Materials, 14(4), 911.

[77] Foroozmehr, A., Badrossamay, M., Foroozmehr, E., & Golabi, S. I. (2016). Finite element simulation of selective laser melting process considering optical penetration depth of laser in powder bed. Materials & Design, 89, 255-263.

[78] Yin, J., Zhu, H., Ke, L., Hu, P., He, C., Zhang, H., & Zeng, X. (2016). A finite element model of thermal evolution in laser micro sintering. The International Journal of Advanced Manufacturing Technology, 83, 1847-1859.

[79] Baykasoglu, C., Akyildiz, O., Candemir, D., Yang, Q., & To, A. C. (2018). Predicting microstructure evolution during directed energy deposition additive manufacturing of Ti-6Al-4V. Journal of Manufacturing Science and Engineering, 140(5), 051003.

[80] Manvatkar, V., De, A., & DebRoy, T. (2014). Heat transfer and material flow during laser assisted multi-layer additive manufacturing. Journal of Applied physics, 116(12).

[81] Tan, J. H. K., Sing, S. L., & Yeong, W. Y. (2020). Microstructure modelling for metallic additive manufacturing: a review. Virtual and Physical Prototyping, 15(1), 87-105.

[82] Wei, H. L., Knapp, G. L., Mukherjee, T., & DebRoy, T. (2019). Three-dimensional grain growth during multi-layer printing of a nickel-based alloy Inconel 718. Additive Manufacturing, 25, 448-459.

[83] Wei, H. L., Elmer, J. W., & DebRoy, T. (2017). Three-dimensional modeling of grain structure

evolution during welding of an aluminum alloy. Acta Materialia, 126, 413-425.

[84] Sun, Z., Tan, X., Tor, S. B., & Chua, C. K. (2018). Simultaneously enhanced strength and ductility for 3D-printed stainless steel 316L by selective laser melting. NPG Asia Materials, 10(4), 127-136.

[85] Rodgers, T. M., Madison, J. D., & Tikare, V. (2017). Simulation of metal additive manufacturing microstructures using kinetic Monte Carlo. Computational Materials Science, 135, 78-89.

[86] Zinovieva, O., Zinoviev, A., & Ploshikhin, V. (2018). Three-dimensional modeling of the microstructure evolution during metal additive manufacturing. Computational Materials Science, 141, 207-220.

[87] Zinoviev, A., Zinovieva, O., Ploshikhin, V., Romanova, V., & Balokhonov, R. (2016). Evolution of grain structure during laser additive manufacturing. Simulation by a cellular automata method. Materials & Design, 106, 321-329.

[88] Gong, X., & Chou, K. (2015). Phase-field modeling of microstructure evolution in electron beam additive manufacturing. Jom, 67, 1176-1182.

[89] Li, X., & Tan, W. (2018). Numerical investigation of effects of nucleation mechanisms on grain structure in metal additive manufacturing. Computational Materials Science, 153, 159-169.

[90] Charles, C., & J€arvstra˚t, N. (2009). Modelling Ti–6Al–4V Microstructure by Evolution Laws Implemented as Finite Element Subroutines: Application to TIG Metal Deposition. Eighth International Conference on Trends in Welding Research (TWR), Pine Mountain, GA, June 1–6, pp. 477–485.

[91] Loughnane, G. T., Kuntz, S. L., Klingbeil, N., Sosa, J. M., Irwin, J., Nassar, A. R., & Reutzel, E. W. (2015). Application of a microstructural characterization uncertainty quantification framework to Widmanstätten α-laths in additive manufactured Ti-6Al-4V.

[92] Kelly, S. M. (2004). Thermal and microstructure modeling of metal deposition processes with application to Ti-6Al-4V. Doctoral dissertation. the Faculty of the Virginia Polytechnic Institute and State University, Blacksburg, Virginia, USA.

[93] Irwin, J., Reutzel, E. W., Michaleris, P., Keist, J., & Nassar, A. R. (2016). Predicting microstructure from thermal history during additive manufacturing for Ti-6Al-4V. Journal of Manufacturing Science and Engineering, 138(11), 111007.

[94] Christian, J. W. (2002). The Thermodynamics of Irreversible Processes. The Theory of Transformations in Metals and Alloys, 95–105.

[95] Sun, W., Shan, F., Zong, N., Dong, H., & Jing, T. (2021). A simulation and experiment study on

phase transformations of Ti-6Al-4V in wire laser additive manufacturing. Materials & Design, 207, 109843.

[96] Kar, S., Searles, T., Lee, E., Viswanathan, G. B., Fraser, H. L., Tiley, J., & Banerjee, R. (2006). Modeling the tensile properties in β-processed α/β Ti alloys. Metallurgical and materials transactions A, 37, 559-566.

[97] Collins, P. C., Haden, C. V., Ghamarian, I., Hayes, B. J., Ales, T., Penso, G., Dixit, V., & Harlow, G. (2014). Progress Toward an Integration of Process–Structure–Property–Performance Models for "Three-Dimensional (3-D) Printing" of Titanium Alloys. JOM, 66(7), 1299–1309.

[98] Ghamarian, I., Samimi, P., Dixit, V., & Collins, P. C. (2015). A constitutive equation relating composition and microstructure to properties in Ti-6Al-4V: as derived using a novel integrated computational approach. Metallurgical and Materials Transactions A, 46, 5021-5037.

[99] Hayes, B. J., Martin, B. W., Welk, B., Kuhr, S. J., Ales, T. K., Brice, D. A., Ghamarian, I., Baker, A. H., Haden, C. H., Harlow, D. G., Fraser, H. L., & Collins, P. C. (2017). Predicting tensile properties of Ti-6Al-4V produced via directed energy deposition. Acta Materialia, 133, 120-133.

[100] Haden, C. V., Collins, P. C., & Harlow, D. G. (2015). Yield strength prediction of titanium alloys. Jom, 67, 1357-1361.

[101] Quintana, M. J., Temple, A. J., Harlow, D. G., & Collins, P. C. (2022). On the prediction of uniaxial tensile behavior beyond the yield point of wrought and additively manufactured Ti-6Al-4V. Integrating Materials and Manufacturing Innovation, 11(3), 327-338.

[102] Yasnikov, I. S., Estrin, Y., & Vinogradov, A. (2017). What governs ductility of ultrafine-grained metals? A microstructure based approach to necking instability. Acta Materialia, 141, 18-28.

Chapter 4: Methodology

The literature review in Chapter 3 demonstrates the challenges of controlling the microstructure and mechanical properties of AM parts. The AM industry would yield great cost and time savings by replacing the traditional trial-and-error methods with model-based prediction techniques before fabricating a real part. This thesis aims to achieve this goal by adopting the reverse engineering method which could provide the processing parameter recipe using mechanistic models that predict the key determining variables in the AM process given the required properties for qualification for specific applications.

Figure 4.1 presents the overall framework of the proposed methodology. A total of three mechanistic models to predict the thermal history, microstructure, and YS of LWD Ti-6Al-4V parts are included. All models are interconnected, as the output of one model is used as the input of the next model in the sequence. The thermal history is predicted by a FEA heat transfer model. The input variables in the FEA model include laser parameters, sample geometry and travel speed, etc. The resultant melt pool profile, solidification rates, and peak temperature are among the specific targeted data. The thesis utilized the microstructure model from the literature [1-2] which reported great accuracy in predicting the ratio of α/β phase fractions and α lath widths. The input of the microstructure model is the temperature-time data extracted from the FEA model, and the output is the quantified phase fractions and size of the α laths. The thesis selected the YS as the studied mechanical property since it's a key design allowable for materials performance. Moreover, many comprehensive and mature studies for predicting the YS of Ti-6Al-4V exist, and more recently, it has been proven to yield high accuracy in predicting the YS of DED-produced Ti-6Al-4V parts [3]. The thesis adopted the recently developed YS prediction model by Hayes et al. [3]. The input of the model is quantified microstructure data such as grain size and phase fraction, acquired from the experimental characterization results.

The whole methodology can be divided into two parts: the left loop for the validation of the methodology and the right loop for the implementation of the methodology. First, a series of Ti-6Al-4V coupons varied in processing parameters were produced by LWD and where a thermal camera recorded the thermal history during the deposition process. Then, experimental procedures are conducted to characterize and quantify the microstructure and to measure the tensile properties.

The methodology is validated by confirming the consistency between experimental and predicted results. On the other hand, after the validation of the models and the methodology, the right loop, which is in the reverse sequence of the left loop, aims to implement the methodology for the fabrication of a part accounting for given design allowable. Following the reverse sequence, the expected microstructure to satisfy the YS requirements in service is determined, which is used to assess the solidification conditions needed to achieve the said microstructure. Lastly, FEA is used to determine the proper combination of processing parameters to achieve the thermal solidification conditions that would yield a microstructure matching the required strength. Given the proposed parameter recipe, the part can be fabricated and tested to confirm the accuracy of the implemented methodology.

The details of the three prediction models will be explained in the following sections. In addition, the parameter recipes for the fabrication of all the deposits will be presented.
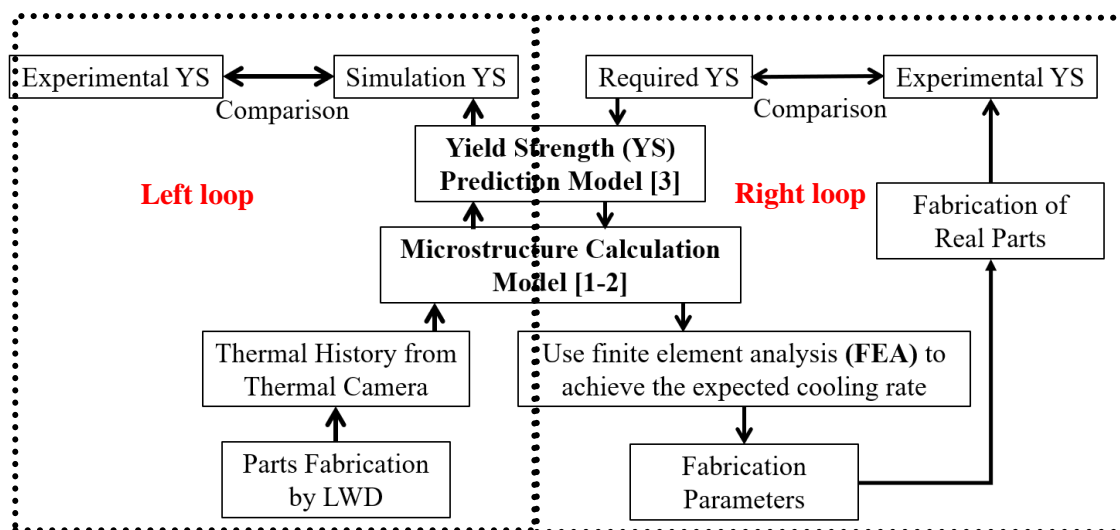
[29]Figure 4.1. Methodology for the fabrication of LWD Ti-6Al-4V parts via the reversed engineering approach.

4.1 Thermal FEA Model

A three-dimensional (3D) transient heat-transfer model was developed using the commercial FEA software ABAQUS/CAE (Dassault Systèmes Simulia Corp. USA). Figure 4.2 shows the flowchart explaining the simulation of the deposition process. The fluid flow was neglected in this work as the heat conduction within the solid was assumed to be the primary heat transfer mechanism. Figure 4.3 (a) shows that minimal deviation in the temperature profile was found when varying the heat

convection coefficient (*h*), supporting the assumption made to neglect the convection by the liquid flow. First, the substrate and deposit geometries were defined based on the dimensions of the real deposits. Then material properties and physical constants including temperature-dependent properties such as the thermal conductivity and the specific heat and temperature-independent properties such as the convection coefficient, the absorption efficiency, the emissivity and the Stefan-Boltzmann constant were assigned to the model. The values of these properties were adopted from Heigel et al. [4], which have been widely implemented in FEA modeling of the thermal behavior of DED Ti-6Al-4V [4-6]. Afterwards, the whole model was meshed. The type of the element was set to be DC3D8 standard 8-node linear heat transfer elements. The mesh size was determined to minimize the computation time and not to compromise the reliability of the results. The FEA model was developed based on the previous work developed by Chekir [6] and Sikan [7]. The corresponding optimized element sizes are 1 mm * 1 mm * 0.5 mm [6] and 1.5 mm * 0.75 mm * 0.5 mm [7]. A mesh sensitivity analysis was conducted to select the optimum mesh size for the current work. Based on the literature [6-7] and the deposit dimension, the investigated element sizes ranged between 1.2 mm * 0.75 mm * 0.5 mm and 0.4 mm * 0.3 mm * 0.6 mm. Figure 4.3 (b) presents the temperature-time comparison between these extreme element sizes. They were extracted from the same locations under the same processing parameters. The data suggest that both have similar cooling curves. The finer mesh was selected as the coarse mesh was likely to cause convergence problems, and the time cost difference was not constraining.
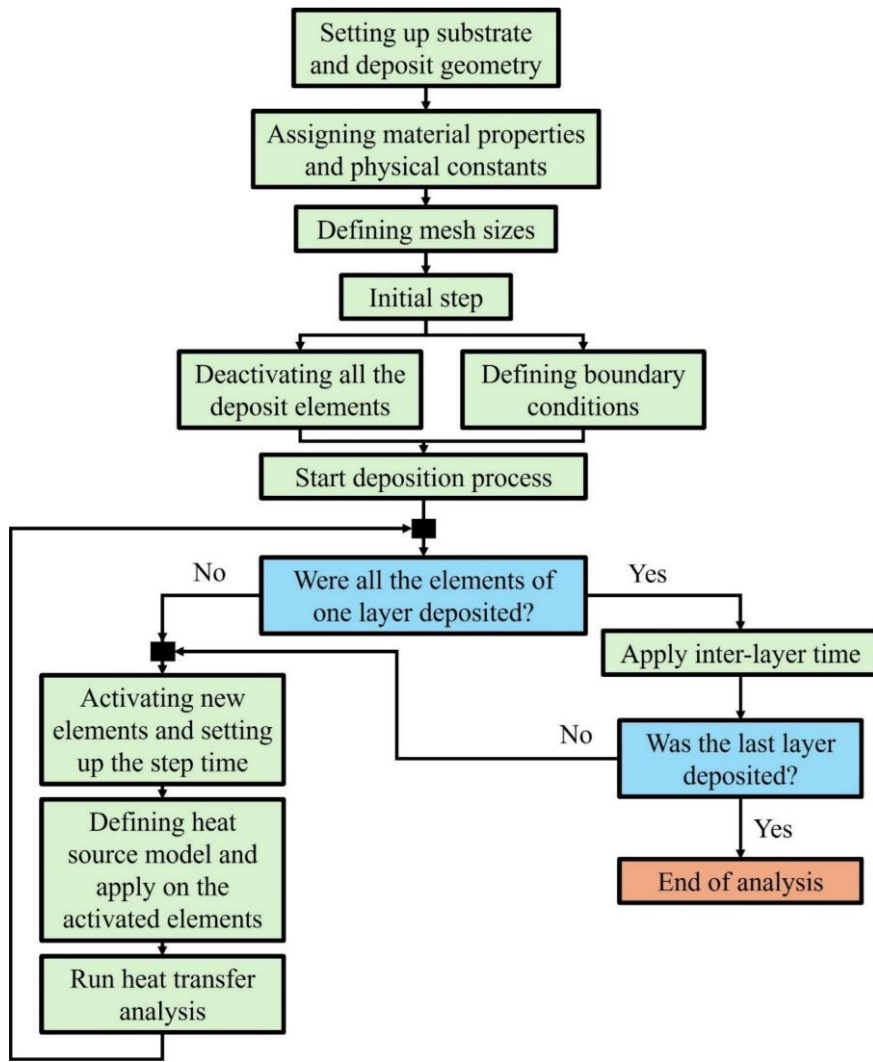
[30]Figure 4.2 Flowchart of the development and the simulation of the FEA thermal model.
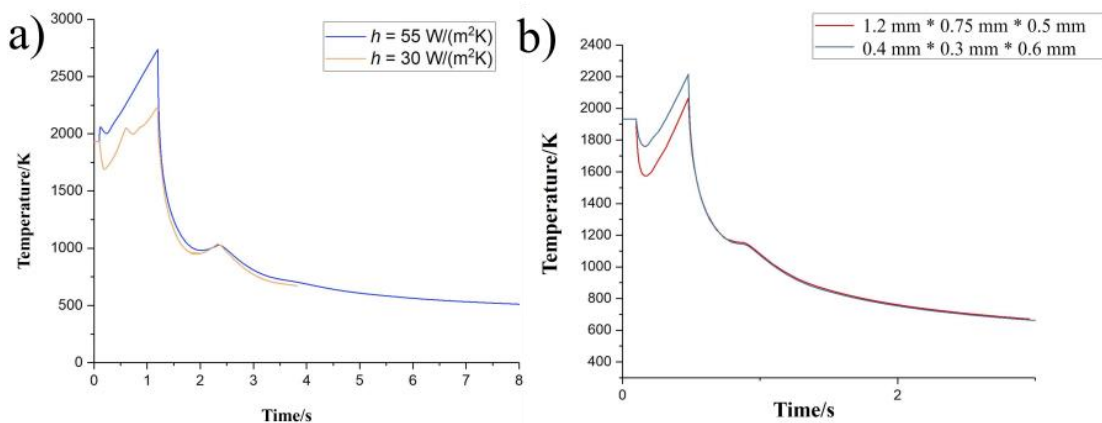
[31]Figure 4.3 (a) Comparison of temperature-time curves with different convection coefficients, h. (b) Comparison of temperature-time curves between element sizes of 1.2 mm * 0.75 mm * 0.5 mm and

0.4 mm * 0.3 mm * 0.6 mm

The deposition process was simulated using the "element birth" technique as mentioned in Chapter 3.4.1. Initially, all the elements associated with the deposit were deactivated. The width of the deposits is characterized by 10 elements. At each step, a total of 6*10= 60 elements were activated at liquidus temperature (1933 K) with a thermal input of the laser source. The number of activated elements at each step was justified because finer elements (length of 0.4 mm) were employed compared to the ones (length of 1.5 mm) used in the literature [7]. The laser source was modeled using the double ellipsoid heat source model developed by Goldak et al. [8]. The width of the ellipsoid was taken as half of the melt pool width, and the penetration depth was measured from the optical micrograph of the interface between the deposit and the substrate. Other parameters such as absorption efficiency were determined based on multiple literature studies [4-5,9-10]. The time of one step was decided by dividing the length of the activated elements by the travel speed. After one layer of deposition, an inter-layer time of 40 s was selected. This process was repeated until all the layers were deposited.

4.2 Microstructure model

The microstructure model was developed to calculate the α/β phase fractions and α lath widths based on the β to α phase transformation kinetics. The martensitic transformation was not considered as the typical cooling rates in the DED process are lower than 410 K/s (critical solidification rate to form) and only α-based microstructure was observed.

In this approach, the temperature-time data from the FEA model during the deposition process was used as input. Figure 4.4 presents the flowchart explaining the calculation of the α phase fractions and α lath widths. An iterative algorithm using the C++ programming language was developed using MATLAB (MathWorks®, USA). As Figure 4.4 shows that the α phase fractions were calculated at each step by comparing the current equilibrium α phase fraction with the current α phase fraction inherited from the precious time step. Depending on the comparison, the α phase will either dissolve or grow.

The dissolution of the α phase is achieved by diffusion-controlled movement of the α/β interface and no nucleation of the β phase within the α grains [1]. The approach considers 1D plate growth of the β phase with a parabolic growth rate, r.

$$r = aT^b$$
<div align="right">Equation 4-1</div>

where T is the current temperature (K), and the coefficient a = $2.21 * 10^{-31}$ $s^{-1/2}$ and b = 0.89 were adopted from Kelly [1] who determined them using ThermoCalc® and DiCTra® simulations. Several assumptions were made here [1]: (1) soft impingement of the diffusion field and the Gibbs-Thompson effect with the curvature of the interface were neglected, which is only significant when the particle size is in the order of tens of nanometers [11]. (2) Both phases were assumed to be plates and grow in 1D (normal to the longest dimension). The β phase was assumed to grow into the α phase with a parabolic thickening rate. (3) The growth rate was based on a diffusion-controlled isothermal β growth model.

The nucleation and growth of the α phase were modeled by the JMA model [12-14] which has been used to describe the evolution of the extent of reaction of the product phase with time. The kinetic parameters were adopted from Kelly [1] who calculated them using time-temperature-transformation diagrams in JMatPro. The assumptions behind the JMA model were: (1) The growing particles were assumed to be spheres. (2) The JMA equation was derived under the ideal condition of isothermal transformations. (3) The site-saturated nucleation was assumed that all nucleation events occur at the beginning.

To apply the aforementioned isothermal models to non-isothermal DED thermal cycles, the principle of additivity developed by Christian [15] was applied. In this approach, a given amount of transformation can be achieved by the cumulative contribution of small isothermal transformations over time. It assumed that the transformation occurred incrementally and that these increments could be superimposed linearly. Figure 4.5 presents the schematic explaining the additivity method using a heating cycle adopted from Kelly [1]. As shown, during heating from T_1 to T_3, the actual time to complete the dissolution reaction was divided into three time-steps. At first, the reaction proceeds following the OA curve with a total fraction evolved at A. At the second time step, when the temperature is heated to T_2, an equivalent time is used based on the starting phase fraction, and

the reaction proceeds following the BC curve. Similarly, the calculation (the DE curve) was made when the temperature is elevated to T_3. The original non-isothermal reaction was modeled with the addition of the OA-BC-DE paths.

The α lath width model followed the work by Charles and Järvstråt [16]. The equilibrium α lath width was calculated using an Arrhenius equation. The parameters were adopted from Irwin et al [17], who optimized the values for DED-fabricated Ti-6Al-4V alloys based on lath width measurements. The incremental calculation was implemented at each step to calculate the α lath width.
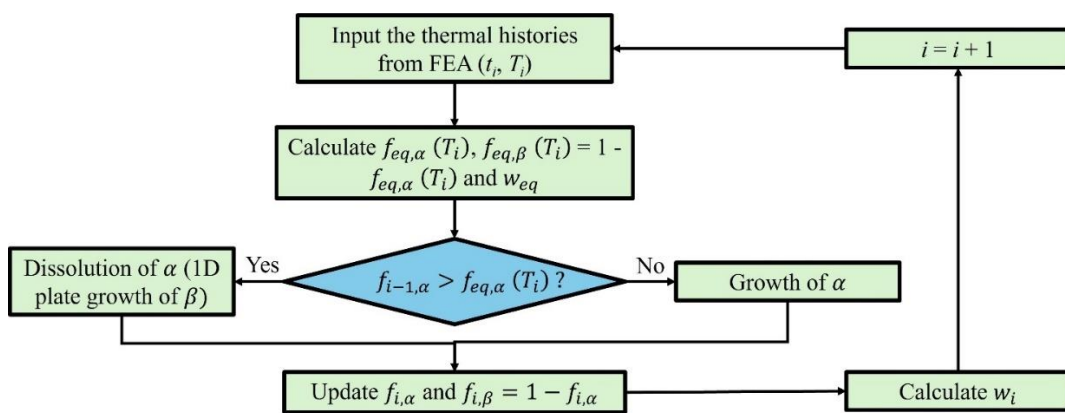
[32]Figure 4.4 Flowchart explaining the algorithm to calculate the microstructure from the thermal history.
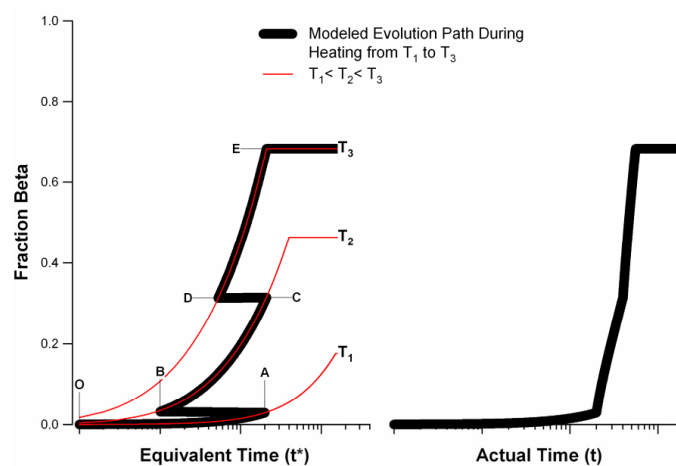
[33]Figure 4.5 Schematic illustrating the additivity method from a heating cycle adopted from Kelly [1].

63

4.3 YS prediction model

The thesis adopted the recently optimized YS prediction model by Hayes et al. [3]. They integrated the artificial neural network and genetic algorithm to derive a phenomenological equation to predict the YS of $\alpha + \beta$ Ti-6Al-4V from a dataset containing the composition, microstructure variables and YS data [18]. The model includes the major strengthening mechanisms such as intrinsic strength, solid solution strengthening, Hall-Petch strengthening and Taylor hardening. The most recent optimizations were developed on the Taylor hardening term by Hayes et al. [3]. This term was originally introduced to designate the increase in strength provided by the basketweave morphology [18] and was optimized as the operation of a Taylor hardening model by Hayes et al. [3]. This term was believed to be effective when the dislocation density is at a high level (10^{14} m^{-2}). Hayes et al. [3] reported that this term was only ~1 MPa for their HIP samples with only dislocation densities of ~10^{10} m^{-2}. In this research, this term was adopted as the dislocation density level was measured to be around 10^{14} m^{-2}.

4.4 Processing Parameters of the Samples

To validate the accuracy of the models, 18 Ti-6Al-4V single bead wall deposits were fabricated varying in travel speed, wire diameter and oxygen contents. The travel speeds investigated in this research are 2.1 mm/s, 4.2 mm/s, 6.4 mm/s, and 7.2 mm/s. This range was selected based on previous work [6] and as they are within the typical window adopted by LWD [19]. The wire diameters investigated are 0.8 mm, 1.1 mm and 1.6 mm. Most of the LWD processes reported in the literature used wires with diameters of about 1.2 mm [6,19-23]. This range was selected to systematically investigate the effect of wire diameter while keeping other parameters the same. The oxygen contents investigated are 0.05 wt.%, 0.067 wt.% and 0.16 wt.%. This range was selected considering two aspects: (1) The maximum oxygen content designated for Ti6Al4V alloys set by AMS 4911 standard is 0.2 wt.%. (2) The selection of wires aimed to cover a wide range of oxygen contents and minimize the variability of other elements. An inter-layer time of 40 s was taken for all deposits. This inter-layer time was determined based on previous work [6] to reduce heat accumulation and prevent distortion. The laser employed has a spot diameter of 0.9 mm and a Gaussian intensity distribution where the energy is highest at the center of the beam and gradually decreases toward the edges. Table 4.1 presents the other processing parameters used to fabricate all the deposits. The parameters were determined based on the optimized parameters used in the

previous work [6] to generate a fully dense deposit. For example, higher laser powers and slower wire feed rates were used for the deposition of large wire diameters of 1.1 and 1.6 mm to ensure complete fusion and minimize the formation of defects. The parameters were designed to ensure that the volume energy density (VED) was at the optimized level. The typical VED ranges are 40-120 J/mm^3 based on Kumar et al. [25]. VED is calculated as Equation 4-2:

$$VED = {P}/{vhw} \qquad\qquad \text{Equation 4-2}$$

where P is the laser power (W), v is the travel speed (mm/s), h is the layer height (mm) and w is the layer thickness (mm). VED is crucial to determine the quality of the deposit because it represents the capability of the laser to melt the material completely. In addition, VED establishes connections among key processing parameters. For example, to ensure VED is at the optimum level, a higher laser power was used to deposit the sample produced with a higher travel speed.

[7]Table 4.1. Processing parameters used to fabricate the Ti-6Al-4V deposits.

Variables	Wire Diameter	Laser Power	Wire Feed Rate	Travel Speed	Volume Energy Density
Travel Speed	0.8 mm	580 W	17.78 mm/s	2.1 mm/s	86.31 J/mm^3
		670 W	18.63 mm/s	4.2 mm/s	87.65 J/mm^3
		780 W	25.4 mm/s	6.4 mm/s	65.95 J/mm^3
Wire Diameter	0.8 mm	950 W	22.86 mm/s	5.1 mm/s	91.13 J/mm^3
	1.1 mm	1050 W	6.79 mm/s		95.32 J/mm^3
	1.6 mm	1200 W	6.79 mm/s		89.13 J/mm^3
Oxygen content	0.8 mm	750 W	26.67 mm/s	7.2 mm/s	68.62 J/mm^3

Table 4.2 presents the chemical compositions of the wire spools used to fabricate all the deposits. For the set of deposits varied in travel speed, wire spool 1 was used. For the set of deposits varied in wire diameter, wire spools 1, 2 and 3 with different wire diameters were used. At the same time, the chemical compositions were kept at similar levels to minimize differences in mechanical properties induced by differences in chemical compositions. For the set of deposits with different oxygen content, wire spools 1, 4 and 5 were used. Other parameters and processing conditions were kept

the same to minimize the number of variables. A total of 5 values of the travel speed were selected for all three sets of deposits to expand the investigated range.

[8]Table 4.2. Chemical composition (wt. %) of wire spools used to fabricate the deposits.

Wire Spool Number	Company	Wire Diameter	Al	V	Fe	C	O	N	H	Y	Ti
1	Astrolite ®, USA	0.8 mm	6.24	3.98	0.098	0.0018	0.067	0.0028	0.0018	-	Balance
2	Astrolite ®, USA	1.1 mm	6.05	4.04	0.089	0.01	0.07	0.0008	0.0016	<0.0005	Balance
3	Polymet, USA	1.6 mm	6.15	4.02	0.069	0.006	0.047	0.004	0.001	<0.0004	Balance
4	Astrolite ®, USA	0.8 mm	6.30	4.08	0.13	0.02	0.05	0.004	0.003	<0.005	Balance
5	Dynamet, USA	0.8 mm	6.10	3.82	0.17	0.025	0.16	0.0087	0.0012	<0.0005	Balance

4.5 Experimental Methods

To validate the aforementioned models, experimental data was compared with the modeled results. To validate the thermal FEA model, the temperature-time data was directly extracted from the files recorded by the thermal camera. However, for the microstructure model and the YS model, experimental characterization and tensile tests were carried out to obtain the corresponding experimental data. In this section, the methods to obtain these experimental data will be presented.

4.5.1 Characterization and Quantification of the Microstructure

BSE SEM micrographs in uncompressed image file format (tiff) were used to characterize and quantify the microstructure. The magnification of 3k~5k was selected to ensure of high resolution of the micrographs [26] containing a large number of grains. The SEM micrographs were first converted to binary images using a thresholding procedure by Image J. The volume fraction of each phase was measured according to the ASTM E562 standard [27]. Using the converted binary

images, the area fractions were estimated by counting the number of bright (α phase) divided by the total number of pixels that represents the volume fraction of the α phase. The thickness of α laths were measured perpendicular to the long axis of the laths. To remove any bias of the location and the number of the dataset, for each measurement, 5 micrographs from 5 random locations were used where 50 measurements were taken from each micrograph. The measurement of the colony size was adopted from Tiley et al. [26] where the images were overlaid with a random line grid and then marked where the lines crossed colony boundaries. The colony size was measured by dividing the line length by the number of marks.

4.5.2 Tensile Results

To minimize the effect of surface roughness, all the deposits were surface milled and polished. Machined subsize tensile specimens according to ASTM E8 [28] with a thickness of about 2 mm, a gauge width of 6 mm, and a gauge length of 25 mm were then extracted from the deposits. The tensile specimens have a grip width of about 11 mm. Figure 4.6 presents the two geometries to accommodate the extraction of tensile specimens from the travel direction (Z-deposit on the left) and the build direction (X-deposit on the right). It should be noted that the schematic is presented only to show the extraction plan but does not necessarily represent the actual dimensions of the deposits. It can be seen that the original lengths of both deposits were reduced by 10 mm for microstructure characterization. For Z-deposit, 5 tensile specimens with a separation of 2 mm considering the material loss during machining were extracted. To compensate for the 10 mm loss on the deposit length, the grip length was reduced from 25 mm to 20 mm considering the dimension tolerance of the actual deposits. For X-deposit, 4 tensile specimens with a separation of 1 mm were extracted due to the 10 mm loss on the deposit length.
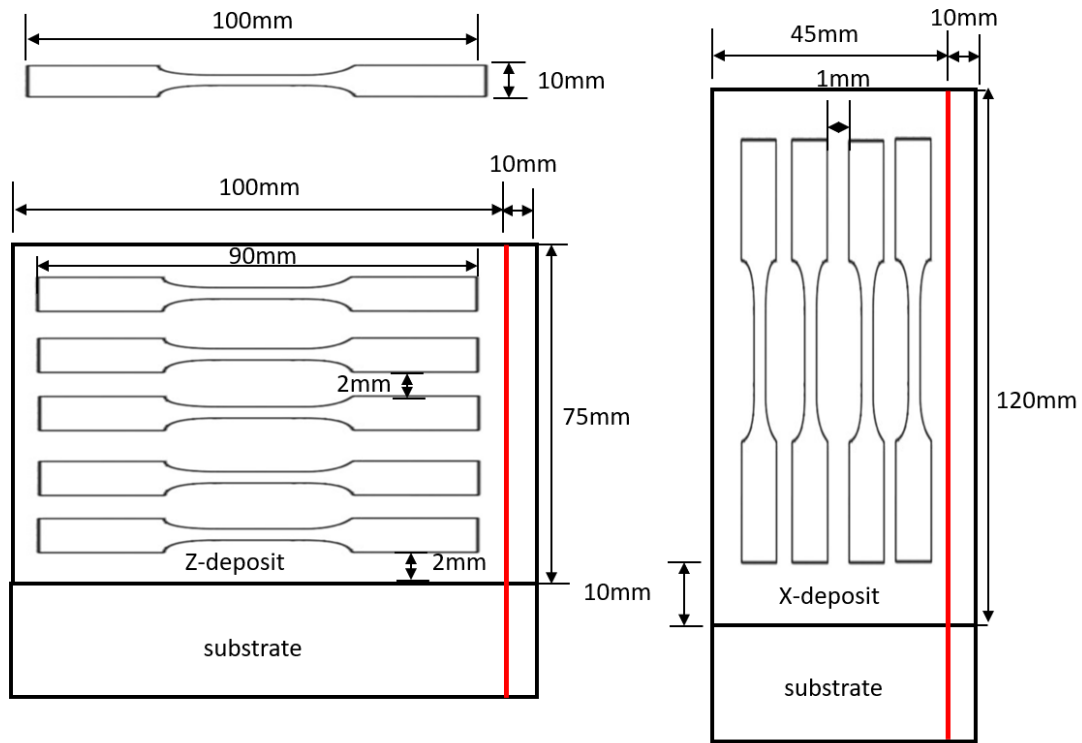
[34]Figure 4.6. Schematic of the extraction of the tensile specimens from the Z-deposit (left) and the X-deposit (right).

4.6 References

[1] Kelly, S. M. (2004). Thermal and microstructure modeling of metal deposition processes with application to Ti-6Al-4V. Doctoral dissertation. the Faculty of the Virginia Polytechnic Institute and State University, Blacksburg, Virginia, USA.

[2] Charles, C., & J€arvstra°t, N. (2009). Modelling Ti–6Al–4V Microstructure by Evolution Laws Implemented as Finite Element Subroutines: Application to TIG Metal Deposition. Eighth International Conference on Trends in Welding Research (TWR), Pine Mountain, GA, June 1–6, pp. 477–485.

[3] Hayes, B. J., Martin, B. W., Welk, B., Kuhr, S. J., Ales, T. K., Brice, D. A., Ghamarian, I., Baker, A. H., Haden, C. H., Harlow, D. G., Fraser, H. L., & Collins, P. C. (2017). Predicting tensile properties of Ti-6Al-4V produced via directed energy deposition. Acta Materialia, 133, 120-133.

[4] Heigel, J. C., Michaleris, P., & Reutzel, E. W. (2015). Thermo-mechanical model development and validation of directed energy deposition additive manufacturing of Ti–6Al–4V. Additive manufacturing, 5, 9-19.

[5] Yang, Q., Zhang, P., Cheng, L., Min, Z., Chyu, M., & To, A. C. (2016). Finite element modeling and validation of thermomechanical behavior of Ti-6Al-4V in directed energy deposition additive manufacturing. Additive Manufacturing, 12, 169-177.

[6] Chekir, N. (2019). Laser wire deposition additive manufacturing of Ti-6Al-4V for the aerospace industry. McGill University (Canada).

[7] Sikan, F. (2022). Electron Beam Wire-fed Deposition of Titanium Alloys for Repair Applications. McGill University (Canada).

[8] Goldak, J., Chakravarti, A., & Bibby, M. (1984). A new finite element model for welding heat sources. Metallurgical transactions B, 15, 299-305.

[9] Michaleris, P. (2014). Modeling metal deposition in heat transfer analyses of additive manufacturing processes. Finite Elements in Analysis and Design, 86, 51-60.

[10] Baykasoglu, C., Akyildiz, O., Candemir, D., Yang, Q., & To, A. C. (2018). Predicting microstructure evolution during directed energy deposition additive manufacturing of Ti-6Al-4V. Journal of Manufacturing Science and Engineering, 140(5), 051003.

[11] Christian, J. W. (1975). The Theory of Transformations in Metals and Alloys. I. Equilibrium and general kinetic theory.

[12] Michaleris, P. (2014). Modeling metal deposition in heat transfer analyses of additive manufacturing processes. Finite Elements in Analysis and Design, 86, 51-60.

[13] Johnson, W. A. (1939). Reaction kinetics in process of nucleation and growth. Transactions of Transactions of the American Institute of Mining and Metallurgical Engineers, 135, 416-458. 99

[14] Avrami, M. (1939). Kinetics of phase change. I General theory. The Journal of chemical physics, 7(12), 1103-1112.

[15] Christian, J. (2002). The theory of transformations in metals and alloys. George Newnes Ltd, London, UK.

[16] Charles, C., & Järvstråt, N. (2008). Modelling Ti-6Al-4V microstructure by evolution laws implemented as finite element subroutines: Application to TIG metal deposition. Eighth International Conference on Trends in Welding Research (TWR), Pine Mountain, GA, June 1– 6, pp. 477–485.

[17] Irwin, J., Reutzel, E. W., Michaleris, P., Keist, J., & Nassar, A. R. (2016). Predicting microstructure from thermal history during additive manufacturing for Ti-6Al-4V. Journal of Manufacturing Science and Engineering, 138(11), 111007

[18] Ghamarian, I., Samimi, P., Dixit, V., & Collins, P. C. (2015). A constitutive equation relating composition and microstructure to properties in Ti-6Al-4V: as derived using a novel integrated computational approach. Metallurgical and Materials Transactions A, 46, 5021-5037.

[19] Saboori, A., Gallo, D., Biamino, S., Fino, P., & Lombardi, M. (2017). An overview of additive manufacturing of titanium components by directed energy deposition: microstructure and mechanical properties. Applied Sciences, 7(9), 883

[20] Bambach, M., Sizova, I., Kies, F., & Haase, C. (2021). Directed energy deposition of Inconel 718 powder, cold and hot wire using a six-beam direct diode laser set-up. Additive Manufacturing, 47, 102269.

[21] Salminen, A. (2010). The filler wire-laser beam interaction during laser welding with low alloyed steel filler wire. Mechanics, 84(4), 67-74.

[22] Sims, H., Pegues, J., Whetten, S., Kustas, A. B., & Moore, D. (2023). Process-structure-property considerations for wire-based directed energy deposition of Ti-6Al-4V. Materials Characterization, 205, 113280.

[23] Chua, B. L., Lee, H. J., Ahn, D. G., & Kim, J. G. (2018). Influence of process parameters on temperature and residual stress distributions of the deposited part by a Ti-6Al-4V wire feeding

type direct energy deposition process. Journal of Mechanical Science and Technology, 32, 5363-5372.

[24] SAE International. (2024). AMS 4911: Titanium Alloy, Sheet, Strip, and Plate, 6Al - 4V, Annealed. SAE International.

[25] Kumar, N., Kumar, M., Kumar, V., & Sharma, A. (2023). Microstructural Heterogeneity and Anisotropy Control of Additive Manufactured Ti-6Al-4V Alloy for Aircraft Components. JOM, 75(5), 1695-1709.

[26] Tiley, J., Searles, T., Lee, E., Kar, S., Banerjee, R., Russ, J. C., & Fraser, H. L. (2004). Quantification of microstructural features in α/β titanium alloys. Materials Science and Engineering: A, 372(1-2), 191-198.

[27] ASTM International. (2008). ASTM E562-16: Standard Test Method for Determining Volume Fraction by Point Count. ASTM International.

[28] ASTM E8/E8M-15a. (2015) Standard Test Methods for Tension Testing of Metallic Materials, Annual Book of ASTM Standards, ASTM International, West Conshohocken, PA, USA.

Chapter 5: Thermo-Microstructural-Mechanical Modeling on Effect of Travel Speeds on Thin Ti-6Al-4V Deposits Developed by Laser Wire Deposition

Qi Zhang[1], Fatih Sikan[1], Nejib Chekir[2] and Mathieu Brochu[1*]

[1]: Department of Mining and Materials Engineering, McGill University, 3610 University St., Montreal, QC, H3A 0C5, Canada

[2]: Liburdi Automation Inc., Dundas, ON L9H 7K4, Canada

This Chapter proposes a platform of three mechanistic models to understand the predictability of YS for thin Ti-6Al-4V deposits developed by LWD. A 3D transient heat transfer FEA model was built to predict and assess the cooling rates during deposition. A microstructure model based on the α/β phase transformation kinetics and the Arrhenius equation was built to predict α/β phase fractions and the α lath width. The constitutive equations composed of the major strengthening mechanisms, such as solid solution strengthening and Hall Petch strengthening, etc., were used to predict the YS and understand the contribution of different strengthening mechanisms. To validate these three mechanistic models, eight thin Ti-6Al-4V deposits were developed with varied travel speeds. A thermal camera was used during deposition to record the thermal history and validate the developed FEA model. The α/β phase fractions and the α lath width calculated from characterized microstructure and experimental YS were compared with the modeled results to validate the microstructure model and YS model. The Chapter also reports the effect of travel speed on the thermal history, microstructure and mechanical properties of Ti-6Al-4V deposits developed by LWD.

5.1 Abstract

This study established a platform of three mechanistic models to understand the predictability of yield strength (YS) for Ti-6Al-4V deposits developed by laser wire deposition (LWD). Eight single-bead, multi-layer Ti-6Al-4V deposits were fabricated by LWD with four travel speeds for subsequent characterization and validation. A finite element analysis (FEA) thermal model was developed to simulate the deposition process and predict the thermal history. A microstructural model based on the α/β phase transformation kinetics was used to predict α/β phase fractions and α lath widths. The constitutive equations integrating the major strengthening mechanisms were used to predict the YS. The accuracy of all models was confirmed by comparison with experimental data. Grain size and tensile strength are statistically different only between the deposits produced with the slowest and fastest travel speeds. Microhardness is statistically similar across all travel speeds. Tensile results for all deposits are above the minimum tensile requirements according to the AMS4999 standard.

5.2 Introduction

Ti-6Al-4V is one of the most widely used titanium alloys in the aerospace industry, reportedly accounting for more than 50 % of the worldwide titanium tonnage due to its outstanding strength-to-weight ratio [1-2]. Additive manufacturing (AM), a layer-by-layer manufacturing process, has gained great interest in producing complex near-net-shape components. This process offers savings over conventional manufacturing technologies that involve the costly production of wrought ingots followed by a subtraction operation that generates a large amount of waste [3]. AM integrates two major processes for fabricating metallic materials: directed energy deposition (DED) and powder bed fusion (PBF). Unlike PBF processes in which a powder bed is selectively melted, the DED process is based on feeding powder or wire into a melt pool created by a high-energy source such as a laser beam. Of the two processes, DED has advantages in producing functionally graded and pure metal components and in repairing and cladding valuable parts that cannot be effectively repaired by other traditional methods [4]. In recent decades, wire-fed processes have received less attention compared to selective powder-bed fusion and powder-fed processes due to their limited geometric freedom. However, the new starting material used in wire feeding has a higher purity and lower contamination potential due to its reduced surface area. Such advantages are critical for aerospace components that require high material quality and repeatability [5]. In addition, the increasing

market demand for serial production of Ti-6Al-4V parts has favored wire-fed processes due to their high deposition rate [6].

Among the various processing parameters of the DED process, travel speed, laser power, and material feed rate have been the most investigated [3-23]. In general, it has been reported that increasing the travel speed, decreasing the laser power, and/or decreasing the feed rate to reduce the grain size resulted in higher strength [14]. Currently, parts are qualified by fabricating them through trial-and-error testing [24]. Predicting the thermal history, microstructure and mechanical properties prior to printing would be helpful in selecting the parameters for testing and would greatly reduce the time and effort required for qualification [25]. Finite element analysis (FEA) modeling using the "element birth" technique has been extensively used in AM processes to predict the cyclic thermal history during deposition [26-34]. Due to the large size of the simulated deposition, saving computational time has been of great interest. Many ways to reduce computation time have been reported in the literature, such as reducing the computational domain to half of the actual build size [31], employing graded meshes to use only fine meshes for regions of interest [36], and activating clumps instead of elements [37-38], etc. Of all the microstructural features for Ti-6Al-4V, α/β phase fractions and α lath widths have been extensively modeled based on the well-known phase transformation kinetics. The phase transformation kinetics during cooling has been successfully modeled by the Johnson– Mehl–Avrami (JMA) equation [39-41] for the isothermal process. Kelly [11] applied this approach to non-isothermal processes using Christian's principle of additivity [35]. Charles and Järvstråt [42] carried out similar research and included the modeling of α lath widths based on the Arrhenius equation. Optimizations of the kinetic models have been made in recent research to accommodate different applications [43]. It is well known that mechanical properties, such as yield strength (YS), essentially depend on the microstructure. Ti-6Al-4V exhibits complex microstructural features that span across length scales. Literature [44-47] has shown that it is possible to perform virtual experiments using an artificial neural network (ANN) to understand the influence of microstructure on the properties of Ti-6Al-4V. Collins et al. [48-49] were able to use ANN to perform virtual experiments to determine the functional dependencies of YS on various microstructural features. More recently, constitutive equations have been developed to predict the YS of Ti-6Al-4V using a hybrid ANN (Artificial Neural Network)/GA (Genetic Algorithms) approach [15].

This paper aims to understand the predictability of YS for Ti-6Al-4V deposits developed by laser wire deposition (LWD). A FEA model was developed to simulate the deposition process and to assist in assessing the thermal history of the deposits. The microstructural model developed by Kelly [11] and Charles and Järvstråt [42] was used to simulate the α/β phase fractions and the α lath width. The constitutive equations developed by Hayes et al. [15] were used to predict the YS of Ti-6Al-4V. The accuracy of all models was confirmed by comparison with the experimental data. It is worth mentioning that although the aforementioned models for predicting the thermal history, microstructure, and mechanical property have been extensively studied, there are no studies on combining all three models by coupling the inter-relationship between thermal history, microstructure, and material property. This research builds a thermo-microstructure-strength model based on the latest mechanistic models.

5.3 Materials and Methods

5.3.1 Sample Fabrication

Eight single-bead thin wall coupons were fabricated using a LAWS 1000[TM] wire-fed automated deposition system (Liburdi, Canada) equipped with an IPG Yb:YAG fiber laser reaching up to 1 kW power. To prevent oxidation, all coupons are deposited in an inert argon environment with oxygen levels below 60 ppm. Wrought Ti-6Al-4V plates are used as the substrate during deposition. A Ti-6Al-4V wire spool manufactured by Astrolite® Alloys Company Inc. (USA) is used to deposit the material. Table 5.1 presents the chemical composition of the Ti-6Al-4V wire. Four travel speeds were investigated: 2.1 mm/s, 4.2 mm/s, 6.4 mm/s and 7.2 mm/s. Two different coupon geometries were deposited to accommodate the extraction of tensile specimens. The first geometry of the deposits (denoted as X) is 110 mm in width, 75 mm in height, and 3 mm in thickness to extract tensile specimens along the travel direction X. The other deposit geometry (denoted as Z) is 55 mm in width, 120 mm in height, and 3 mm in thickness to extract tensile specimens along the build direction Z. The respective dimensions of the substrates are 110 mm in width, 21 mm in height, and 6 mm in thickness for X deposits and 55 mm in width, 21 mm in height, and 6 mm in thickness for Z deposits. Figure 5.1 shows the image of two representative Z- and X-deposited plates printed at 2.1 mm/s. The deposited coupons are subsequently used for heat treatment, microstructural characterization, and mechanical property evaluation.

[9]Table 5.1. Chemical composition (wt. %) of Ti-6Al-4V wire spool used in the study.

Components	Al	V	Fe	C	O	N	H	Y	Ti
Composition	6.24	3.98	0.098	0.0018	0.067	0.0028	0.0018	-	Balance
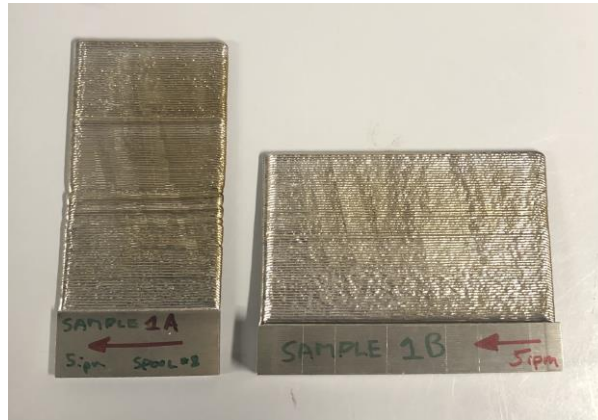
[35]Figure 5.1. Picture of two deposited plates in the Z and X direction produced with 2.1 mm/s.

5.3.2 Temperature Measurement and Modeling

During the deposition process, temperature measurements are undertaken using the Optris PI 08M (Optris, Germany). Optris infrared cameras are fully radiometric stationary thermographic systems with a high dynamic CMOS detector with up to 764 x 480 pixels resolution. It has a spectral range of 800 nm and a wide temperature range of 573 °C to 1900 °C. It provides a line scan mode that is used for deposition processes to record the thermal history of the deposits.

A three-dimensional (3D) transient thermal model of the LWD was developed using the commercial FEA software ABAQUS/CAE (Dassault Systèmes Simulia Corp. USA). The analysis was performed on a system with an 8-core AMD Ryzen 7-1700 CPU at 3.00 GHz with 64 GB of physical memory (RAM). The governing 3D energy balance equation of heat transfer can be expressed as Equation 5-1:

$$\frac{\partial}{\partial x}\left(k\frac{\partial T}{\partial x}\right) + \frac{\partial}{\partial y}\left(k\frac{\partial T}{\partial y}\right) + \frac{\partial}{\partial z}\left(k\frac{\partial T}{\partial z}\right) + Q = \frac{\partial(\rho C_p T)}{\partial t} \qquad \text{Equation 5-1}$$

where T is the temperature (K), k is the temperature-dependent thermal conductivity ($\frac{W}{mK}$), C_p is the temperature-dependent specific heat ($\frac{J}{kgK}$), ρ is the density ($\frac{kg}{m^3}$), and is assumed to be independent

of temperature, t is the time (s), Q is the power (W) generated per unit volume, and x, y, and z are the local coordinates of a point on the part geometry.

The laser beam heat source was modeled using Goldak's double ellipsoid heat source model [50]. This model has been widely used to describe the laser heat source during the LWD process, as shown in Equation 5-2:

$$Q(x, y, z) = \frac{6\sqrt{3}P\eta f}{abc\pi^{3/2}} e^{\left(-3\frac{x^2}{a^2} - 3\frac{y^2}{b^2} - 3\frac{z^2}{c^2}\right)} \hspace{4cm} \text{Equation 5-2}$$

where P is the laser power (W), η is the absorption efficiency, f is the scaling factor, x, y, and z are the local coordinates of a point on the part geometry, and a, b, and c are the transverse, depth, and longitudinal semi-axes of the ellipsoid, respectively. The effect of the heat source on the deposition track in the LWD process is generally considered to be circular because the laser beam moves slowly [34,39]. Therefore, a and c are generally taken as half of the layer thickness and b as the penetration depth. The heat source parameters such as laser power (W), layer thickness (m), and penetration depth (m) were determined according to the processing parameters. The absorption efficiency η is assumed to be 0.54, and the scaling factor f is assumed to be 1 based on literature studies [34,39].

The thermal heat losses on the part were simulated by thermal boundary conditions. The surface heat losses due to convection and radiation are given respectively as Equation 5-3 and Equation 5-4, respectively:

$$q_{conv} = h(T_{srf} - T_{\infty}) \hspace{5cm} \text{Equation 5-3}$$

$$q_{rad} = \varepsilon\sigma(T_{srf}^4 - T_{\infty}^4) \hspace{5cm} \text{Equation 5-4}$$

where h is the convection coefficient ($\frac{W}{m^2 K}$), T_{srf} is the surface temperature of the part (K), T_{∞} is the ambient temperature (298 K), ε is the emissivity, and σ is the Stefan–Boltzman constant ($\frac{W}{m^2 K^4}$). Table 5.2 lists the thermal parameters used in the model [34,51]. Table 5.3 shows the temperature-dependent thermal properties of the Ti-6Al-4V alloy implemented in the model for both the

substrate and the deposit. Thermal conductivity and specific heat with respect to temperature have been defined [51] and are shown in Table 5.3.

[10]Table 5.2. Thermal parameters used in the FEA model [34,51].

Absorption efficiency, η	0.54
Emissivity, ε	0.54
Convection coefficient, h	$55 \frac{W}{m^2 K}$
Stefan–Boltzmann constant, σ	$5.67 \times 10^{-8} \frac{W}{m^2 K^4}$

[11]Table 5.3. Temperature-dependent thermal properties of Ti-6Al-4V [51].

Temperature (K)	Thermal conductivity, k $(\frac{W}{mK})$	Specific heat, C_p $(\frac{J}{kgK})$
294	6.56	566.29
364	7.27	566.42
477	9.10	575.83
523	9.73	587.43
588	10.61	603.68
698	12.61	651.12
771	13.92	683.51
812	14.61	701.44
922	17.52	771.35
1032	17.52	859.70
1072	17.52	896.07
1143	17.52	960.72

DC3D8 standard 8-node linear heat transfer elements were used in the analysis. A representative 10-layer model was built to reduce computational time. A substrate of 55 mm x 21 mm x 6 mm was adopted. Materials were deposited on a 55 mm by 6 mm surface. The width of the bead was 3 mm. Figure 5.2(a) shows an overview of the mesh layout and Figure 5.2(b) shows a magnified version of the mesh. For the substrate mesh part, an increase in the size of the elements away from the interface was applied to reduce the computational time. For the deposit mesh part, the mesh size is

constant. The mesh size was selected according to the layer thickness, and the width of the bead is associated with five elements. The "element birth" technique was used to simulate the deposition process. All elements related to the deposition part preexisted and were initially set to the deactivated state. Figure 5.2(b) shows that the heat source was applied as a body heat flux to newly activated elements and previous elements in the range of beam diameter and penetration depth. Deposited elements were activated at the liquidus temperature (1933 K), while other elements were set to the initial temperature (298 K). Sixty elements were activated in each step. The step time was selected to simulate the travel speed of the heat source in the real deposition process. It was calculated by dividing the bead length by the selected travel speed. An interpass time of 40 s was selected to reduce heat accumulation of the part and mimic the real deposition process. Mesh sensitivity was performed to ensure the repeatability and credibility of the results. No significant differences were found in the thermal results for different mesh sizes. The mesh size mentioned here was chosen for further analysis to maximize computational efficiency.
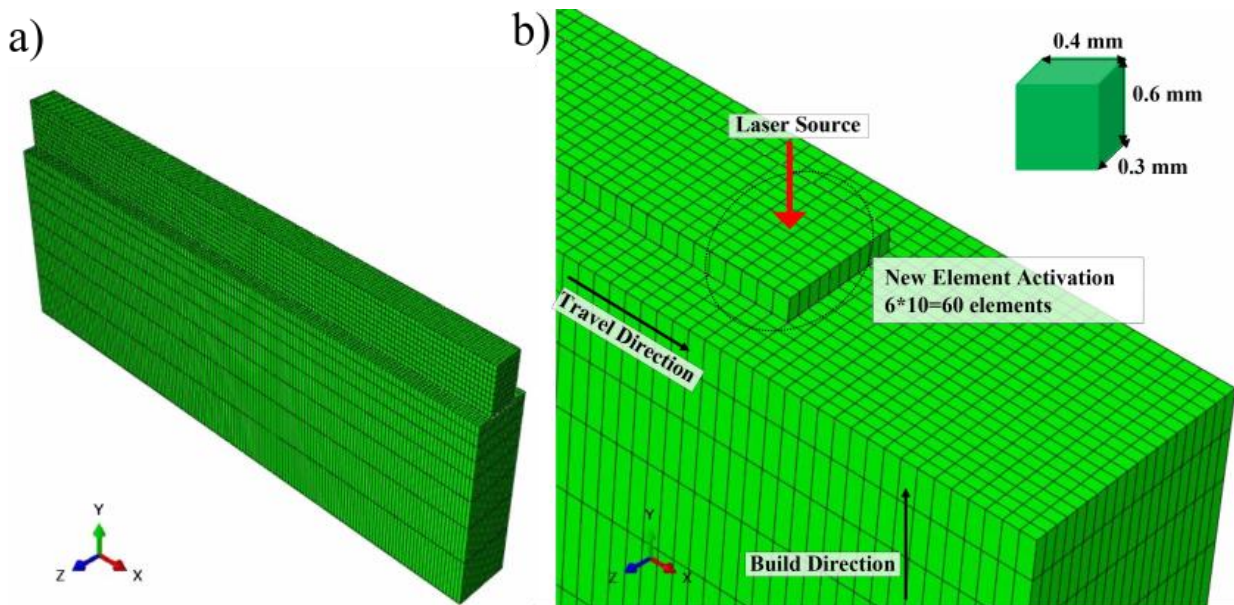
[36]Figure 5.2. (a) Overview of the mesh layout for the substrate and 10-layer deposit. (b) A magnified version of the mesh showing the element activation and moving laser source. The size sketch of each element on the deposit is shown in the top right corner.

5.3.3 Material Characterization and Testing

A stress relief (SR) cycle (held at 593 ℃ for 2 hours followed by furnace cooling), according to AMS2901 standard [52], was performed to reduce the residual stresses from the deposition process while keeping the structural features.

Metallographic evaluations were conducted in two different areas: the middle zone (i.e., the steady-state region) associated with the banding structure [8] and the top zone (i.e., the transient region) without the banding structure.

All samples were extracted along the build direction combining the middle zone (the steady state region) and the top zone (the transient region). After mounting in bakelite, these samples were ground from 400 SiC grit to 1200 SiC grit, followed by polishing with 1 μm diamond suspension and a finish with 0.05 μm colloidal silica. A Kroll's Reagent etchant containing 91 % deionized water (H_2O), 6 % nitric acid (HNO_3), and 3 % hydrofluoric acid (HF) was then used on the mounted samples to reveal structural features. Metallography was observed using a VHX-7000 series digital microscope (Keyence, Canada) and a SU-3500 cold field SEM (Hitachi, Ltd., Japan). A sample was extracted from the middle zone (i.e., the steady-state region) for the deposit built at 7.2 mm/s and used for dislocation characterization. It was first cut to a thickness of 500 μm with a slow-cutting machine and then ground to 50-60 μm. A small disk of 3 mm diameter was punched from the sample, which was later prepared by twin-jet polishing with a solution consisting of 0.9 L methanol with 50 mL H_2SO_4. Dislocation characterization was performed using a Talos F200X TEM (Thermo Fisher Scientific Inc., USA).

Vickers hardness was measured using a Clark Microhardness (CM-100AT) indenter (Sun-Tec Corporation, USA) under a 100 g load. Three measurements were done along the same layer for each of the reported values.

Tensile properties, including YS, ultimate tensile strength (UTS), and elongation, were tested using a 600 DX universal testing frame (Instron®, USA) with a calibrated load cell and extensometer. Machined subsize specimens according to ASTM E8 [53] with a thickness of about 2 mm, a gauge width of 6 mm, and a gauge length of 25 mm were extracted from SR plates. Four tensile specimens were extracted for deposits built in the Z direction, and five tensile specimens were extracted for deposits built in the X direction. They were tested at room temperature at a strain rate of 0.005

in/min to yield and 0.05 in/min after yield to fracture. Fractography was later analyzed using the same Keyence digital microscope and Hitachi SU-3500 cold field SEM as mentioned above.

5.3.4 Statistical Analysis

Statistical analysis was performed using one-way analysis of variance (ANOVA) and Tukey's *post hoc* analysis to determine the statistical difference in grain size, microhardness, YS, UTS, and elongation among all deposits ($\alpha = 0.05$). Analysis was performed using the one-way ANOVA application in Origin Pro 2024 software (Origin Lab, USA).

5.4. Results and Discussion

5.4.1 Effect of Travel Speeds on Thermal History

The thermal FEA model was first validated with thermal camera measurements of experimental deposition processes. The simulated temperature data were obtained at the same location where the thermal camera recorded the experimental data. Figure 5.3(a) shows that nodes at the end of each layer were selected to extract the temperature-time profile. Figures 5.3(b-e) show the temperature comparison between the experimental measurements and the FEA model results for all travel speeds at the first four layers. Note that for deposits with travel speeds of 2.1, 4.2, and 6.4 mm/s, both experimental and simulation results are in good agreement. Figure 5.3(f) shows that the cooling rates at β-transus temperature were also calculated from the extracted data. Table 5.4 lists calculated cooling rates from FEA and thermal camera, and the deviation for most layers is less than 10 % between thermal camera and FEA results. There is a larger discrepancy between FEA and thermal camera at the locations of the first layer and the high travel speed of 7.2 mm/s. This can be due to the combination of the proximity to the substrate and the high travel speed leading to the instability of the initial phase where the deposition parameters were adjusted to ensure the stability of the melt pool. It can be seen that with the deposition of the fourth layer, the FEA model results showed better fitting with the experimental measurements as the deposition reached a more stable stage. It should be noted that the cooling rates of the samples produced at 7.2 mm/s show smaller cooling rates compared to those produced at 6.4 mm/s. This is because a lower laser power was used for 7.2 mm/s and considering that the travel speeds and the substrate geometry are at a similar level, a reduced heat input resulted in similar cooling rates for the subsequent layers of the 7.2 mm/s and 6.4 mm/s deposits.
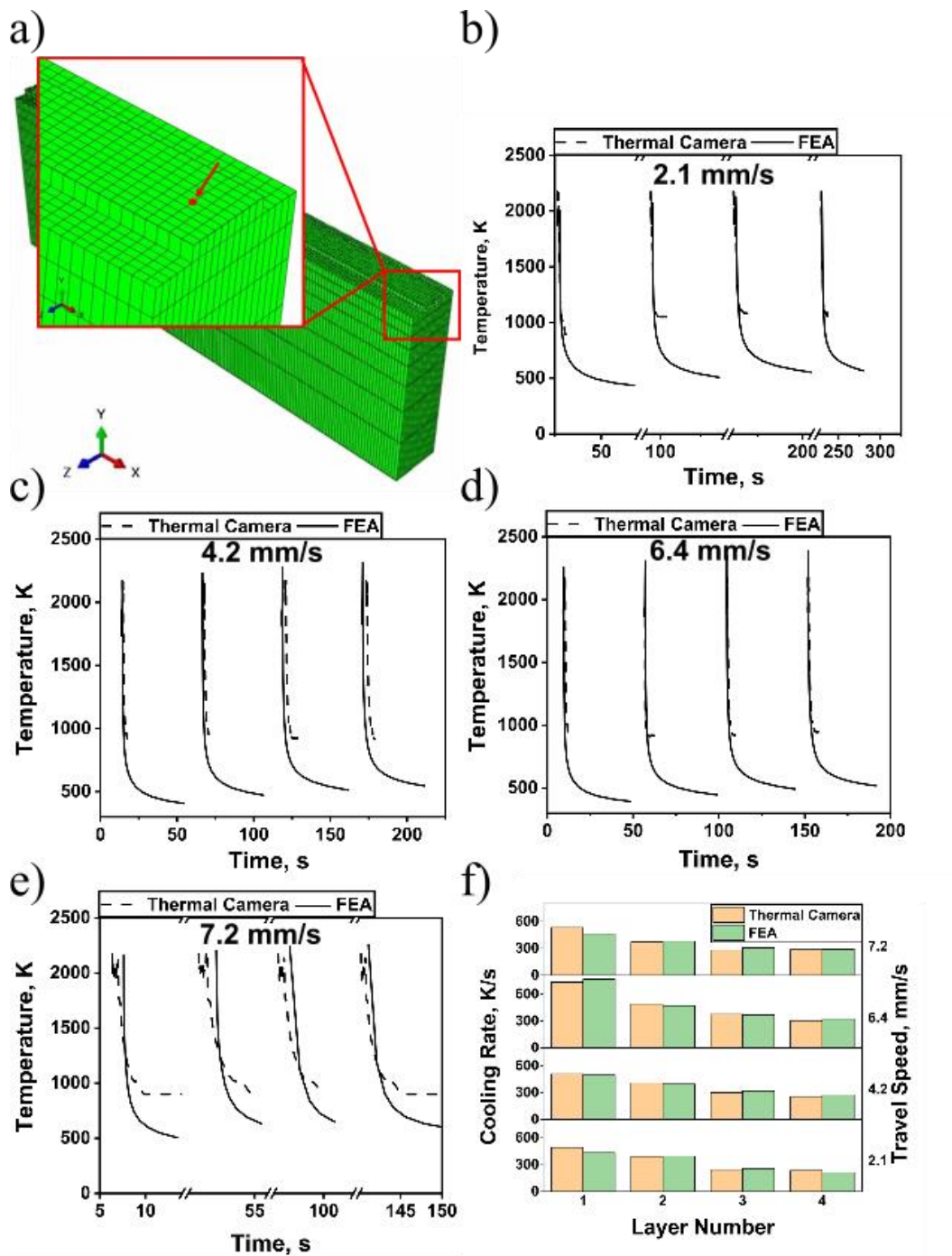
[37]Figure 5.3. (a) Position of the node on the first layer of the FEA model to extract the temperature data. The same position was used for the other layers. (b)-(e) Comparison of temperature-time profile between the FEA model and thermal camera measurements for travel speeds of 2.1, 4.2, 6.4, and 7.2 mm/s, respectively. (f) Comparison of calculated cooling rates between FEA and thermal camera measurements.

[12]Table 5.4. Comparison between calculated cooling rates (K/s) from FEA and the thermal camera.

83

Travel speed (mm/s)	Layer number	Cooling rates (K/s) from FEA	Cooling rates (K/s) from thermal camera	Percent Deviation (%)
2.1	1	494	434	12.1
	2	394	397	0.8
	3	245	258	5.3
	4	234	214	8.5
4.2	1	511	498	2.5
	2	409	397	2.9
	3	301	322	7.0
	4	257	276	7.4
6.4	1	736	767	4.2
	2	491	473	3.7
	3	378	370	2.1
	4	305	325	6.6
7.2	1	534	464	13.1
	2	370	381	3.0
	3	281	309	10.0
	4	287	291	1.4

It is well known that the cooling rates at β-transus are critical for the subsequent microstructural development. The Ti-6Al-4V deposits produced by LWD in this study consist of up to 130 layers. However, it would be unrealistic to build a FEA model with hundreds of layers due to computational time and cost. Therefore, to confirm the hypothesis that the 10-layer FEA model can be used to infer the cooling rates of the deposits, a 20-layer FEA model with a travel speed of 2.1 mm/s was built to investigate the evolution of the cooling rates at β-transus and peak temperature with the deposition of layers. The end node for each layer was selected to calculate the cooling rates at β-transus when the last layer was deposited. The highest temperature reached at each layer during the 20-layer deposition was extracted as the peak temperature. Figure 5.4(a) shows the evolution of peak temperature and the cooling rate at β-transus of each layer for the 20-layer FEA model. At the initial stage of the deposition process, the peak temperature increases, and the cooling rate decreases with the deposition of subsequent layers due to heat accumulation. However, around the 6th to 10th layer, a balance between heat accumulation and thermal losses of the part is achieved.

The deposition reaches at the stable stage where the peak temperature and cooling rate show negligible changes. Figure 5.4(b) shows the evolution of the peak temperature and cooling rate at β-transus for each layer of the 10-layer FEA model with travel speeds of 2.1, 4.2, 6.4, and 7.2 mm/s. It also confirms that the cooling rates and the peak temperature can reach stability around the 6th layer. This has confirmed the hypothesis that the 10-layer FEA model used in the study is credible to represent the thermal history that the real deposit went through at the stable stage. Figure 5.4(b) demonstrates that the peak temperatures and cooling rates increase with the increase of the travel speed. This follows the same trend reported in the literature [8,17]. However, all cooling rates are within the range of 200 ± 50 K/s with a difference of no more than 80 K/s.
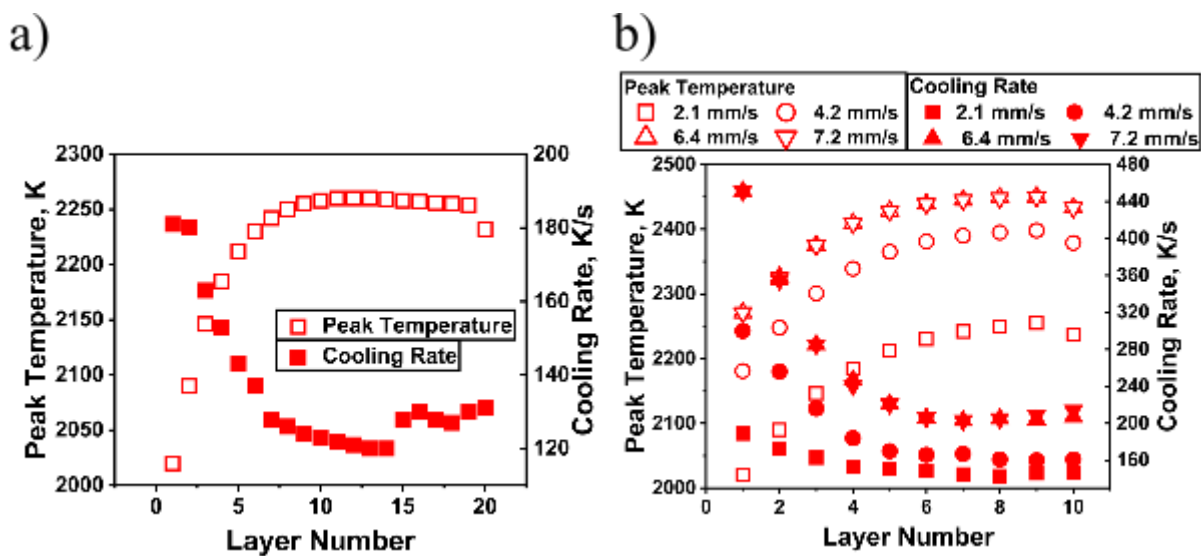
[38]Figure 5.4. (a) Peak temperatures and cooling rates at β-transus temperature of each layer for the 20-layer FEA model. (b) Peak temperatures and cooling rates at β-transus temperature of each layer for travel speed 2.1, 4.2, 6.4, and 7.2 mm/s of the 10-layer FEA model.

Figure 5.5 shows the temperature contours of the isotherm profiles at the β-transus temperature (1273 K) extracted from the FEA models (on the left) at the time when the last layer was deposited. The numbers of layers included in these temperature contours are compared with the optical micrographs of the top regions (on the right). As shown, the top regions of the optical micrographs for deposits produced with various travel speeds are composed of the same number of layers then the temperature contours from the FEA models. This further validates the accuracy of the FEA model.
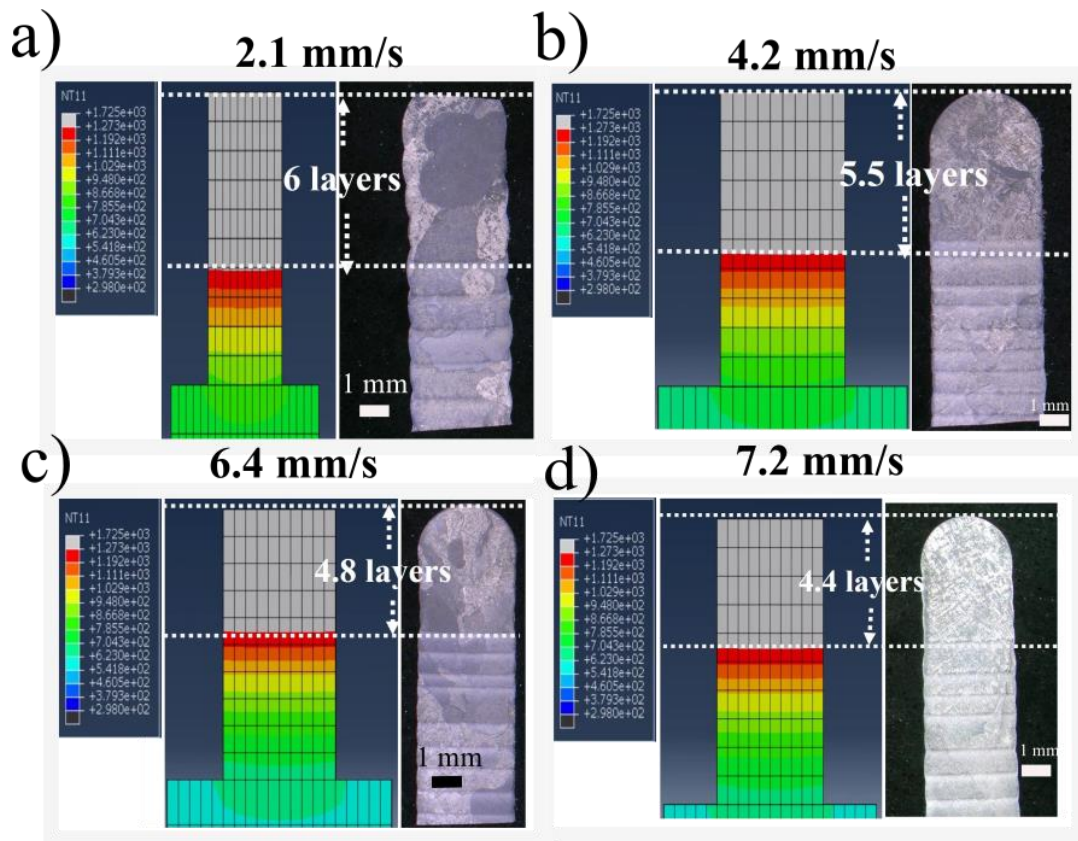
[39]Figure 5.5. Temperature contours of the isotherm profiles at the β-transus temperature (1273 K) from the FEA model (on the left) and the optical micrographs of the top regions (on the right) for deposits fabricated with travel speeds of (a) 2.1 mm/s, (b) 4.2 mm/s, (c) 6.4 mm/s, and (d) 7.2 mm/s.

5.4.2 Structure Evaluation

5.4.2.1 Macrostructure

Figure 5.6 presents the macrostructure of Ti-6Al-4V deposits at different travel speeds. Columnar prior β grains (grain boundaries outlined with red dashed lines) are observed at all travel speeds. Table 5.5 demonstrates that larger grains were developed at slower travel speeds such as 2.1 and 4.2 mm/s. The faster travel speeds, such as 6.4 and 7.2 mm/s, developed thinner columnar prior β grain.

Figure 5.6 shows another typical feature associated with Ti-6Al-4V: the presence of the banding structure. For all Ti-6Al-4V deposits, there is a region at the top that is characterized by the absence of bands. This region, where all the layers were heated above β-transus when the last layer is deposited, is called the top zone (the transient region) [8]. These repetitive bands are formed due to the successive thermal cycles that one layer goes through by the deposition of the subsequent layers. As reported, banding features are formed by α/β allotropic phase transformations during reheating

to just below β-transus and are associated with a higher percentage of alpha colony [17,26]. The distance between each band was measured to be about 0.6 mm, which is associated with the predefined laser head increment, as the β-transus isotherm was raised to the same distance when another layer was deposited. The zone with the previously described bands is often referred to as the steady-state region [8]. Table 5.6 lists the size of the top region for Ti-6Al-4V deposits at different travel speeds. It can be seen that the top region becomes shallower as the travel speed increases. This is because the volumetric heat input was lower at higher travel speeds, so the amount of the material heated above β-transus was less.

[13]Table 5.5. Width of columnar prior β grains for Ti-6Al-4V deposits at different travel speeds.

Sample label/ Travel speed (mm/s)	2.1	4.2	6.4	7.4
Z	3.3 ± 1.2 mm	1.6 ± 0.3 mm	1.0 ± 0.3 mm	1.1 ± 0.3 mm
X	2.9 ± 1.0 mm	1.5 ± 0.5 mm	1.6 ± 1.0 mm	1.0 ± 0.3 mm

[14]Table 5.6. Height of top region for Ti-6Al-4V deposits at different travel speeds.

Sample label/ Travel speed (mm/s)	2.1	4.2	6.4	7.4
Z	5.73 mm	4.46 mm	3.75 mm	3.53 mm
X	5.51 mm	4.27 mm	3.5 mm	3.44 mm

Figure 5.6(h) displays another macrostructural feature associated with some Ti-6Al-4V deposits. Unlike the columnar prior β grains developed for most deposits, a certain percentage of equiaxed prior β grains were observed on the edge region (labeled with a purple box) and the region between the 60th pass to the 110th pass (labeled with purple arrows) of the deposit produced at 7.2 mm/s. This type of grain structure has been reported in the literature and can form due to different solidification conditions. The morphology of the solidification structure is mainly decided by two critical parameters: the thermal gradient, G, and the growth rate, R. To confirm the solidification structure of this region, G and R were calculated at these two regions of the deposits using the thermal data obtained from the thermal camera. G can be calculated using Equation 5-5:

$$G = {\Delta T}/{\Delta x} \qquad\qquad\text{Equation 5-5}$$

where ΔT (K) is the temperature difference along the travel direction between the center and the tail of the melt pool and Δx (cm) is the distance between these two points. The solidification cooling rate, CR, was calculated using Equation 5-6:

$$CR = {\Delta T}/{\Delta t} \qquad\qquad\text{Equation 5-6}$$

where ΔT (K) and Δt (s) is the temperature and time difference at the solidification temperature. Then, R (cm/s) can be calculated by Equation 5-7:

$$R = {CR}/{G} \qquad\qquad\text{Equation 5-7}$$

The calculated data were then compared with a solidification map for Ti-6Al-4V [26] to predict the solidification microstructures. Figure 5.7 presents the superposition of the calculated G and R with the solidification map. The points calculated on the edge (labeled with hollow points) for the 20th - 22nd passes, 60th – 62nd passes, and 109th - 110th passes along the build height have a G in the range of 276 K/cm to 1031 K/cm. The average values of G are statistically similar (p>0.05) among the three groups. On the other hand, the point calculated at the center (labeled with a filled red box) has a G of 1100 K/cm. As shown, most of the points calculated on the edge region fall in the fully equiaxed grain structure region, while the point calculated on the center of the 109th pass falls in the mixed grain structure region. This result agrees well with the macrostructure observation shown in Figure 5.6(h). The equiaxed structures on the edge can be due to the heat accumulation that altered the solidification conditions. On the other hand, equiaxed structures were observed after the 80th pass, thus the different solidification conditions that promoted the development of the equiaxed structures on the middle region of the 109th pass was inferred to be due to an interruption at the 80th pass that was taken during the deposition process.
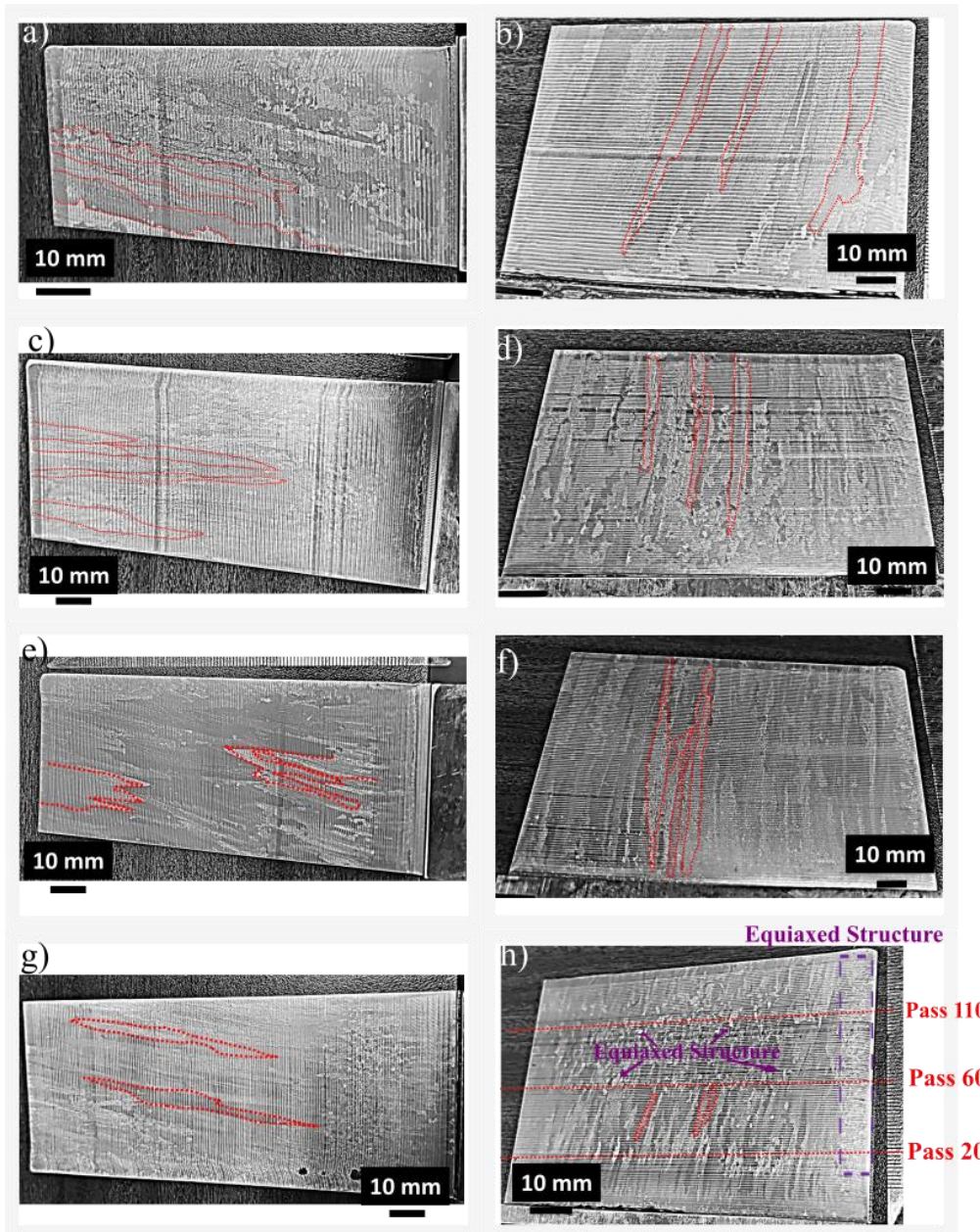
[40]Figure 5.6. The macrostructure of Ti-6Al-4V deposits built in the Z direction with travel speeds 2.1 (a), 4.2 (c), 6.4 (e), and 7.2 (g) mm/s, respectively; and of the deposits built in the X direction with travel speeds 2.1 (b), 4.2 (d), 6.4 (f), and 7.2 (h) mm/s, respectively.
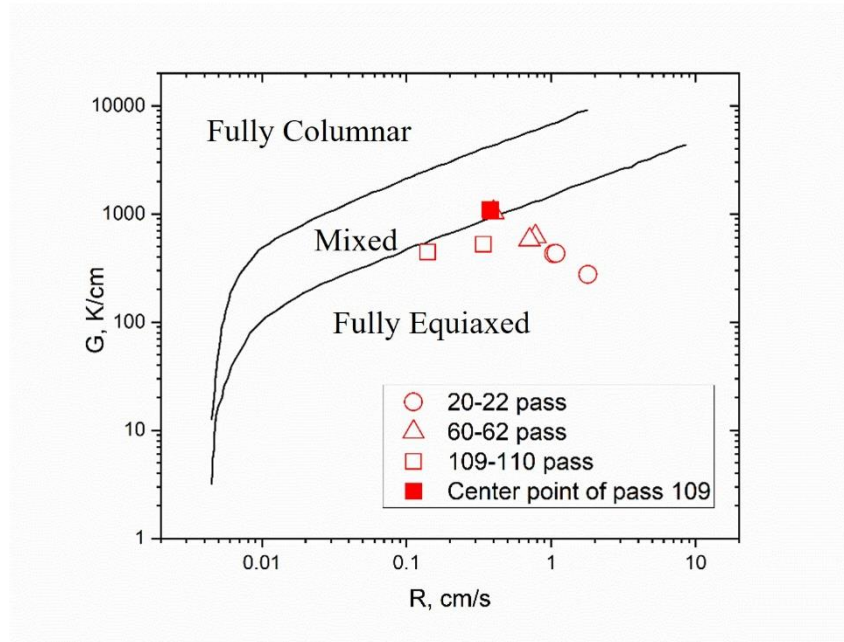
[41]Figure 5.7. The comparison between the calculated *G* and *R* values from different locations of the deposits shown in Figure 5.6(h) and the Ti-6Al-4V solidification map [26].

5.4.2.2 Microstructure

Similar microstructures were observed between deposits built in the Z and X directions. Figure 5.8 shows the high magnification SEM micrographs for the top region (transient) and the middle region (steady state) of the Ti-6Al-4V deposits built in the X direction produced at different travel speeds. Figure 5.8 demonstrates that all micrographs are composed of basketweave α/β morphology, while Figure 5.8(d) also shows α colony morphology. A small amount of allotriomorphic (grain boundary) α was also observed in Figure 5.8(d). During cooling to β-transus temperature, the BCC β phase is transformed into the HCP α phase with allotropic phase transformation. The HCP α phase starts to nucleate at the β grain boundaries according to the crystallographic relationship called Burger's relationship. The size of the alpha plates reflects the effects of thermal history and the cooling rate on the final microstructure. At higher cooling rates, the sizes of α plates and α colonies decrease [7].

Table 5.7 lists the measured α lath widths for the top region (transient) and the middle region (steady state). The measured α lath widths are comparable to those reported in the literature. Chekir et al. [8] measured $0.812 \pm 0.169 \, \mu m$ and $0.538 \pm 0.143 \, \mu m$ for SR LWD Ti-6Al-4V deposits produced at 1.4 mm/s and 7.2 mm/s, respectively. The ANOVA analysis reports that α lath widths are statistically different between deposits produced at 2.1 mm/s and 7.2 mm/s ($p<0.05$). No

statistical difference is found among the rest of the groups ($p>0.05$). Thinner α laths were developed at 7.2 mm/s than at 2.1 mm/s, which is consistent with the higher cooling rate experienced at higher travel speeds mentioned in section 3.1. The ANOVA analysis demonstrates that statistically finer α laths can only be produced if the travel speeds are high enough. Table 5.7 also shows that the middle region (steady state) has coarser α laths than the top region (transient) for all deposits. This is also consistent with what Chekir et al. [8] and Brandl et al. [17] reported. The coarsening of the α lath in the middle region (steady state) is induced by the repeated thermal cycles experienced by the subsequent layers, while all layers at the top region (transient) were heated above β-transus when the last layer was deposited.

[15]Table 5.7. α lath width of the transient region and steady-state region for all deposits.

Sample label	Region/Travel speed (mm/s)	2.1	4.2	6.4	7.2
Z	Top region (transient)	$0.63 \pm 0.22\ \mu m$	$0.57 \pm 0.21\ \mu m$	$0.57 \pm 0.17\ \mu m$	$0.53 \pm 0.15\ \mu m$
	Middle region (steady state)	$0.86 \pm 0.25\ \mu m$	$0.76 \pm 0.17\ \mu m$	$0.77 \pm 0.16\ \mu m$	$0.74 \pm 0.20\ \mu m$
X	Top region (transient)	$0.84 \pm 0.30\ \mu m$	$0.58 \pm 0.18\ \mu m$	$0.50 \pm 0.11\ \mu m$	$0.68 \pm 0.23\ \mu m$
	Middle region (steady state)	$0.88 \pm 0.22\ \mu m$	$0.81 \pm 0.20\ \mu m$	$0.77 \pm 0.20\ \mu m$	$0.67 \pm 0.15\ \mu m$
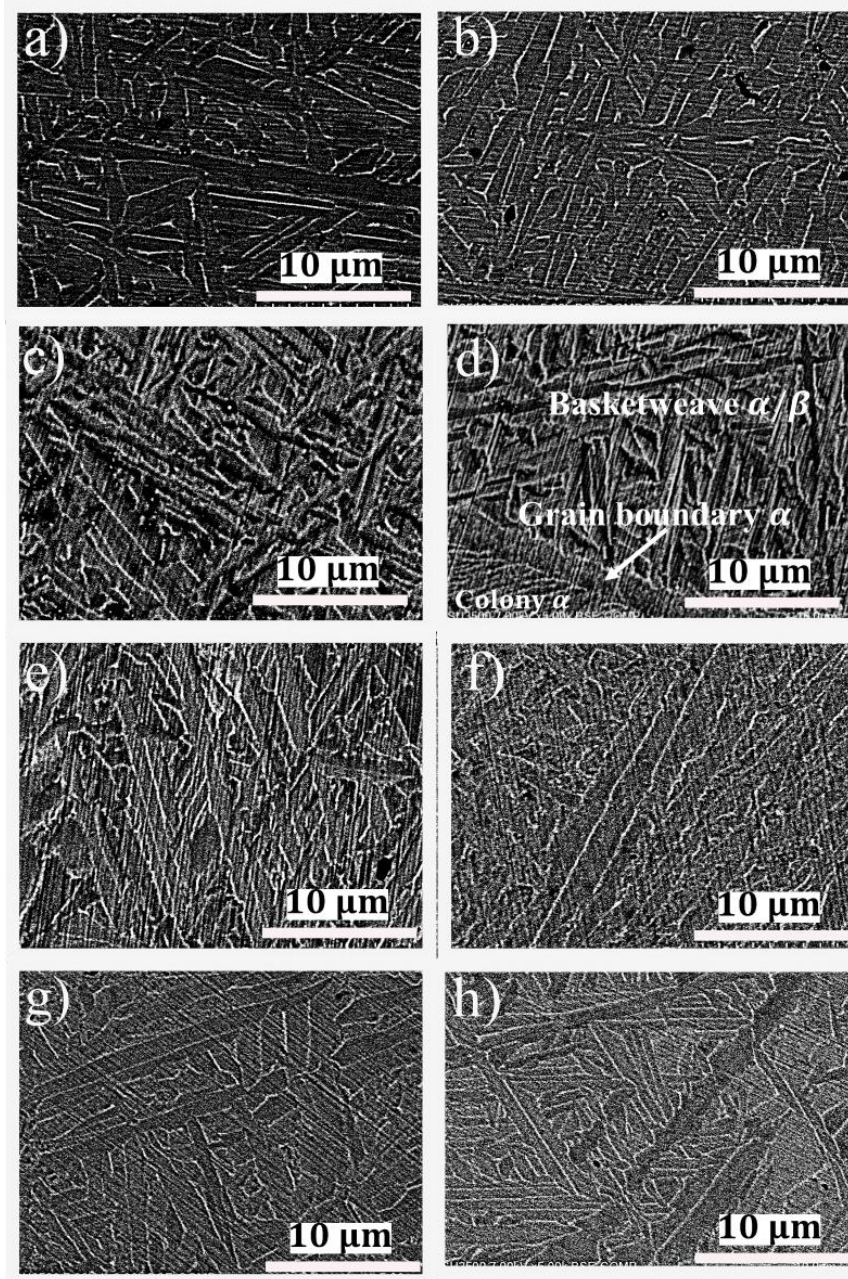
Figure 5.8. The SEM micrographs of the top region (transient) for deposits processed at (a) 2.1, (c) 4.2, (e) 6.4, and (g) 7.2 mm/s, respectively. The SEM micrographs of the middle region (steady state) for deposits processed at (b) 2.1, (d) 4.2, (f) 6.4, and (h) 7.2 mm/s, respectively.

5.4.2.3 Dislocation Structure

Figure 5.9 shows typical dislocation structures in the plate-like α grains corresponding to the middle region (steady state) of the deposit built in the X direction processed at 7.2 mm/s. Plastic deformation in the α phase occurs mainly by dislocation slip, with prismatic slip as the dominant

92

deformation mode, followed by basal slip [54]. The presence of Al inhibits twinning, although it is a common deformation mechanism for HCP materials [15,54-55]. The microstructure contains 53.6 $\pm$ 6.1 % basketweave phase. The selected region of interest is within the basketweave microstructure. The basketweave morphology is reported to strengthen the material, as this structure would be stronger since slip transmission between adjacent α laths that are different variants would be prevented (or greatly reduced) [15]. The method for quantifying the dislocation density was adopted by Ham. [55]. The calculated dislocation density is $8.60 \pm 3.57 * 10^{13}$ m^{-2}. This is consistent with what has been reported in the literature about the dislocation density of AM Ti-6Al-4V. Murr et al. [54] reported a dislocation density of 10^{14} m^{-2} for EBM Ti-6Al-4V.
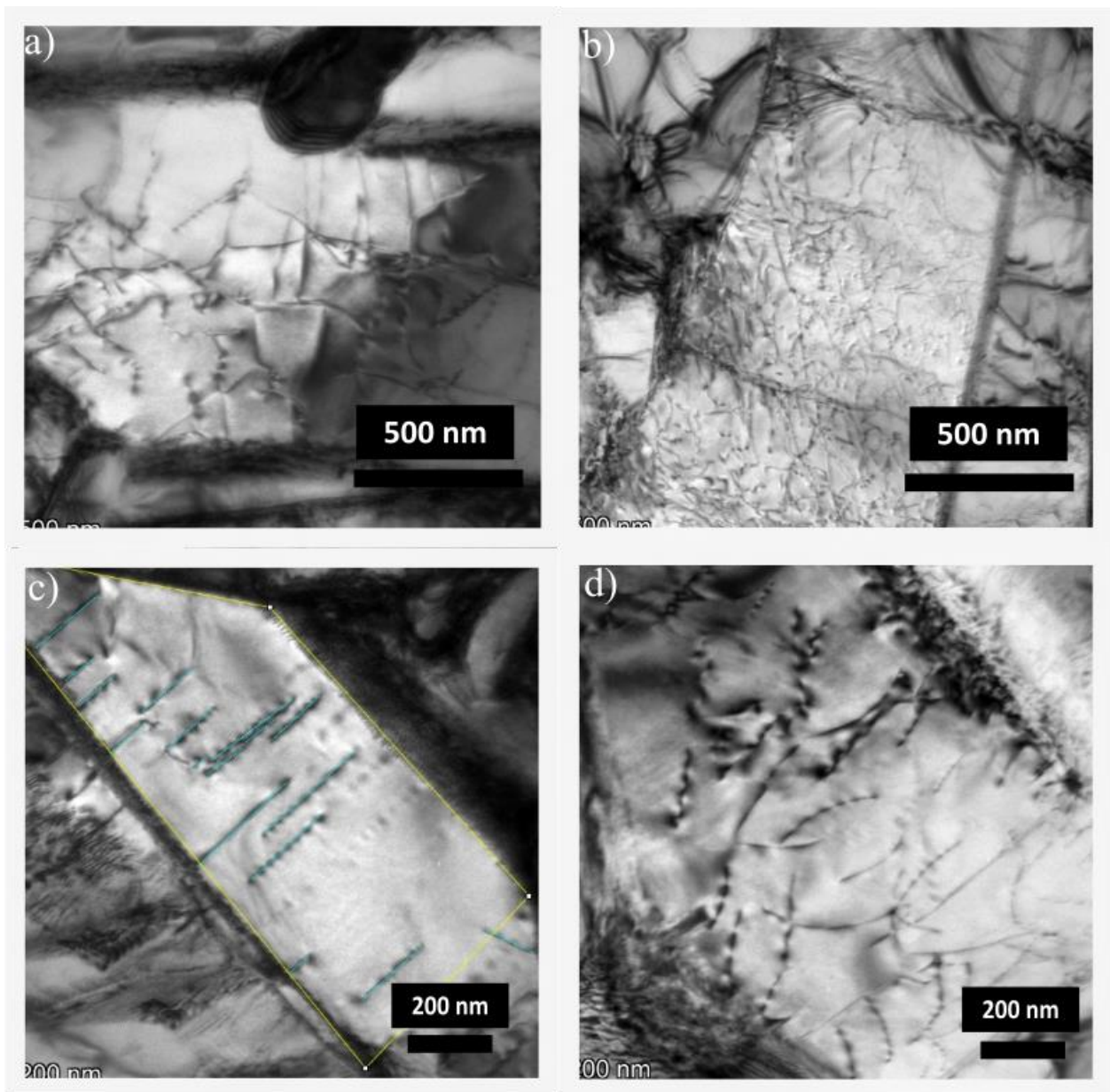
[43]Figure 5.9. TEM bright-field micrographs showing dislocation structures in the α plates of the middle region (steady state) for the deposit built in the X direction processed at 7.2 mm/s.

5.4.3 Hardness

Figure 5.10 presents the microhardness measured at different heights including the interface, initial layers, middle region (steady state), and top region (transient). Figure 5.11 shows the calculated average microhardness in different regions for samples processed at different travel speeds. Greater microhardness is observed at the interface for all conditions due to the finer microstructure developed at the interface. A higher cooling rate is experienced in this region because the cold substrate acts as a heat sink and there was no heat accumulation at the beginning of the deposition. As previously shown in Table 5.4, the cooling rate at the interface is up to more than 410 K/s and α' martensite was observed. The microhardness values are comparable to those reported by Chekir et al. [8], who measured 312 ± 11 HV and 327 ± 10 HV for LWD Ti-6Al-4V deposits processed at 1.4 mm/s and 7.2 mm/s, respectively. The ANOVA analysis shows that the microhardness is statistically similar among the deposits produced at different travel speeds ($p>0.05$). As mentioned above, Checkir et al. [8] reported statistically equivalent microhardness with different travel speeds. This conclusion was expected considering that the hardness-strengthening mechanisms mainly include grain boundary strengthening, precipitation hardening, and solid solution strengthening. As mentioned above, the microstructure analysis (Section 3.2.2) demonstrated that the α lath widths are statistically similar among most of the deposits. Therefore, grain boundary strengthening is expected to be similar among all deposits. Precipitation strengthening is ruled out because the literature suggests that strengthening by Ti_3Al precipitation requires an aluminum concentration greater than 7.2 %, which is greater than that used in this study [8]. Besides, thermodynamically, segregation of Al is considered to be more favored for strained, non-equilibrium microstructures (martensitic and bimodal or duplex) at shorter tempering times [56]. Since the same wire spool was used for deposition, solid solution strengthening was also discussed to be similar. Therefore, the microhardness is more influenced by the morphology of the location where the measurements were performed. Considering the variability observed in the α lath widths, it is understandable that similar microhardness values with high deviation are obtained from different grain morphologies.
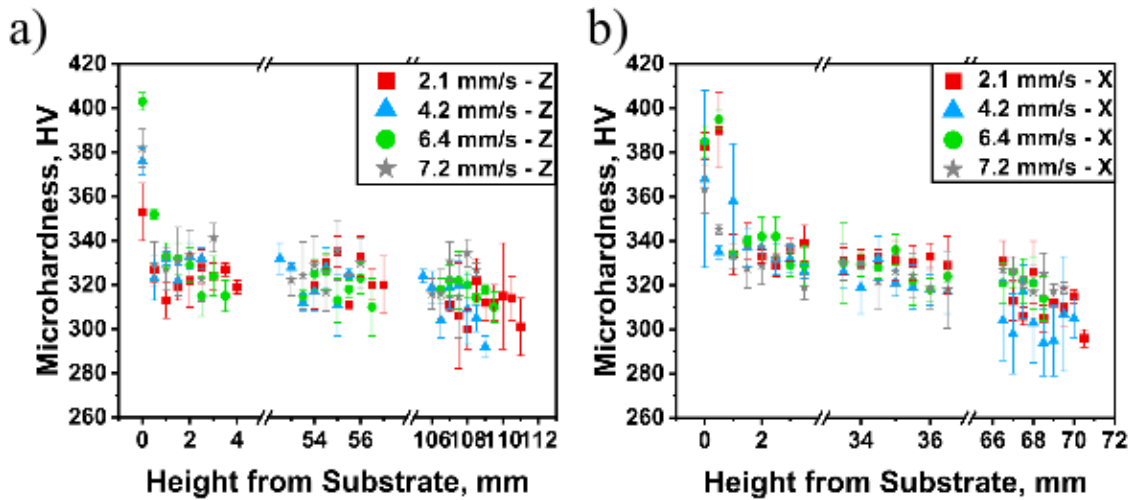
[44]Figure 5.10. (a) Microhardness at different heights from the substrate for all deposits built in the Z direction. (b) Microhardness at different heights from the substrate for all deposits built in the X direction.
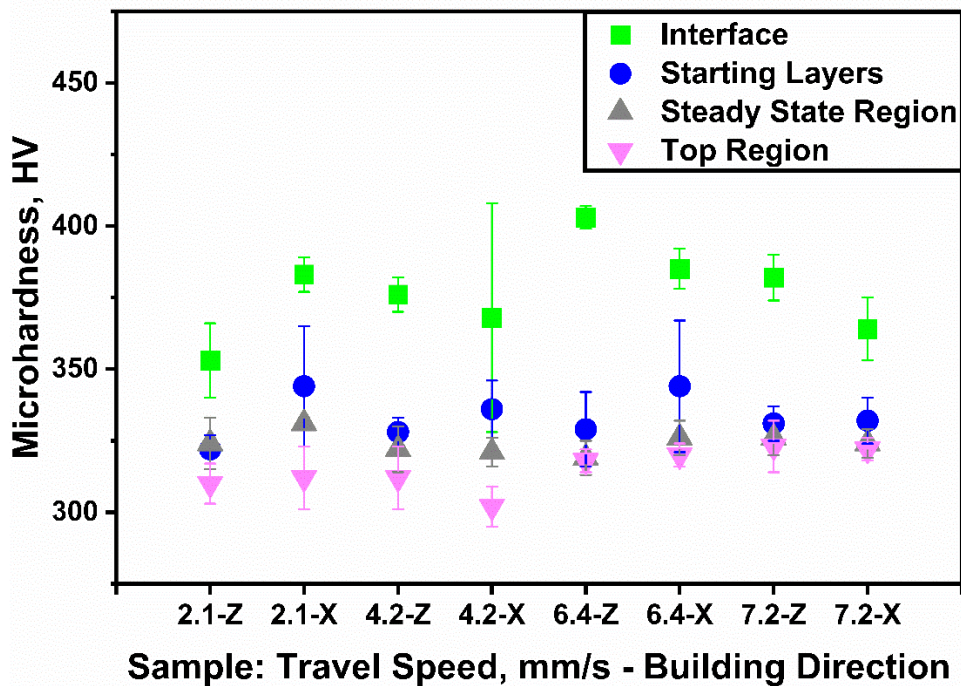
[45]Figure 5.11. Calculated microhardness in different regions of samples built in the Z and X directions processed at 2.1, 4.2, 6.4, and 7.2 mm/s.

5.4.4 Mechanical Properties

5.4.4.1 SR Static Tensile Properties

Figure 5.12 presents the tensile results compared to the minimum requirements for DED Ti-6Al-4V parts manufactured according to AMS 4999 [57]. All results are consistently above the DED

minimum requirements. The ANOVA analysis shows that YS and UTS are statistically different between the deposits produced at 2.1 mm/s and 7.2 mm/s ($p<0.05$). YS and UTS are statistically similar among the rest of the groups ($p>0.05$). This indicates that the deposits produced at 7.2 mm/s have increased YS and UTS compared to the deposits produced at 2.1 mm/s. This is in agreement with the conclusion from section 3.2.2 where the ANOVA shows that the deposits produced at 7.2 mm/s exhibit finer α laths than those produced at 2.1 mm/s. In comparison, Ellyson et al. [58] reported increased YS and UTS for LWD Ti-6Al-4V deposits produced at 7.5 mm/s compared to ones produced at 1.4 mm/s. With respect to the elongation among different travel speeds, ANOVA shows that no significant difference was observed among different travel speeds ($p>0.05$).

The anisotropy in DED Ti-6Al-4V deposits has been reported in the literature [13,59]. It is attributed to the difference in texture, the columnar prior β grain morphology, and the presence of grain boundary α from different tensile directions. The difference in tensile properties can result from the texture difference due to the preferential orientation of soft slip systems, which are oriented such that the resolved stress is quite high, resulting in a lower external stress to achieve yielding [59]. Besides, the grain boundary and the morphology of the columnar prior β grain on specimens produced in the X direction can hinder the movement of the defect and result in higher external stress to achieve yielding [13]. ANOVA was also performed between Z and X directions for all travel speeds to investigate whether there is anisotropic behavior. The analysis shows that for deposits produced at 2.1 mm/s, 4.2 mm/s, and 7.2 mm/s, they exhibited statistically different strengths in the Z and X directions ($p<0.05$) - anisotropic behavior. Deposits produced at 6.4 mm/s had statistically similar strengths ($p>0.05$) between the Z and X directions. The deposit produced in the X direction and 6.4 mm/s does not exhibit the expected higher strength than the Z direction due to the porosity in the sample developed from the instability of the fabrication process. Figure 5.13 shows optical micrographs taken from different positions along the build height, showing the porosity defects generated from the fabrication process.
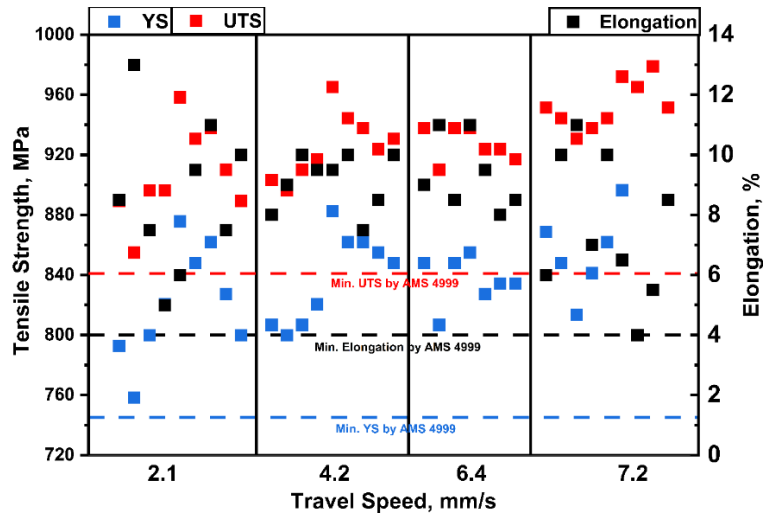
[46]Figure 5.12. Yield strength (YS), ultimate tensile strength (UTS), and elongation for all tensile coupons with minimum tensile properties set by AMS 4999 [57] marked by dotted lines.
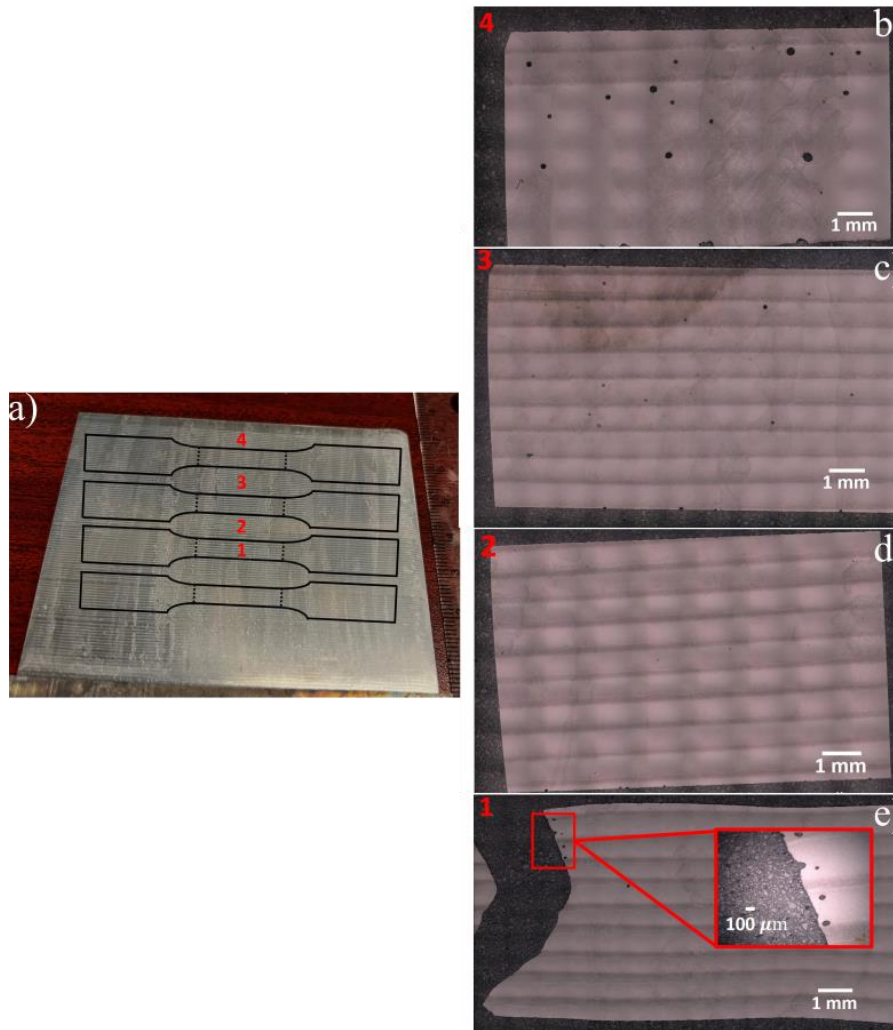
[47]Figure 5.13. (a) Image of the deposit produced at 6.4 mm/s in the X direction. (b-e) Optical

micrographs of porosity defect from position 4, 3, 2, and 1, respectively.

5.4.4.2 Fracture Mechanisms

Figures 5.14(a-b) show the optical micrographs of the XZ surfaces at fracture, parallel to the loading direction, for specimens built in the X direction and processed at 2.1 and 6.4 mm/s. It is well established that the main failure mechanism of the Ti-6Al-4V alloy involves crack formation and progression through microvoid formation, growth, and coalescence [7,13]. Due to the strength difference and strain incompatibility between α laths and β matrix, microvoid formation tends to occur at the α /β interfaces [60]. Figure 5.14(a) presents a clear grain boundary α at the fracture surface of the 2.1 mm/s specimen, indicating that crack propagation occurred along the grain boundary α and has propagated mainly along the grain boundaries. The crack tip deflects at the grain boundaries when neighboring grains or colonies have multiple crystallographic orientations [59]. Higher magnification SEM fractographs (Figure 5.14(e-f)) show clusters of uniformly distributed fine and deep dimpled structures, indicating a high degree of ductility in titanium alloys [13]. The measured dimple sizes are $3.6 \pm 1.7 \, \mu$m and $2.1 \pm 1.1 \, \mu$m for 2.1 mm/s and 6.4 mm/s, respectively. The homogeneity of the dimple size indicates that there are no pre-existing defects during deformation.

Figure 5.14(c) displays SEM fractographs of terrace-like features with equiaxed shallow dimples generated by local plastic deformation (marked with red boxes). The magnified SEM fractograph (Figure 5.14(e)) shows a close-up of this feature. As can be seen, a terrace-like feature is composed of a facet with uniformly distributed fine and deep dimples surrounding it. This can be due to the crack propagating along the prior β grain boundary, considering the morphology of prior β grains in samples built in the X direction. Shrestha et al. [59] also reported a similar structure, which they inferred to be the result of crack propagation around laths of similar orientation generated from prior grains with low angular misorientation. Another possibility for the terrace-like features can be the pre-existence of parallel cracks within the tensile coupons that propagated into the terrace-like structure during the loading process. Figure 5.14(d) shows no terrace-like structure for deposits developed at 6.4 mm/s as α colonies are kinetically favored for lower travel speeds.
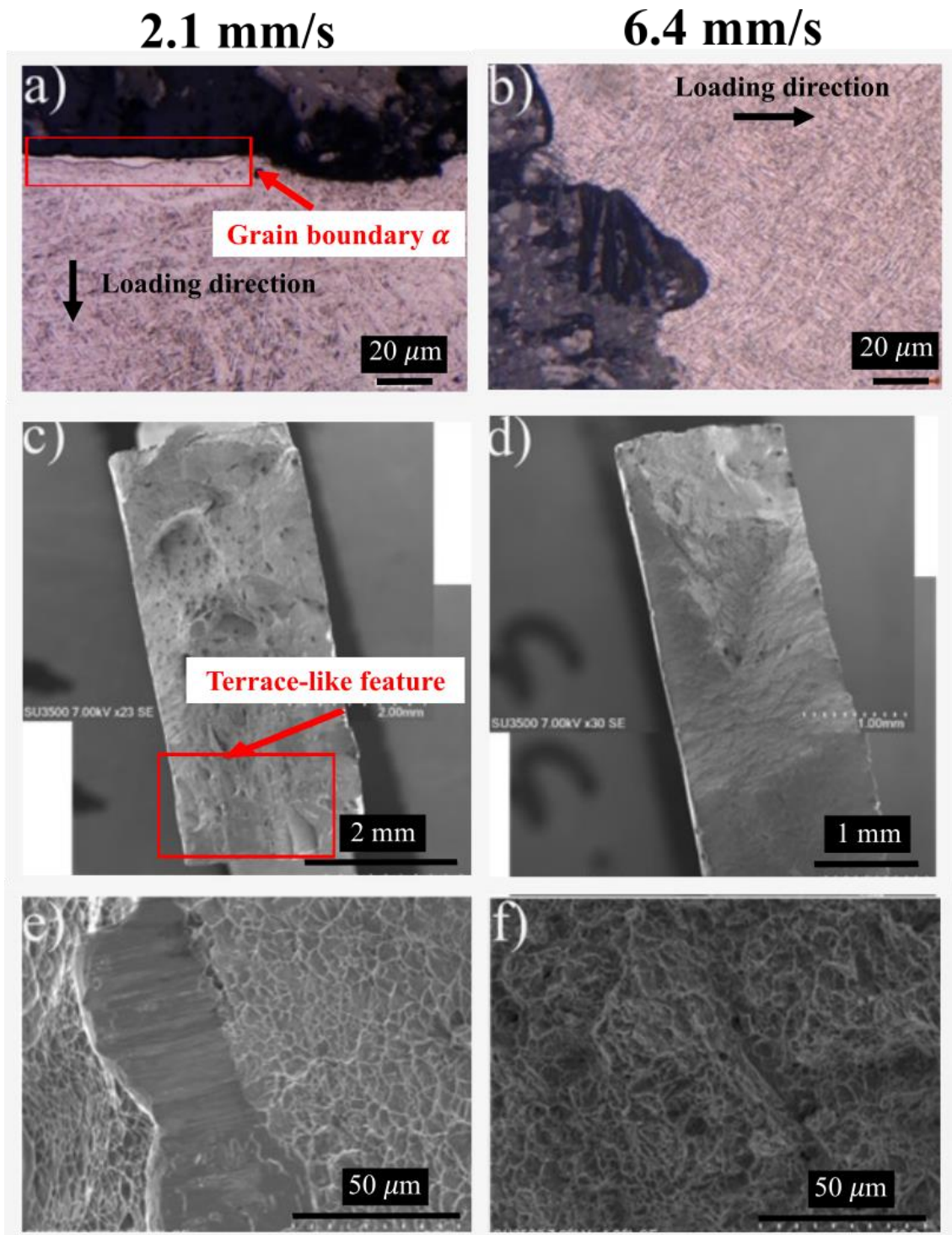
[48]Figure 5.14. (a-b) Optical micrographs of fracture profiles of SR tensile specimens built in the X direction processed at 2.1 mm/s and 6.4 mm/s. (c, e) SEM fractography of SR tensile specimens built in the X direction processed at 2.1 mm/s. (d, f) SEM fractography of SR tensile specimens built in the X direction processed at 6.4 mm/s.

5.4.5 Thermo-Microstructural-Mechanical Modeling of LWD Ti-6Al-4V

This study proposed a new approach using three mechanistic models to predict the thermal history, microstructure, and mechanical properties of LWD Ti-6Al-4V. Figure 5.15 presents the flowchart for the new methodology. There are three models in the approach: the YS prediction model based on the work of Hayes et al. [15], the microstructure prediction model that predicts α/β phase fractions and α lath width based on Kelly [11] and Charles and Järvstråt [42], and the FEA thermal model the from previous section 3.1. All three models were validated using the experimental data presented in sections 3.1, 3.2, and 3.4. The validation criterion is based on whether the simulation result can agree with the experimental result within a certain margin of error.
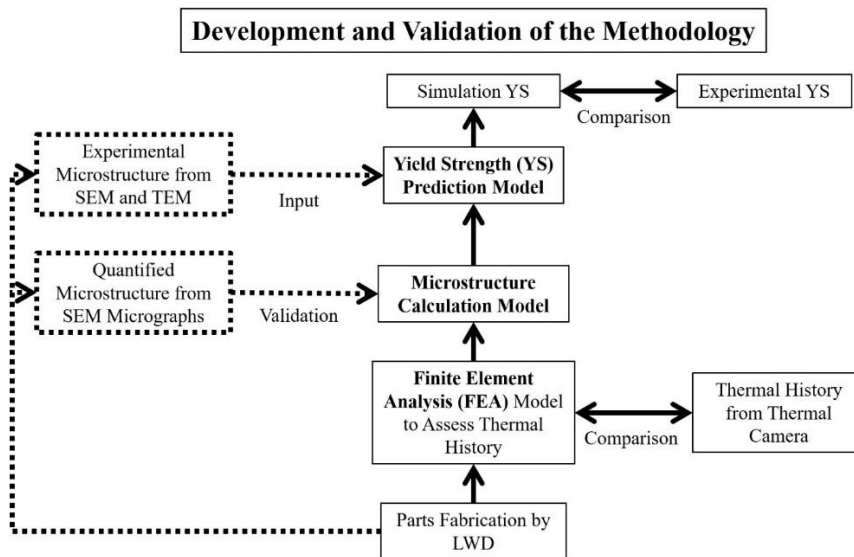
[49]Figure 5.15. Flowchart of the methodology.

5.4.5.1 Microstructure Model
The microstructure of the solid-state Ti-6Al-4V titanium alloy is modeled using the volumetric phase fractions by considering only the Widmanstätten colony and basketweave α phase fractions during the diffusion-controlled transformation of the β phase. The martensitic transformation was not included in the microstructure model because the microstructure results shown in section 3.2.2 show only an α-based microstructure. In this approach, depending on the comparison between the current α/β phase fractions, $f_{i,\alpha}/f_{i,\beta}$, and the equilibrium α/β phase fractions, $f_{eq,\alpha}/f_{eq,\beta}$, the α phase either dissolves or grows. The equilibrium α/β phase fractions, $f_{eq,\alpha}/f_{eq,\beta}$, can be found on

Figure 5.16 from Kelly [11]. Accordingly, if $f_{i,\alpha} > f_{eq,\alpha}$, the α phase dissolves. The transformed α phase is modeled as one-dimensional plate growth of the β phase with a parabolic growth rate, r:

$$r = aT_i^b \qquad\qquad \text{Equation 5-8}$$

where T_i is the current temperature (K), and r is the parabolic thickening rate, where the coefficient $a = 2.21 * 10^{-31}$ s$^{-1/2}$ and $b = 0.89$ adopted from Kelly [11]. The equivalent time for α phase dissolution, which represents the time needed to transform the β phase fraction at the previous time step, $f_{i-1,\beta}$, to the equilibrium β phase fraction, $f_{eq,\beta}$, is as follow:

$$t^* = \left(\frac{f_{i-1,\beta}}{f_{eq,\beta}r}\right)^2 \qquad\qquad \text{Equation 5-9}$$

The transformed β phase is calculated as follows:

$$f_{i,\beta} = f_{eq,\beta}\zeta_\beta, \text{ and } \zeta_\beta = r(t^* + t)^{0.5} \qquad\qquad \text{Equation 5-10}$$

where ζ_β is the extent of the reaction between $0 - 1$, and t is the time of one step (s). If $f_{i,\alpha} < f_{eq,\alpha}$, the α phase grows. The transformed α/β phases are calculated as follows:

$$f_{i,\alpha} = f_{eq,\alpha}\zeta_\alpha, \text{ and } f_{i,\alpha} + f_{i,\beta} = 1 \qquad\qquad \text{Equation 5-11}$$

where ζ_α is the extent of the reaction in the range of 0 - 1 and can be modeled using the JMA equation [39-41] with a time-temperature-transformation (TTT) diagram:

$$\zeta_\alpha = 1 - exp(-k(t + t')^n), \text{ and } t' = \left(-log\left(1 - f_{i-1,\alpha}/f_{eq,\alpha}\right)/k\right)^{1/n} \qquad \text{Equation 5-12}$$

where t' is the equivalent time for α phase growth, which is the time required to transform the α phase fraction at the previous time step, $f_{i-1,\alpha}$, to the equilibrium α phase fraction, $f_{eq,\alpha}$, $k(T_i)$ can be found by a table look-up based on the temperature, T_i, from Kelly [11]. $n = 5/2$ is the Avrami exponent [11]. The α lath width is modeled using the α lath width model developed by Charles and Järvstråt [42]. The α lath width can be modeled by the following equation:

101

$$w_i = \left(w_{i-1}f_{i-1,\alpha} + w_{eq}\left(f_{i,\alpha} - f_{i-1,\alpha}\right)\right)/f_{i,\alpha} \hspace{4cm} \text{Equation 5-13}$$

where w_{i-1} and $f_{i-1,\alpha}$ are the α lath width and α phase fraction from the previous time-step, and w_{eq} is the equilibrium value of α lath width, which can be calculated according to the Arrhenius equation:

$$w_{eq} = k_w exp(-T_{act}/T_i) \hspace{5cm} \text{Equation 5-14}$$

where k_w is the prefactor and was originally set to 18400, T_{act} is the activation temperature and was set to 10000K [42], T_i is the temperature at the time step. In this study, the values for k_w and T_{act} were taken from the work by Irwin et al. [36], who optimized the values for DED-fabricated Ti-6Al-4V alloys.
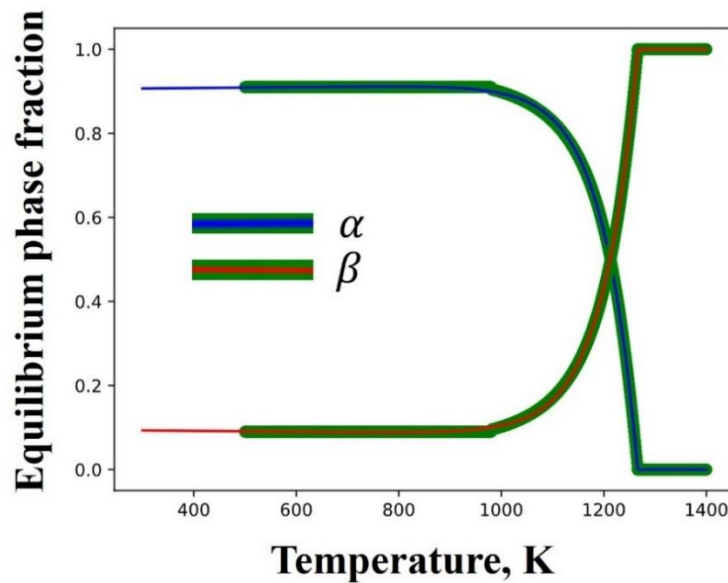
[50]Figure 5.16. Equilibrium α and β phase fractions adopted from Kelly [11].

The thermal history from the FEA model (section 3.1) was used as input to the microstructure model. Figure 5.17 shows the predicted α phase fraction and α lath width compared to the measured α phase fraction and α lath width. The predicted microstructure is in good agreement with the measured experimental microstructure. No statistical difference was observed for the

predicted α phase fraction at different travel speeds, as it is mainly influenced by the alloying elements.
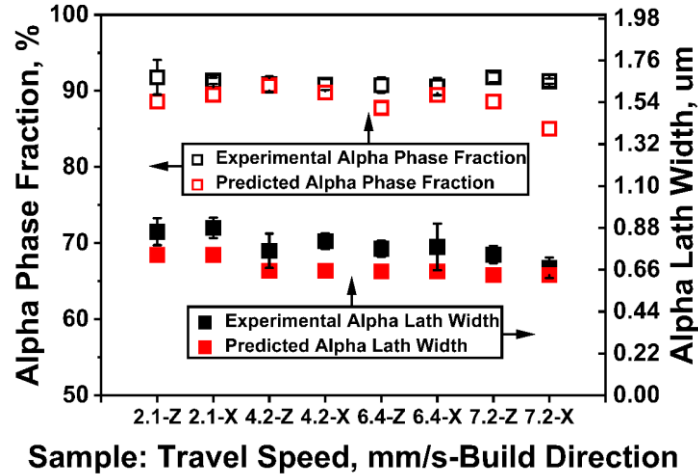
[51]Figure 5.17. Comparison between experimental and predicted α phase fractions and α lath widths.

5.4.5.2 Yield Strength Prediction Model

Equation 5-15 shows the general form of the equation for predicting the YS, where F_V is the volume fraction of the designated phases/microstructure, X_B is the concentration of element B (i.e., Al, O, Fe, V), $t_{feature}$ is the thickness of the given feature (i.e., the α lath, β lath, the colony width), α is the prefactor term (set to 1), M is the Taylor factor, which is typically between 2.0 and 3.2 for hcp α, G is the shear modulus of titanium (44 GPa), b is the Burgers vector (0.3 nm), and ρ is the dislocation density. All coefficients are taken from Hayes et al. [15]. The equation incorporates a) intrinsic flow stress of the hcp α and bcc β phases, b) solid solution strengthening of hcp α by oxygen and aluminum, c) solid solution strengthening of bcc β by vanadium and iron, d-e) microstructural length scale effects, and f) Taylor hardening factor, which was added by Hayes et al. [15] to include the strengthening effect of the basketweave morphology.

$$\sigma_{ys} = F_V^\alpha * 89 + F_V^\beta * 45 + \qquad \text{a)}$$

$$F_V^\alpha * (149 * x_{Al}^{0.667} + 759 * x_O^{0.667}) + \qquad \text{b)}$$

$$F_V^\beta * ((22 * x_V^{0.7})^{0.5} + (235 * x_{Fe}^{0.7})^{0.5})^2 + \qquad \text{c)} \qquad \text{Equation 5-15}$$

$$F_V^{Col} * 150 * (t_{\alpha-lath})^{-0.5} * (t_{\beta-rib})^{0.5} + \qquad \text{d)}$$

$$F_V^{Col} * 125 * (t_{Col})^{-0.5} + \qquad \text{e)}$$

$$F_V^{BW} \alpha MGb\sqrt{\rho} \hspace{4cm} \text{f)}$$

All the microstructural variables were quantified using procedures developed by Tiley et al. [61] using high magnification SEM micrographs and calculated dislocation density from TEM micrographs from section 3.2.3.

Figure 5.18(a) shows the predicted yield strength and the comparison with the experimental yield strength reported in 3.4.1. The mismatch is less than 10 % for all values. The model predicts highly credible yield strength values. Figure 5.18(b) shows the sensitivity of the yield strength to the different strengthening mechanisms, presented in a manner analogous to the work of Hayes et al. [15]. As can be seen, solid solution strengthening has the largest contribution, which is the same as reported by Hayes et al. [15]. Since all the specimens were produced with the same wire stock, the contribution of solid solution strengthening is the same for all the specimens. Another dominant microstructural strengthening parameter is the Taylor hardening effect. The contribution of Taylor hardening was mainly affected by the dislocation density and the basketweave phase fraction and was found to be similar among all samples. Hayes et al. [15] found from the dataset that thicker α laths are expected to have marginally lower dislocation densities. As reported from the ANOVA analysis (section 3.2.2), most of the samples in this study have statistically similar α lath widths, indicating similar dislocation densities. The measured basketweave phase fractions are similar (about 60 %) for all samples. Hayes et al. [15] investigated the minimum and maximum yield strength by varying the microstructure with uncertainties and found that the uncertainty in the measurement of the α laths changed the Hall-Petch term by less than 3.5 MPa. This also helps to explain the similar strength observed for the specimens in this study.
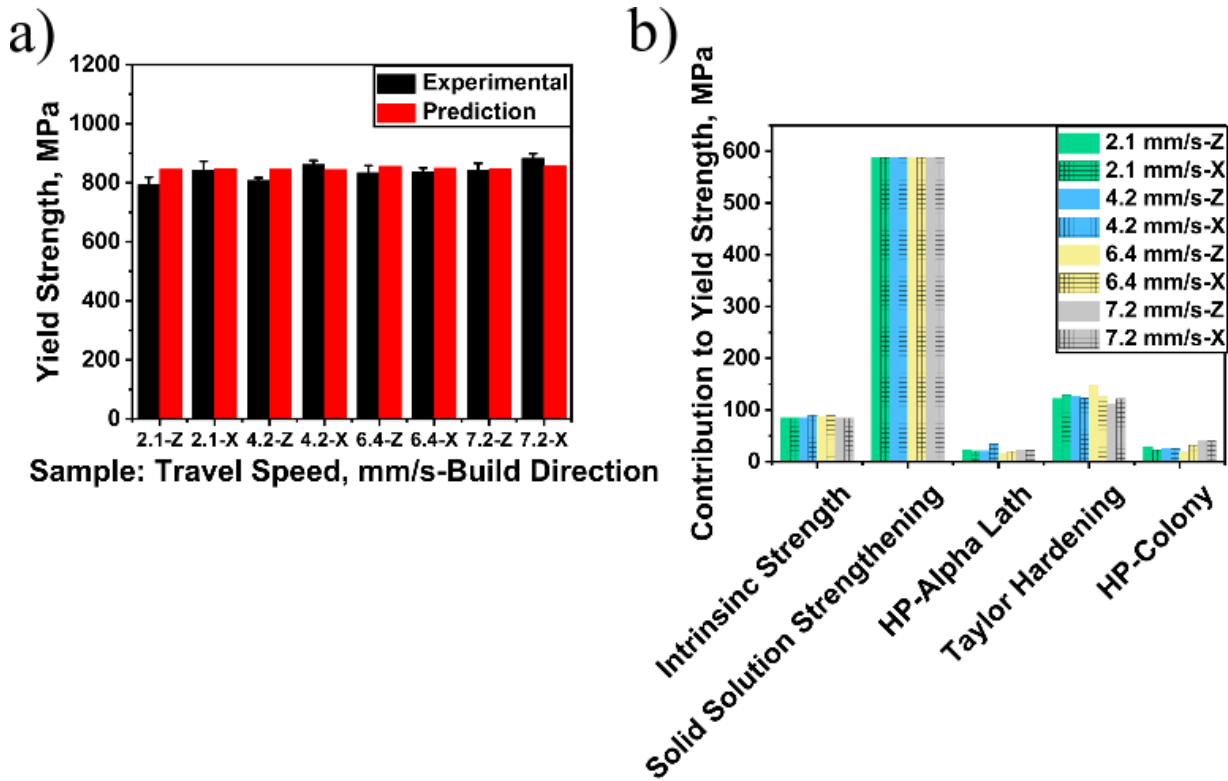
[52]Figure 5.18. (a) Comparison between experimental and predicted YS for all travel speeds. (b) The contribution of the individual terms to the absolute YS for different travel speeds.

5.5 Conclusion

In this study, a thermal-microstructural-mechanical modeling approach was proposed to understand the predictability of YS for LWD Ti-6Al-4V deposits. Eight single-bead Ti-6Al-4V deposits varied in four travel speeds were produced by LWD for thermal history recording, microstructural characterization, and tensile testing to validate the accuracy of the methodology. The main conclusions are as follows:

a) A 3D transient heat transfer FEA model was built using ABAQUS software to simulate the LWD deposition process and predict the thermal history. Calculated cooling rates were compared between FEA and the thermal camera for deposits produced at four travel speeds. Despite the instability during the near-substrate layer, which resulted in a deviation of more than 10 %, the percentage deviation is below 10 % for the remaining data between FEA and the thermal camera. The microstructural model was validated with measured α/β phase fractions

and α lath widths for all travel speeds. The YS prediction model was validated with less than a 10 % deviation from the experimental YS. Solid solution strengthening and Taylor hardening were analyzed to be the main contributions to the absolute YS. The first term is similar because it depends on the chemical composition, and the same wire stock was used for all production in this study. The second term is also similar as it is mainly affected by the dislocation density and the basketweave fraction, which was about 60 % for all the deposits.

b) The macrostructure is mainly composed of columnar β grains due to the high G. However, equiaxed structures were also observed on some regions of the deposit produced at 7.2 mm/s. The equiaxed structures were further investigated by comparing the calculated G and R with the solidification map for Ti-6Al-4V. It was concluded that the different solidification conditions promoted the formation of the equiaxed structures.

c) The microstructure is composed of α colony and α/β basketweave. The middle region (steady state) exhibited coarser α laths than the top region (transient) due to repeated thermal cycles. The ANOVA analysis reported that the α lath widths were only statistically different ($p<0.05$) between deposits produced at 2.1 mm/s and 7.2 mm/s. This indicates that the α lath width is statistically similar for most of the travel speed groups, and a statistically different α lath width is only observed between the slowest and fastest travel speeds in this study.

d) The dislocation structure in the basketweave morphology was measured to be in the order of 10^{13} m^{-2}. Considering that the α lath width was statistically similar among all travel speed groups, the dislocation density was considered to be similar as well.

e) The ANOVA analysis showed that microhardness was statistically similar ($p>0.05$) among all travel speeds. Higher microhardness was observed in the near-substrate regions due to martensite structures developed at cooling rates above 410 K/s.

f) The YS, UTS, and elongation of all deposits were above the minimum tensile properties for DED Ti-6Al-4V deposits set by AMS 4999. The ANOVA analysis reported a significant difference ($p<0.05$) in YS and UTS only between 2.1 mm/s and 7.2 mm/s, consistent with the previous conclusion for α lath width. Anisotropic behavior was observed for 2.1 mm/s, 4.2 mm/s, and 7.2 mm/s. The porosity of the X deposits produced at 6.4 mm/s was the reason for the lower YS and UTS and thus the unexpected anisotropy.

5.7 References

[1] Mok, S. H. (2007). Deposition of Ti-6Al-4V using a high power diode laser and wire. Doctoral dissertation. University of Nottingham, Nottingham, UK.

[2] Chong, Y., Bhattacharjee, T., & Tsuji, N. (2019). Bi-lamellar microstructure in Ti–6Al–4V: Microstructure evolution and mechanical properties. Materials Science and Engineering: A, 762, 138077.

[3] Brandl, E., Schoberth, A., & Leyens, C. (2012). Morphology, microstructure, and hardness of titanium (Ti-6Al-4V) blocks deposited by wire-feed additive layer manufacturing (ALM). Materials Science and Engineering: A, 532, 295-307.

[4] Saboori, A., Gallo, D., Biamino, S., Fino, P., & Lombardi, M. (2017). An overview of additive manufacturing of titanium components by directed energy deposition: microstructure and mechanical properties. Applied Sciences, 7(9), 883.

[5] Brandl, E., Palm, F., Michailov, V., Viehweger, B., & Leyens, C. (2011). Mechanical properties of additive manufactured titanium (Ti–6Al–4V) blocks deposited by a solid-state laser and wire. Materials & Design, 32(10), 4665-4675.

[6] Brandl, E., Baufeld, B., Leyens, C., & Gault, R. (2010). Additive manufactured Ti-6Al-4V using welding wire: comparison of laser and arc beam deposition and evaluation with respect to aerospace material specifications. Phys. Procedia, 5(Pt 2), 595-606.

[7] Lütjering, G., Williams, J. C., Lütjering, G., & Williams, J. C. (2003). Titanium matrix composites (pp. 313-328). Springer Berlin Heidelberg.

[8] Chekir, N., Tian, Y., Gauvin, R., Brodusch, N., Sixsmith, J. J., & Brochu, M. (2018). Effect of travel speed and stress relief on thin Ti-6Al-4V laser wire deposits. Materials Science and Engineering: A, 724, 335-347.

[9] Kelly, S. M., & Kampe, S. L. (2004). Microstructural evolution in laser-deposited multilayer Ti-6Al-4V builds: Part I. Microstructural characterization. Metallurgical and Materials Transactions A, 35, 1861-1867.

[10] Baufeld, B., Brandl, E., & Van der Biest, O. (2011). Wire based additive layer manufacturing: Comparison of microstructure and mechanical properties of Ti–6Al–4V components fabricated by laser-beam deposition and shaped metal deposition. Journal of Materials Processing Technology, 211(6), 1146-1158.

[11] Kelly, S. M. (2004). Thermal and microstructure modeling of metal deposition processes with application to Ti-6Al-4V. Doctoral dissertation. the Faculty of the Virginia Polytechnic Institute and State University, Blacksburg, Virginia, USA.

[12] Baufeld, B., & Van der Biest, O. (2009). Mechanical properties of Ti-6Al-4V specimens produced by shaped metal deposition. Science and technology of advanced materials, 10(1), 015008.

[13] Sikan, F., Wanjara, P., Gholipour, J., & Brochu, M. (2023). Use of miniature tensile specimens for measuring mechanical properties in the steady-state and transient zones of Ti–6Al–4V wire-fed electron beam deposits. Materials Science and Engineering: A, 862, 144487.

[14] Narayana, P. L., Kim, J. H., Lee, J., Choi, S. W., Lee, S., Park, C. H., et al. (2021). Optimization of process parameters for direct energy deposited Ti-6Al-4V alloy using neural networks. The International Journal of Advanced Manufacturing Technology, 114(11), 3269-3283.

[15] Hayes, B. J., Martin, B. W., Welk, B., Kuhr, S. J., Ales, T. K., Brice, D. A., et al. (2017). Predicting tensile properties of Ti-6Al-4V produced via directed energy deposition. Acta Materialia, 133, 120-133.

[16] Kistler, N. A., Corbin, D. J., Nassar, A. R., Reutzel, E. W., & Beese, A. M. (2019). Effect of processing conditions on the microstructure, porosity, and mechanical properties of Ti-6Al-4V repair fabricated by directed energy deposition. Journal of Materials Processing Technology, 264, 172-181.

[17] Brandl, E., Michailov, V., Viehweger, B., & Leyens, C. (2011). Deposition of Ti–6Al–4V using laser and wire, part I: Microstructural properties of single beads. Surface and Coatings Technology, 206(6), 1120-1129.

[18] Yu, J., Rombouts, M., Maes, G., & Motmans, F. (2012). Material properties of Ti6Al4 v parts produced by laser metal deposition. Physics Procedia, 39, 416-424.

[19] Shamsaei, N., Yadollahi, A., Bian, L., & Thompson, S. M. (2015). An overview of Direct Laser Deposition for additive manufacturing; Part II: Mechanical behavior, process parameter optimization and control. Additive manufacturing, 8, 12-35.

[20] Baufeld, B. (2012). Effect of deposition parameters on mechanical properties of shaped metal deposition parts. Proceedings of the Institution of Mechanical Engineers, Part B: Journal of Engineering Manufacture, 226(1), 126-136.

[21] Wang, T., Zhu, Y. Y., Zhang, S. Q., Tang, H. B., & Wang, H. M. (2015). Grain morphology evolution behavior of titanium alloy components during laser melting deposition additive manufacturing. Journal of Alloys and Compounds, 632, 505-513.

[22] Brandl, E., Michailov, V., Viehweger, B., & Leyens, C. (2011). Deposition of Ti–6Al–4V using laser and wire, part II: Hardness and dimensions of single beads. Surface and Coatings Technology, 206(6), 1130-1141.

[23] Thompson, S. M., Bian, L., Shamsaei, N., & Yadollahi, A. (2015). An overview of Direct Laser Deposition for additive manufacturing; Part I: Transport phenomena, modeling and diagnostics. Additive Manufacturing, 8, 36-62.

[24] DebRoy, T., Mukherjee, T., Wei, H. L., Elmer, J. W., & Milewski, J. O. (2021). Metallurgy, mechanistic models and machine learning in metal printing. Nature Reviews Materials, 6(1), 48-68.

[25] Tofail, S. A., Koumoulos, E. P., Bandyopadhyay, A., Bose, S., O'Donoghue, L., & Charitidis, C. (2018). Additive manufacturing: scientific and technological challenges, market uptake and opportunities. Materials today, 21(1), 22-37.

[26] Sikan, F., Wanjara, P., Gholipour, J., Kumar, A., & Brochu, M. (2021). Thermo-mechanical modeling of wire-fed electron beam additive manufacturing. Materials, 14(4), 911.

[27] Cao, J., Gharghouri, M. A., & Nash, P. (2016). Finite-element analysis and experimental validation of thermal residual stress and distortion in electron beam additive manufactured Ti-6Al-4V build plates. Journal of Materials Processing Technology, 237, 409-419.

[28] Parry, L., Ashcroft, I. A., & Wildman, R. D. (2016). Understanding the effect of laser scan strategy on residual stress in selective laser melting through thermo-mechanical simulation. Additive Manufacturing, 12, 1-15.

[29] Ahn, J., He, E., Chen, L., Wimpory, R. C., Dear, J. P., & Davies, C. M. (2017). Prediction and measurement of residual stresses and distortions in fibre laser welded Ti-6Al-4V considering phase transformation. Materials & design, 115, 441-457.

[30] Rae, W. (2019). Thermo-metallo-mechanical modelling of heat treatment induced residual stress in Ti–6Al–4V alloy. Materials Science and Technology, 35(7), 747-766.

[31] Mukherjee, T., Zhang, W., & DebRoy, T. (2017). An improved prediction of residual stresses and distortion in additive manufacturing. Computational Materials Science, 126, 360-372.

[32] Lundbäck, A., & Lindgren, L. E. (2011). Modelling of metal deposition. Finite Elements in Analysis and Design, 47(10), 1169-1177.

[33] Lindgren, L. E., Lundbäck, A., Fisk, M., Pederson, R., & Andersson, J. (2016). Simulation of additive manufacturing using coupled constitutive and microstructure models. Additive Manufacturing, 12, 144-158.

[34] Baykasoglu, C., Akyildiz, O., Candemir, D., Yang, Q., & To, A. C. (2018). Predicting microstructure evolution during directed energy deposition additive manufacturing of Ti-6Al-4V. Journal of Manufacturing Science and Engineering, 140(5), 051003.

[35] Christian, J. (2002). The theory of transformations in metals and alloys. George Newnes Ltd, London, UK.

[36] Irwin, J., Reutzel, E. W., Michaleris, P., Keist, J., & Nassar, A. R. (2016). Predicting microstructure from thermal history during additive manufacturing for Ti-6Al-4V. Journal of Manufacturing Science and Engineering, 138(11), 111007.

[37] Kiran, A., Li, Y., Hodek, J., Brázda, M., Urbánek, M., & Džugan, J. (2022). Heat source modeling and residual stress analysis for metal directed energy deposition additive manufacturing. Materials, 15(7), 2545.

[38] Malmelöv, A. (2016). Modeling of additive manufacturing with reduced computational effort. Master's thesis. Luleå University of Technology, Luleå, Sweden.

[39] Michaleris, P. (2014). Modeling metal deposition in heat transfer analyses of additive manufacturing processes. Finite Elements in Analysis and Design, 86, 51-60.

[40] Johnson, W. A. (1939). Reaction kinetics in process of nucleation and growth. Transactions of Transactions of the American Institute of Mining and Metallurgical Engineers, 135, 416-458.

[41] Avrami, M. (1939). Kinetics of phase change. I General theory. The Journal of chemical physics, 7(12), 1103-1112.

[42] Charles, C., & Järvstråt, N. (2008). Modelling Ti-6Al-4V microstructure by evolution laws implemented as finite element subroutines: Application to TIG metal deposition. Eighth

International Conference on Trends in Welding Research (TWR), Pine Mountain, GA, June 1–6, pp. 477–485.

[43] Sun, W., Shan, F., Zong, N., Dong, H., & Jing, T. (2021). A simulation and experiment study on phase transformations of Ti-6Al-4V in wire laser additive manufacturing. Materials & Design, 207, 109843.

[44] Kar, S., Searles, T., Lee, E., Viswanathan, G. B., Fraser, H. L., Tiley, J., et al. (2006). Modeling the tensile properties in β-processed α/β Ti alloys. Metallurgical and materials transactions A, 37, 559-566.

[45] Ghamarian, I., Hayes, B., Samimi, P., Welk, B. A., Fraser, H. L., & Collins, P. C. (2016). Developing a phenomenological equation to predict yield strength from composition and microstructure in β processed Ti-6Al-4V. Materials Science and Engineering: A, 660, 172-180.

[46] Ghamarian, I., Samimi, P., Dixit, V., & Collins, P. C. (2015). A constitutive equation relating composition and microstructure to properties in Ti-6Al-4V: as derived using a novel integrated computational approach. Metallurgical and Materials Transactions A, 46, 5021-5037.

[47] Haden, C. V., Collins, P. C., & Harlow, D. G. (2015). Yield strength prediction of titanium alloys. Jom, 67, 1357-1361.

[48] Collins, P. C., Haden, C. V., Ghamarian, I., Hayes, B. J., Ales, T., Penso, G., et al. (2014). Progress toward an integration of process–structure–property–performance models for "three-dimensional (3-D) printing" of titanium alloys. Jom, 66, 1299-1309.

[49] Collins, P. C., Koduri, S., Welk, B., Tiley, J., & Fraser, H. L. (2013). Neural networks relating alloy composition, microstructure, and tensile properties of α/β-processed TIMETAL 6-4. Metallurgical and Materials Transactions A, 44, 1441-1453.

[50] Goldak, J., Chakravarti, A., & Bibby, M. (1984). A new finite element model for welding heat sources. Metallurgical transactions B, 15, 299-305.

[51] Chekir, N., Tian, Y., Gauvin, R., Brodusch, N., Sixsmith, J. J., & Brochu, M. (2018). Laser wire deposition of thick Ti-6Al-4V buildups: Heat transfer model, microstructure, and mechanical properties evaluations. Metallurgical and Materials Transactions A, 49, 6490-6508.

[52] AMS2901. (2014). Heat Treatment of Titanium Alloy Parts. SAE International, Warrendale, PA, USA.

[53] ASTM E8/E8M-15a. (2015) Standard Test Methods for Tension Testing of Metallic Materials, Annual Book of ASTM Standards, ASTM International, West Conshohocken, PA, USA.

[54] Murr, L. E., Esquivel, E. V., Quinones, S. A., Gaytan, S. M., Lopez, M. I., Martinez, E. Y., et al. (2009). Microstructures and mechanical properties of electron beam-rapid manufactured Ti–

6Al–4V biomedical prototypes compared to wrought Ti–6Al–4V. Materials characterization, 60(2), 96-105.

[55] Ham, R. K. (1961). The determination of dislocation densities in thin films. Philosophical Magazine, 6(69), 1183-1184.

[56] Vilane, V. N., Knutsen, R. D., & Westraadt, J. E. (2024). Hydrogen promoted Ti3Al precipitation during Ti-6Al-4V martensite tempering. Materials Today Communications, 39, 108826.

[57] AMS 4999. (2016). Titanium Alloy Direct Deposited Products 6Al−4V Annealed. SAE International, Warrendale, PA, USA.

[58] Ellyson, B., Chekir, N., Brochu, M., & Brochu, M. (2017). Characterization of bending vibration fatigue of WBD fabricated Ti-6Al-4V. International Journal of Fatigue, 101, 36-44.

[59] Shrestha, S., Panakarajupally, R. P., Kannan, M., Morscher, G., Gyekenyesi, A. L., & Scott-Emuakpor, O. E. (2021). Analysis of microstructure and mechanical properties of additive repaired Ti–6Al–4V by Direct Energy Deposition. Materials Science and Engineering: A, 806, 140604.

[60] Sikan, F., Wanjara, P., Gholipour, J., Atabay, S. E., & Brochu, M. (2022). Effect of substrate condition on wire fed electron beam additive deposition. Materials Science and Engineering: A, 849, 143448.

[61] Tiley, J., Searles, T., Lee, E., Kar, S., Banerjee, R., Russ, J. C., et al. (2004). Quantification of microstructural features in α/β titanium alloys. Materials Science and Engineering: A, 372(1-2), 191-198.

Chapter 6: Thermo-Microstructural-Mechanical Modeling of the Effect of Wire Diameters on Single-bead Ti-6Al-4V Wall Deposits by Laser Wire Deposition

Qi Zhang[1], Nejib Chekir[2], and Mathieu Brochu[1*]

[1]: Department of Mining and Materials Engineering, McGill University, 3610 University St., Montreal, QC, H3A 0C5, Canada

[2]: Liburdi Automation Inc., Dundas, ON L9H 7K4, Canada

To further validate the methodology proposed in Chapter 5, wire diameter is selected as the variable for fabrication of Ti-6Al-4V deposits. Furthermore, this Chapter fills the knowledge gap by investigating the effect of wire diameter on the thermal history, microstructure and mechanical properties of thin Ti-6Al-4V deposits developed by LWD. Wall profiles are also investigated to compare the consistency of the melt pool sizes among different wire diameters. Increasing of wire diameters leads to nonuniform wall profiles and inconsistent melt pool sized, which indicates an unstable thermal history. This Chapter demonstrated that increasing of wire diameters results in larger heat accumulation and lower cooling rates. As a result, coarser microstructure and lower strengths are found in deposits produced with larger wire diameters. A greater number of defects are found on the fracture surfaces of tensile coupons associated with larger wire diameters, which lead to premature failure and lower strength.

6.1 Abstract

Six Ti-6Al-4V deposits with two geometries to extract tensile coupons from the build direction (Z) and travel direction (X), were produced by laser wire deposition (LWD) with different wire diameters. Inconsistent wall profiles were found for deposits produced with wire diameters of 1.1 and 1.6 mm due to the inhomogeneous melt pool sizes generated during the deposition process, indicating the unstable thermal history. It was found that increasing the wire diameter resulted in increased heat input, which produced coarser grains and resulted in decreased strength. Fractography analysis showed that greater amounts of defects were observed on the fracture surfaces of deposits produced with increased wire diameters, which weakened the tensile properties. The grain boundary α and the surrounding colony α facilitated crack propagation and caused early failure. This research proposed a platform using modeling techniques to control cooling rates, microstructure (α/β phase fractions and α lath widths) and yield strength of LWD Ti-6Al-4V. The accuracy of all models was validated by comparing them with experimental data.

6.2 Introduction

In recent decades, additive manufacturing (AM) has gained significant interest in producing near-net-shape components by adding materials layer by layer. AM offers considerable time and cost savings compared to conventional manufacturing technologies [1-2]. AM is generally categorized by the type of feedstock (powder or wire) and heat source (laser, electron beam, plasm arc, etc.). Directed energy deposition (DED), as one of the major AM processes, builds parts by feeding powder or wire into a melt pool using a high-energy source such as a laser beam. Recently, wire-fed DED processes have received less attention than powder-fed DED processes due to their limited geometrical freedom [3]. However, wire-fed DED processes can offer advantages such as reduced contamination, potential large part size, and high material quality and repeatability [4-5]. One of the commonly used materials with wire-fed processes is Ti-6Al-4V. This workhorse titanium alloy is widely employed in the aerospace industry due to its high strength-to-weight ratio, excellent corrosion resistance and high fracture toughness [6]. It is therefore of great importance to understand the effects of different processing parameters on the thermal history, microstructure and mechanical properties of wire-fed AM Ti-6Al-4V.

Among the different processing parameters, most studies [7-12] conducted so far have aimed to investigate the effect of energy density which is a combination of travel speed, laser power, and material feed rate. It was found that a combination of high travel speeds, low laser powers, and low material feed rates results in a low energy density and finer microstructure. In addition, hatch patterns [8], interlayer time [8,11-12], and substrate temperature and size [8,11-12] have also been investigated as they can affect the thermal distribution, porosity, microstructure, and final mechanical properties. The cross-hatch pattern can reduce residual stress concentration and mitigate the directional stresses compared to the parallel-hatch pattern [8]. Smaller substrate size, higher substrate temperature, and lower interlayer time were also reported to promote heat build-up in the part and coarser microstructure [8,11-12]. However, few studies focused on the effect of wire diameter. For most of the wire-fed DED processes reported in the literature [13-17], the wire diameter was set to about 1 mm (and no more than 1.2 mm), especially for the energy source using a laser beam, due to its low intensities and small diameters. A major issue with wire-fed DED components is the poor dimensional accuracy and low geometric resolution. Shaikh et al. [3] attempted to use micro fine wire (0.1 mm) to improve the dimensional accuracy and geometric resolution. However, the deposition rate was substantially reduced and the fine wire increased surface roughness and created voids and defects when a subsequent layer was deposited. Salminen et al. [14] compared the laser weld quality using different welding parameters and wire diameters of 0.8 mm and 1 mm. They found that laser welding with filler wire can be adopted when the correct parameter combinations are selected. They observed, for example, that the wire diameter must be smaller than the air gap width. They also noticed that there is an optimum welding speed and wire feed rate for different wire diameters to ensure complete fusion. Using a large wire diameter of 1.6 mm, Gibson et al. [17] observed inconsistent wall geometry for deposits produced without closed-loop control of melt pool sizes during the deposition process. Despite all these efforts, the range of wire diameters reported in the literature remains limited and there is a knowledge gap in systematically investigating how wire diameters can affect the geometric consistency, thermal history, microstructure, and mechanical properties of Ti-6Al-4V parts made by wire-fed DED.

In addition, great progress has been made over the past few decades in mechanistic models to help predict and control the thermal history, microstructure, and mechanical properties of AM Ti-6Al-4V parts before production [18-20]. For the thermal history, the finite element analysis (FEA) with the "element birth" technique has been widely adopted [20-28]. For the microstructure, Baykasoglu et al. [28], Irwin et al. [29], and Sun et al. [30] have successfully optimized the microstructure models

originally developed by Kelly [31] and Charles and Järvstråt [32] based on the Johnson-Mehl-Avrami (JMA) equation [39-41] to simulate the α/β phase transformation and the scale of microstructural features (α lath widths) of Ti-6Al-4V. For the mechanical properties, artificial neural network (ANN) and genetic algorithm (GA) methods were adopted and constitutive equations including the major strengthening mechanisms were successfully built [99-42] to quantitatively predict the yield strength (YS) of Ti-6Al-4V from the microstructure. Unfortunately, little research has been conducted on combining the above three models to couple the relationships between thermal history, microstructure, and mechanical properties.

This research investigates the effect of wire diameter on the thermal history, microstructure, and tensile properties of Ti-6Al-4V parts produced by laser wire deposition (LWD). Moreover, a FEA model was built to simulate the deposition process and predict the thermal history. In addition, the microstructural model developed by Kelly [31] and Charles and Järvstråt [32] was used to predict the α/β phase fractions and α lath widths. The constitutive equations developed by Hayes et al. [99] were also used to predict the YS of the Ti-6Al-4V parts. The accuracy of all models was validated by comparison with experimental data.

6.3 Materials and Methods

6.3.1 Sample Fabrication
This study used a wire-fed LAWS 1000^{TM} automated deposition system (Liburdi, Canada) equipped with an IPG Yb:YAG fiber laser of up to 1 kW power to produce a total of six single-bead Ti-6Al-4V plates. The deposition environment was an inert argon environment with oxygen levels below 60 ppm to prevent oxidation. All substrates used for deposition were wrought Ti-6Al-4V plates. Three Ti-6Al-4V wire spools with different wire diameters were used to deposit the material. Table 6.1 lists the wire diameter and chemical composition of the spools. Table 6.2 presents the processing parameters used to fabricate Ti-6Al-4V parts. The processing parameters used in this work were based on optimized parameters used in previous work [7] to generate a fully dense deposit. Non-destructive testing methods such as ultrasonic testing and radiographic testing were used to investigate the density of the deposits for validation. Table 6.2 shows that higher laser power and slower wire feed rate were used for larger wire diameters to ensure complete fusion and minimize the formation of defects such as lack of fusion. Two different coupon geometries were deposited to accommodate the extraction of tensile specimens in the build direction Z and travel

direction X. The first geometry of the deposits (denoted as X) is 110 mm in width and 75 mm in height to extract tensile specimens along travel direction X. The other geometry of the deposits (denoted as Z) is 55 mm in width and 120 mm in height to extract tensile specimens along the build direction Z. For the set of coupons produced with a wire diameter of 0.8 mm, the corresponding substrate dimensions are 110 mm in width, 21 mm in height, and 10 mm in thickness for X deposits and 55 mm in width, 21 mm in height, and 6 mm in thickness for Z deposits. For the set of coupons produced with wire diameters of 1.1 mm, and 1.6 mm, the corresponding substrate dimensions are 110 mm in width, 21 mm in height, and 10 mm in thickness for X deposits and 110 mm in width, 21 mm in height, and 10 mm in thickness for Z deposits. All coupons were deposited at a travel speed of 5.1 mm/s. Figure 6.1 shows the image of six deposited plates in the Z and X directions printed with wire diameters of 0.8 mm, 1.1 mm, and 1.6 mm. The deposits were subsequently used for stress relief (SR) treatment, microstructure characterization, and mechanical property evaluation.

[16]Table 6.1. Chemical composition (wt. %) of Ti-6Al-4V wire spools.

Company	Wire Diameter	Al	V	Fe	C	O	N	H	Y	Ti
Astrolite®, USA	0.8 mm	6.24	3.98	0.098	0.0018	0.067	0.0028	0.0018	-	Balance
Astrolite®, USA	1.1 mm	6.05	4.04	0.089	0.01	0.07	0.0008	0.0016	<0.0005	Balance
Polymet, USA	1.6 mm	6.15	4.02	0.069	0.006	0.047	0.004	0.001	<0.0004	Balance

[17]Table 6.2. Processing parameters used to fabricate the Ti-6Al-4V parts.

Wire Diameter	Laser Power	Wire Feed Rate	Inter-Pass Waiting Time	Spot Diameter
0.8 mm	950 W	22.86 mm/s	40 s	0.9 mm
1.1 mm	1050 W	6.79 mm/s	40 s	0.9 mm
1.6 mm	1200 W	6.79 mm/s	40 s	0.9 mm
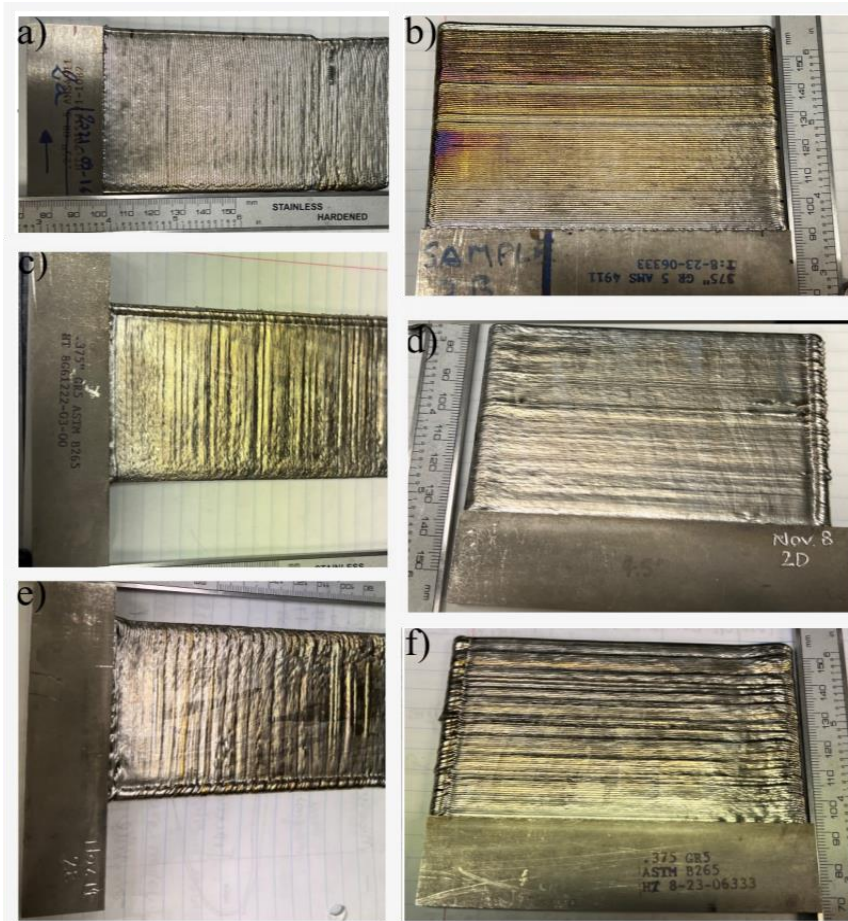
[53]Figure 6.1. Pictures of all deposited plates in the Z direction with wire diameters of (a) 0.8 mm, (c) 1.1 mm, and (e) 1.6 mm, respectively. Picture of all deposited plates in the X direction with wire diameters of (b) 0.8 mm, (d) 1.1 mm, and (f) 1.6 mm, respectively.

6.3.2 Temperature Measurement

During the deposition process, an Optris PI 08M thermal camera (Optris, Germany) was used to record the temperature. The recorded temperature was selected from three layers at the initial, middle, and final stages of the deposition process for all coupons. The Optris' infrared cameras are fully radiometric stationary thermographic systems that feature a line scan mode used during deposition processes to record the thermal history of the deposits.

6.3.3 Material Characterization and Testing

A SR cycle (held at 593 ℃ for 2 hours followed by furnace cooling), according to the AMS2901 standard [43], was performed to reduce residual stresses from the deposition process while preserving structural features.

Metallographic evaluations were conducted for all deposits. Samples were extracted from the middle region. After mounting in bakelite, they were ground from 400 SiC grit to 1200 SiC grit, followed by polishing with 1 μm diamond suspension and a finish with 0.05 μm colloidal silica. A Kroll's Reagent etchant containing 91 % deionized water (H_2O), 6 % nitric acid (HNO_3), and 3 % hydrofluoric acid (HF) was then used on the mounted samples to reveal structural features. The metallographic and fractographic specimens were observed using a VHX-7000 digital microscope (Keyence, Canada) and a SU-3500 cold field SEM (Hitachi, Ltd., Japan).

Vickers' hardness was measured along the build height for all deposits using a Clark Microhardness (CM-100AT) indenter (Sun-Tec Corporation, USA) under a 100 g load. A total of 3 measurements were done along the same layer for each of the reported values.

Tensile properties, including YS, ultimate tensile strength (UTS), and elongation, were tested using a 600 DX universal testing frame (Instron®, USA) with a calibrated load cell and extensometer. Machined subsize specimens were extracted from SR deposits with a thickness of about 2 mm, a gauge width of 6 mm, and a gauge length of 25 mm according to ASTM E8 standard [44]. For deposits built in the Z and X directions, 4 and 5 tensile coupons were extracted, respectively. They were tested at room temperature at a strain rate of 0.005 in/in/min to yield and 0.05 in/in/min after yield to fracture. After fracture, the cross-section of the fracture surface was characterized and analyzed using the Hitachi SU-3500 cold field SEM as mentioned above.

After fracture, the grain intercepts were measured by firstly drawing three random straight lines near the fracture surfaces. Then, the average of the divisions between the number of the prior β grain boundaries and the length of the straight lines was taken as the average grain intercept.

6.3.4 Statistical Analysis

To determine if a statistical difference in grain size, microhardness, YS, UTS, and elongation among all deposits ($\alpha=0.05$) exists between the data sets, a statistical analysis was performed using the one-way analysis of variance (ANOVA) application in Origin Pro 2024 software (Origin Lab, USA) and Tukey's *post hoc* analysis.

6.4 Results and Discussion

6.4.1 Wall Geometry Comparison

Figure 6.2 shows the wall geometry profiles of all deposits. The XZ plane with a distance of 10 mm to the side was selected as the region of interest. At least 10 sets of data points were selected at the bottom (0-10 mm from the substrate), middle (55-65 mm from the substrate for Z deposits and 35-45 mm from the substrate for X deposits), and top regions (100-110 mm from the substrate for Z deposits and the 60-70 mm from substrate for X deposits), respectively. It is important to note that the aspect ratio of the displayed wall geometry profiles is deceiving because the values have been compressed along the Z-axis. Table 6.3 presents the measured layer widths and heights for all deposits. Deposits with the smallest wire diameter, 0.8 mm, show the most consistent wall widths, where the wall profile tracks well together. This observation can also be made for the layer width and height measurements. As the wire diameter increases, the layer widths and heights show increased deviations, which is likely related to the increased heat input. This leads to a more unstable thermal history and thus instability in the melt pool size. Moreover, it can be seen (Table 6.3) that the layer widths and heights increase as the wire diameter increases. Gibson et al. [17] also investigated the wall geometry profiles for LWD deposits and reported that inconsistent wall geometry profiles were due to heat accumulation as the deposited layers evolved, resulting in unstable melt pool sizes. The authors demonstrated that modulation of laser power, travel speeds, and/or deposit rates during the deposition process can help control melt pool sizes and maintain a consistent wall geometry profile. In this study, all processing parameters were held constant after the first five layers. As a result, heat accumulation in subsequent layers increased as the wire diameter increased, resulting in inconsistent melt pool sizes and wall profiles.
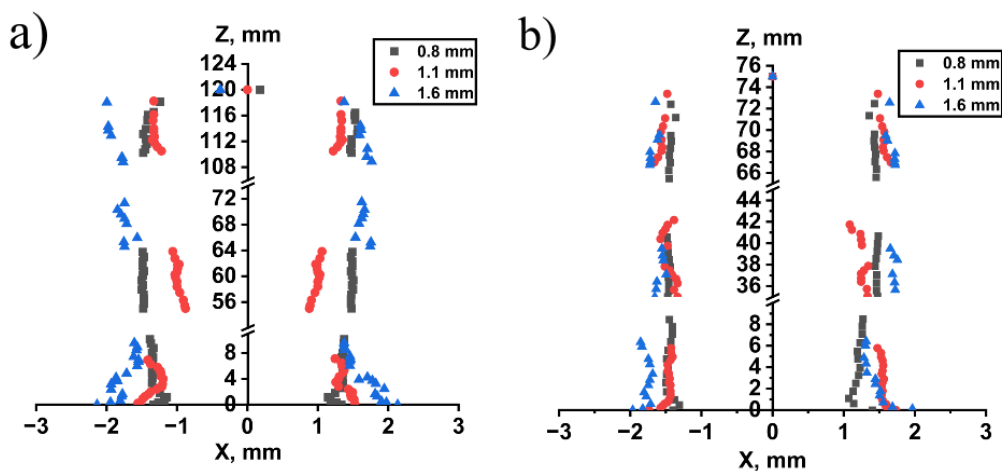
[54]Figure 6.2. (a) Wall geometry profiles for samples built in the Z direction with wire diameters 0.8 mm, 1.1 mm, and 1.6 mm. (b) Wall geometry profiles for samples built in the X direction with wire diameters 0.8 mm, 1.1 mm, and 1.6 mm.

[18]Table 6.3. Measured layer widths and layer heights for all the deposits.

Wire diameter, Sample label	0.8 mm, Z	0.8 mm, X	1.1 mm, Z	1.1 mm, X	1.6 mm, Z	1.6 mm, X
Layer Width	2.8 ± 0.2 mm	2.8 ± 0.1 mm	2.4 ± 0.4 mm	3.0 ± 0.2 mm	3.4 ± 0.3 mm	3.3 ± 0.2 mm
Layer Height	0.7 ± 0.1 mm	0.6 ± 0.1 mm	0.6 ± 0.4 mm	0.5 ± 0.4 mm	0.7 ± 0.5 mm	0.6 ± 0.3 mm

6.4.2 Effect of Wire Diameter on Thermal History

The thermal history of the LWD deposition process was simulated using the FEA model developed previously. A representative 10-layer model with dimensions corresponding to the real deposits was built. All processing parameters used in the deposition process were applied to the FEA thermal model. Details of the model can be found in Zhang et al. [45]. Figures 6.3(a-c) show comparisons of the thermal history between thermal camera measurements and FEA calculations for the deposition of the first three layers. Good agreement between experimental and simulation results can be observed for most of the layers for all the wire diameters. Figure 6.3(c) displays that there is a mismatch for the second layer of the deposit produced with a wire diameter of 1.6 mm. For this layer, a large deviation is observed between the temperature measured with the thermal camera and the FEA model. This may be due to the increase in heat input with increasing wire diameter, which causes instability during the initial stage of deposition.

Figure 6.3(d) presents the calculated cooling rates at β-transus temperature for the first three layers from the thermal camera and FEA for all deposits. During cooling, the β phase starts to transform to the α phase at around 1273 K [7]. This temperature is called the β-transus temperature. Each layer experienced heating and cooling cycles as the subsequent layers were deposited. At the end node of each layer, the cooling rate was calculated at β-transus temperature when the last layer was deposited. Cooling rates at β-transus temperature are critical to the subsequent α/β morphology and grain size development. They were calculated as:

$$CR = {\Delta T}/{\Delta t} \qquad\qquad\qquad \text{Equation 6-1}$$

where CR is the cooling rate (K/s), ΔT and Δt are the temperature differences (K) and the time differences (s) at the β-transus temperature, respectively. With the increase of the layers, there is a decrease in the cooling rate due to heat accumulation. For the first three layers, the cooling rates with wire diameters of 1.1 mm and 1.6 mm are greater than the ones of 0.8 mm. This is due to the heat sink effect of the substrate. Since the deposits made with wire diameters of 1.1 mm and 1.6 mm were produced on the larger substrates, they dissipated more heat.

Figure 6.4 shows the calculated cooling rates at the β-transus temperature for each layer when the last layer was deposited using the FEA model. The deposits produced with wire diameters of 1.1 mm (red points) and 1.6 mm (blue points) showed a higher cooling rate in the initial portion of the built (1st - 5th layers) due to the heat sink effect of the larger substrate size (110 mm * 21 mm * 10 mm) than the substrate used for the deposit with the wire diameter of 0.8 mm (55 mm * 21 mm * 6 mm). However, it could be seen that as the deposition continued, all experienced a higher reduction in the cooling rates compared to the deposit produced with a wire diameter of 0.8 mm (grey-filled points), which is believed to be from the larger heat input. At the 10th layer, the cooling rates are similar between the deposits, independent of the wire diameters. Another FEA model was built for the deposits with a wire diameter of 0.8 mm using the same substrate size as deposits produced with wire diameters of 1.1 mm and 1.6 mm. As shown, even with the same substrate size, at the 10th layer mark, the cooling rates are similar for all wire diameters and the heat sink effect becomes negligible. The actual deposits are composed of hundreds of layers, so it was inferred that the significantly higher heat accumulation associated with large wire diameters will promote a lower cooling rate in the middle part of the deposit.
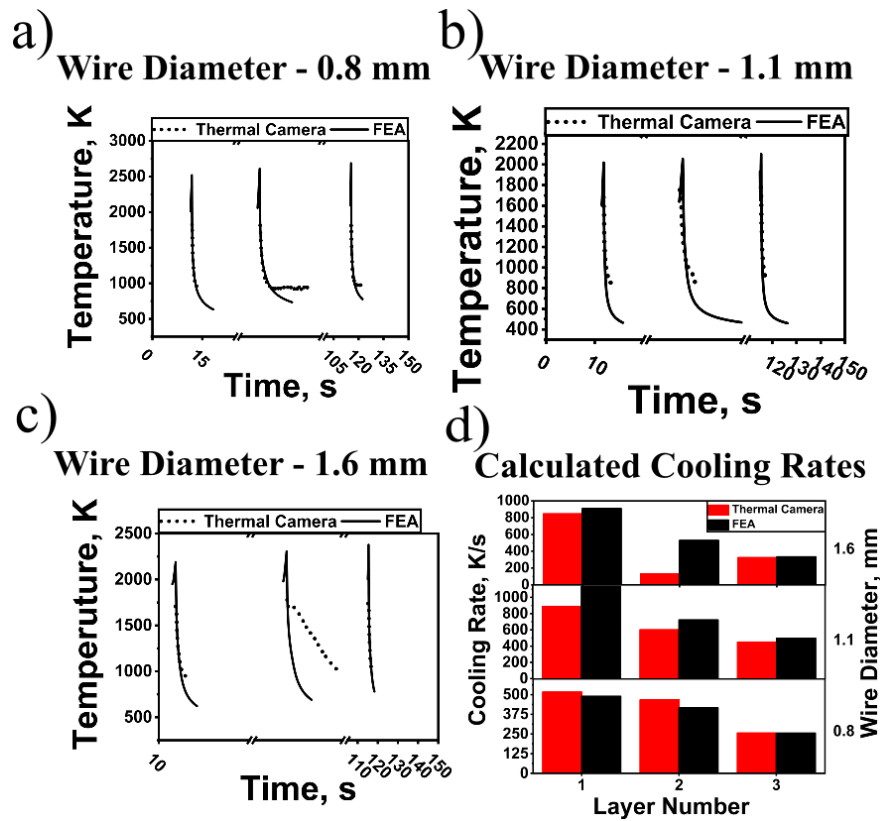
Figure 6.3. Comparison of temperature-time profiles between the FEA model and thermal camera measurements for deposits produced with wire diameters of (a) 0.8 mm, (b) 1.1 mm, and (c) 1.6 mm, respectively. (d) Comparison of calculated cooling rates between FEA and thermal camera measurements.
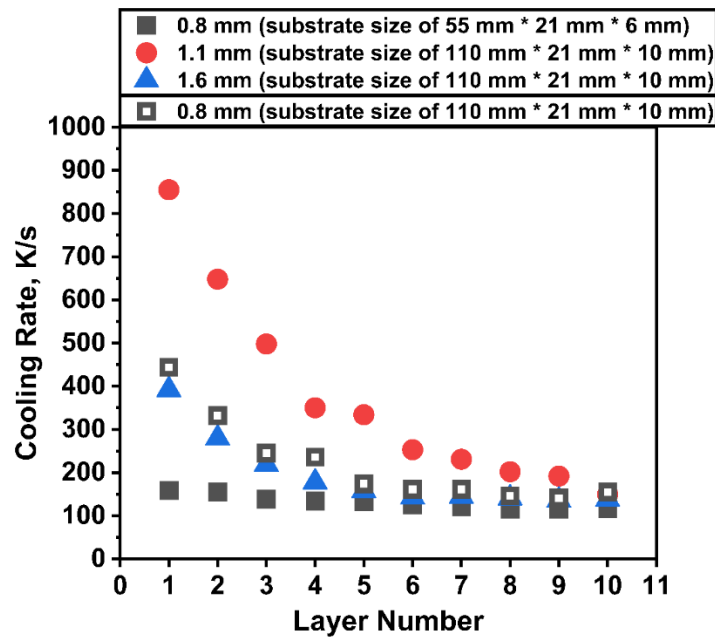
[56]Figure 6.4. Cooling rate at β-transus temperature of each layer when the last layer was deposited

for deposits produced with wire diameters of 0.8, 1.1, and 1.6 mm from the FEA model.

6.4.3 Structure Evaluation

6.4.3.1 Macrostructure

Figure 6.5 presents the macrostructure of all deposits produced with different wire diameters. Columnar prior β grains can be observed in all samples due to the high thermal gradient, G, generated in the LWD process. The morphology of the solidification structure is mainly decided by two critical parameters: G and the growth rate, R. A high G and low R will promote a columnar structure. Interestingly, Figure 6.5 shows that a small percentage of equiaxed structure can still be observed in all samples. This is due to changes in the solidification conditions during the deposition process. As can be seen, all deposits tend to have some percentage of equiaxed structure at the edge. This is due to the heat accumulation that lowered G and promoted CET. It can also be seen that samples produced with increased wire diameters tend to have equiaxed structures in non-edge regions as well. This is inferred to be due to the instability of the deposition process, which can alter the solidification conditions that promote CET.

Figure 6.5(d) shows that equiaxed structures were observed in the middle section (about the 74th layer) of the deposit produced with a wire diameter of 1.1 mm in the X direction. The corresponding time vs temperature diagram at the 74th layer from the thermal camera was evaluated and graphed in Figure 6.6. As shown, a temperature fluctuation of about 20 K occurred during the process. However, around seconds 14-18 and 20-24, a significant fluctuation in the temperature of up to 150 K can be observed. Higher temperatures were observed during these periods matching the higher heat input. This could lead to lower G and promote the formation of the equiaxed structure. This supports that at the later half of the 74th layer, the process was unstable, and the solidification conditions were altered.

Figure 6.5 shows another typical structure, a band structure. These repetitive bands are formed due to the cyclic thermal history of the LWD process. When the laser processes the next layer, the β-transus isotherm follows the part growth. Therefore, the band structure depicts the temperature increase during the deposition of the above layer but reaches just below the β-transus temperature. The spacing between the center of each band is related to the layer height. Figure 6.5 shows as well

that the spacing between the center of each band is non-uniform along the build height for large wire diameters due to the inhomogeneity of melt pool sizes.

Table 6.4 shows the measured widths of the columnar prior β grains for the Ti-6Al-4V deposits produced with different wire diameters. The ANOVA analysis reveals that there is a statistical difference in the widths of columnar prior β grains among the different wire diameters ($p<0.05$). Increasing the wire diameter developed thicker columnar β grains due to increased heat input.

[19]Table 6.4. Widths of columnar prior β grains for Ti-6Al-4V deposits produced with different wire diameters.

Sample Label/ Wire Diameter	0.8 mm	1.1 mm	1.6 mm
Z	1.9 ± 0.8 mm	2.6 ± 0.9 mm	3.2 ± 1.2 mm
X	2.7 ± 1.2 mm	2.9 ± 1.1 mm	4.2 ± 1.1 mm
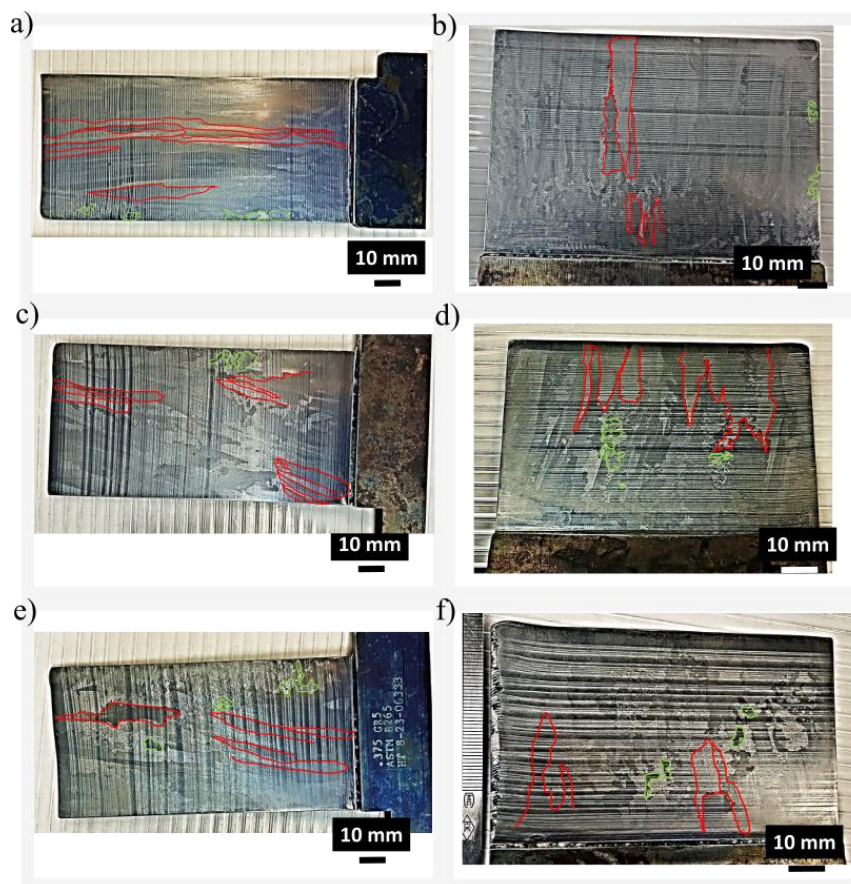
[57]Figure 6.5. The macrostructure of Ti-6Al-4V deposits developed in the Z direction with wire

diameters of (a) 0.8 mm, (c) 1.1 mm, and (e) 1.6 mm, respectively. The macrostructure of Ti-6Al-4V deposits developed in the X direction with wire diameters of (b) 0.8 mm, (d) 1.1 mm, and (f) 1.6 mm, respectively.
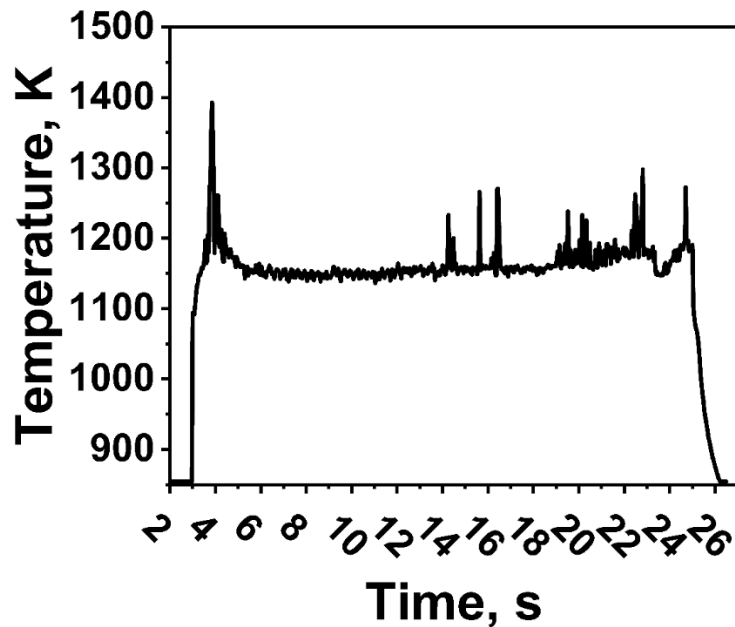
[58]Figure 6.6. Time vs temperature diagram of the 74th layer of the deposit produced with a wire diameter of 1.1 mm in the X direction.

6.4.3.2 Microstructure

Figure 6.7 shows optical micrographs of deposits produced with different wire diameters. The regions with prior β grain boundaries were selected of interest. The grain boundary α can be observed at the prior β grain boundaries. When Ti-6Al-4V is cooled at sufficiently low rates from the β phase field to the (α+β) phase field, the α phase, which is incoherent with respect to the β phase, first preferentially nucleates at β grain boundaries, leading to a continuous α layer along β grain boundaries [46]. This is how the grain boundary α is formed. During continuous cooling, α plates nucleate either at the interface of the grain boundary α or at the β grain boundary and grow into the β grain as parallel plates of the same variant, called an α colony. The α colony is favored at high temperatures and low cooling rates that kinetically allow diffusion-controlled growth. The α colonies continue to grow into the β grain interior until they encounter other α colonies nucleated with other variants of the Burgers relationship. With increased cooling rates, new α plates begin to nucleate by point contact on the broad face of an existing α plate and tend to grow nearly

perpendicular to that plate. At lower temperatures, diffusion is limited, and growth is controlled by interfacial and ledge-wise diffusional growth of α laths [47]. This results in a characteristic microstructure called a "basket weave" structure. Figures 6.7(c and e) show the α colony structure near the grain boundary α for deposits produced with wire diameters of 1.1 mm and 1.6 mm. This is due to the higher heat input and lower cooling rate than the ones produced with a wire diameter of 0.8 mm.
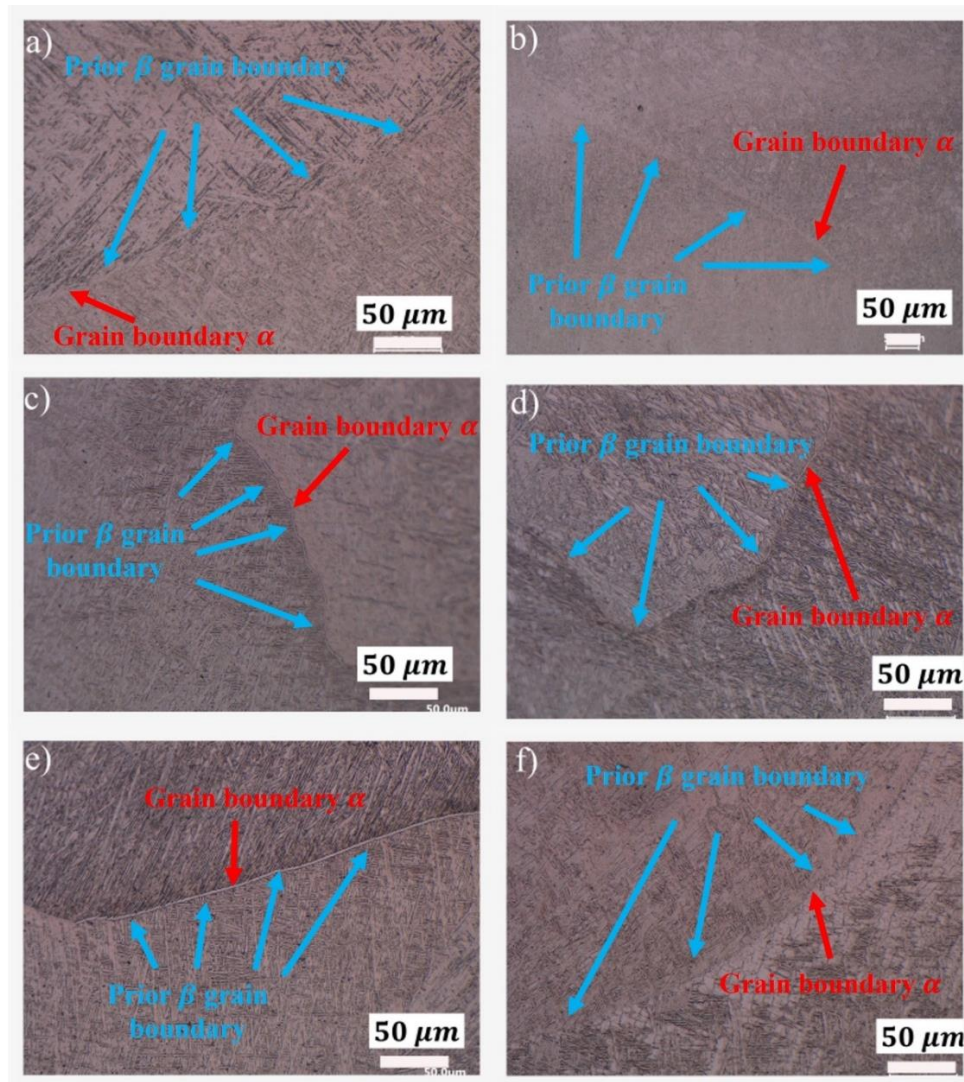
[59]Figure 6.7. Optical micrographs of grain boundary α at prior β grain boundary for samples built in the Z direction with wire diameters of (a) 0.8 mm, (c) 1.1 mm, and (e) 1.6 mm, and for samples built in the X direction with wire diameters of (b) 0.8 mm, (d) 1.1 mm, and (f) 1.6 mm, respectively.

Figure 6.8 presents SEM micrographs of all deposits produced with different wire diameters. Typical basketweave α structures were observed in all deposits, which are characterized by the

competitive growth of α laths following the Burgers relationship. Table 6.5 lists the measured α lath widths of all deposits produced with different wire diameters. The ANOVA analysis shows that the α lath widths are statistically different for deposits produced with different wire diameters ($p<0.05$). It can be seen that the width of the α lath increases with increasing wire diameter due to increasing heat input. It can also be seen that there is a large deviation for deposits produced with large wire diameters due to unstable heat input.
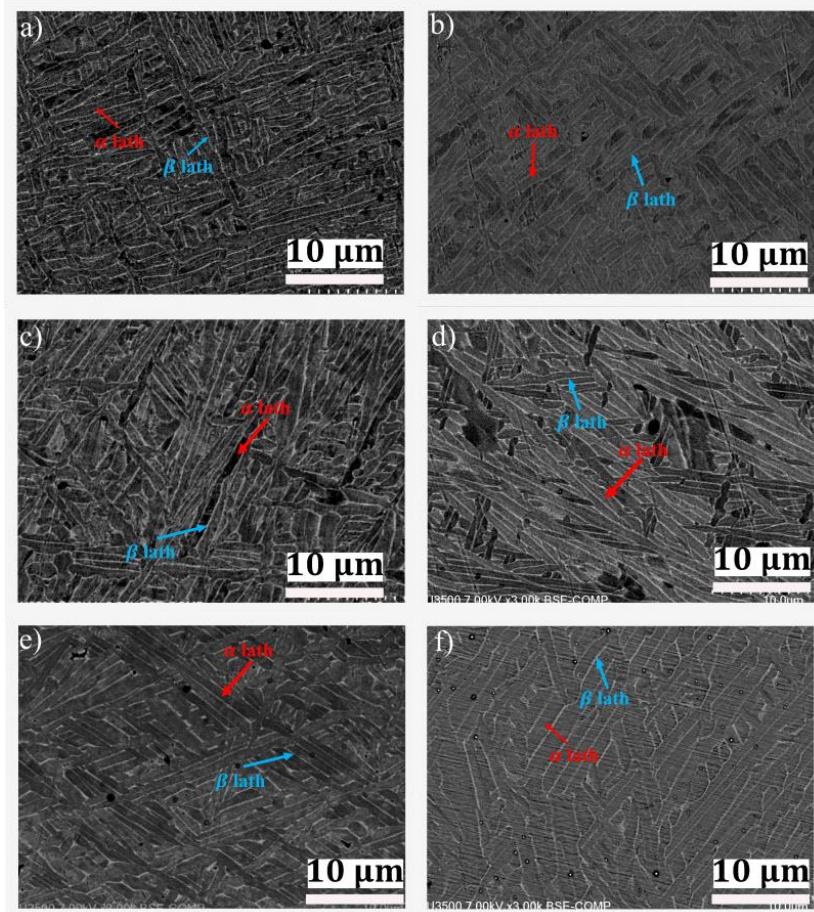
[60]Figure 6.8. SEM micrographs of Ti-6Al-4V deposits built in the Z direction with wire diameters of (a) 0.8 mm, (c) 1.1 mm, and (e) 1.6 mm, respectively. SEM micrographs of Ti-6Al-4V deposits built in the X direction with wire diameters of (b) 0.8 mm, (d) 1.1 mm, and (f) 1.6 mm, respectively.

[20]Table 6.5. Measured α lath widths for all deposits produced with various wire diameters.

Sample Label/ Wire Diameter	0.8 mm	1.1 mm	1.6 mm
Z	0.62 ± 0.27 μm	0.87 ± 0.34 μm	1.09 ± 0.38 μm

X	$0.62 \pm 0.33 \ \mu$m	$0.69 \pm 0.22 \ \mu$m	$1.00 \pm 0.35 \ \mu$m

6.4.4 Mechanical Properties

6.4.4.1 Microhardness

Figure 6.9 presents the average microhardness values at different build heights for deposits produced with different wire diameters. A higher microhardness was observed at the interface due to the developed α' martensite. Since the cold substrate acts as a heat sink and there was no heat accumulation at the beginning of deposition, cooling rates at the interface can reach up to over 410 K/s (section 3.2). Due to the wide distribution of α lath widths, the ANOVA analysis shows no statistical difference in microhardness between different wire diameters ($p > 0.05$). This is because microhardness is mainly affected by individual lath sizes rather than collective morphology [48].
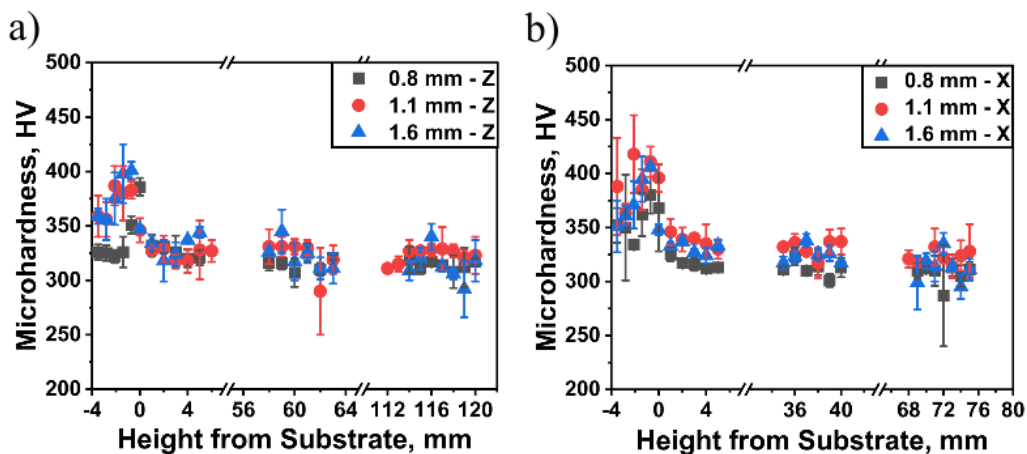
[61]Figure 6.9. (a) Average microhardness along the build height for deposits built in the Z direction. (b) Average microhardness along the build height for deposits built in the X direction.

6.4.4.2 SR Static Tensile Properties

Figure 6.10(a) presents the static tensile properties of SR specimens for all wire diameters in comparison with the minimum tensile properties for DED Ti-6Al-4V according to AMS 4999 [49]. All tensile strengths are above the minimum requirements. The ANOVA analysis shows that with the increase in wire diameters, there is a decrease in YS and UTS ($p < 0.05$) due to the coarser microstructure developed from the increased heat input. Figure 6.10(b) shows the correlation between YS, σ_y, and α lath width, w, by plotting σ_y against $w^{-0.5}$ according to the Hall-Petch mechanism. The correlation is good with a coefficient R^2 of 0.92. This indicates that the decrease in strength with the increase in wire diameter is mainly due to the coarser microstructure. The

ANOVA analysis reported that the elongations are statistically similar among the deposits produced with different wire diameters ($p>0.05$). It can be seen that the elongations of a few tensile coupons are below the AMS 4999 standards for deposits produced with large wire diameters. Several factors can be responsible for the low elongations, such as coarse grains, grain boundary α, α colony, and defects generated during the deposition process, which will be discussed in the following section.
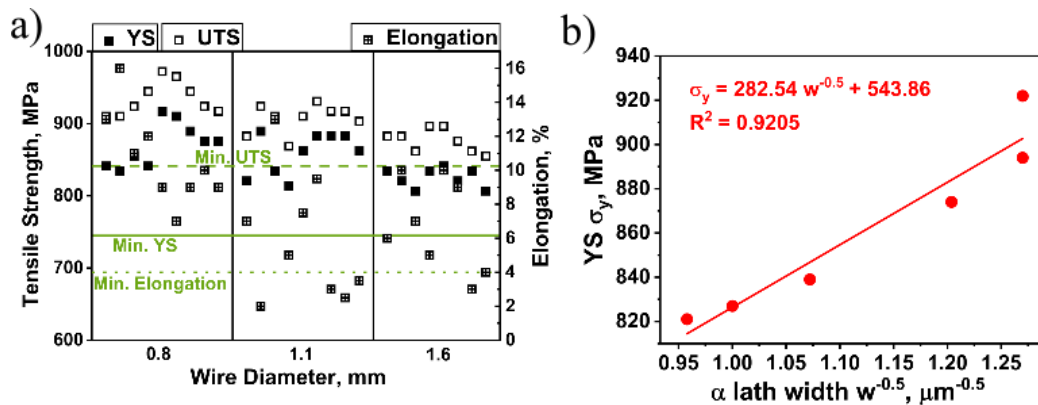
[62]Figure 6.10. (a) The YS, UTS, and elongation of all tensile coupons extracted from the deposits produced with different wire diameters. Minimum tensile properties of Ti-6Al-4V produced by DED according to AMS 4999 [49] are indicated by green lines. (b) Variation of YS, σ_y with the inverse of the square root of the α lath width, w.

Figures 6.11(a and b) present measured aspect ratios for prior β grains at different locations of the deposits produced in the Z and X directions. The locations were selected to be where tensile coupons were extracted. Figures 6.11(c and d) show the YS, UTS, and elongation of all tensile coupons for deposits produced in the Z and X directions. The labels of the tensile coupons on the horizontal axis correspond to locations where calculations for aspect ratios of prior β grains were performed.

The ANOVA analysis shows that YS, UTS, and elongation are statistically different between Z and X directions for deposits produced with a wire diameter of 0.8 mm ($p<0.05$), indicating anisotropic behavior. However, for wire diameters of 1.1 and 1.6 mm, the tensile results between the Z and X directions are statistically similar ($p>0.05$). This can be due to the higher percentages of equiaxed prior β grains (reported in section 3.3.1 on microstructure) which weakened the texture effect. The anisotropy is attributed to the difference in texture, the columnar β grain morphology, and the presence of grain boundary α from different tensile directions. A strong β phase texture generates a

strong α texture, which results in a difference in critical resolved shear stress (CRSS) along different loading directions. The tensile strength of the samples along the build direction was reduced according to the Hall-Petch relationship [50]. The prior β grain boundary is decorated with grain boundary α, which is well documented to tend to reduce elongation by furnishing a preferential path for damage accumulation along the prior β grain boundary [51-52]. Figure 6.7 demonstrates for all deposits that the prior β grain boundaries are furnished by grain boundary α. Tensile coupons extracted from the X direction have more amounts of grain boundary α exposed to a tensile opening mode when tension is applied perpendicular to the grain boundaries.

Similar effects can be observed elsewhere. As mentioned in section 3.3.1, there is a high percentage of equiaxed prior β grain at the edge of the deposits due to the CET phenomenon caused by heat accumulation. Figure 6.11(a) shows reduced aspect ratios for tensile coupons extracted from the edge regions of Z deposits. Some grains have aspect ratios < 2 and therefore have an apparently equiaxed morphology [53]. As a result, more amounts of grain boundary α are exposed to a tensile opening mode compared to center-closed coupons where columnar prior β grains are the dominant structure.

Figure 6.11(c) shows the corresponding tensile properties of coupons. No significant difference in tensile strength was observed for tensile coupons with different aspect ratios of prior β grain. On the other hand, strong correlations were observed between the different aspect ratios of the prior β grains and the corresponding elongation values. Lower elongations were observed for low aspect ratios due to a higher number of grain boundaries having allomorphic α. Keist and Palmer [54] attributed the lack of correlation on tensile strengths to the reduced number of grain intercepts, which would effectively reduce the overall contribution of grain boundary strengthening. Figure 6.12 shows the optical micrographs of the cross-section of the fracture surfaces on tensile coupons where the prior β grain boundaries are identified with the red dashed lines. Figure 6.13 (a) presents the measured average grain intercepts for all the deposits. Figure 6.13 (b) shows that there is no clear correlation between grain intercepts and the corresponding YS. As shown, the average grain intercepts were all below 2 mm^{-1}. Keist and Palmer [54] reported that the correlation between grain intercepts and yield strengths was obvious when the average grain intercept was larger than 4 mm^{-1}. Therefore, the lack of correlation in this study matches the small number of grain intercepts.
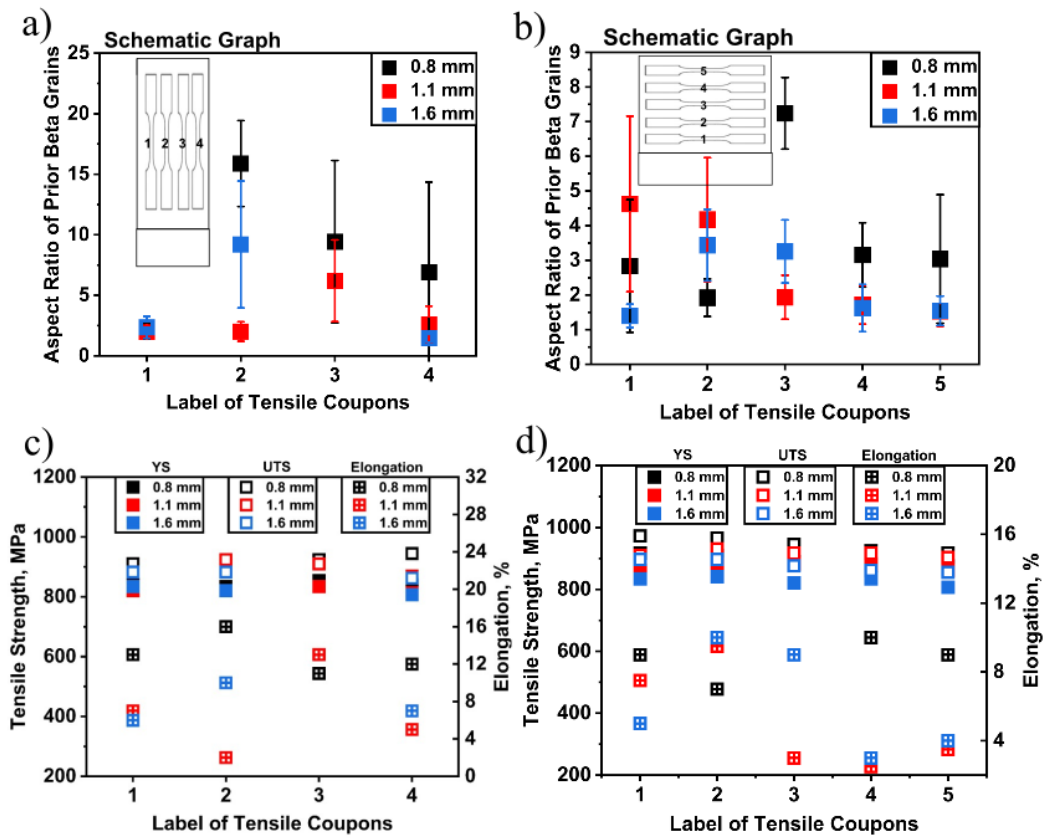
[63]Figure 6.11. (a–b) Measured aspect ratios of prior β grains at different locations of deposits produced in the Z and X directions, respectively; (c–d) The corresponding tensile properties in the Z and X directions, respectively.
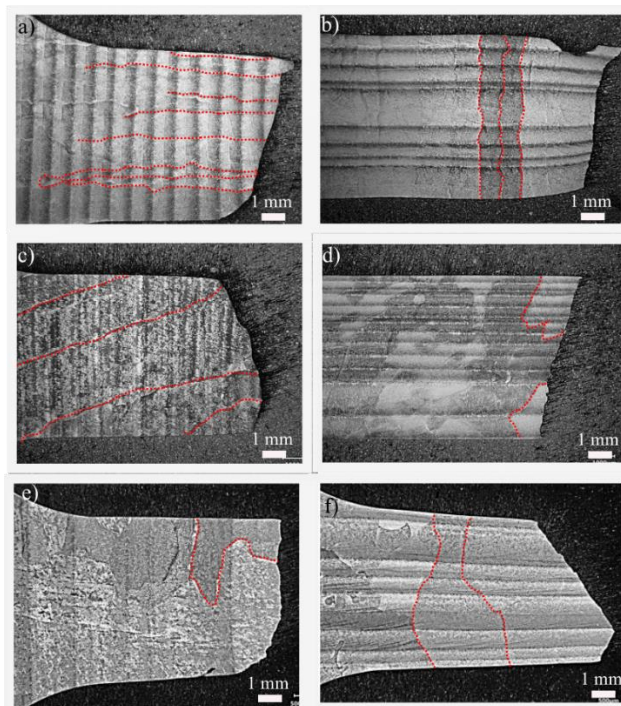
[64]Figure 6.12. Optical micrographs of the fracture surface of the tensile coupons from the deposits built in the Z direction with wire diameters of (a) 0.8 mm, (c) 1.1 mm, and (e) 1.6 mm, respectively. Optical micrographs of the fracture surface of the tensile coupons from the deposits built in the X direction with wire diameters of (b) 0.8 mm, (d) 1.1 mm, and (f) 1.6 mm, respectively.
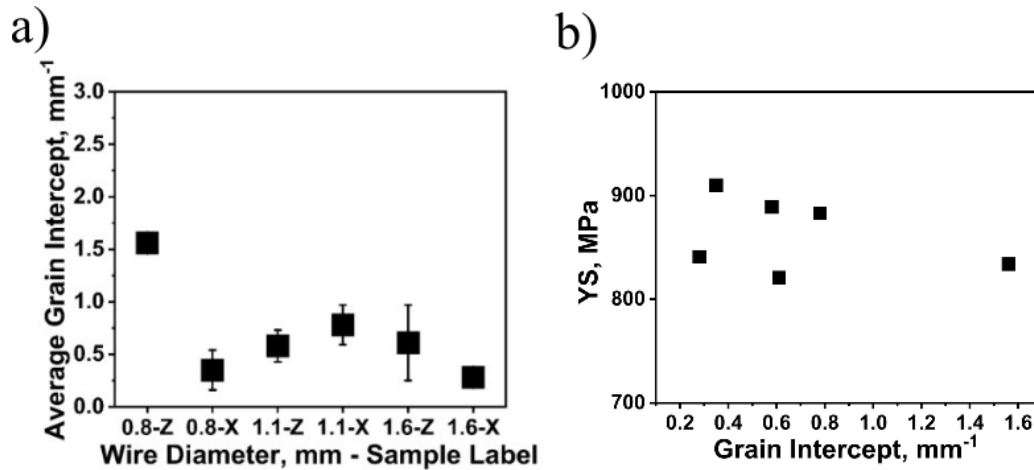
[65]Figure 6.13. (a) Measured average grain intercepts near fracture surfaces of tensile coupons for all deposits. (b) The corresponding YS vs grain intercepts for all tensile coupons.

6.4.4.3 Fracture Mechanisms

Figure 6.14 shows SEM micrographs of fracture surfaces for tensile coupons produced with different wire diameters and tensile directions. Figures 6.14(a-b) present cone-like fracture surfaces indicating ductility, while Figures 6.14(c-f) show flat fracture surfaces indicating lower ductility. For deposits produced with a wire diameter of 0.8 mm, the fracture surface is mainly occupied by fine and deep dimple structures, indicating microvoid accumulation fractures with a high degree of ductility. For deposits produced with a wire diameter of 1.1 mm, the fracture surface shows, in addition to the dimple structure, seam and void structures, which are possibly related to incomplete fusion and serve as crack nucleation sites during tensile deformation and lower tensile strength and elongation. Seams up to 1 mm in length were observed in fracture surfaces of deposits produced with wire diameters of 1.1 mm and 1.6 mm, indicating crack propagations, which explains the low elongation and tensile strength associated with large wire diameters. Fan et al. [50] investigated the effect of α colony surrounding the grain boundary α on the tensile properties of AM Ti-6Al-4V. They reported that it facilitated dislocation movement and accumulation, especially at larger grain sizes, since the laths were of the same orientation and dislocations were relatively easier to move within. Figures 6.14(c-2 and d-2) show the grain boundary α observed at the fracture surface for

deposits produced with a wire diameter of 1.1 mm. Figures 6.7(c and e) show clear α colonies near the grain boundary with a width of about 10 μm, which can have assisted in crack propagation and caused early failures. Figure 6.14(f-2) shows another terrace-like structure resembling the shape of prior β grains. The width of this structure (100 μm) corresponds well to the widths of prior β grains. Dharmendra et al. [55] and Shrestha et al. [56] reported similar terrace-like structures and related them to crack propagations along prior β grain boundaries as well.
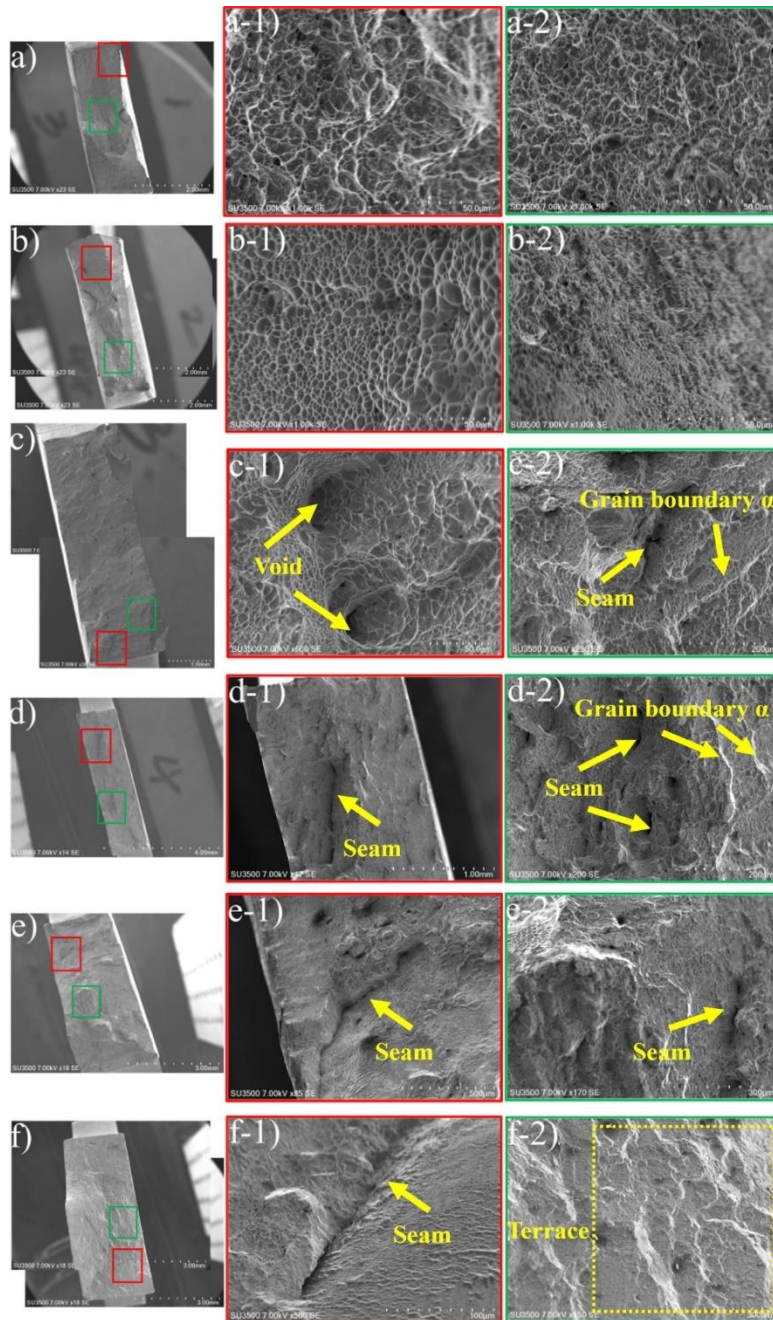
[66]Figure 6.14. SEM micrographs of fractography of tensile specimens built in the Z direction with wire diameters of (a) 0.8 mm, (c) 1.1 mm, and (e) 1.6 mm, respectively. SEM micrographs of

fractography of tensile specimens built in the X direction with wire diameters of (b) 0.8 mm, (d) 1.1 mm, and (f) 1.6 mm, respectively.

6.4.5 Thermo-Microstructural-Mechanical Modeling of LWD Ti-6Al-4V

This research proposes a platform to control the microstructure and YS of LWD Ti-6Al-4V using modeling techniques. Figure 6.15 presents the methodology of the platform. The YS is predicted by the constitutive equations developed by Hayes et al. [99] with the quantified microstructure as input. The microstructure (α/β phase fractions and α lath width) is predicted by the model developed by Kelly [31] and Charles and Järvstråt [32] based on the thermal history. The cooling rate is predicted by the thermal FEA model by adjusting the input processing parameters. All the models are interconnected and validated by experimental results. The validation of the FEA model was demonstrated above (see section 3.2) using a thermal history obtained from the thermal camera.
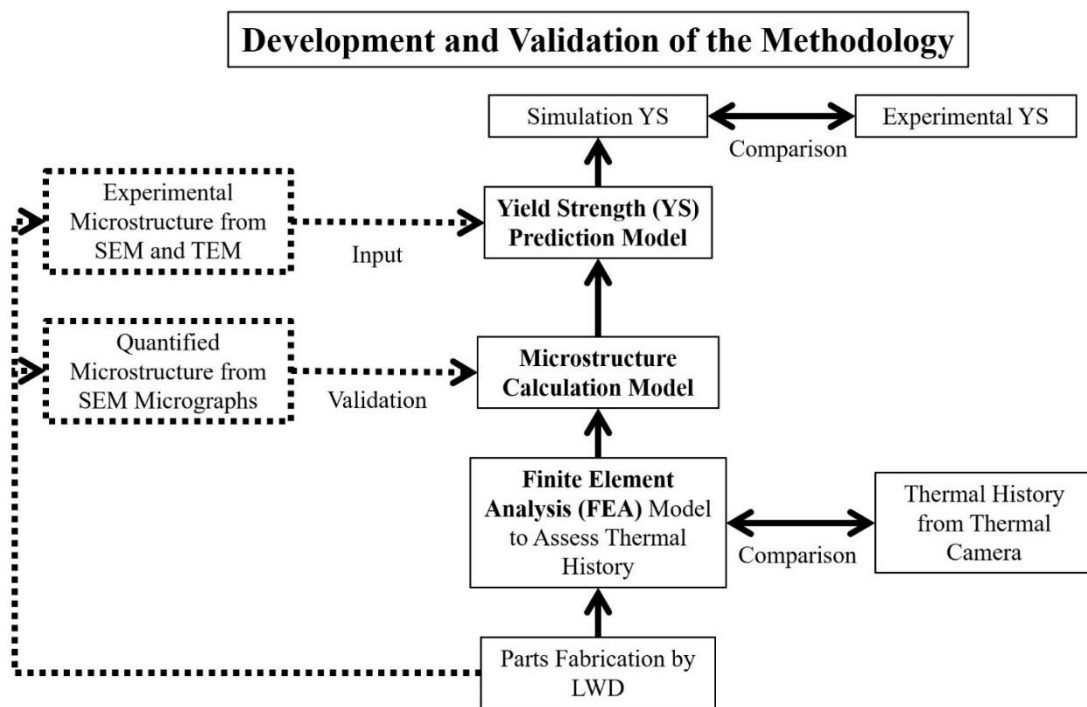
[67]Figure 6.15. Flowchart of the methodology.

6.4.5.1 Microstructural Model

The microstructure model predicts α/β phases without considering the martensite phase transformation because the martensite phase was not produced in the deposits produced in this study (see section 3.2.2). In this approach, the α phase either dissolves or grows depending on the

comparison between the current α/β phase fractions, $f_{i,\alpha}/f_{i,\beta}$, and the equilibrium α/β phase fractions, $f_{eq,\alpha}/f_{eq,\beta}$. Accordingly, if $f_{i,\alpha} < f_{eq,\alpha}$, the α phase grows. The transformed α/β phases are calculated as follows:

$$f_{i,\alpha} = f_{eq,\alpha}\zeta_\alpha, \text{ and } f_{i,\alpha} + f_{i,\beta} = 1 \qquad\qquad \text{Equation 6-2}$$

where $f_{eq,\alpha}$ is the equilibrium α phase fraction that can be found in the Temperature vs Equilibrium Phase Fraction diagram of Kelly [31] (see Figure 6.16) and ζ_α is the extent of the reaction in the range of 0-1 which is modeled using the JMA equation [39-41] with a time-temperature-transformation (TTT) diagram:

$$\zeta_\alpha = 1 - exp(-k(t + t')^n), \text{ and } t' = \left(-log\left(1 - f_{i-1,\alpha}/f_{eq,\alpha}\right)/k\right)^{1/n} \qquad \text{Equation 6-3}$$

In this equation, the kinetic parameter, $k\ (T_i)$, can be found in Kelly [31] for each temperature T_i, t' is the equivalent time (s) for the growth of the α phase, which is the time required to transform the α phase fraction at the previous time step, $f_{i-1,\alpha}$, to the equilibrium α phase fraction, $f_{eq,\alpha}$, t is the time of one step (s), $n = 5/2$ is the Avrami exponent [31]. Accordingly, if $f_{i,\alpha} > f_{eq,\alpha}$, the α phase dissolves. The transformed α phase is modeled as one-dimensional plate growth of the β phase with a parabolic growth rate, r:

$$r = aT_i^b \qquad\qquad \text{Equation 6-4}$$

where T_i is the current temperature (K), and r is the parabolic reaction rate, where the coefficient a = 2.21 * 10^{-31} s$^{-1/2}$ and b = 0.89 [31]. An equivalent time (s), t^*, is introduced to represent the time required to transform the β phase fraction at the previous time step, $f_{i-1,\beta}$, to the equilibrium β phase fraction, $f_{eq,\beta}$:

$$t^* = \left(\frac{f_{i-1,\beta}}{f_{eq,\beta}r}\right)^2 \qquad\qquad \text{Equation 6-5}$$

The resulting β phase is calculated as follows:

$$f_{i,\beta} = f_{eq,\beta}\zeta_\beta, \text{ and } \zeta_\beta = r(t^* + t)^{0.5}$$ Equation 6-6

where ζ_β is the extent of the reaction between 0 and 1. The α lath model follows the work by Charles and Järvstråt [32]. The equilibrium α lath width (μm), w_{eq}, is calculated using an Arrhenius equation:

$$w_{eq} = k_w exp(-T_{act}/T_i)$$ Equation 6-7

where k_w is the prefactor that was originally set to 18400, T_{act} is the activation temperature and was taken to be 294 K [32]. An optimization was made for k_w to 0.9. In this study, the values for k_w and T_{act} were taken from the work of Irwin et al. [29], who optimized the values for DED-fabricated Ti-6Al-4V alloys. Then, the resulting α lath width (μm), w_i, was calculated as:

$$w_i = \left(w_{i-1}f_{i-1,\alpha} + w_{eq}\left(f_{i,\alpha} - f_{i-1,\alpha}\right)\right)/f_{i,\alpha}$$ Equation 6-8

where w_{i-1} and $f_{i-1,\alpha}$ are the α lath width (μm) and α phase fraction from the previous time step.
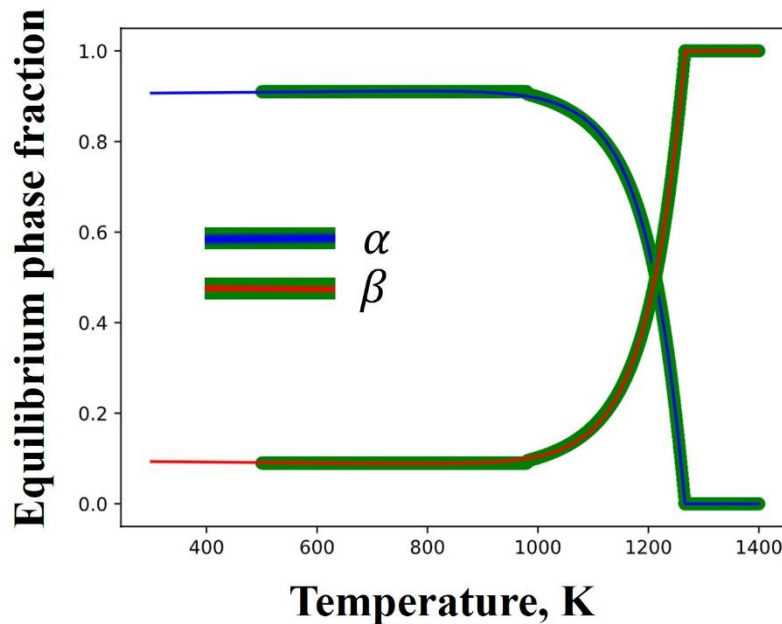
[68]Figure 6.16. Equilibrium α and β phase fractions from Kelly [31].

The temperature-time data obtained from the FEA model (see section 3.2) were used as input to the microstructure model. Figure 6.17 shows the comparison between the predicted α phase fractions and α lath widths and the measured experimental results for different wire diameters. The predicted α phase fractions agree well with the experimental results and are statistically similar ($p>0.05$) among different wire diameters, as they are mainly affected by alloying elements. The predicted α lath widths are similar for deposits produced with different wire diameters because the cooling rates measured from the FEA model (see Figure 6.4) are similar starting from the 10th layer. In addition, the mismatch between the predicted and experimental α lath widths may be caused by two factors: (1) The α lath coarsening during the heating of the subsequent layers was not considered in the model. (2) The measured α lath width from the two-dimensional SEM micrographs could introduce errors considering the three-dimensional nature of α laths. The measured average α lath width for the deposit produced with the largest wire diameter is higher than the predicted α lath width which could be due to the higher heat input that led to a longer time of thermal coarsening.
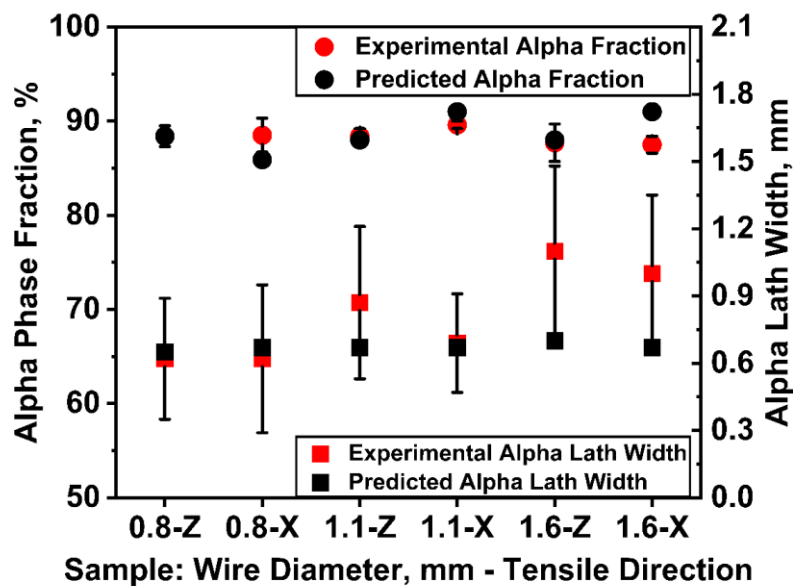
[69]Figure 6.17. Comparison between experimental and predicted α phase fractions and α lath widths.

6.4.5.2 YS Model

Constitutive equations developed by Hayes et al. [99] were used in this study. The equations incorporate the intrinsic flow stress of the hcp α and bcc β phases (Equation 6-9-1), solid solution strengthening of the α phase from oxygen and aluminum (Equation 6-9-2), solid solution strengthening of the β phase from vanadium and iron (Equation 6-9-3), Hall-Patch strengthening

(Equation 6-9-4 and Equation 6-9-5), and Taylor hardening (Equation 6-9-6), which includes the strengthening effect of the basketweave morphology, where F_V is the volume fraction of the designated phases/microstructure, X_B is the concentration (wt. %) of element B (i.e., Al, O, Fe, V), $t_{feature}$ is the thickness (μm) of the given feature (i.e., the α lath, β lath, and the colony width), α is the prefactor term (set to 1) [99], M is the Taylor factor, which is typically between 2.0 and 3.2 for hcp α [99], G is the shear modulus of titanium (44 GPa) [99], b is the Burgers vector (0.3 nm) [99], and ρ is the dislocation density (m^{-2}).

$$\sigma_{ys} = F_V^\alpha * 89 + F_V^\beta * 45 + \qquad \text{Equation 6-9-1}$$

$$F_V^\alpha * (149 * x_{Al}^{0.667} + 759 * x_O^{0.667}) + \qquad \text{Equation 6-9-2}$$

$$F_V^\beta * ((22 * x_V^{0.7})^{0.5} + (235 * x_{Fe}^{0.7})^{0.5})^2 + \qquad \text{Equation 6-9-3}$$

$$F_V^{Col} * 150 * (t_{\alpha-lath})^{-0.5} * (t_{\beta-rib})^{0.5} + \qquad \text{Equation 6-9-4}$$

$$F_V^{Col} * 125 * (t_{Col})^{-0.5} + \qquad \text{Equation 6-9-5}$$

$$F_V^{BW} \alpha M G b \sqrt{\rho} \qquad \text{Equation 6-9-6}$$

Figure 6.18(a) presents the comparison between predicted and experimental YS. They are in good agreement as the deviations are all below 10 %. A sensitivity analysis was conducted to analyze the contribution of different strengthening mechanisms. Figure 6.18(b) shows that major differences in strength are due to solid solution strengthening and the Hall-Petch mechanism. The differences in the chemical compositions of the wire spools used to produce all deposits produce differences in strengths of up to 20-50 MPa. Another reason for the low strength of deposits produced with large wire diameters is the reduced contribution of Hall-Patch strengthening due to the coarser grain sizes.
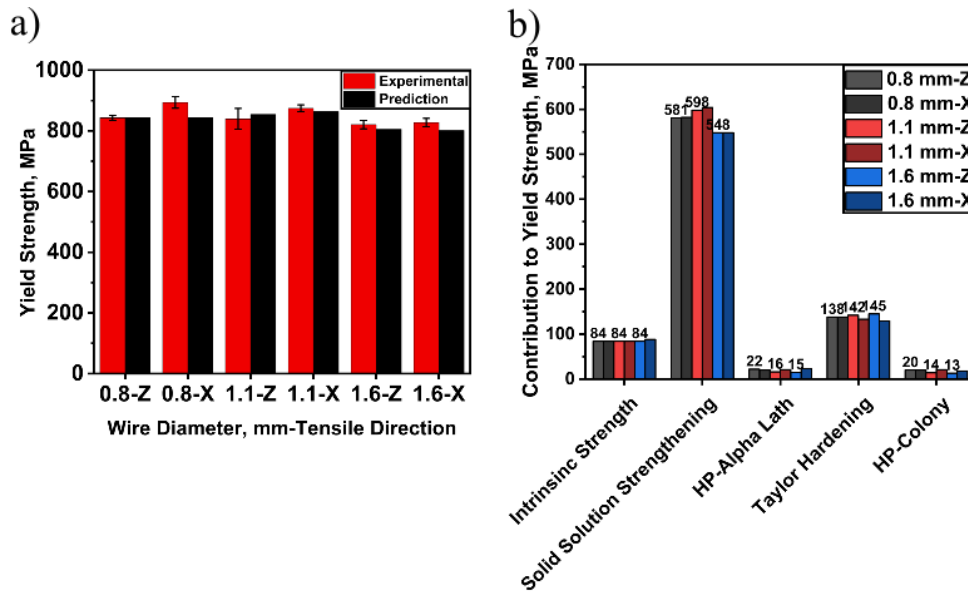
[70]Figure 6.18. (a) Comparison between experimental and predicted YS for all deposits. (b) The contribution of different strengthening terms to the absolute YS for all deposits.

6.5 Conclusion

This research fills the knowledge gap of the effect of wire diameter on the thermal history, microstructure, and mechanical properties of thin Ti-6Al-4V deposits developed by LWD. Wall profiles were investigated to compare the consistency of the melt pool sizes among different wire diameters. Within the tested window of parameters, the increasing in wire diameters led to nonuniform wall profiles and inconsistent melt pool sizes, and larger heat accumulation and lower cooling rates leading to, coarser grains and lower strengths. A greater number of defects were found on the fracture surfaces of the tensile coupons associated with the larger wire diameter, which led to lower strength and premature failure. Furthermore, this research proposed a platform combining FEA modeling, a microstructure prediction model based on α phase fractions and α lath widths, and a YS prediction model to quantitatively predict and control the deposit properties. All three models have been validated with a thermal camera, quantification of α phase fraction and α lath width from SEM micrographs, and with experimentally acquired YS. The main conclusions are:

- Deposits with wire diameters of 1.1 and 1.6 mm exhibited higher cooling rates at the initial stage due to the heat sink effect of the larger substrate size than the deposit produced with a wire diameter of 0.8 mm. However, at the 10th layer, the higher heat accumulation with the large wire diameters of 1.1 and 1.6 mm compensated for the heat sink effect of the larger

substrate, and they showed similar cooling rates (about 130 K/s) compared to the deposit with a wire diameter of 0.8 mm.

- Columnar prior β grain structures were mainly observed in all deposits. An equiaxed grain structure was also observed on the edge due to heat accumulation that altered solidification conditions.

- The sensitivity analysis conducted on the different strengthening mechanisms of the yield strength prediction model shows that the decrease in strength was mainly due to the decrease in the contribution of the solid solution strengthening term and the Hell-Patch strengthening term.

6.6 Acknowledgements

6.7 References

[1] Brandl, E., Schoberth, A., & Leyens, C. (2012). Morphology, microstructure, and hardness of titanium (Ti-6Al-4V) blocks deposited by wire-feed additive layer manufacturing (ALM). Materials Science and Engineering: A, 532, 295-307.

[2] Saboori, A., Gallo, D., Biamino, S., Fino, P., & Lombardi, M. (2017). An overview of additive manufacturing of titanium components by directed energy deposition: microstructure and mechanical properties. Applied Sciences, 7(9), 883.

[3] Shaikh, M. O., Chen, C. C., Chiang, H. C., Chen, J. R., Chou, Y. C., Kuo, T. Y., Ameyama, K., & Chuang, C. H. (2020). Additive manufacturing using fine wire-based laser metal deposition. Rapid Prototyping Journal, 26(3), 473-483.

[4] Brandl, E., Palm, F., Michailov, V., Viehweger, B., & Leyens, C. (2011). Mechanical properties of additive manufactured titanium (Ti–6Al–4V) blocks deposited by a solid-state laser and wire. Materials & Design, 32(10), 4665-4675.

[5] Brandl, E., Baufeld, B., Leyens, C., & Gault, R. (2010). Additive manufactured Ti-6Al-4V using welding wire: comparison of laser and arc beam deposition and evaluation with respect to aerospace material specifications. Phys. Procedia, 5(Pt 2), 595-606.

[6] Mok, S. H. (2007). Deposition of Ti-6Al-4V using a high power diode laser and wire. Doctoral dissertation. University of Nottingham, Nottingham, UK.

[7] Chekir, N., Tian, Y., Gauvin, R., Brodusch, N., Sixsmith, J. J., & Brochu, M. (2018). Effect of travel speed and stress relief on thin Ti-6Al-4V laser wire deposits. Materials Science and Engineering: A, 724, 335-347.

[8] Kistler, N. A., Corbin, D. J., Nassar, A. R., Reutzel, E. W., & Beese, A. M. (2019). Effect of processing conditions on the microstructure, porosity, and mechanical properties of Ti-6Al-4V repair fabricated by directed energy deposition. Journal of Materials Processing Technology, 264, 172-181.

[9] Brandl, E., Michailov, V., Viehweger, B., & Leyens, C. (2011). Deposition of Ti–6Al–4V using laser and wire, part I: Microstructural properties of single beads. Surface and Coatings Technology, 206(6), 1120-1129.

[10] Shamsaei, N., Yadollahi, A., Bian, L., & Thompson, S. M. (2015). An overview of Direct Laser Deposition for additive manufacturing; Part II: Mechanical behavior, process parameter optimization and control. Additive manufacturing, 8, 12-35.

[11] Brandl, E., Michailov, V., Viehweger, B., & Leyens, C. (2011). Deposition of Ti–6Al–4V using laser and wire, part II: Hardness and dimensions of single beads. Surface and Coatings Technology, 206(6), 1130-1141.

[12] Thompson, S. M., Bian, L., Shamsaei, N., & Yadollahi, A. (2015). An overview of Direct Laser Deposition for additive manufacturing; Part I: Transport phenomena, modeling and diagnostics. Additive Manufacturing, 8, 36-62.

[13] Bambach, M., Sizova, I., Kies, F., & Haase, C. (2021). Directed energy deposition of Inconel 718 powder, cold and hot wire using a six-beam direct diode laser set-up. Additive Manufacturing, 47, 102269.

[14] Salminen, A. (2010). The filler wire-laser beam interaction during laser welding with low alloyed steel filler wire. Mechanics, 84(4), 67-74.

[15] Sims, H., Pegues, J., Whetten, S., Kustas, A. B., & Moore, D. (2023). Process-structure-property considerations for wire-based directed energy deposition of Ti-6Al-4V. Materials Characterization, 205, 113280.

[16] Chua, B. L., Lee, H. J., Ahn, D. G., & Kim, J. G. (2018). Influence of process parameters on temperature and residual stress distributions of the deposited part by a Ti-6Al-4V wire feeding type direct energy deposition process. Journal of Mechanical Science and Technology, 32, 5363-5372.

[17] Gibson, B. T., Bandari, Y. K., Richardson, B. S., Henry, W. C., Vetland, E. J., Sundermann, T. W., & Love, L. J. (2020). Melt pool size control through multiple closed-loop modalities in laser-wire directed energy deposition of Ti-6Al-4V. Additive Manufacturing, 32, 100993.

[18] DebRoy, T., Mukherjee, T., Wei, H. L., Elmer, J. W., & Milewski, J. O. (2021). Metallurgy, mechanistic models and machine learning in metal printing. Nature Reviews Materials, 6(1), 48-68.

[19] Tofail, S. A., Koumoulos, E. P., Bandyopadhyay, A., Bose, S., O'Donoghue, L., & Charitidis, C. (2018). Additive manufacturing: scientific and technological challenges, market uptake and opportunities. Materials today, 21(1), 22-37.

[20] Sikan, F., Wanjara, P., Gholipour, J., Kumar, A., & Brochu, M. (2021). Thermo-mechanical modeling of wire-fed electron beam additive manufacturing. Materials, 14(4), 911.

[21] Cao, J., Gharghouri, M. A., & Nash, P. (2016). Finite-element analysis and experimental validation of thermal residual stress and distortion in electron beam additive manufactured Ti-6Al-4V build plates. Journal of Materials Processing Technology, 237, 409-419.

[22] Parry, L., Ashcroft, I. A., & Wildman, R. D. (2016). Understanding the effect of laser scan strategy on residual stress in selective laser melting through thermo-mechanical simulation. Additive Manufacturing, 12, 1-15.

[23] Ahn, J., He, E., Chen, L., Wimpory, R. C., Dear, J. P., & Davies, C. M. (2017). Prediction and measurement of residual stresses and distortions in fibre laser welded Ti-6Al-4V considering phase transformation. Materials & design, 115, 441-457.

[24] Rae, W. (2019). Thermo-metallo-mechanical modelling of heat treatment induced residual stress in Ti–6Al–4V alloy. Materials Science and Technology, 35(7), 747-766.

[25] Mukherjee, T., Zhang, W., & DebRoy, T. (2017). An improved prediction of residual stresses and distortion in additive manufacturing. Computational Materials Science, 126, 360-372.

[26] Lundbäck, A., & Lindgren, L. E. (2011). Modelling of metal deposition. Finite Elements in Analysis and Design, 47(10), 1169-1177.

[27] Lindgren, L. E., Lundbäck, A., Fisk, M., Pederson, R., & Andersson, J. (2016). Simulation of additive manufacturing using coupled constitutive and microstructure models. Additive Manufacturing, 12, 144-158.

[28] Baykasoglu, C., Akyildiz, O., Candemir, D., Yang, Q., & To, A. C. (2018). Predicting microstructure evolution during directed energy deposition additive manufacturing of Ti-6Al-4V. Journal of Manufacturing Science and Engineering, 140(5), 051003.

[29] Irwin, J., Reutzel, E. W., Michaleris, P., Keist, J., & Nassar, A. R. (2016). Predicting microstructure from thermal history during additive manufacturing for Ti-6Al-4V. Journal of Manufacturing Science and Engineering, 138(11), 111007.

[30] Sun, W., Shan, F., Zong, N., Dong, H., & Jing, T. (2021). A simulation and experiment study on phase transformations of Ti-6Al-4V in wire laser additive manufacturing. Materials & Design, 207, 109843.

[31] Kelly, S. M. (2004). Thermal and microstructure modeling of metal deposition processes with application to Ti-6Al-4V. Doctoral dissertation. the Faculty of the Virginia Polytechnic Institute and State University, Blacksburg, Virginia, USA.

[32] Charles, C., & Järvstråt, N. (2008). Modelling Ti-6Al-4V microstructure by evolution laws implemented as finite element subroutines: Application to TIG metal deposition. Eighth International Conference on Trends in Welding Research (TWR), Pine Mountain, GA, June 1–6, pp. 477–485.

[33] Michaleris, P. (2014). Modeling metal deposition in heat transfer analyses of additive manufacturing processes. Finite Elements in Analysis and Design, 86, 51-60.

[34] Johnson, W. A. (1939). Reaction kinetics in process of nucleation and growth. Transactions of Transactions of the American Institute of Mining and Metallurgical Engineers, 135, 416-458.

[35] Avrami, M. (1939). Kinetics of phase change. I General theory. The Journal of chemical physics, 7(12), 1103-1112.

[36] Hayes, B. J., Martin, B. W., Welk, B., Kuhr, S. J., Ales, T. K., Brice, D. A., Ghamarian, I., Baker, A. H., Haden, C. H., Harlow, D. G., Fraser, H. L., & Collins, P. C. (2017). Predicting tensile properties of Ti-6Al-4V produced via directed energy deposition. Acta Materialia, 133, 120-133.

[37] Kar, S., Searles, T., Lee, E., Viswanathan, G. B., Fraser, H. L., Tiley, J., & Banerjee, R. (2006). Modeling the tensile properties in β-processed α/β Ti alloys. Metallurgical and materials transactions A, 37, 559-566.

[38] Ghamarian, I., Hayes, B., Samimi, P., Welk, B. A., Fraser, H. L., & Collins, P. C. (2016). Developing a phenomenological equation to predict yield strength from composition and microstructure in β processed Ti-6Al-4V. Materials Science and Engineering: A, 660, 172-180.

[39] Ghamarian, I., Samimi, P., Dixit, V., & Collins, P. C. (2015). A constitutive equation relating composition and microstructure to properties in Ti-6Al-4V: as derived using a novel integrated computational approach. Metallurgical and Materials Transactions A, 46, 5021-5037.

[40] Haden, C. V., Collins, P. C., & Harlow, D. G. (2015). Yield strength prediction of titanium alloys. Jom, 67, 1357-1361.

[41] Collins, P. C., Haden, C. V., Ghamarian, I., Hayes, B. J., Ales, T., Penso, G., Dixit, V., & Harlow, G. (2014). Progress toward an integration of process–structure–property–performance models for "three-dimensional (3-D) printing" of titanium alloys. Jom, 66, 1299-1309.

[42] Collins, P. C., Koduri, S., Welk, B., Tiley, J., & Fraser, H. L. (2013). Neural networks relating alloy composition, microstructure, and tensile properties of α/β-processed TIMETAL 6-4. Metallurgical and Materials Transactions A, 44, 1441-1453.

[43] AMS2901. (2014). Heat Treatment of Titanium Alloy Parts. SAE International, Warrendale, PA, USA.

[44] ASTM E8/E8M-15a. (2015) Standard Test Methods for Tension Testing of Metallic Materials, Annual Book of ASTM Standards, ASTM International, West Conshohocken, PA, USA.

[45] Zhang, Q., Sikan, F., Chekir, N., & Brochu, M. (2024). Thermo-Microstructural-Mechanical Modeling on Effect of Travel Speeds for Thin Ti-6Al-4V Deposits Developed by Laser Wire Deposition. Journal of Materials Research and Technology.

[46] Lütjering, G., Williams, J. C., Lütjering, G., & Williams, J. C. (2003). Titanium matrix composites (pp. 313-328). Springer Berlin Heidelberg.

[47] Kherrouba, N., Bouabdallah, M., Badji, R., Carron, D., & Amir, M. (2016). Beta to alpha transformation kinetics and microstructure of Ti-6Al-4V alloy during continuous cooling. Materials Chemistry and Physics, 181, 462-469.

[48] Sikan, F., Wanjara, P., Gholipour, J., & Brochu, M. (2023). Use of miniature tensile specimens for measuring mechanical properties in the steady-state and transient zones of Ti–6Al–4V wire-fed electron beam deposits. Materials Science and Engineering: A, 862, 144487.

[49] AMS 4999. (2016). Titanium Alloy Direct Deposited Products 6Al−4V Annealed. SAE International, Warrendale, PA, USA.

[50] Fan, W., Peng, Y., Wang, Y., Qi, Y., Feng, Z., Tan, H., Zhang, F., & Lin, X. (2024). Effect of grain boundary Widmanstätten α colony on the anisotropic tensile properties of directed energy deposited Ti-6Al-4V alloy. Journal of Materials Science & Technology, 184, 145-156.

[51] Carroll, B. E., Palmer, T. A., & Beese, A. M. (2015). Anisotropic tensile behavior of Ti–6Al–4V components fabricated with directed energy deposition additive manufacturing. Acta Materialia, 87, 309-320.

[52] Tian, X., Zhu, Y., Lim, C. V. S., Williams, J., Boyer, R., Wu, X., Zhang, K., & Huang, A. (2021). Isotropic and improved tensile properties of Ti-6Al-4V achieved by in-situ rolling in direct energy deposition. Additive Manufacturing, 46, 102151.

[53] Hunt, J. D. (1984). Steady state columnar and equiaxed growth of dendrites and eutectic. Materials science and engineering, 65(1), 75-83.

[54] Keist, J. S., & Palmer, T. A. (2016). Role of geometry on properties of additively manufactured Ti-6Al-4V structures fabricated using laser based directed energy deposition. Materials & Design, 106, 482-494.

[55] Dharmendra, C., Hadadzadeh, A., Amirkhiz, B. S., Lloyd, A., & Mohammadi, M. (2020). Deformation mechanisms and fracture of electron beam melted Ti–6Al–4V. Materials Science and Engineering: A, 771, 138652.

[56] Shrestha, S., Panakarajupally, R. P., Kannan, M., Morscher, G., Gyekenyesi, A. L., & Scott-Emuakpor, O. E. (2021). Analysis of microstructure and mechanical properties of additive repaired Ti–6Al–4V by Direct Energy Deposition. Materials Science and Engineering: A, 806, 140604.

Chapter 7: Effect of Oxygen Content on Thin Ti-6Al-4V Deposits by Laser Wire Deposition

Qi Zhang[1], Nejib Chekir[2] and Mathieu Brochu[1]*

[1]: Department of Mining and Materials Engineering, McGill University, 3610 University St., Montreal, QC, H3A 0C5, Canada

[2]: Liburdi Automation Inc., Dundas, ON L9H 7K4, Canada

This Chapter targets oxygen content as the studied variable because the YS model in Chapter 5 and 6 demonstrated that solid solution strengthening by interstitial oxygen was the highest contribution to the absolute total YS. Hence, three wire spools with varied oxygen contents were used to develop thin Ti-6Al-4V deposits. Structural development and mechanical properties were investigated. Dramatically increased tensile strength and hardness were found for deposits with increased oxygen content. Chapter 5 and 6 reported CET through the change of modified solidification conditions during deposition. This chapter investigates the effect of interruption during deposition on prior β grain morphology and CET. A combination of columnar and equiaxed prior β grains was observed after an interruption during deposition. This Chapter demonstrated that the interruption during deposition can change the solidification conditions and promote CET. This finding can provide another angle in achieving CET for DED titanium alloys components.

This Chapter was submitted to Journal of Alloys and Compounds. (JALCOM-D-24-14183)

7.1 Abstract

Six Ti-6Al-4V deposits with two geometries to enable the extraction of tensile coupons from the build direction (Z) and the travel direction (X), were produced by laser wire deposition (LWD). Three wires with different oxygen contents were selected for deposition. A combination of columnar and equiaxed macrostructures was observed through columnar to equiaxed transition (CET) due to the change in solidification conditions. The oxygen contents selected in this study produced negligible differences in the refinements of the prior β grains. It was found that an interruption during the deposition process altered the solidification conditions and promoted CET. Dramatically increased tensile strength and hardness were found for deposits with increased oxygen content. The constitutive equations including the major strengthening mechanisms were used to predict the yield strength of Ti-6Al-4V and to analyze the contributions of various strengthening mechanisms. Solid solution strengthening by the addition of oxygen was found to be the major contribution to the yield strength enhancement.

7.2 Introduction

Additive Manufacturing (AM) has provided unprecedented opportunities for producing near-net-shape components in a layer-by-layer fashion, resulting in large cost savings compared to conventional subtractive manufacturing methods. [2] One of the AM technologies, directed energy deposition (DED), allows parts to be built by simultaneously feeding the melt pool with a focused heat source and materials. In fact, DED can be categorized based on the heat sources (laser, electron beam, arc plasma, etc.) and feeding materials (wire or powder) employed. Compared with powder-fed processes, wire-fed processes have great advantages such as high deposition rate, reduced contamination, and high material quality and repeatability. [3-5] One of the common materials utilized with DED is Ti-6Al-4V, an alloy widely used in the aerospace industry because it demonstrates a high strength-to-weight ratio, excellent corrosion resistance, and high fracture toughness. [6-7]

Unfortunately, large anisotropies tend to exist in the macrostructures and mechanical properties of AM Ti-6Al-4V components. Due to a high thermal gradient (G), the typical macrostructure of the DED-built Ti-6Al-4V alloy is characterized by columnar prior β grains. Various solutions that

promote a columnar-to-equiaxed transition (CET) to minimize grain anisotropy have been proposed to solve this problem.

The addition of chemical grain refiners is a promising solution to promote CET and minimize grain anisotropy. In recent decades, significant research efforts have been made to investigate the effects of various solutes on the microstructure and mechanical properties of titanium alloys. [8-46] Notable solutes in the titanium system include Be, B, Si, C, O, N, Fe, and Cr. [8] These solutes can provide a population of potent heterogeneous nuclei and significantly retard the growth of the solid by lowering the local liquidus temperature. Gil et al. [15], for example, investigated the grain growth kinetics of titanium alloys with different oxygen contents. They found that grain growth kinetics, activation energy for grain growth and mechanical strength increase with increasing oxygen content. Moreover, Bermingham et al. [9] reported that the grain size of as-cast titanium alloys decreased with increasing oxygen content. In fact, it is well documented [17-23] that the addition of oxygen can dramatically enhance the strength and hardness of titanium alloys via solid solution strengthening. Sun et al. [17] calculated the reinforcement effect of oxygen solid solution to be 769.8 MPa/mass % [O] on 0.2 % YS. Kwasniak et al. [22] have systematically investigated the intrinsic mechanisms of solid solution strengthening in α-Ti by various elements. They reported that the robust strengthening of the Ti-O solution is attributed to interstitial oxygen that suppresses dislocation emission in all slip modes by enhancing the maximum restoring forces and stacking faults energies. [22] Besides, the addition of oxygen solute can increase the lattice parameters (c/a ratio) and restrict the number of slip planes, thus enhancing the tensile strength of titanium alloys. [20] However, the ductility can be severely reduced by very small amounts of oxygen. Yan et al. [24] estimated a threshold oxygen content of 0.22 wt. % in AM Ti-6Al-4V, after which the material exhibits complete brittleness. To address this issue, Halisch et al. [25] investigated how a shielding gas chamber with different oxygen content levels affected the embrittlement of AM Ti-6Al-4V parts. Despite these efforts, little research has been conducted to systematically investigate the effect of different oxygen contents of the wire feedstock on Ti-6Al-4V components fabricated by the wire-fed DED process.

Modifying the solidification conditions during the deposition process is another solution to promote CET. [26-28] This can be achieved by altering processing parameters and deposition strategies. Zhang et al. [26], for example, attempted to achieve CET by periodically alternating the processing parameters. While Wang et al. [27] reported that decreasing the welding current has a drastic

influence on the percentage of equiaxed β grains. Adjustments and interruptions during deposition are also likely to alter the solidification conditions and promote CET during the DED process. [28] Unfortunately, little research has been conducted to understand the effect of interruption during deposition on the CET.

This research aims to fill this knowledge gap by fabricating Ti-6Al-4V parts by laser wire deposition (LWD) using wire spools with different oxygen contents to better understand the effect of oxygen content on the microstructure and mechanical properties. The effect of interruptions during deposition on the CET is also discussed.

7.3. Materials and Methods

7.3.1 Sample Fabrication

Six single-bead thin wall coupons were fabricated using a LAWS 1000[TM] wire-fed automated deposition system (Liburdi, Canada) equipped with an IPG Yb:YAG fiber laser reaching up to 1 kW power. An inert argon environment with oxygen levels below 60 ppm was adapted during deposition to prevent oxidation. Wrought Ti-6Al-4V plates were used as substrates. Three Ti-6Al-4V wire spools with different oxygen contents were used for deposition. Table 7.1 presents the chemical compositions of these Ti-6Al-4V wire spools. Depending on the oxygen content, they are labeled as O - 0.05 wt. %, O - 0.067 wt. %, and O - 0.16 wt. %. Two different geometries were adapted to accommodate tensile specimen extractions in the build direction (Z) and the travel direction (X). The first deposit geometry (denoted as Z) is 55 mm in width and 120 mm in height. The other deposit geometry (denoted as X) is 110 mm in width and 75 mm in height. All deposits were produced with a travel speed of 6.4 mm/s. Figure 7.1 shows the picture of O – 0.16 wt. % deposits in the Z and X directions. Deposits were subsequently used for stress relief (SR) heat treatment, microstructure characterization, and mechanical property evaluation.

[21]Table 7.1. Chemical composition (wt. %) of Ti-6Al-4V wire spools used in the study.

Company	Al	V	Fe	C	O	N	H	Y	Ti
Astrolite	6.30	4.08	0.13	0.02	0.05	0.004	0.003	<0.005	Balance
Astrolite	6.24	3.98	0.098	0.0018	0.067	0.0028	0.0018	-	Balance
Dynamet	6.10	3.82	0.17	0.025	0.16	0.0087	0.0012	<0.0005	Balance
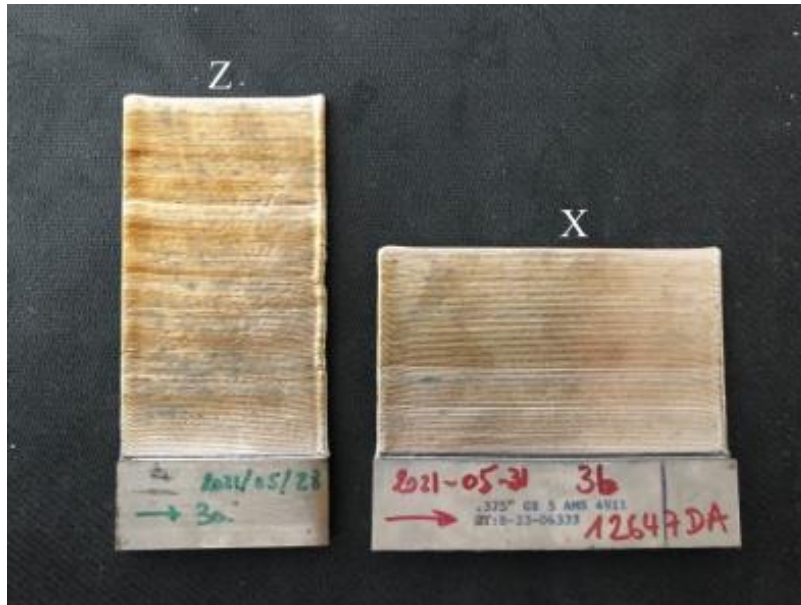
[71]Figure 7.1. O – 0.16 wt. % deposits in the Z and X directions.

7.3.2 Material Characterization and Testing

Inert gas fusion was employed according to ASTM E1409-13 [29] to analyze the oxygen content using an ONH836 Oxygen/Nitrogen/Hydrogen Elemental Analyzer (Horiba Ltd., Japan). Three samples of at least 1 gram in weight were extracted along the build height: bottom (10 mm from the substrate), center (55 mm from the substrate for Z deposits and 35 mm from the substrate for X deposits), and top (100 mm from the substrate for Z deposits and the 60 mm from substrate for X deposits).

A SR cycle, held at 593 °C for 2 hours followed by furnace cooling according to AMS2901 [30], was performed to reduce residual stresses from the deposition process while keeping the structural features.

Metallographic evaluations were conducted for all deposits in the center region mentioned above. After mounting in bakelite, samples were ground from 400 SiC grit up to 1200 SiC grit, followed by polishing with 1 μm diamond suspension and a finish with 0.05 μm colloidal silica. A Kroll's Reagent etchant with 91 % deionized water (H_2O), 6 % nitric acid (HNO_3), and 3 % hydrofluoric acid (HF) was then used on the mounted samples to reveal the structural features. Metallography and fractography were observed using a VHX-7000 series digital microscope (Keyence, Canada)

and a SU-3500 cold field SEM (Hitachi, Ltd., Japan). The inverse pole figure (IPF) maps of the $\alpha +$ β phases of the O – 0.16 wt. % deposit built in the X direction was analyzed by electron back-scattered diffraction (EBSD) using a Hitachi SU3500 tungsten filament scanning electron microscope (SEM) (Hitachi, Tokyo, Japan) with operating conditions of 15 kV voltage and 5 µm step size. The parent phase reconstruction was performed using AZtecCrystal software (Oxford instruments plc, UK).

Vickers hardness was measured using a Clark Microhardness (CM-100AT) indenter (Sun-Tec Corporation, USA) under a 100 g load. Each reported value is the average of three measurements along the same layer.

A 600 DX (Instron®, USA) universal testing frame with a calibrated load cell and extensometer was used to test tensile properties including yield strength (YS), ultimate tensile strength (UTS), and elongation. Machined subsize specimens according to ASTM E8 [31] with a thickness of about 2 mm, a gauge width of 6 mm, and a gauge length of 25 mm have been extracted from SR plates. Four tensile coupons were extracted from each Z deposit and five tensile coupons were extracted from each X deposit. They were tested at room temperature at a strain rate of 0.005 in/min to yield and 0.05 in/min after yield to fracture. After the fracture, the cross-section of the fracture surface was characterized and analyzed using a SU-3500 cold field SEM as mentioned above.

7.3.3 Statistical Analysis

One-way analysis of variance (ANOVA) and Tukey's *post hoc* analysis were adapted to determine the statistical difference in grain size, microhardness, YS, UTS, and elongation among all deposits ($\alpha = 0.05$). The analysis was performed using the one-way ANOVA application in Origin Pro 2024 software (Origin Lab, USA).

7.4. Results and Discussion

7.4.1 Measured Oxygen Contents from Inert Gas Fusion

Figure 7.2 presents the measured oxygen contents along the build height for all deposits produced with different oxygen contents in the Z and X directions. The oxygen solutes are homogeneously distributed along the build height for all deposits with a maximum difference of no more than 0.01

wt. % O. The measured oxygen contents are in good agreement with the specifications of the wire feedstocks, indicating no oxygen pick-up during the deposition process. It is well documented [19] that the reactivity of Ti-6Al-4V with oxygen increases at temperatures above 550 °C and the α-case oxidation product can cause embrittlement of the alloy. Halisch et al. [25] reported that when the oxygen content in the shielding gas chamber is above the chemical requirements of the ASTM titanium grade 5 standard [32], the oxygen contents in the part increase compared to the wire feedstock. In this study, all deposits were produced in an inert argon environment with oxygen levels below 60 μg/g. Since the wire spools used for O – 0.05 wt. % and O – 0.067 wt. % deposits contain similar oxygen contents (Figure 7.2), the measured oxygen contents appear to be statistically similar.
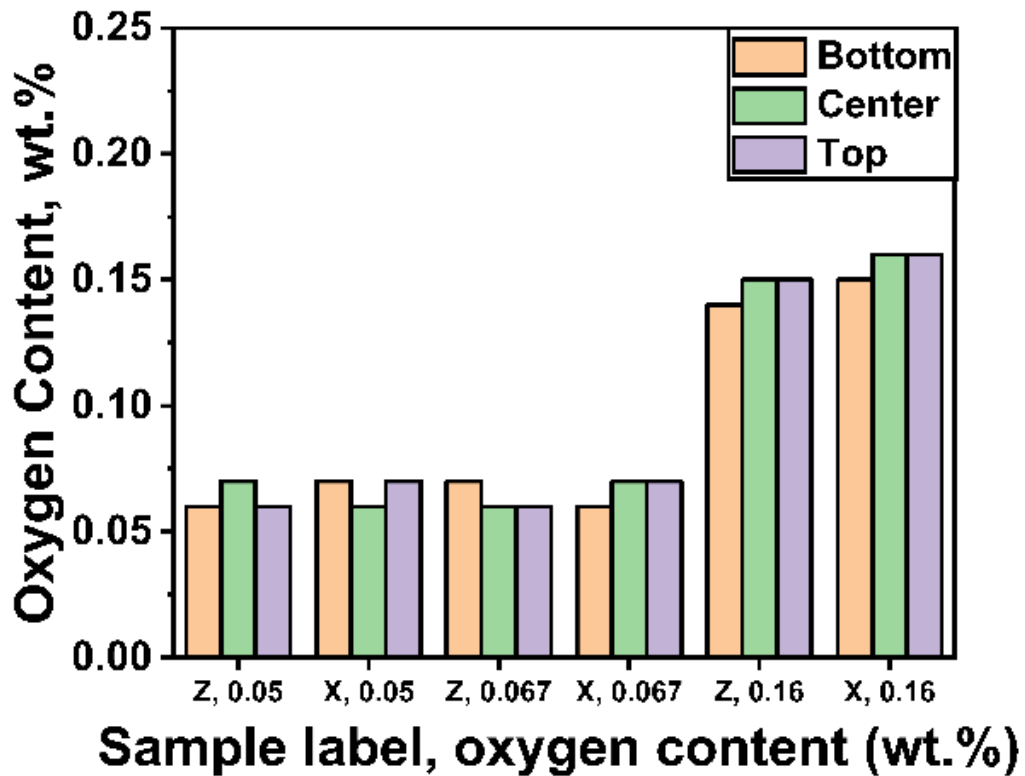
[72]Figure 7.2. Oxygen contents at different heights for all deposits.

7.4.2 Structure Evaluation

7.4.2.1 Macrostructure

Figure 7.3 presents the macrostructure of all deposits built with different oxygen contents in the Z and X directions. The macrostructure is mainly decorated with columnar β grains due to the high G generated in LWD processes. However, some percentage of equiaxed grains can be observed through CET. In fact, the morphology of the structure is mainly decided by two critical parameters, G and the growth rate R, which can promote CET through two possible mechanisms. The first one is related to the solidification conditions, which can be altered to promote CET. For example, due to the complicated thermal history of the deposition process, Figure 7.3 shows that equiaxed grains can be observed at the edges of all deposits due to heat accumulation, which promoted CET. The second mechanism is due to the potent growth-restricting solutes present in titanium systems. They tend to promote CET from two principal approaches [8]: 1) a population of heterogeneous nuclei that enables the heterogeneous nucleation at small constitutional undercooling (CU) below the liquidus point. They can provide more nucleation sites and thus a smaller grain size; 2) the addition can impede the further growth of the primary solid by lowering the liquidus temperature and increasing the CU zones. This promotes heterogeneous nucleation and reduces the grain size, which promotes CET.

In this study, the differences in oxygen contents demonstrate negligible morphological differences in the macrostructure. Figure 7.3 shows that as the oxygen content increases, the percentage of equiaxed grains does not necessarily increase. In comparison, Bermingham et al. [12] reported significant prior β grain size refinements with increasing oxygen contents up to 0.22 wt. %. Gil et al. [15], on the other hand, investigated the effect of different oxygen contents on the grain growth kinetics of commercially pure titanium heat treated at different temperatures and times and reported significant grain size refinement at 1.05 wt. % oxygen content. In this study, the oxygen content (0.15 wt. %) is not sufficient to induce grain refinement. The complicated solidification conditions play a major role in affecting the final morphology of prior β grains. During the deposition process, interruptions due to process parameters adjustments can also alter the solidification conditions and promote CET. This will be discussed in detail in the next section.

Table 7.2 lists the measured prior β grain sizes for different oxygen contents. The ANOVA analysis reported that prior β grain sizes are statistically similar ($p>0.05$) among deposits with different

oxygen contents. Since the same sets of process parameters were used for all deposits, similar cooling rates were expected for all deposits.
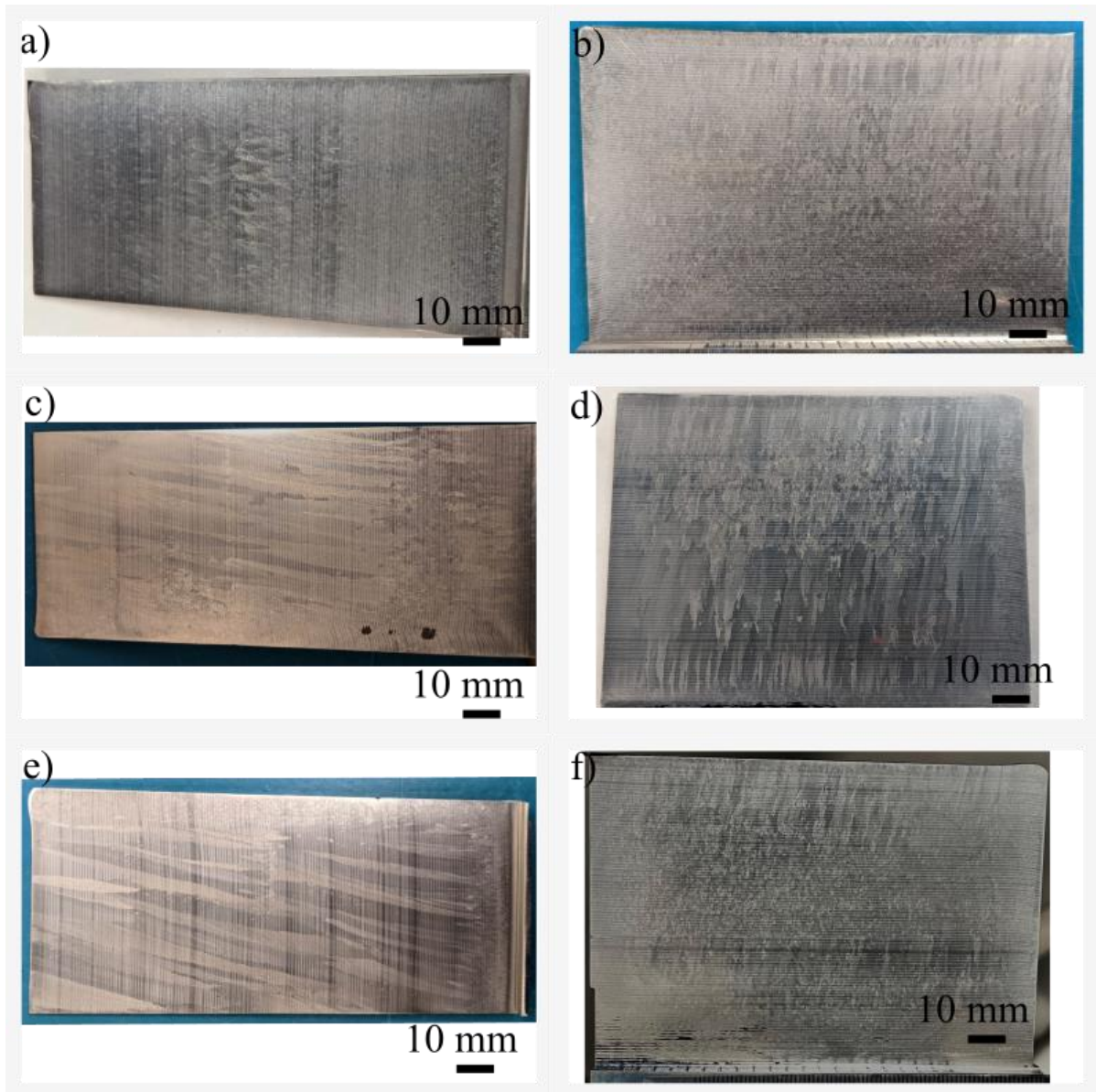
[73]Figure 7.3. (a, c, and e) The macrostructure of Ti-6Al-4V deposits built in the Z direction for O - 0.05 wt. %, O - 0.067 wt. %, and O - 0.16 wt. %, respectively, and (b, d, and f) the macrostructure of Ti-6Al-4V deposits built in the X direction for O - 0.05 wt. %, O - 0.067 wt. %, and O - 0.16 wt. %, respectively.

[22]Table 7.2. Columnar prior β grains widths for different oxygen contents.

Sample Label/ Oxygen Contents	O - 0.05 wt. %	O - 0.067 wt. %	O - 0.16 wt. %

Z	1.0 ± 0.4 mm	1.7 ± 0.5 mm	1.5 ± 0.7 mm
X	1.1 ± 0.5 mm	1.1 ± 0.6 mm	0.8 ± 0.4 mm

7.4.2.2 Investigation of the Formation of the Solidification Structure

A representative solidification structure of the O – 0.16 wt. % Ti-6Al-4V deposit built in the X direction was selected for this section. Figure 7.4(a) presents the macrostructure in a combination of both columnar and equiaxed structures. Davis et al. [33] reported that the formation of the equiaxed structure can be achieved through twining at a high wire feed rate (52.9 mm/s) for Ti-6Al-4V deposits produced by wire-arc additive manufacturing (WAAM). They found that the curvature of the fusion boundary can promote twining during deposition. In addition, high wire feed rates promoted this phenomenon by reducing the remelting depth and altering the melt-pool geometry. To investigate if the observed equiaxed structures were formed through the twinning mechanism, EBSD was conducted on the areas associated with equiaxed structures. Figure 7.4 presents the reconstructed β phase EBSD maps of the areas associated with equiaxed structures. The common β phase twinning boundary relationships ($51°$ rotation around $< 110 >_\beta$ (green) and $60°$ around $< 111 >_\beta$ (red)) suggested by Davis et al. [33] were highlighted. It can be seen that no twinning boundary is observed. This could be due to the low wire feed rate (26.67 mm/s) used in this study. Even if there were equiaxed grains formed through twinning, the chance of observing the twinning boundary is low as they would be wiped out by the remelting of the subsequent layers. These twinning systems are more often observed in metastable-β titanium alloys due to the formation of ω phase [34]. From literature studies [33-34], the dendrite twinning during solidification was hardly documented in titanium alloys. However, previous work [35] on other BCC metals (aluminum) shows that twins tend to occur during solidification with high thermal gradients ($G > 10^3$ K/m) and growth rates ($R > 10^{-3}$ m/s). The WAAM process used by Davis et al. [33] has a higher G than the LWD process and is more likely to develop twin structures. Donoghue et al. [34] also observed twinning in the Ti-6Al-4V deposits fabricated by high deposition rate WAAM with in-process deformation and attributed this to the rapid re-heating of the deformed WAAM microstructure.
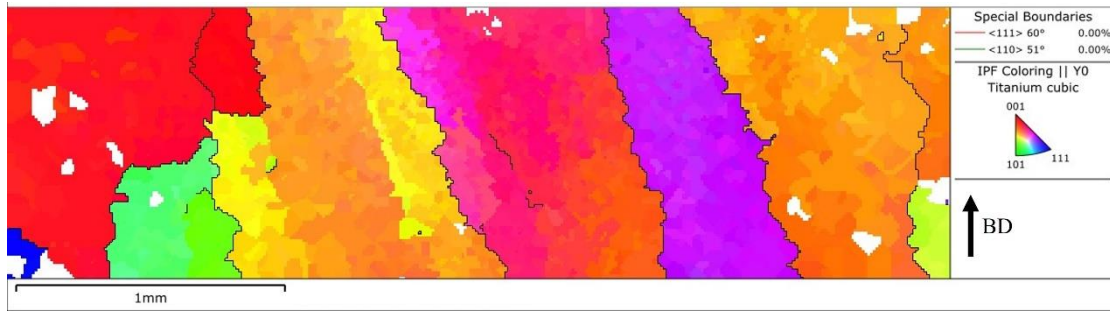
[74]Figure 7.4. Reconstructed β phase EBSD maps of the areas associated with equiaxed structures with the common β phase twinning boundary relationships (51° rotation around $< 110 >_\beta$ (green) and 60° around $< 111 >_\beta$ (red)) highlighted.

Besides, the morphology of solidification structures can also be determined by G and R. Therefore, to confirm the solidification structure of this region, G and R were calculated at several locations as labeled in Figure 7.5 (a) with different symbols. G can be calculated using Equation 7-1:

$$G = {\Delta T}/{\Delta x} \qquad \text{Equation 7-1}$$

where ΔT (K) is the temperature difference along the travel direction between the center and the tail of the melt pool and Δx (cm) is the distance between these two points. The solidification cooling rate, CR, was calculated using Equation 7-2:

$$CR = {\Delta T}/{\Delta t} \qquad \text{Equation 7-2}$$

where ΔT (K) and Δt (s) is the temperature and time difference at the solidification temperature. Then, R (cm/s) can be calculated by Equation 7-3:

$$R = {CR}/{G} \qquad \text{Equation 7-3}$$

The calculated data were then compared with a solidification map for Ti-6Al-4V [28] to predict the solidification structures. It could be seen that most of the points fell on the mixed region explaining the observed equiaxed structure. In addition, it could be seen that a lower G was observed with the increase of the layers due to the heat accumulation. For example, G at the 26th layer was lower than

the 24th layer and the solidification structure was switching to the full columnar region. The 99th layer had the lowest G due to the highest heat accumulation.
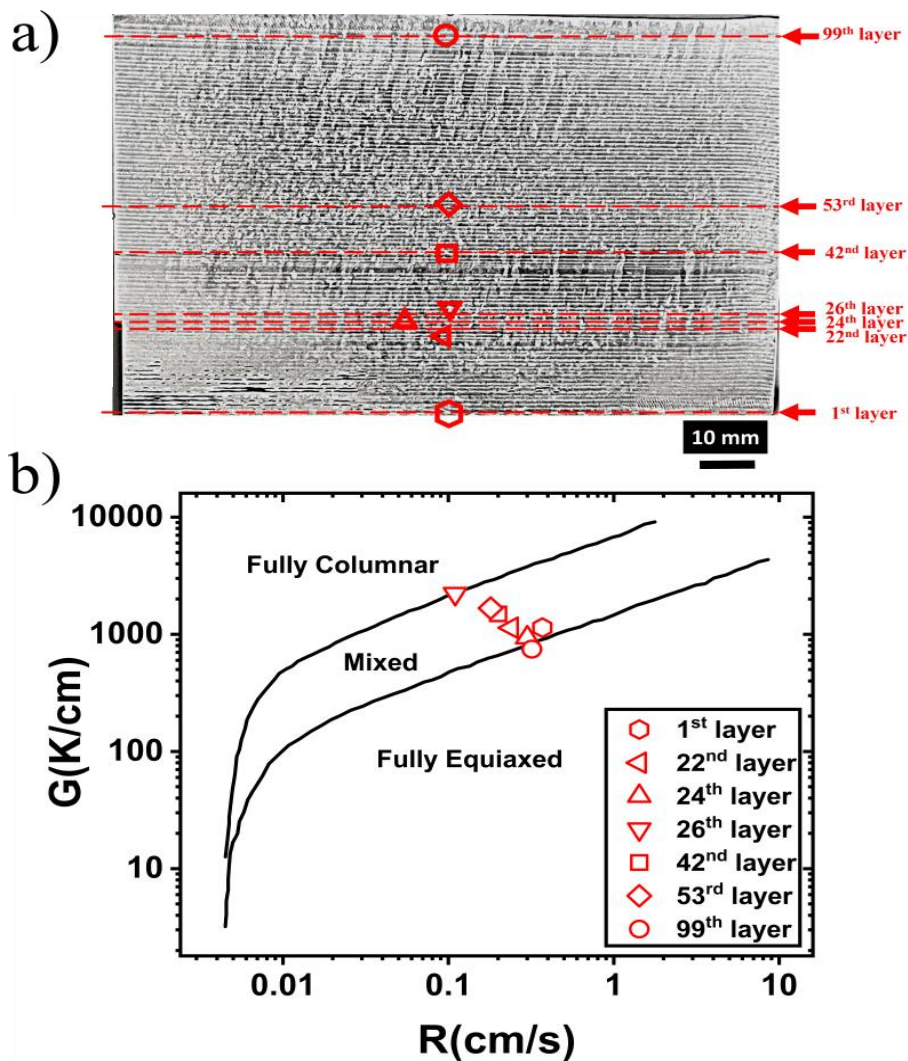
[75]Figure 7.5. (a) Solidification structure with interruptions labeled as blue and green. The locations where G and R were calculated were labeled by the corresponding symbols. (b) The comparison between the calculated G and R values from different locations of the deposits shown in (a) and the Ti-6Al-4V solidification map [28].

7.4.2.3 Microstructure

Figure 7.6 presents the SEM micrographs for all deposits with different oxygen contents built in the Z and X directions. During cooling upon β-transit temperature, the α phase starts to nucleate at β grain boundaries following the Burgers Orientation Relationship (BOR), where the most densely packed planes of the body centred cubic (BCC) β phase {110} transform to the basal planes {0001}

of the hexagonal close packed (HCP) α phase. A typical basketweave microstructure was observed in all deposits due to the high cooling rates experienced in the LWD process. Table 7.3 shows the measured α lath widths for all deposits. The ANOVA analysis shows that α lath widths are statistically similar ($p>0.05$) among deposits produced with different oxygen contents. This agrees well with the previous measurements of prior β grain sizes in macrostructure (section 7.4.2.1) as similar thermal histories were experienced.
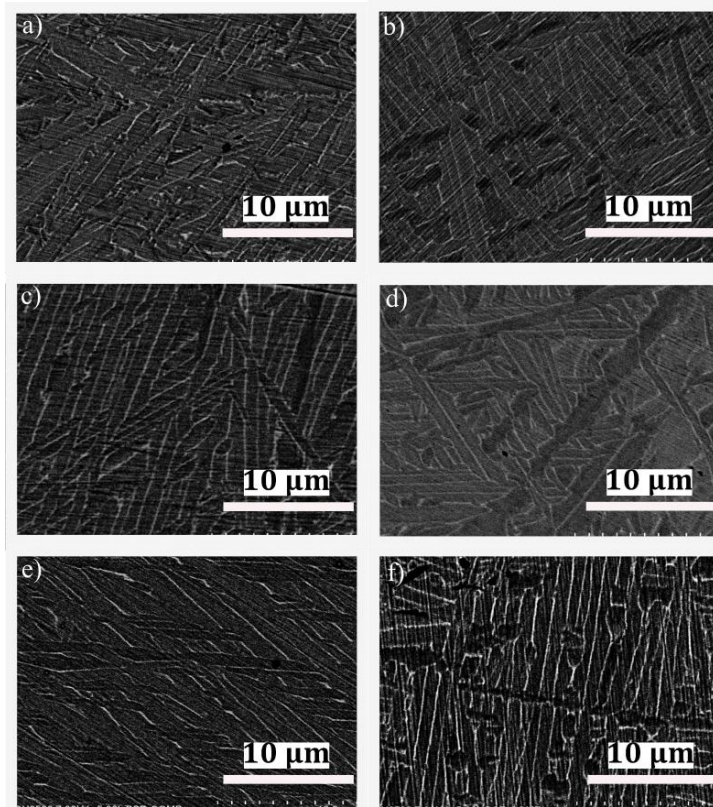
[76]Figure 7.6. (a, c, and e) The microstructure of Ti-6Al-4V deposits built in the Z direction for O - 0.05 wt. %, O - 0.067 wt. %, and O - 0.16 wt. %, respectively. (b, d, and f) The microstructure of Ti-6Al-4V deposits built in the X direction for O - 0.05 wt. %, O - 0.067 wt. %, and O - 0.16 wt. %, respectively.

[23]Table 7.3. α lath widths for all deposits produced with different oxygen contents.

Sample Label/ Oxygen Contents	O - 0.05 wt. %	O - 0.067 wt. %	O - 0.16 wt. %
Z	$0.69 \pm 0.18 \ \mu$m	$0.74 \pm 0.20 \ \mu$m	$0.77 \pm 0.19 \ \mu$m

X	$0.69 \pm 0.14 \mu$m	$0.67 \pm 0.15 \mu$m	$0.69 \pm 0.17 \mu$m

7.4.3 Mechanical Properties

7.4.3.1 Microhardness

Figure 7.7 presents the microhardness values measured at different build heights for samples produced with different oxygen contents in the Z and X directions. Higher microhardness was observed at the interface due to the finer microstructure. This is because a higher cooling rate was experienced at the interface as the cold substrate acted as a heat sink and there was no heat accumulation when the deposition started. The ANOVA analysis shows that the microhardness is statistically different ($p<0.05$) between the O - 0.16 wt. % deposits and the O – 0.05 wt. % deposits and the O – 0.067 wt. %. The microhardness of the O – 0.05 wt. % deposits and the O – 0.067 wt. % deposits are statistically similar ($p>0.05$). A dramatic increase in microhardness is observed with increasing oxygen contents (333 HV/wt. % O). Sun et al. [17] also reported a dramatic reinforcement effect of oxygen on hardness, which was calculated to be 287.9 HV/wt. % O. The dramatic improvement in hardness by solute oxygen is attributed to the increase in lattice parameters (c/a ratio), which restricts the number of slip systems in HCP α-Ti [20-21].
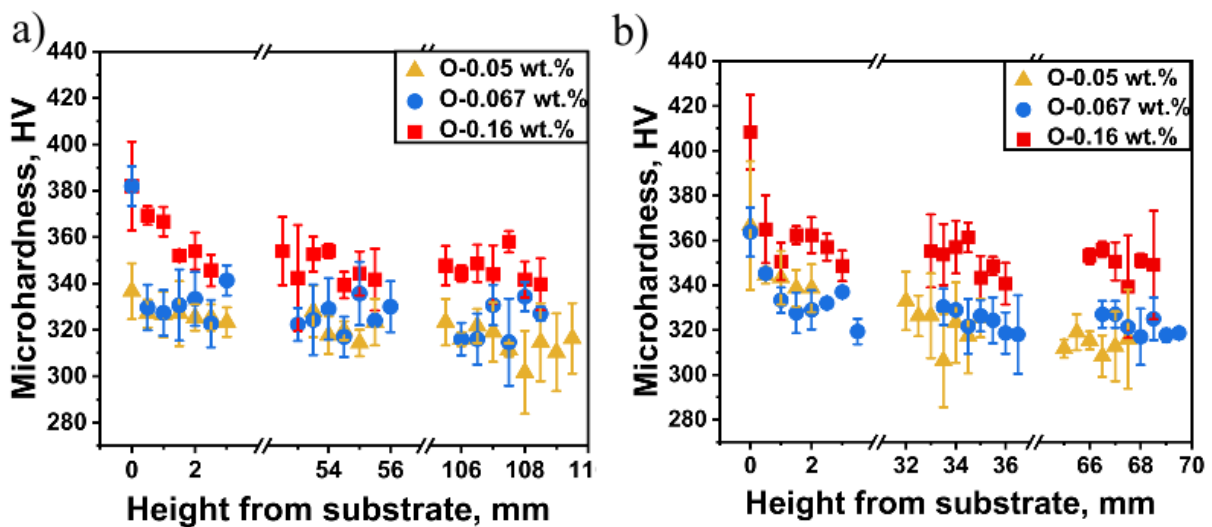
[77]Figure 7.7. (a) Microhardness at different heights for deposits built in the Z direction. (b) Microhardness at different heights for deposits built in the X direction.

7.4.3.2 SR Static Tensile Properties

Figure 7.8 presents the room temperature static tensile properties of the SR tensile specimens for all oxygen contents in comparison with the minimum tensile requirements for DED Ti-6Al-4V according to AMS 4999 [36]. As can be seen, all tensile results are above the minimum tensile requirements. The ANOVA analysis shows that the tensile strengths are statistically different ($p<0.05$) for all deposits produced between the Z and X directions. This indicates that all deposits exhibit anisotropic tensile strength, where tensile coupons extracted from the Z direction show lower tensile strengths (i.e. 896 MPa on average on 0.2 % YS for the O - 0.16 wt. % Z-deposit) than those from the X direction (i.e. 949 MPa on average on 0.2 % YS for the O - 0.16 wt. % x-deposit). The anisotropic strength has been well investigated [37-40] for AM Ti-6Al-4V parts and can be attributed to two major mechanisms: 1) the texture difference, where the strong texture of β phase generates a strong α texture obeying the BOR, which produces a difference in the critical resolved shear stress (CRSS) along different loading directions; and 2) the morphology of the columnar β grain, where the tensile strength of samples along the build direction Z was reduced according to the Hall-Petch relationship. However, the ANOVA analysis shows that the elongations are statistically similar ($p>0.05$) for all deposits produced between Z and X directions. The anisotropic elongation was attributed to the presence of grain boundary α on prior β grain boundary, which reduces the elongation by furnishing a preferential path for damage accumulation along the prior β grain boundary. However, the macrostructure (section 7.4.2.1) shows equiaxed grain structures through CET, which has weakened this effect. No anisotropic elongation was observed in this study.

The ANOVA analysis shows that the tensile strengths are statistically different ($p<0.05$) between the O - 0.16 wt. % deposits and the O – 0.05 wt. % deposits and the O – 0.067 wt. %. The tensile strengths of the O – 0.05 wt. % deposits and the O – 0.067 wt. % deposits are statistically similar ($p>0.05$). The tensile strength was dramatically increased even with a small increase in oxygen content (733 MPa/wt. % [O] on 0.2 % YS and 822 MPa/wt. % [O] on UTS). The deposits produced with O - 0.05 wt. % and O - 0.067 wt. % show similar tensile strengths as the measured oxygen contents are at a similar level as mentioned in the section about measured oxygen contents from inert gas fusion (section 7.4.1). The dramatic strengthening effects of oxygen solutes in titanium alloys are well documented in the literature [17-23]. Sun et al. [17] calculated the solid solution strengthening effect of oxygen to be 769.8 MPa/mass % [O] on 0.2 % YS. Wei et al. [18] reported that the UTS of e Ti–22.5Nb–0.7Ta–2Zr alloy is increased by 40 % over that of the original alloy

when the oxygen content is increased to 1.0 wt. %. Oxygen can fit well into the octahedral vacancy of α-Ti because it shares a similar radius (about 0.06 nm). [19] The lattice parameter (c/a ratio) of pure Ti and Ti alloys is reported to increase with an increase of the oxygen content. [20-21] This increases the strength by limiting the number of slip planes in the HCP structure. Kwasniak et al. [22] calculated restoring forces and stacking fault energies of pure Ti and Ti-O alloys from first principles and reported a dramatic enhancement with interstitial oxygen solutes, which improved solid solution strengthening by suppressing dislocation emission in all slip modes. Moreover, Yu et al. [23] compared the size of the screw dislocation core between Ti-0.1 wt. % O and Ti-0.3 wt. % O with high-resolution TEM, and reported that the displacement field is more tightly confirmed to the core with an average width of ~0.5 nm in width for Ti-0.3 wt. % O as the increased oxygen content resulted in a strong pinning effect on screw dislocations. However, the ductility can be severely reduced even at very low oxygen levels. This is due to the limitation of the basal, prismatic and pyramidal dislocation nucleation caused by the structure stiffening provided by the Ti–O bonds that prevents extensive atomic relaxation. [21] In this study, the deposits with increased oxygen content still present excellent elongation. However, the O - 0.067 wt. % deposit produced in the X direction exhibits reduced elongation, which is explained in the next section.
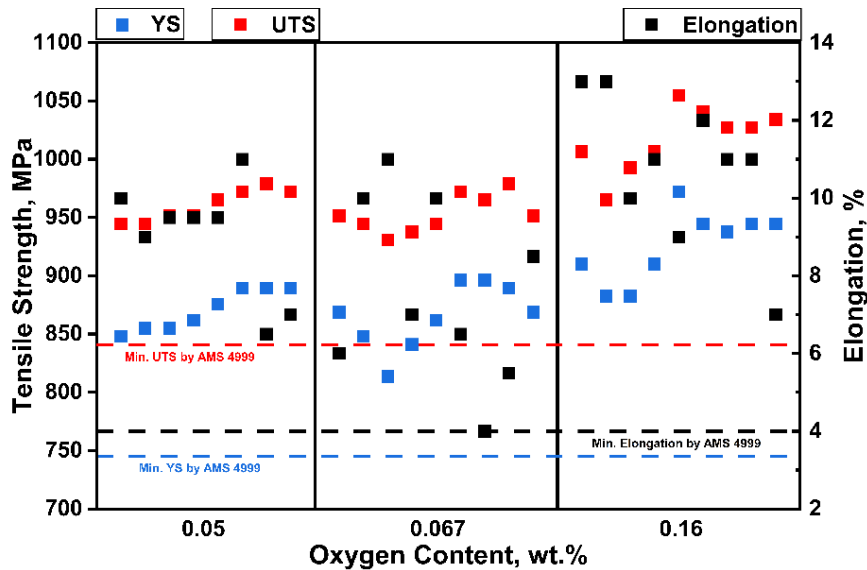
[78]Figure 7.8. YS, UTS, and elongation of all tensile coupons varied in oxygen contents. The minimum tensile requirements for DED Ti-6Al-4V set by AMS 4999 [36] are noted by dashed lines.

7.4.3.3 Contributions of Different Strengthening Mechanisms for Absolute Yield Strength

Hayes et al. [41] have reported constitutive equations to predict the YS of DED Ti-6Al-4V. These equations were developed using a hybrid ANN (Artificial Neural Network)/GA (Genetic

Algorithms) on a database with inputs of quantified microstructure features including α/β phase fractions, α/β lath width, α colony size, α/β basketweave fraction, chemical composition, etc. These equations incorporate a) the intrinsic flow stress of hcp α and bcc β phases, b) solid solution strengthening of hcp α by O and Al, c) solid solution strengthening of bcc β by V and Fe, d) and e) Hall-Patch strengthening, and f) Taylor hardening to include the strengthening effect of the basketweave morphology:

$$\sigma_{ys} = F_V^\alpha * 89 + F_V^\beta * 45 + \qquad \text{a)}$$

$$F_V^\alpha * (149 * x_{Al}^{0.667} + 759 * x_O^{0.667}) + \qquad \text{b)}$$

$$F_V^\beta * ((22 * x_V^{0.7})^{0.5} + (235 * x_{Fe}^{0.7})^{0.5})^2 + \qquad \text{c)} \qquad\qquad \text{Equation 7-4}$$

$$F_V^{Col} * 150 * (t_{\alpha-lath})^{-0.5} * (t_{\beta-rib})^{0.5} + \qquad \text{d)}$$

$$F_V^{Col} * 125 * (t_{Col})^{-0.5} + \qquad \text{e)}$$

$$F_V^{BW} \alpha M G b \sqrt{\rho} \qquad \text{f)}$$

where F_V represents the volume fraction of certain phases (i.e. α, β), x_B represents the concentration of element B (i.e. Al, O, Fe, V), t_i represents the thickness of the given feature (i.e., the α lath, β lath, the colony width), α is the prefactor term (set to 1), M is the Taylor factor, which is typically between 2.0 and 3.2 for hcp α, G is the shear modulus of titanium (44 GPa), b is the Burgers vector (0.3 nm), and ρ is the dislocation density.

These equations were used in this study to understand the contributions of different strengthening mechanisms to the total YS. Figure 7.9(a) presents the comparison between predicted and experimental YS. They are in good agreement with a deviation of below 10 %. Figure 7.9(b) presents the contributed strengths from different strengthening mechanisms for all deposits produced with different oxygen contents. It can be seen that the major differences in absolute YS are due to the solid solution strengthening by the oxygen solute (up to 100 MPa). No significant difference is found for other strengthening terms as the developed microstructure is similar due to the similar thermal history generated under the same set of processing parameters.
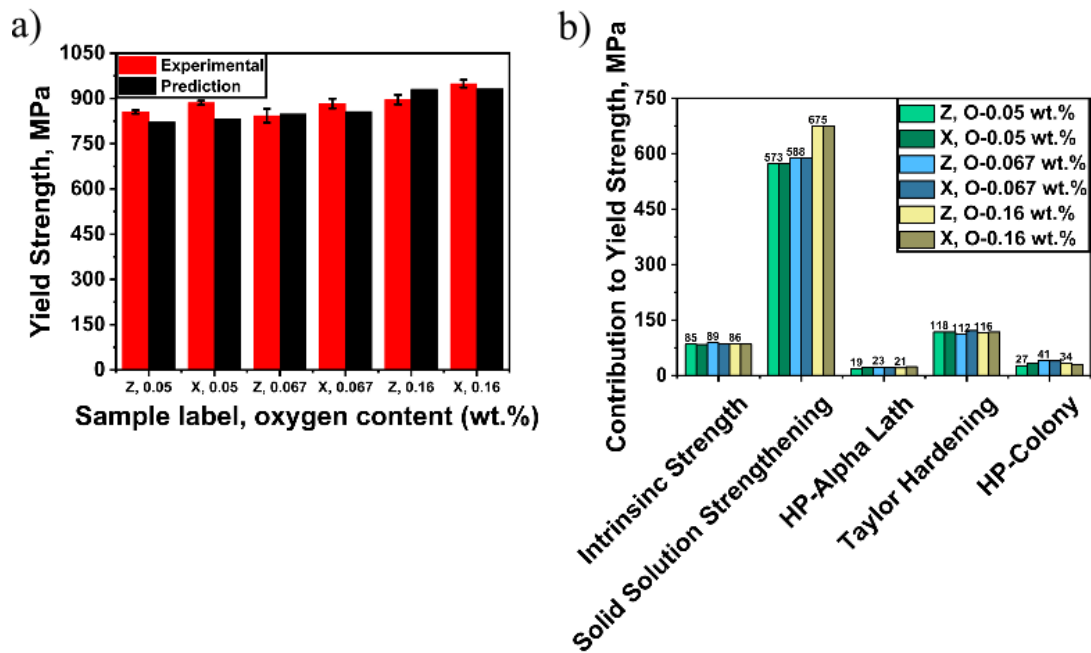
[79]Figure 7.9. (a) Comparison between experimental and predicted cooling rates for all oxygen contents. (b) The contribution of the individual terms to the absolute yield strength for different oxygen contents.

7.4.3.4 Fracture Mechanisms

Figure 7.10 presents the SEM micrographs of the fracture surfaces for all tensile coupons built with different oxygen contents in the Z and X directions. The fracture surface is mainly occupied by fine and deep dimple structures, indicating microvoid accumulation fracture for high ductility in titanium alloys for all deposits except the sample built with O - 0.067 wt. % in the X direction. These ductile fracture surfaces present small seams and microvoids because of microvoid coalescence by plastic deformation. However, Figure 7.10(d) presents that for the O - 0.067 wt. % sample built in the X direction, there is a notable cleavage facet feature with shallow and elongated dimples, indicating pre-existing defects in the tensile coupons that acted as crack initiation sites, facilitated crack propagation, and caused premature failure. This explains the lower elongation observed in the SR Static Tensile Properties section (section 7.4.3.2).
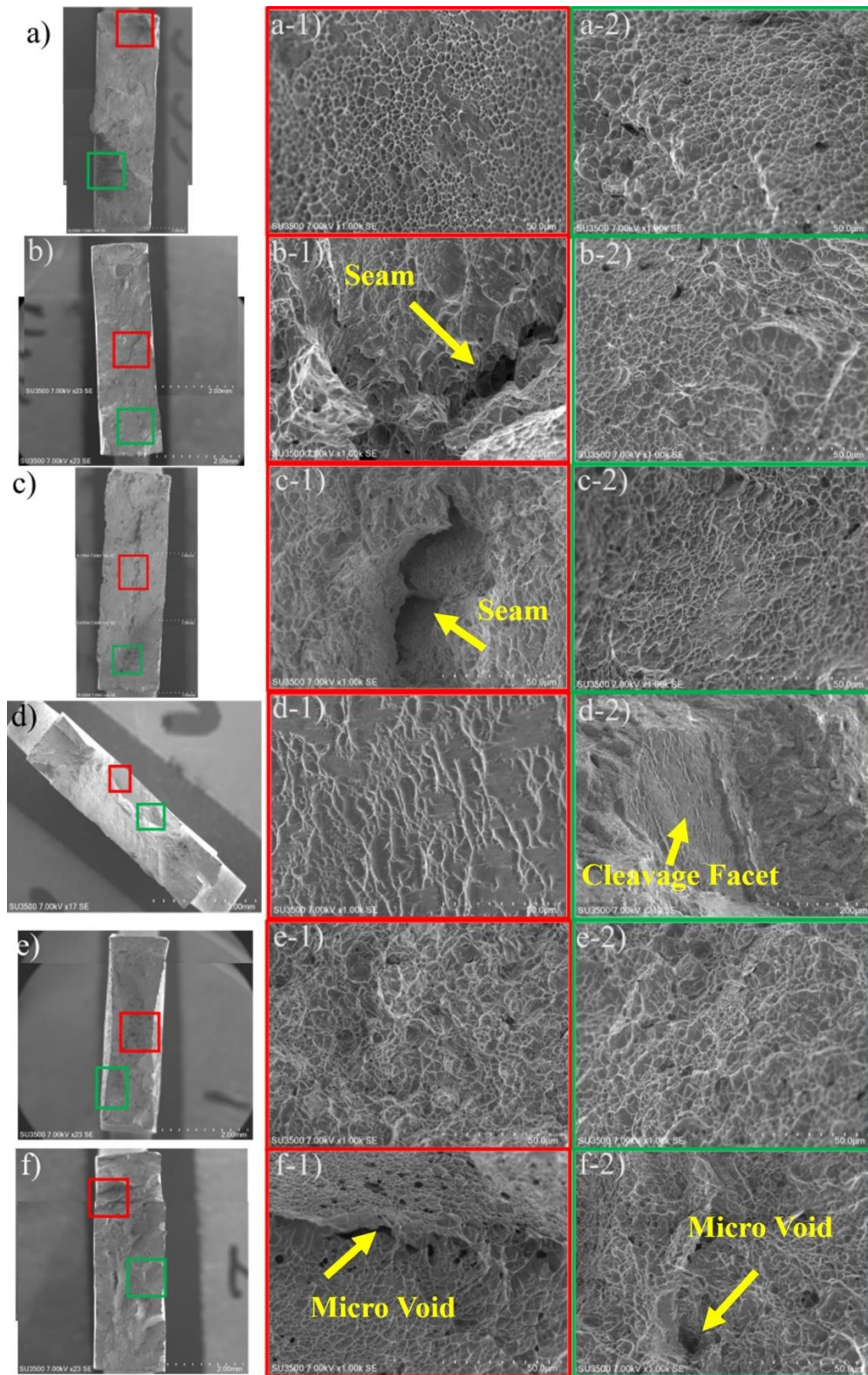
Figure 7.10. (a, c, and e) SEM micrographs of fractography for tensile specimens built in the Z direction with O - 0.05 wt. %, O - 0.067 wt. %, and O - 0.16 wt. %, respectively. (b, d, and f) SEM micrographs of fractography for tensile specimens built in the X direction with O - 0.05 wt. %, O - 0.067 wt. %, and O - 0.16 wt. %, respectively.

7.5 Conclusion

Three wire spools with different oxygen contents were used to produce LWD Ti-6Al-4V deposits. All deposits exhibited typical columnar prior β grain structures due to the high G in the LWD process. An equiaxed morphology was observed along the build height, which was mainly attributed to the altered solidification conditions during the deposition process that promoted CET. Typical basketweave α laths were observed, and α lath widths are statistically similar for all deposits because they were produced with the same process parameters. The deposits with increased oxygen content exhibit dramatically increased tensile strength and hardness, which is attributed to the expansion of lattice parameters restricting the number of slip systems in HCP α-Ti. The contribution of different strengthening mechanisms was analyzed with the YS prediction constitutive equations developed by Hayes et al. [41], and it is confirmed that the major improvements in YS are due to the increase in solid solution strengthening from solute oxygen.

7.6 Acknowledgements

7.7 References

[1] Brandl, E., Schoberth, A., & Leyens, C. (2012). Morphology, microstructure, and hardness of titanium (Ti-6Al-4V) blocks deposited by wire-feed additive layer manufacturing (ALM). Materials Science and Engineering: A, 532, 295-307.

[2] Saboori, A., Gallo, D., Biamino, S., Fino, P., & Lombardi, M. (2017). An overview of additive manufacturing of titanium components by directed energy deposition: microstructure and mechanical properties. Applied Sciences, 7(9), 883.

[3] Shaikh, M. O., Chen, C. C., Chiang, H. C., Chen, J. R., Chou, Y. C., Kuo, T. Y., Ameyama, K., & Chuang, C. H. (2020). Additive manufacturing using fine wire-based laser metal deposition. Rapid Prototyping Journal, 26(3), 473-483.

[4] Brandl, E., Palm, F., Michailov, V., Viehweger, B., & Leyens, C. (2011). Mechanical properties of additive manufactured titanium (Ti–6Al–4V) blocks deposited by a solid-state laser and wire. Materials & Design, 32(10), 4665-4675.

[5] Brandl, E., Baufeld, B., Leyens, C., & Gault, R. (2010). Additive manufactured Ti-6Al-4V using welding wire: comparison of laser and arc beam deposition and evaluation with respect to aerospace material specifications. Phys. Procedia, 5(Pt 2), 595-606.

[6] Mok, S. H. (2007). Deposition of Ti-6Al-4V using a high power diode laser and wire. Doctoral dissertation. University of Nottingham, Nottingham, UK.

[7] Chong, Y., Bhattacharjee, T., & Tsuji, N. (2019). Bi-lamellar microstructure in Ti–6Al–4V: Microstructure evolution and mechanical properties. Materials Science and Engineering: A, 762, 138077.

[8] Tedman-Jones, S. N., McDonald, S. D., Bermingham, M. J., StJohn, D. H., & Dargusch, M. S. (2019). Investigating the morphological effects of solute on the β-phase in as-cast titanium alloys. Journal of Alloys and Compounds, 778, 204-214.

[9] Bermingham, M. J., StJohn, D. H., Krynen, J., Tedman-Jones, S., & Dargusch, M. S. (2019). Promoting the columnar to equiaxed transition and grain refinement of titanium alloys during additive manufacturing. Acta Materialia, 168, 261-274.

[10] Sui, S., Chew, Y., Weng, F., Tan, C., Du, Z., & Bi, G. (2022). Study of the intrinsic mechanisms of nickel additive for grain refinement and strength enhancement of laser aided additively manufactured Ti–6Al–4V. International Journal of Extreme Manufacturing, 4(3), 035102.

[11] Welk, B. A., Taylor, N., Kloenne, Z., Chaput, K. J., Fox, S., & Fraser, H. L. (2021). Use of alloying to effect an equiaxed microstructure in additive manufacturing and subsequent heat treatment of high-strength titanium alloys. Metallurgical and Materials Transactions A, 52, 5367-5380.

[12] Bermingham, M. J., McDonald, S. D., StJohn, D. H., & Dargusch, M. S. (2009). Segregation and grain refinement in cast titanium alloys. Journal of Materials Research, 24(4), 1529-1535.

[13] Meng, X., Min, J., Sun, Z., Zhang, W., Chang, H., & Han, Y. (2021). Columnar to equiaxed grain transition of laser deposited Ti6Al4V using nano-sized B4C particles. Composites Part B: Engineering, 212, 108667.

[14] Bermingham, M. J., McDonald, S. D., Dargusch, M. S., & StJohn, D. H. (2010, October). Effect of oxygen on the β-grain size of cast titanium. In Materials Science Forum (Vol. 654, pp. 1472-1475). Trans Tech Publications Ltd.

[15] Gil, F. J., Aparicio, C., & Planell, J. A. (2002). Effect of oxygen content on grain growth kinetics of titanium. Journal of Materials Synthesis and Processing, 10(5), 263-266.

[16] Kherrouba, N., Bouabdallah, M., Badji, R., Carron, D., & Amir, M. (2016). Beta to alpha transformation kinetics and microstructure of Ti-6Al-4V alloy during continuous cooling. Materials Chemistry and Physics, 181, 462-469.

[17] Sun, B., Li, S., Imai, H., Mimoto, T., Umeda, J., & Kondoh, K. (2013). Fabrication of high-strength Ti materials by in-process solid solution strengthening of oxygen via P/M methods. Materials Science and Engineering: A, 563, 95-100.

[18] Wei, Q., Wang, L., Fu, Y., Qin, J., Lu, W., & Zhang, D. (2011). Influence of oxygen content on microstructure and mechanical properties of Ti–Nb–Ta–Zr alloy. Materials & Design, 32(5), 2934-2939.

[19] Carrozza, A., Aversa, A., Mazzucato, F., Lombardi, M., Biamino, S., Valente, A., & Fino, P. (2020). An innovative approach on directed energy deposition optimization: A study of the process environment's influence on the quality of Ti-6Al-4V samples. Applied Sciences, 10(12), 4212.

[20] Oh, J. M., Lee, B. G., Cho, S. W., Lee, S. W., Choi, G. S., & Lim, J. W. (2011). Oxygen effects on the mechanical properties and lattice strain of Ti and Ti-6Al-4V. Metals and Materials International, 17, 733-736.

[21] Cai, Z., Xiang, T., Bao, W., Chen, J., Gao, T., & Xie, G. (2022). Enhancing strength and ductility of pure titanium by interstitial oxygen atoms. Materials Science and Engineering: A, 854, 143806.

[22] Kwasniak, P., Garbacz, H., & Kurzydlowski, K. J. (2016). Solid solution strengthening of hexagonal titanium alloys: Restoring forces and stacking faults calculated from first principles. Acta Materialia, 102, 304-314.

[23] Yu, Q., Qi, L., Tsuru, T., Traylor, R., Rugg, D., Morris Jr, J. W., Chrzan, DC., & Minor, A. M. (2015). Origin of dramatic oxygen solute strengthening effect in titanium. Science, 347(6222), 635-639.

[24] Yan, M., Xu, W., Dargusch, M. S., Tang, H. P., Brandt, M., & Qian, M. (2014). Review of effect of oxygen on room temperature ductility of titanium and titanium alloys. Powder metallurgy, 57(4), 251-257.

[25] Halisch, C., Milcke, B., Radel, T., Rentsch, R., & Seefeld, T. (2023). Influence of oxygen content in the shielding gas chamber on mechanical properties and macroscopic structure of Ti-6Al-4V during wire arc additive manufacturing. The International Journal of Advanced Manufacturing Technology, 124(3), 1065-1076.

[26] Zhang, G., Lu, X., Li, J., Chen, J., Lin, X., Wang, M., Tan, H., & Huang, W. (2022). In-situ grain structure control in directed energy deposition of Ti6Al4V. Additive Manufacturing, 55, 102865.

[27] Wang, J., Lin, X., Wang, J., Yang, H., Zhou, Y., Wang, C., Li, Q., & Huang, W. (2018). Grain morphology evolution and texture characterization of wire and arc additive manufactured Ti-6Al-4V. Journal of Alloys and Compounds, 768, 97-113.

[28] Sikan, F., Wanjara, P., Gholipour, J., Kumar, A., & Brochu, M. (2021). Thermo-mechanical modeling of wire-fed electron beam additive manufacturing. *Materials*, *14*(4), 911.

[29] ASTM E1409-13. (2021). Standard Test Method for Determination of Oxygen and Nitrogen in Titanium and Titanium Alloys by Inert Gas Fusion 2021. ASTM International, West Conshohocken, PA, USA.

[30] AMS2901. (2014). Heat Treatment of Titanium Alloy Parts. SAE International, Warrendale, PA, USA.

[31] ASTM E8/E8M-15a. (2015) Standard Test Methods for Tension Testing of Metallic Materials, Annual Book of ASTM Standards, ASTM International, West Conshohocken, PA, USA.

[32] ASTM Grade 5-UNS R56400. (2021). Standard Specification for Titanium and Titanium Alloy Bars and Billets. ASTM International, West Conshohocken, PA, USA.

[33] Davis, A. E., Wainwright, J., Sahu, V. K., Dreelan, D., Chen, X., Ding, J., Flint, T., Williams, S., & Prangnell, P. B. (2024). Achieving a Columnar-to-Equiaxed Transition Through Dendrite Twinning in High Deposition Rate Additively Manufactured Titanium Alloys. Metallurgical and Materials Transactions A, 1-23.

[34] Donoghue, J., Davis, A. E., Daniel, C. S., Garner, A., Martina, F., Da Fonseca, J. Q., & Prangnell, P. B. (2020). On the observation of annealing twins during simulating β-grain refinement in Ti–6Al–4V high deposition rate AM with in-process deformation. Acta Materialia, 186, 229-241.

[35] Salgado-Ordorica, M. A., & Rappaz, M. (2008). Twinned dendrite growth in binary aluminum alloys. Acta Materialia, 56(19), 5708-5718.

[36] AMS 4999. (2016). Titanium Alloy Direct Deposited Products 6Al−4V Annealed. SAE International, Warrendale, PA, USA.

[37] Dharmendra, C., Hadadzadeh, A., Amirkhiz, B. S., Lloyd, A., & Mohammadi, M. (2020). Deformation mechanisms and fracture of electron beam melted Ti–6Al–4V. Materials Science and Engineering: A, 771, 138652.

[38] Shrestha, S., Panakarajupally, R. P., Kannan, M., Morscher, G., Gyekenyesi, A. L., & Scott-Emuakpor, O. E. (2021). Analysis of microstructure and mechanical properties of additive repaired Ti–6Al–4V by Direct Energy Deposition. Materials Science and Engineering: A, 806, 140604.

[39] Carroll, B. E., Palmer, T. A., & Beese, A. M. (2015). Anisotropic tensile behavior of Ti–6Al–4V components fabricated with directed energy deposition additive manufacturing. Acta Materialia, 87, 309-320.

[40] Tian, X., Zhu, Y., Lim, C. V. S., Williams, J., Boyer, R., Wu, X., Zhang, K., & Huang, A. (2021). Isotropic and improved tensile properties of Ti-6Al-4V achieved by in-situ rolling in direct energy deposition. Additive Manufacturing, 46, 102151.

[41] Hayes, B. J., Martin, B. W., Welk, B., Kuhr, S. J., Ales, T. K., Brice, D. A., Ghamarian, Iman., Baker, A. H., Haden, C. V., Harlow, D. G., Fraser, H. L., & Collins, P. C. (2017). Predicting tensile properties of Ti-6Al-4V produced via directed energy deposition. Acta Materialia, 133, 120-133.

Chapter 8: General Discussions

8.1 Introduction

AM of metals has been one of the fastest-growing manufacturing technologies because of its capability to produce parts with complicated geometry while reducing the number of generalized wastes and lead time with a low buy-to-fly ratio [1-2]. AM of metals has been widely used in various fields such as aerospace [3], healthcare [4], automotive [5], and consumer products. One of the major variants of AM is the type of feedstock, such as powder or wire. Powder-fed AM processes have attracted more attention than wire-fed processes, mainly due to their potential for more geometric freedom. However, wire-fed AM could provide high deposition rates, low contamination rates, and the ability of producing large-scale parts, which could be beneficial economically. The specific AM process considered in this thesis is the LWD AM approach for large-scale structural applications. The LWD process is characterized by a large number of parameters such as power, travel speed, wire feed diameter, and laser spot size. The selection of parameters is critical as it results in microstructural changes that affect the final mechanical properties.

Titanium alloys, especially α/β Ti-6Al-4V, have been intensively studied over the past few decades due to their high specific strength and excellent corrosion resistance, especially in the aerospace industry. The mechanical properties of Ti-6Al-4V have been shown to be strongly dependent on the alloying element content as well as the microstructural arrangements [6]. The Ti-6Al-4V alloy exhibits complex $\alpha+\beta$ microstructures rich in microstructural features that are interconnected across length scales. In particular, the size and volume fraction of α/β have been shown to have the greatest influence on mechanical properties [7]. Oxygen content can greatly influence material strength, as it is well documented that the addition of oxygen could dramatically enhance the strength and hardness of titanium alloys via solid solution strengthening [8-14].

The conventional way of controlling the microstructure, defects and properties of LWD Ti-6Al-4V components is often achieved by conducting many experiments to explore a large range of process parameters. Achieving high-quality parts by trial and error is not optimal for AM, as it can lead to high costs of feedstock and machines [5]. The rapidly developing mechanistic models can help resolve this problem by providing the connection between process parameters, microstructure, and mechanical properties of a given alloy. Finite element analysis (FEA) has been widely used to

model heat transfer in the AM process. It can predict the output cooling rates, temperature-time history, and melt pool features based on various process variables. The FEA heat transfer model is the core and foundation for other simulation models and physical phenomena such as fluid flow and stress formation. Great progress has been made in predicting the microstructure evolution of Ti-6Al-4V. The kinetics of diffusional phase transformation has been successfully described by the Johnson-Mehl-Avrami-Kolmogorov (JMAK) equation for Ti-6Al-4V [15], which can be used to model the amount of α phase and the size of α lath based on the thermal condition. The complicated inter-connected microstructural features of Ti-6Al-4V alloy, as well as their effects on the mechanical properties, make it quite challenging to build a quantified relationship between them. Over the past few decades, with the rapid development of ANN and GA, a constitutive equation incorporating the key strengthening mechanisms has been developed to predict the YS of Ti-6Al-4V from various quantified microstructural features, which has been proven with high accuracy for DED Ti-6Al-4V components [16].

This thesis aims to propose an adaptive methodology that includes mechanistic models based on recent research efforts to produce qualified LWD Ti-6Al-4V components. The goal of the methodology is to utilize the mechanistic models and adopt the reverse engineering method to assess the acquired microstructure, the needed solidification conditions and the process variables to achieve the required properties. Besides, this thesis aims to fill the knowledge gap on the effects of less studied key LWD process parameters such as wire diameter and oxygen composition on the deposited geometries, the developed microstructure and the subsequent mechanical properties of Ti-6Al-4V components.

8.2 Travel Speed

The travel speed is selected as the first process variable to be investigated as the literature has reported that increasing the travel speed would increase cooling rates, decrease grain size, and result in higher strength [17]. Multiple single-bead Ti-6Al-4V deposits varied in travel speeds were built by LWD. A 3D transient FEA model specified as the experimental deposits, was developed to simulate the LWD process with different travel speeds. The model was validated by comparing temperature data measured by the thermal camera during the deposition process. The deviation in cooling rates at β-transus temperature between measured and modeled results was found to be less than 10%. The main sources of error were considered to be the adjustment during the deposition

process and the modeling assumptions, which neglected liquid flow and convective heat transfer within the melt pool. The FEA model found that after about ten layers of deposition, a thermal balance between heat accumulation and heat loss can be achieved. In other words, the change in cooling rates at β-transus temperature and peak temperature is negligible after deposition of about ten layers. This conclusion confirms the feasibility of the model to simulate the solidification conditions for large deposits with hundreds of layers.

The macrostructure of all deposits is mainly decorated with columnar prior β grains as a result of epitaxial growth due to the high thermal gradient, G, in LWD. Increased cooling rates led to finer grain sizes. However, equiaxed morphology was found in some regions due to CET. The morphology in terms of columnar or equiaxed type was further validated by the solidification map for Ti-6Al-4V [18]. The interruption during the deposition was discussed as the reason for the CET as it provided time for the deposit to cool down and altered the solidification condition, which promoted CET. A more equiaxed morphology was found at the edge of the deposit due to heat accumulation at the edge, which lowered the thermal gradient and promoted CET. Another typical feature is the banding structures along the deposits. These repetitive bands are formed due to the successive thermal cycles that a layer goes through by the deposition of subsequent layers. Due to the cyclic nature and the same thermal history that went through all layers, the zone with the previously described bands is often called the steady state region. The region characterized by the absence of the bands is called the top region. The size of the top region is associated with β-transus isotherm. Increased travel speeds produced a shallower isotherm, resulting in a finer top region. Coarser α laths were found in the steady state region due to the repeated thermal cycles experienced by subsequent deposited layers. The measured α lath size decreased as the travel speed increased due to the increased cooling rate. However, great variation existed for each measurement, indicating the wide distribution of α lath widths. TEM was conducted to quantify the dislocation density in the deposits following the quantification method of Ham [19]. The calculated dislocation density is $8.60 \pm 3.57 * 10^{13}$ m^{-2}, which is reasonable with literature-reported values for AM Ti-6Al-4V.

The tensile properties of all deposits consistently exceeded the minimum DED requirements as set by the AMS4999 specification. Anisotropic tensile properties were found for deposits between the build direction (Z) and the travel direction (X). The anisotropy is attributed to differences in texture, columnar prior β grain morphology, and the presence of grain boundary α from different tensile directions. Increased travel speeds produced a finer microstructure, which induced higher strength. The fractography suggested that the main

failure mechanism involved crack formation and progression through micro-void formation, growth and coalescence. The SEM fractography demonstrated groups of uniformly distributed fine and deep dimpled structures, which indicates a high degree of ductility in titanium alloys. The optical micrographs suggested that crack propagation happened along the grain boundary α. The presence of grain boundary α can facilitate crack propagation and lead to premature failure, which explains the low strength of the deposit with decreased travel speed. Microhardness was found to be statistically similar for all travel speeds, indicating that it is mainly affected by individual lath size rather than collective morphology. However, significantly higher microhardness was found at the interface, which was attributed to the martensite structure. The interface was closer to the substrate, which acted as a heat sink and experienced high cooling rates up to more than 410 K/s, and martensite structure was developed and observed.

The microstructure model adapted in this thesis incorporated the α/β phase fractions prediction model developed by Kelly [20] and the α lath with prediction model developed by Charles and J€arvstra˚t [21]. Temperature-time data from FEA were input and the modeled results were compared with the experimentally measured phase fraction and grain size. The predicted microstructure is in good agreement with the measured experimental microstructure. No statistical difference was observed for the predicted α phase fraction at different travel speeds, as it is mainly affected by the alloying elements. The modeled α lath widths showed decreasing trends with increased cooling rates as well. The constitutive equation developed by Hayes et al. [16] was used in this thesis to predict YS from microstructural features. This equation is validated by experimental YS with deviation of less than 10%. Besides, this model proved that the maximum change in the YS difference due to the Hall-Petch strengthening term from the measurement of α lath width is less than 3.5 MPa, which explains the similar strength observed for samples with different α lath widths due to the different cooling rates from various travel speeds. The range of α lath widths resulted in this study providing negligible strength differences.

8.3 Wire Diameter

Thesis selected wire diameter as another studied process variable since there is no systematic investigation on the effect of wire diameter for LWD Ti-6Al-4V. Six single bead Ti-6Al-4V deposits with various wire diameters were produced by LWD. The major issue caused by large wire diameters is the low dimensional accuracy and geometry consistency, especially for laser beams

with low intensity and small beam diameters. Layer widths and heights were measured for all deposits. Layer heights were statistically similar for all wire diameters as the predefined distance between two layers was set the same for all depositions. Layer height increased as expected with the increase of wire diameter, as more volume of material was deposited during each time period. However, the increased wire diameter led to inconsistent wall geometry due to the non-uniform melt pool size generated from the unstable deposition process. Gibson et al. [22] reported an inconsistent melt pool profile as well with a large wire diameter, and the authors proposed to resolve this issue by creating a closed-loop control of the melt pool size by modulating the laser power, travel speed, and/or deposit rate. The unstable deposition process with increased wire diameter was further confirmed by the thermal history obtained from the thermal camera. The recorded thermal data for the large wire diameter indicated a dramatic fluctuation in the cooling rates during the first three layers, rather than slightly decreased trends due to heat accumulation with the deposition of the subsequent layers. The FEA heat transfer model from the previous section was adapted to compute the thermal history for the wire diameter set of deposits as well. The calculated cooling rates of all the layers from the FEA demonstrated that increased wire diameter induced more heat accumulation, which resulted in decreased cooling rates for the subsequent deposition of the layers.

The epitaxially grown columnar prior β grain is the major macrostructure for all deposits. Increased wire diameter led to coarser grains due to higher heat accumulation. Similarly, equiaxed grains can be found at the edge of the deposits since heat accumulation reduced G and promoted CET. The deposits fabricated with increased wire diameter demonstrated a higher percentage of equiaxed grains due to more heat accumulation, and equiaxed grains can be observed in non-edge regions, indicating CET from the altered solidification conditions, which could be due to unstable thermal conditions associated with increased wire diameter. The microstructural characterization demonstrated that, besides the basketweave morphology, the grain boundaries of prior β grain were mostly decorated with grain boundary α. For deposits with increased wire diameter, colony α structure was observed near grain boundary α as a result of increased heat input and decreased cooling rate, which kinetically favoured diffusion-controlled grown colony α structure. The measurements of the α lath width showed decreased grain size with increased wire diameter, and the deviation was larger, indicating a wider distribution of α lath width associated with increased wire diameter.

175

As expected, the deposits with increased wire diameter demonstrated reduced tensile strength due to coarser grains. The anisotropic tensile properties between the Z and X directions were similar to the previous section. It is well known that the grain boundary α can dramatically reduce elongation by furnishing a preferential path for damage accumulation along the prior β grain boundary [23-24]. The average aspect ratio of prior β grains in the gauge were calculated for all tensile coupons to understand the dominant morphology: either columnar or equiaxed. A low aspect ratio was found for coupons extracted near the edge of the deposit, indicating an equiaxed morphology. Strong correlations were observed between varied aspect ratios of prior β grains and corresponding elongation values, and lower elongation was found to be associated with these tensile coupons since more amount of the grain boundary α phase was exposed to a tensile opening mode. However, no significant difference in tensile strength was observed for tensile coupons with varied aspect ratios of prior β grain. This lack of correlation can be attributed to the small amount of grain intercepts that would effectively induce the grain boundary strengthening mechanisms [25]. The deposits with increased wire diameter showed dramatically reduced elongation. The reduced elongation was discussed to be attributed to three aspects. First, the fractography showed seam and void defects for deposits with increased wire diameter, possibly related to incomplete fusion, which could act as crack initiation sites and reduce elongation. Besides, the observed colony α structure near prior β grain boundaries for deposits with increased wire diameter can facilitate dislocation movement and accumulation and lead to premature failure. Another feature observed was the terrace-like structure, which corresponds well to the width of the prior β grains. The reduced elongation for deposits with increased wire diameter could be due to the increased amount of equiaxed morphology that promoted these terrace-like fracture structures indicating crack propagation along prior β grain boundaries.

The experimental results such as thermal history, quantified microstructural features, and YS were further used to compare with the modeled results and showed good agreement with a deviation of less than 10%. The YS model suggested that the YS difference for deposits fabricated with various wire diameters was mainly due to the difference in the contribution of the Hall-Petch strengthening mechanism and the solid solution strengthening mechanism due to the different wire stocks used in the deposition.

8.4 Oxygen Content

Another process variable studied in this thesis is the oxygen content in the wire feedstock. It is well known that the addition of oxygen could dramatically enhance the strength and hardness of titanium alloys through solid solution strengthening. Six single bead Ti-6Al-4V deposits were produced by LWD with wires of different oxygen contents in two geometries to accommodate the need to extract tensile coupons from the Z and X directions. Inert gas fusion was conducted on samples extracted from different heights along the build for all deposits to ensure the homogeneous distribution of oxygen and consistency with the specification of the wire feedstock. All deposits were fabricated under the same set of processing parameters; therefore, solidification conditions were expected to be similar for all deposits.

Besides the columnar prior β grains resulting from the high G in the LWD process, the macrostructure exhibits a certain percentage of equiaxed grains. Two possible mechanisms have been discussed to be behind the CET. The first mechanism could be due to the potent growth-restricting solutes in titanium alloys. These solutes could provide more nucleation sites, increase the constitutional undercooling (CU) zones, and promote CET. Literature has reported significant prior β grain refinement with the increase of oxygen content up to 0.22 wt.% [26]. However, this mechanism was discussed to be less dominant in this study, as the deposits with decreased oxygen content managed to exhibit a visibly higher percentage of equiaxed grains than the deposits with increased oxygen content. Another mechanism considered in the study was the altered solidification conditions that promoted CET during the deposition process. This change could be induced by heat accumulation, instability of the melt pool, and interruption of the build. For example, heat accumulation at the edge of the deposit could lower the G and promote CET. Thus, more equiaxed grains were observed at the edge, which is consistent with the resultant macrostructure from previous sections. Interruption during deposition was discussed to play a major role in changing the solidification conditions and promoting CET in this study. One deposit was taken as a case study to investigate the effect of interrupted deposition on CET. By knowing the time and location of the interruptions, it was found that there was a strong correlation between the pattern of morphology and the location of the interruptions. The columnar morphology was disrupted by the first thirty minute interruption, which cooled down the parts and promoted CET, and appeared later due to heat accumulation with the deposition of subsequent layers. This pattern of morphology was repeated with the second 21-minute interruption. Further research can be conducted to utilize interruption

during deposition to control the grain morphology of the deposits. The quantified average α lath width for all deposits appeared statistically similar, as expected, since the thermal conditions were similar for all deposits.

The deposits with increased oxygen content demonstrated dramatically increased tensile strength (733 MPa/wt.% [O] on 0.2% YS and 822 MPa/wt.% [O] on UTS). Dramatic increase in microhardness is observed with the increase of oxygen content (333 HV/wt.% O). Many researchers have investigated the dramatic strengthening mechanism for titanium alloys by oxygen. The major mechanisms can be summarized as follows. The addition of oxygen content could increase the lattice parameter of titanium alloys since oxygen can fit well in the octahedral vacancy of α-Ti since it shares a similar radius [10]. The interstitial oxygen solute could dramatically enhance the restoring forces and stacking fault energies for titanium alloys and improve solid solution strengthening by suppressing dislocation emission in all slip systems [13]. Yu et al. [14] reported that with a high amount of oxygen content, the displacement field was more tightly conformed to the screw dislocation core from the observation of high-resolution TEM, and this could result in a strong pinning effect on screw dislocation, which strengthened the alloys. However, the addition of oxygen solute could be detrimental to the ductility as Ti-O bands can stiffen the crystal structure, prevent atomic relaxation, and limit the basal, prismatic and pyramidal dislocations nucleation [12]. In this study, the deposits with increased oxygen content maintained both excellent tensile strength and excellent elongation. The fractography demonstrated fine and deep dimple structures, indicating a high degree of ductility for the deposits.

The experimental YS was compared with the modeled YS, and the model showed credible accuracy. Besides, it was confirmed by the YS model that the major strength improvements for deposits with increased oxygen content were due to the contribution of the solid solution strengthening mechanism.

8.5 Case Study – Implementation of the Methodology

In this section, a case study is conducted to implement the developed methodology to a space component from Chekir [1]. Based on the methodology, a combination of travel speed, wire diameter, and oxygen content values are proposed to fabricate the space component with satisfied service requirements/

Figure 8.1 presents the CAD model and identifications of the individual part geometries. For the different regions, Chekir [1] selected different printing strategies respectively. The key geometrical difference is the thickness between Region II and Region III. Region II is characterized by a thickness of 1.1 mm; thus, a single-bead deposition was employed. In contrast, Region III is characterized by a thickness of 6.1 mm, which required a deposition of multiple beads along the same layer. As a result, different microstructural features were developed in Region II and Region III due to the different thermal histories. More percentage of globular α grains and grain boundary α were observed in Region III than Region II due to the slower cooling rates experienced in Region II. These types of microstructures tend to weaken the mechanical properties. Chekir [1] only reported tensile properties of samples produced at Region III, and the tensile strengths were below the typical strengths of the wrought Ti-6Al-4V due to the coarser microstructure.
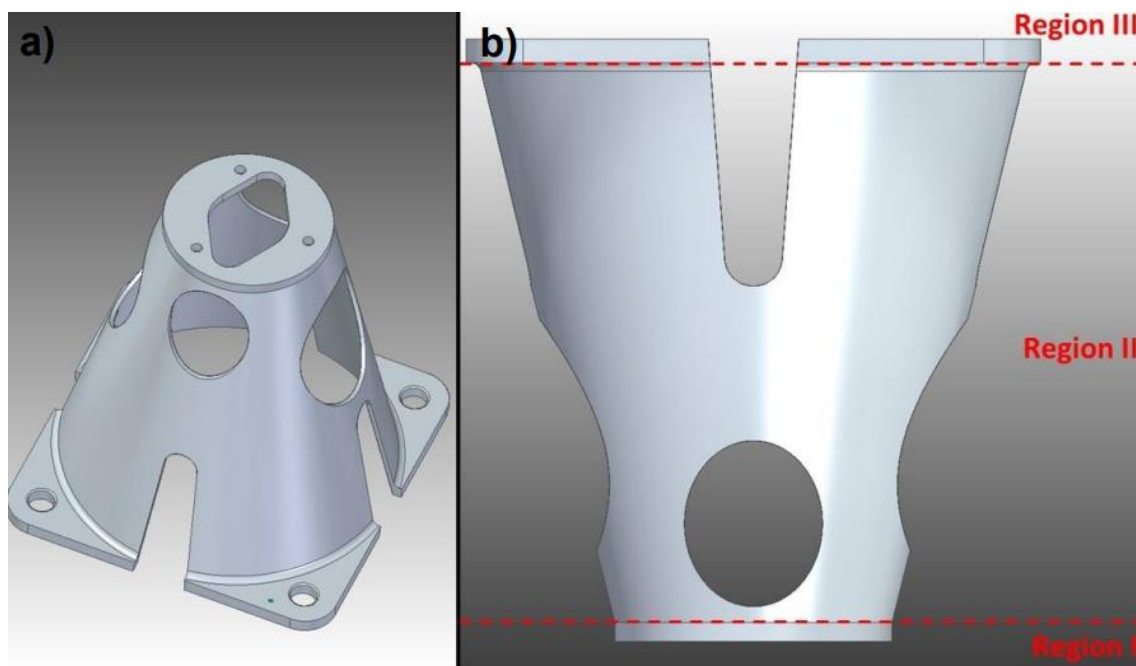
[81]Figure 8.1. a) CAD model of the space bracket, adapted from Chekir [1]. b) The cross-section view with identification of the individual part geometries, adapted from Chekir [1].

Chapters 5, 6, and 7 have summarized the effect of travel speed, wire diameter, and oxygen content on the thermal history, microstructure and mechanical properties of LWD-developed Ti-6Al-4V. Furthermore, through a combination of thermos-microstructural-mechanical models, the

predictability of YS through the combination of process parameters was better understood. To fabricate an eligible space component, a requirement of YS of above 800 MPa was set. Due to the geometrical differences between Region II and Region III, Table 8.1 presents the proposed different combinations of process parameters, respectively. Process parameters besides the ones listed in Table 8.1, such as laser power, material feed rate, etc., are tailored according to the selections of travel speeds and wire diameters to ensure a stable deposition process with minimum defects generated.

A travel speed of 7.2 mm/s was selected for both regions because the finest microstructure and best mechanical properties without developing defects were produced with this travel speed. Chapter 6 presented that the deposits produced with wire diameters of 1.1 and 1.6 mm showed increased defects detrimental to tensile properties. Therefore, a wire diameter of 0.8 mm was selected for both regions. Larger wire diameters could be considered when employing a laser beam with different configurations such as spot size. For Region II with a thickness of 1.1 mm, lower heat accumulation and higher cooling rate were expected than in Region III. To be above the YS of 800 MPa, the proposed oxygen content is larger than 0.05 wt. % considering that the deposits produced at 7.2 mm/s with a wire spool of oxygen content of 0.067 wt. % showed an average of 843 MPa. An increase of 147 MPa in YS by an increase of 0.1 wt. % in oxygen content was predicted by the methodology. Therefore, a minimum oxygen content of 0.05 wt. % was proposed for Region II. On the other hand, Region III is expected to develop larger heat accumulation and a slower cooling rate than in Region II. Therefore, to compensate for the loss of YS by the microstructure, a higher oxygen content was proposed to increase the YS through solid solution strengthening. Chekir [1] reported an average of 748 MPa for YS of Region III. Chapter 7 reported an average of 896 MPa for YS of deposits produced at an oxygen content of 0.16 wt. %. Therefore, considering that the predicted enhancement in YS by oxygen contents is 147 MPa/0.1 wt. %, the proposed oxygen content for Region III is larger than 0.1 wt. %. To validate the methodology, the fabrication of the space component with the proposed process parameters is planned in the near future.

[24]Table 8.1. Combinations of process parameters proposed for Region II and III.

Parameters	Region II	Region III
Travel speed	7.2 mm/s	7.2 mm/s

Wire diameter	0.8 mm	0.8 mm
Oxygen content	>0.05 wt. %	>0.1 wt.%

8.6 References

[1] Chekir, N. (2019). Laser wire deposition additive manufacturing of Ti-6Al-4V for the aerospace industry. McGill University (Canada).

[2] DebRoy, T., Mukherjee, T., Wei, H. L., Elmer, J. W., & Milewski, J. O. (2021). Metallurgy, mechanistic models and machine learning in metal printing. Nature Reviews Materials, 6(1), 48-68.

[3] Shinde, M. S., & Ashtankar, K. M. (2017). Additive manufacturing–assisted conformal cooling channels in mold manufacturing processes. Advances in mechanical engineering, 9(5), 1687814017699764.

[4] Bose, S., Ke, D., Sahasrabudhe, H., & Bandyopadhyay, A. (2018). Additive manufacturing of biomaterials. Progress in materials science, 93, 45-111.

[5] DebRoy, T., Mukherjee, T., Milewski, J. O., Elmer, J. W., Ribic, B., Blecher, J. J., & Zhang, W. (2019). Scientific, technological and economic issues in metal printing and their solutions. Nature materials, 18(10), 1026-1032.

[6] Haden, C. V., Collins, P. C., & Harlow, D. G. (2015). Yield strength prediction of titanium alloys. Jom, 67, 1357-1361.

[7] Collins, P. C., Koduri, S., Welk, B., Tiley, J., & Fraser, H. L. (2013). Neural networks relating alloy composition, microstructure, and tensile properties of α/β-processed TIMETAL 6-4. Metallurgical and Materials Transactions A, 44, 1441-1453.

[8] Sun, B., Li, S., Imai, H., Mimoto, T., Umeda, J., & Kondoh, K. (2013). Fabrication of high-strength Ti materials by in-process solid solution strengthening of oxygen via P/M methods. Materials Science and Engineering: A, 563, 95-100.

[9] Wei, Q., Wang, L., Fu, Y., Qin, J., Lu, W., & Zhang, D. (2011). Influence of oxygen content on microstructure and mechanical properties of Ti–Nb–Ta–Zr alloy. Materials & Design, 32(5), 2934-2939.

[10] Carrozza, A., Aversa, A., Mazzucato, F., Lombardi, M., Biamino, S., Valente, A., & Fino, P. (2020). An innovative approach on directed energy deposition optimization: A study of the process environment's influence on the quality of Ti-6Al-4V samples. Applied Sciences, 10(12), 4212.

[11] Oh, J. M., Lee, B. G., Cho, S. W., Lee, S. W., Choi, G. S., & Lim, J. W. (2011). Oxygen effects

on the mechanical properties and lattice strain of Ti and Ti-6Al-4V. Metals and Materials International, 17, 733-736.

[12] Cai, Z., Xiang, T., Bao, W., Chen, J., Gao, T., & Xie, G. (2022). Enhancing strength and ductility of pure titanium by interstitial oxygen atoms. Materials Science and Engineering: A, 854, 143806.

[13] Kwasniak, P., Garbacz, H., & Kurzydlowski, K. J. (2016). Solid solution strengthening of hexagonal titanium alloys: Restoring forces and stacking faults calculated from first principles. Acta Materialia, 102, 304-314.

[14] Yu, Q., Qi, L., Tsuru, T., Traylor, R., Rugg, D., Morris, J. W., Asta, M., Chrzan, D. C., & Minor, A. M. (2015). Origin of dramatic oxygen solute strengthening effect in titanium. Science, 347(6222), 635–639.

[15] Baykasoglu, C., Akyildiz, O., Candemir, D., Yang, Q., & To, A. C. (2018). Predicting microstructure evolution during directed energy deposition additive manufacturing of Ti-6Al-4V. Journal of Manufacturing Science and Engineering, 140(5), 051003.

[16] Hayes, B. J., Martin, B. W., Welk, B., Kuhr, S. J., Ales, T. K., Brice, D. A., Ghamarian, I., Baker, A. H., Haden, C. H., Harlow, D. G., Fraser, H. L., & Collins, P. C. (2017). Predicting tensile properties of Ti-6Al-4V produced via directed energy deposition. Acta Materialia, 133, 120-133.

[17] Narayana, P. L., Kim, J. H., Lee, J., Choi, S.-W., Lee, S., Park, C. H., Yeom, J.-T., Reddy, N. G. S., & Hong, J.-K. (2021). Optimization of process parameters for direct energy deposited Ti-6Al-4V alloy using neural networks. The International Journal of Advanced Manufacturing Technology, 114(11–12), 3269–3283.

[18] Brandl, E., Palm, F., Michailov, V., Viehweger, B., & Leyens, C. (2011). Mechanical properties of additive manufactured titanium (Ti–6Al–4V) blocks deposited by a solid-state laser and wire. Materials & Design, 32(10), 4665-4675.

[19] Ham, R. K. (1961). The determination of dislocation densities in thin films. Philosophical Magazine, 6(69), 1183-1184.

[20] Kelly, S. M. (2004). Thermal and microstructure modeling of metal deposition processes with application to Ti-6Al-4V. Doctoral dissertation. the Faculty of the Virginia Polytechnic Institute and State University, Blacksburg, Virginia, USA.

[21] Charles, C., & J€arvstra˚t, N. (2009). Modelling Ti–6Al–4V Microstructure by Evolution Laws Implemented as Finite Element Subroutines: Application to TIG Metal Deposition. Eighth International Conference on Trends in Welding Research (TWR), Pine Mountain, GA, June 1–6,

pp. 477–485.

[22] Gibson, B. T., Bandari, Y. K., Richardson, B. S., Henry, W. C., Vetland, E. J., Sundermann, T. W., & Love, L. J. (2020). Melt pool size control through multiple closed-loop modalities in laser-wire directed energy deposition of Ti-6Al-4V. Additive Manufacturing, 32, 100993.

[23] Carroll, B. E., Palmer, T. A., & Beese, A. M. (2015). Anisotropic tensile behavior of Ti–6Al–4V components fabricated with directed energy deposition additive manufacturing. Acta Materialia, 87, 309-320.

[24] Tian, X., Zhu, Y., Lim, C. V. S., Williams, J., Boyer, R., Wu, X., Zhang, K., & Huang, A. (2021). Isotropic and improved tensile properties of Ti-6Al-4V achieved by in-situ rolling in direct energy deposition. Additive Manufacturing, 46, 102151.

[25] Keist, J. S., & Palmer, T. A. (2016). Role of geometry on properties of additively manufactured Ti-6Al-4V structures fabricated using laser based directed energy deposition. Materials & Design, 106, 482-494.

[26] Bermingham, M. J., McDonald, S. D., StJohn, D. H., & Dargusch, M. S. (2009). Segregation and grain refinement in cast titanium alloys. Journal of Materials Research, 24(4), 1529-1535.

Chapter 9: Conclusions and Future Work

This research proposed a reverse-engineering-based manufacturing methodology composed of three mechanistic models for the fabrication of LWD Ti-6Al-4V deposits. A series of coupons with varied travel speeds, wire diameters and oxygen contents were fabricated to validate the methodology. The effect of travel speed, wire diameter and oxygen content on the thermal history, microstructure and mechanical properties of LWD Ti-6Al-4V deposits were also investigated. The main conclusions can be summarized as follows:

1. This research built a new platform composed of three mechanistic models to predict and control the thermal history, microstructure and YS of LWD Ti-6Al-4V deposits. A FEA model was developed to predict the thermal history under various processing conditions. A microstructure model was developed to predict α/β phase fractions and α lath widths, which referenced the well-documented JMAK-based phase fraction prediction model and the Arrhenius equation. The constitutive equations composed of major strengthening mechanisms were used to predict the YS and analyze the contributions of different strengthening mechanisms to the absolute total YS. All three models were validated by comparing them with the experimental results.

2. Increasing travel speeds resulted in faster cooling rates, finer microstructure and higher strengths. In this study, statistically different grain sizes and tensile properties only existed between deposits produced at 7.2 mm/s and 2.1 mm/s, which means that the travel speeds need to be large enough to induce statistically different properties.

3. Nonuniform wall profiles and inconsistent melt pool sizes were found for deposits produced with wire diameters of 1.1 mm and 1.6 mm, which indicated that the large heat accumulation associated with large wire diameters led to an unstable thermal condition. Furthermore, the unstable deposition process associated with wire diameters of 1.1 mm and 1.6 mm promoted more defects as observed from the fracture surfaces. In addition, more colony α and grain boundary α were observed due to larger heat accumulation associated with wire diameters of 1.1 mm and 1.6 mm. As a result, the deposits produced with wire diameters of 1.1 mm and 1.6 mm showed lower elongation and strengths.

4. Increasing oxygen content led to a dramatic increase in microhardness and strengths. The solid solution strengthening by interstitial oxygen was found to be the largest contribution to the absolute total YS.

5. An interesting relation between the interruption during deposition and the prior β grain morphology was found in this study. The interruption during deposition can change the solidification conditions and promote CET.

6. Lower elongation was found for tensile coupons extracted from the edge of the deposit in the Z direction. This is because more equiaxed grains were developed on the edge due to heat accumulation. As a result, more amounts of grain boundary α are exposed to a tensile opening mode compared to center-closed coupons where columnar prior β grains are the dominant structure. A strong correlation was found between the average aspect ratio of the prior β grains and the elongation of the corresponding tensile coupons for deposits produced in the Z direction. Lower elongations were found to be associated with lower aspect ratios due to more grain boundary α.

7. Anisotropic strength was found for all deposits between the Z and X directions. The deposits in the X direction exhibited higher strengths than in the Z direction due to the difference in texture, the columnar β grain morphology, and the presence of grain boundary α from different tensile directions. However, elongations were statistically similar between the Z and X directions because of the equiaxed structure induced by the altered solidification conditions.

8. A case study on a space component was discussed to implement the methodology. Due to the geometrical difference between the two regions within the component, two different recipes of process parameters were proposed for Region II and Region III to satisfy the required YS of 800 MPa. Future work focuses on fabricating the space component with the proposed parameters to validate the feasibility of the methodology.

Chapter 10: Contributions to the Original Knowledge

Thesis summarized the contributions to the original knowledge as follows:

1. This research proposed a platform using three mechanistic models to quantitively control the thermal history, microstructure, and YS of Ti-6Al-4V produced by LWD.
2. The effect of wire diameter on the wall profile, thermal history, microstructure, and mechanical properties for LWD Ti-6Al-4V deposits was studied for the first time.
3. The effect of interruption during deposition on the CET and morphology of the prior β grains for LWD Ti-6Al-4V deposits were investigated for the first time.
4. The effect of wire spools with different oxygen contents on the microstructure, and mechanical properties for LWD Ti-6Al-4V deposits was studied for the first time.
5. For the first time in literature, a 10-layer FEA model was used to infer the cooling rates of the LWD Ti-6Al-4V deposit with hundreds of layers by investigating the evolution of cooling rates and peak temperatures with the layer.
6. For the first time in literature, the microstructure model to predict α/β phase fractions and α lathe width based on the α/β phase transformation kinetics and the Arrhenius equation were validated by experimental data of Ti-6Al-4V deposits produced by LWD.
7. For the first time in literature, the constitutive equations to predict the YS were validated by experimental YS of Ti-6Al-4V deposits produced by LWD.
8. For the first time in the literature, the research proposed a recipe of processing parameters for a space component to satisfy the required YS by implementing the proposed methodology.